# SETUP OF A PROTOTYPE FOR THE SHIP SPECTROMETER STRAW TRACKER

## Aufbau eines Prototyps für den SHiP Spektrometer Straw Tracker

Abschlussarbeit zur Erlangung des akademischen Grades

Master of Science

im Studiengang Physik

an der

Universität Hamburg

Fakultät für Mathematik, Informatik und Naturwissenschaften

Fachbereich Physik

von

Benedict Oliver Albert Kaiser

geboren am

12.01.1995 in Tübingen

Vorgelegt am:     10. Oktober 2019
Erstgutachterin:  Frau Prof. Dr. Caren Hagner
Zweitgutachter:   Herr Dr. Daniel Bick

# Aufbau eines Prototyps für den SHiP Spectrometer Straw Tracker

Benedict Oliver Albert Kaiser
16. Oktober 2019

**Zusammenfassung**

Das „Search for Hidden Particles" Experiment am CERN ist ein multifunktionales beam-dump Experiment welches 400 GeV Protonen verwenden wird und sich momentan in der Entwurfsphase befindet. Eines der Hauptziele von SHiP ist die erstmalige Detektion der schweren neutralen Leptonen (engl. HNLs), welche unter anderem dunkle Materie sowie die baryonische Asymmetrie und Neutrinomassen erklären können. Dafür wird SHiP aus einer Vielzahl diverser Subdetektoren bestehen, wovon der „Spektrometer Straw Tracker" (SST) ein Teil ist. Seine Aufgabe wird die Rekonstruktion der Vertizes und der Massen der verborgenen Teilchen sein. Der SST wird aus vier Stationen bestehen, wobei jede Station aus einem mit Straw-Modulen bestückten Stahlrahmen bestehen wird. Pro Station werden insgesamt ca. 4000 Straws mit einer bisher präzedenzlosen Länge von 5 m eingesetzt. In dieser Masterarbeit wird entscheidende Entwicklungsarbeit für die Auslegung des SSTs geleistet. Dazu wird ein Funktionsmuster, bestehend aus einer einzelnen Straw, entworfen, aufgebaut und in Betrieb genommen. Driftzeitspektren kosmischer Myonen sowie die Signalabschwächung entlang der Röhre und das Rauschen werden vermessen. Im nächsten Schritt wird ein Prototyp mit vier Röhren entwickelt und aufgebaut, mit dem Ziel das für den SST vorgeschlagene Design zu testen. Es wird gezeigt, dass sich sowohl der Durchhang der Straws als auch der Durchhang der Anodendrähte im erwarteten Bereich befinden. Weiterhin werden Schäden an den Straws, welche insbesondere beim Zusammenbau des Prototyps leicht entstehen können, mittels eines Rasterelektronenmikroskops untersucht. Abschließend werden der aktuelle Status der Integration des Designs in größere Module sowie der Stahlrahmen präsentiert.

# Setup of a prototype for the SHiP Spectrometer Straw Tracker

Benedict Oliver Albert Kaiser

October 16, 2019

**Abstract**

The 'Search for Hidden Particles' (SHiP) experiment at CERN is a multi-purpose beam-dump experiment utilising $400\,\text{GeV}$ protons that is currently in the design phase. One of SHiP's main goals is the detection of heavy neutral leptons (HNLs) which can, amongst others, explain dark matter, the universe's baryonic asymmetry and non-zero neutrino masses. To fulfil its goals the SHiP detector consists of various different subdetectors, one of which is the Spectrometer Straw Tracker (SST). The SST's main goal is the reconstruction of the hidden particles' masses and trajectories and will consist of four stations. Each station is planned to consist of a large steel frame in which several straw tube modules will be installed. In total, each frame will hold roughly 4000 straw tubes with an unprecedented length of $5\,\text{m}$. In this thesis crucial prototyping for the design of the SST is performed. A functional model consisting of a single straw tube is designed, assembled and commissioned. Drift-time spectra of cosmic muons as well as the attenuation along the straw tube and the noise are measured. Moreover, a prototype using four straws is designed and assembled to test the proposed mechanical design for the SST. The sagging of the straw tubes and the anode wires are measured to be within the expected range. Furthermore, damages to the straw tubes which can occur during the assembly are analysed using a scanning electron microscope. Lastly, the current status on the large scale integration of the straw tubes into modules and the large mounting frames is presented.

*'Neutrinos, they are very small.*
*They have no charge and have no mass*
*And do not interact at all.*
*The earth is just a silly ball*
*To them, through which they simply pass,*
*Like dustmaids down a drafty hall*
*Or photons through a sheet of glass.*
*They snub the most exquisite gas,*
*Ignore the most substantial wall,*
*Cold-shoulder steel and sounding brass,*
*Insult the stallion in his stall,*
*And, scorning barriers of class,*
*Infiltrate you and me! Like tall*
*And painless guillotines, they fall*
*Down through our heads into the grass.*
*At night, they enter at Nepal*
*And pierce the lover and his lass*
*From underneath the bed - you call*
*It wonderful; I call it crass. '*

John Updike, 'Cosmic Gall'. In *The New Yorker*, December 17, 1960 P. 36

# CONTENTS

# INTRODUCTION

In the current form of the Standard Model (SM) of particle physics quarks are the building blocks of hadrons. In total, there are six different quarks named *up, down, charm, strange, top* and *bottom.* They are accompanied by an equally large set of six leptons, the *electron, muon, tau* and their corresponding *neutrinos*. Together with the gauge bosons $W, Z^{\pm}$ and $\gamma$ they form the elementary particles. Quarks carry colour charge between which, according to quantum chromodynamics (QCD), the strong interaction is mediated through gluons. The electroweak theory describes the weak and the electromagnetic force as two manifestations of a single underlying interaction. Together with the QCD the electroweak theory forms the Standard Model of Particle physics [Gia09]. The SM describes the building blocks of matter as well as the interactions among themselves well. However, in recent years a number of observations were made which cannot be explained using the Standard Model. These include the observed imbalance between baryonic and antibaryonic matter within the universe, the existence and nature of dark matter and neutrino oscillations. To accommodate these observations the SM can be extended by three, hitherto undiscovered, Heavy Neutral Leptons. This extension results in the Neutrino Minimal Standard model ($\nu$MSM).

Amongst other physical goals such as the first direct discovery of the anti-tau-neutrino the discovery of these Heavy Neutral Leptons is a main goal of the SHiP experiment. SHiP, meaning 'Search for Hidden Particles' is a multi-purpose beam-dump experiment utilising 400 GeV protons accelerated by CERN's Super Proton Synchrotron (SPS). The SHiP experiment will consist of various detectors such as a $\tau$-neutrino detector and the Hidden Sector Detector. Part of the Hidden Sector Detector is the Spectrometer Straw Tracker (SST), whose main goal is to reconstruct the vertices and masses of the hidden particles. To minimise background signals the SST will consist of four stations that each use approximately 4000 straw tubes – a form of gaseous ionisation detector. Multiple straw tubes together will be mounted in modules, which in turn are installed in a large mounting frame. With a length of five metres the straw tubes used for the SHiP experiment have an unprecedented length.

It is thus of the utmost importance to design a series of functional models and prototypes of the SST that allow to test the performance and, most importantly, the mechanical design. Within the scope of this thesis, a functional model consisting of a single five metre long straw tube is successfully designed and assembled using a simple but effective mounting technique. The goal of the functional mode is to test a simple, single straw tube setup under laboratory conditions. First tests and measurements, including drift-time spectra and the signal attenuation along the straw tube are performed.

For straw tubes in general and for long ones in particular sagging is a large problem. Both the anode wire and the straw itself experience gravitational sag. However, the sagging behaviour of both parts differs resulting in a net wire displacement that changes the electrical field inside the straw and thus the signals. Moreover, it can also promote potentially damaging sparkovers. It is thus critical to find measures that alleviate the straws' sagging. In this thesis a hybrid design to minimise the sagging is presented. It consists of packs of tensioned straw tubes that are glued together for self-support and additionally held by an external carbon fibre tow. Due to the tensioning, the gas pressure, and material relaxation large forces of up to 25 t act dynamically on each mounting frame. This can result in significant bending of the mounting frame and can thus elongate the straw tubes and anode wires mounted within it. However, the range in which the straws and the wires can be elongated is limited. Thus, the design of a suitable mounting frame that is as light as possible but sufficiently strong is highly important. The design evolution of the mounting frame including simulation results of the mechanical load capacity, as well as the design evolution of the modules, are also outlined within this thesis.

Mounting the straw tubes to the modules while ensuring adequate gas flow and a proper high voltage supply is a difficult task that requires a fairly complex mechanical design. While large numbers of eight metre long drift-tubes, another type of gaseous ionisation detector similar to straw tubes, were successfully instrumented by the Hamburg University in the OPERA experiment the requirements for straw tubes and for the SHiP SST are slightly different. In this thesis, a possible mechanical design is presented. To test the suitability of this design a prototype using four straw tubes with a length of slightly more than five metres is designed and built. Moreover, the sagging of both the straws and the anode wires is determined using an optical microscope and an optical level. To measure the wire sagging a high power LED system is required that shines through the straw tube and thus makes the wire visible. The LED system is developed from ground up.

Another aspect that is examined within this thesis are surface analyses of the conductive coating on the inside of a straw tube. Due to

their nature straw tubes are highly sensitive objects requiring very careful handling. Surface damages such as scratches or kinks can easily occur, not only during transport but especially during the installation process. Using a scanning electron microscope artificially caused damages to a straw tube's coating are analysed. Moreover, the question of whether or not tensioning and thus elongating the straws can cause significant damage to the coating is pursued. The difficulty in this measurement lies in the fact that the sample must be placed inside the microscope while simultaneously being elongated highly accurately. To do so, a special straw tensioning frame is designed.

This thesis is divided in two parts, with part i covering the theoretical basics. Here, chapter 2 outlines neutrino physics. A focus is placed on the Standard Model of particle physics, the history of the neutrino from its 'invention' until today and the properties of the neutrino. The SHiP experiment is outlined in chapter 3. Besides a short summary of SHiP specific physics such as tau-neutrino production and Heavy Neutral Leptons the main focus on this chapter lies on the experiment setup. A brief summary of every subdetector of SHiP is given, starting upstream of the proton target and moving downstream. Note that the information given in this chapter is based on the Technical Proposal of the experiment [Ane+15] and subject to change. A newly updated comprehensive overview of SHiP's experimental setup is expected to be published at the end of 2019. The chapter about SHiP is followed by chapter 4, covering the basic working principle of straw tubes and outlining effects on the performance of straw tube based detectors. Part ii mainly covers the development and setup of the functional model and the prototype. The single-straw functional model is described in chapter 5. Here, the design, assembly and measurements are elucidated. Chapter 6 describes in detail each individual part used for the quad-straw prototype. Moreover, the assembly of these parts as well as measurements of the wires' and straws' sagging are explained. The surface analyses of the straws' conductive coating are outlined in chapter 7. In chapter 8 the design as well as the design evolution of the modules and the mounting frame intended to hold the modules are presented. Note that each chapter has its own summary and outlook. Finally, a brief general conclusion and general outlook are given in chapter 9.

# Part I

<span style="color:red">THEORETICAL FOUNDATIONS</span>

'Felix, qvi potvit rervm cognoscere cavsas.'

*'That man has all the luck who can understand what makes the world tick.'*

— Virgil (29BC), *The Georgics*, Book II, Verse CDXC, as translated by Peter Fallon, Virgil, Georgics, Oxford World Classics, Oxford University Press

Within the first part of this work the theoretical background is covered. Here, chapter 2 covers the basics of the neutrino physics including the neutrino's history and its properties. In chapter 3, the scientific objectives of the SHiP (Search for Hidden Particles) experiment as well as the SHiP's detector itself are outlined. Finally, chapter 4 elucidates the working principle of straw tubes and the effect of certain quantities on their performance.

# NEUTRINO PHYSICS

Neutrinos are the only fundamental fermions in the Standard Model which do not carry any electric charges and play an exceptional role within particle and nuclear physics, so much so that international collaborations consisting of a many individual research groups commit themselves to neutrino research. This chapter is dedicated to the Standard Model of particle physics as well as the history of the neutrino and its properties, which are described in sections 2.2 and 2.3 respectively.

## 2.1 THE STANDARD MODEL

The Standard Model – often just abbreviated as SM – contains the current state of knowledge concerning the elementary particles and their interactions. It is a gauge theory based on the symmetry group

$$G = SU(3)_C \otimes SU(2)_L \otimes U(1)_Y. \tag{2.1}$$

The SM describes the electromagnetic, weak and strong interactions via the exchange of the corresponding spin-1 gauge fields [Pic12]. For the electromagnetic interaction this includes the single massless photon $\gamma$, for the weak interaction the three massive bosons $Z$ and $W^\pm$ (bosons are particles with integer spin that are not subject to Pauli's exclusion principle) and for the strong interaction eight massless gluons. Together with the Higgs Boson $H$ the $\gamma, Z$ and $W^\pm$ form the vector bosons, i.e. those bosons whose spin is 1. This Higgs boson introduces the masses of the elementary particles through the Higgs field and is evoked by the Spontaneous Symmetry Braking, or SSB in short. In vacuo the gauge symmetry is broken by the vacuum, which triggers the SSB of the electroweak group to the electromagnetic subgroup [Pic12]:

$$SU(3)_C \otimes SU(2)_L \otimes U(1)_Y \xrightarrow{\text{SSB}} SU(3)_C \otimes U(1)_{\text{QED}}. \tag{2.2}$$

*Note that the SM does neither describe the gravitation nor answer the question why gravitation is so much smaller than the electromagnetic force (hierarchy problem).*

The Higgs boson was discovered in 2012 at CERN [Aad+12]. One year later, Peter Higgs and Francois Englert were awarded the Nobel Prize in Physics for developing the Higgs mechanism.

In contrast to the bosons the fermions are particles with half-integral spin. In the Standard Model these fermions are divided into leptons
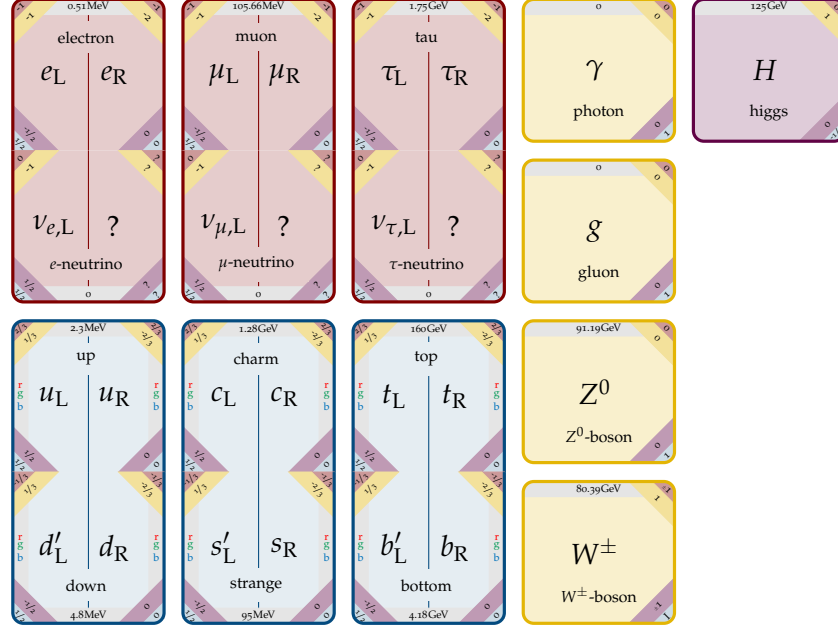
Figure 2.1: The Standard Model including the properties of the particles. The elementary fermions, shown as left- and right-handed versions, are depicted in their three generations. Concerning the quarks, $d', s', b'$ are mixed states in regard to the strong interaction eigenstates $d, s, b$. In the top corners are the electric charges $Q$ (red) and the weak hypercharges $Y$ (yellow) of the particles. The bottom corners contain the weak isospins $I_3$ (purple) and $I$ (blue). At the top (or bottom) are the particles' masses (grey). Antiparticles, which are not depicted in this representation, have the same quantum numbers but with opposite signs.

and quarks – the latter are subject to all three interactions, while leptons are only subject to the electromagnetic and weak interactions. The leptons make up half of the total of twelve fermions in the Standard Model. The electron, muon, and tau – in shorthand noted as $e$, $\mu$ and $\tau$ – are the electrically charged leptons and are accompanied by their corresponding neutrinos $\nu_e$, $\nu_\mu$ and $\nu_\tau$, which are electrically neutral. The six quarks, viz. the up, down, charm, strange, top and bottom quarks – or in shorthand just $u, d, c, s, t, b$ – have fractional charges of either $2/3$ or $-1/3$. Moreover, leptons and quarks are organised in three generations of fermions, as shown in figure 2.1. Here, other properties such as the particles' masses $m$ are also shown. Note that for every fermion a corresponding anti-fermion also exists. While having the same mass as the 'normal' particles, the anti-particles' additive quantum numbers have opposite signs.

One issue of the Standard Model, at least in its most basic, 'pure' form, is that neutrinos are treated as massless particles. Hence, an expansion of the SM is needed for it to contain neutrino masses and thus neutrino oscillations. Moreover, neutrinos with non-zero mass are

not confined to possess fixed helicities of $-1/2$ and $+1/2$ for neutrinos and antineutrinos respectively. Instead, neutrinos could have positive helicities and antineutrinos negative helicities in beyond the Standard Model physics.

### 2.1.1 *Electromagnetic interaction (QED)*

The electromagnetic force is the main force responsible for holding atoms and molecules together with the underlying quantum theory being Quantum electro dynamics (QED). The electromagnetic interaction is mediated through photons coupling to electric charges – a typical Feynman graph for such an interaction is shown in figure 2.2. Hence, all charged particles such as the charged leptons, quarks or $W^\pm$ bosons are affected by the electromagnetic interaction. Due to the fact that photons are massless, their lifetime is infinite and the electromagnetic force has thus an infinite range. The neutral charge of photons results in no self coupling.
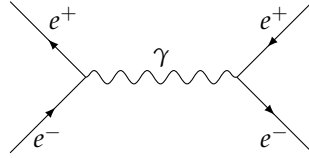


Figure 2.2: Feynman graph for Bhabha scattering ($e^+e^- \rightarrow e^+e^-$). The annihilation of an electron and a positron creates a photon which then produces a new electron positron pair.

### 2.1.2 *Weak interaction*

The weak interaction affects all Fermions – albeit only left-handed particles and right-handed antiparticles. This makes the weak interaction the only interaction that violates the conservation of parity. It is mediated through the exchange of the electrically neutral $Z^0$ gauge boson (mediating the neutral current – or NC in short) and the electrically charged $W^\pm$ gauge bosons (mediating the charged currents – CC in short). These gauge bosons have masses of $M_{Z^0} = (91.1876 \pm 0.0021)\,\text{GeV}$ and $M_{W^\pm} = (80.379 \pm 0.012)\,\text{GeV}$ [Tan+18]. Hence, via the uncertainty relation

$$\Delta E \Delta t = \frac{\hbar}{2\pi} \qquad (2.3)$$

their lifetime, and further, via

$$\Delta x = c_0 \Delta t, \qquad (2.4)$$

the range $\Delta x$ of the weak interaction can be calculated. Assuming the particles move with the speed of light $c_0$, this gives a range of

*The parity violation of the weak interaction was discovered in the Wu experiment – named after Chien-Shiung Wu – in 1956 [Wu+57]. In 1957, Wu's colleagues, Lee and Yang, who proposed the experiment were honoured with the Nobel Prize for the Wu experiment [AB18a]. Wu herself was not awarded the nobel prize but received the first Wolf Prize in Physics in 1978 [Fou18].*

approximately $\mathcal{O}(10^{-18})$ m, making the weak interaction the weakest of the three interactions. Figure 2.3 shows Feynman graphs of typical weak interactions, viz. neutral current $\nu_e$ scattering and $\nu_e e$ charged current scattering.
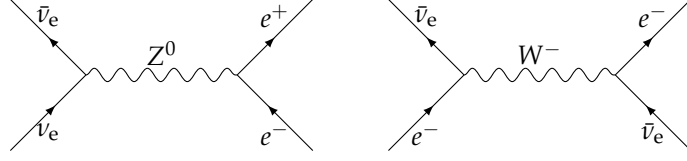


Figure 2.3: Feynman graph for the neutral current (NC) electron-neutrino scattering (left side) and for charged current (CC) electron-neutrino and electron scattering (right side).

### 2.1.3   Electroweak unification (GSW)

*GSW stands for Glashow-Salam-Weinberg, in honour of the three Nobel laureates S. Glashow, A. Salam and S. Weinberg [AB18b] who significantly contributed to the theory of electroweak unification.*

The electroweak unification, also called GSW theory, is a unified theory consisting of the weak and electromagnetic interactions. It is based on the group $\mathrm{SU}(2)_\mathrm{L} \otimes \mathrm{U}(1)_\mathrm{Y}$. The gauge fields of $\mathrm{SU}(2)_\mathrm{L}$ which describe the weak isospin $I_3$ are the triplet $W^1, W^2, W^3$ and couple to left-handed fermions or right-handed antifermions. This coupling is conducted via the universal coupling constant $g$, meaning the coupling strength is equal for all particles – an effect called *Lepton Universality*. The gauge field of $\mathrm{U}(1)_\mathrm{Y}$ is the singlet $B$ and describes the couplings of the weak hypercharge $Y$ via a coupling constant $g'$ affecting both left- and right-handed fermions [Hol10]. The physical vector bosons are given by

$$W^\pm = \frac{1}{\sqrt{2}}(W_1 \mp iW_2). \tag{2.5}$$

They are the force carriers of weak charged currents (CC) with a coupling constant $g_\mathrm{CC}$ given by

$$g_\mathrm{CC} = \frac{g}{2\sqrt{2}}. \tag{2.6}$$

The fields of the physical gauge bosons $Z^0$ and the photon $\gamma$, viz. $Z_\mu$ and $A_\mu$, are given by [Pic12]:

$$\begin{pmatrix} Z_\mu \\ A_\mu \end{pmatrix} \begin{pmatrix} \cos\theta_\mathrm{w} & -\sin\theta_\mathrm{w}, \\ \sin\theta_\mathrm{w} & \cos\theta_\mathrm{w}. \end{pmatrix} = \begin{pmatrix} W^3_\mu \\ B_\mu. \end{pmatrix} \tag{2.7}$$

*The weak mixing angle is sometimes also referred to as Weinberg angle, named after the US-American physicist and nobel laureate Steven Weinberg.*

Here, $\cos\theta_\mathrm{w}$ is the weak mixing angle, for which

$$\cos\theta_\mathrm{w} = \frac{g}{\sqrt{g^2 + g'^2}}, \tag{2.8}$$

$$\sin\theta_\mathrm{w} = \frac{g'}{\sqrt{g^2 + g'^2}}. \tag{2.9}$$

$A_\mu$, which corresponds to the photon $\gamma$ mediates the electromagnetic interaction and couples to electric charges via a coupling constant $e = \sqrt{4\pi\alpha_{\text{em}}}$ [Pie18] – the elementary electric charge – which can be expressed using $g$ and $g'$ as per

$$e = \frac{gg'}{\sqrt{g^2 + g'^2}} = g\sin\theta_{\text{w}} = g'\cos\theta_{\text{w}}. \tag{2.10}$$

The $Z^0$ boson mediates the weak neutral currents (NC) which are a mixed state of $W_\mu^3$ and $B_\mu$ and couple via a coupling constant

$$g_{\text{NC}} = \frac{1}{2}\sqrt{g^2 + g'^2} = \frac{e}{2\sin\theta_{\text{w}}\cos\theta_{\text{w}}}. \tag{2.11}$$

Both the $W^\pm$ and $Z^0$ bosons couple to fermions as well as anti-fermions. Their masses arise from the scalar Higgs field – which is a weak isospin doublet with four components $\Phi_1$ to $\Phi_4$ – given by

$$\Phi = \begin{pmatrix} \Phi^+ \\ \Phi^- \end{pmatrix} = \frac{1}{\sqrt{2}}\begin{pmatrix} \Phi_1 + i\Phi_2 \\ \Phi_3 + i\Phi_4 \end{pmatrix}, \quad \langle\Phi_0\rangle = \frac{1}{\sqrt{2}}\begin{pmatrix} 0 \\ v \end{pmatrix}. \tag{2.12}$$

Here, $\langle\Phi_0\rangle$ is the non-vanishing vacuum expectation value [Pie18]. In short, the coupling to the Higgs field causes the isospin rotation symmetry of the massless gauge fields $W_i^\mu$ to break spontaneously. This in turn leads to non-diagonal mass terms in the Lagrangian energy density ultimately resulting in the following masses of the gauge bosons:

$$M_W = \frac{gv}{2}, \tag{2.13}$$

$$M_Z = \frac{v}{2}\sqrt{g^2 + g'^2} = \frac{M_W}{\cos\theta_{\text{W}}}, \tag{2.14}$$

$$M_A = 0. \tag{2.15}$$

### 2.1.4 *Strong interaction (QCD)*

The strong interaction is described by the theory of quantum chromodynamics (QCD), which in itself is a theory set up in the framework of the Yang-Mills theory. It is a non-abelian gauge theory based on a $SU(3)_C$ gauge symmetry that is mediated through gluons. Gluons are electrically neutral, zero-mass particles coupling to colour – which is the charge of the strong interaction. This colour charge can be red, green, blue $(r, g, b)$ or anti-red, anti-green or anti-blue $(\bar{r}, \bar{g}, \bar{b})$ respectively. In contrast to e.g. photons, gluons themselves are carriers of (anti) colour charge. The number of possible (anti) colour combinations can be derived from the group theory and is given by $3 \otimes \bar{3} = 8 \oplus 1$, meaning that the direct product of a colour triplet and an anti-colour triplet forms a direct sum of an octet and a singlet – the latter being, omitting the normalisation factor, $r\bar{r} + g\bar{g} + b\bar{b}$. However,

*The Yang-Mills theory is named after the two physicists Chen Ning Yang and Robert L. Mills. Both were awarded the Rumford Prize of the American Academy of Arts & Sciences in 1980 [Art18].*

due to symmetry of the singlet, only the gluons of the colour octet exist.

Another effect caused by the gluons carrying colour charge themselves is self-coupling. This self-coupling leads to an amplification of the interaction with growing distance, resulting in the creation of quark-antiquark pairs being energetically favourable to greater dislodgement of two individual quarks. Hence, quarks never exist as individual, isolated particles but only as bound states confined in colour-neutral hadrons (in mesons $q\bar{q}$ and in baryons $qqq$) [Sch11; Hol10]. This is the so-called quark confinement, making the strong interaction short ranged with interaction lengths of $\sim 1.5\,\mathrm{fm}$. Figure 2.4 shows a Feynman graph for a strong interaction.
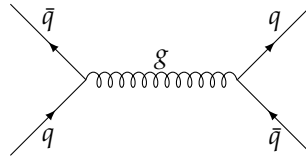


Figure 2.4: Feynman graph for a quark-antiquark annihilation and creation with the exchange of a gluon.

## 2.2 HISTORY OF THE NEUTRINO

Before the next section outlines the physical properties of neutrinos, the purpose of this section is to present some of the main steps in the vivid history of the neutrino. Naturally, not all neutrino-related experiments can be covered within this work, although figure 2.5 shows a relatively extensive timeline of the neutrino history.

### 2.2.1 *Invention of the neutrino (1930)*

```
   I have hit upon a desperate remedy to save the "ex-
change theorem" [...]  of statistics and the law of
conservation of energy.  Namely, the possibility that
in the nuclei there could exist electrically neutral
particles, which I will call neutrons, that have spin
1/2 and obey the exclusion principle and that further
differ from light quanta in that they do not travel
with the velocity of light.
```

This excerpt of a letter from WOLFGANG PAULI from December 4$^{\text{th}}$, 1930 addressed to a physicist meeting in Tübingen, Germany, is the first written record of the neutrino hypothesis. With the introduction of the neutrino, back then still called neutron, Pauli aimed to solve the issue of energy and momentum conservation occurring at the beta decay.

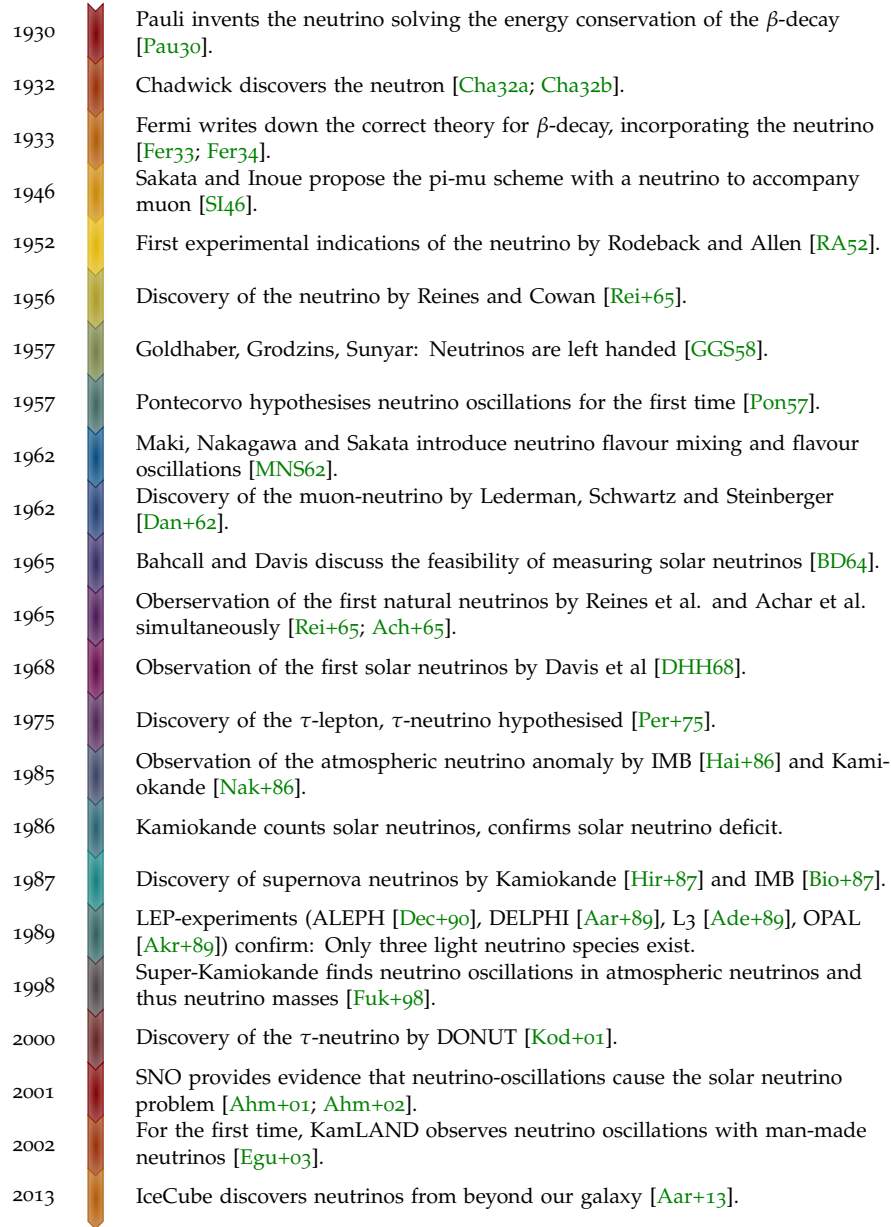| | |
|---|---|
| 1930 | Pauli invents the neutrino solving the energy conservation of the $\beta$-decay [Pau30]. |
| 1932 | Chadwick discovers the neutron [Cha32a; Cha32b]. |
| 1933 | Fermi writes down the correct theory for $\beta$-decay, incorporating the neutrino [Fer33; Fer34]. |
| 1946 | Sakata and Inoue propose the pi-mu scheme with a neutrino to accompany muon [SI46]. |
| 1952 | First experimental indications of the neutrino by Rodeback and Allen [RA52]. |
| 1956 | Discovery of the neutrino by Reines and Cowan [Rei+65]. |
| 1957 | Goldhaber, Grodzins, Sunyar: Neutrinos are left handed [GGS58]. |
| 1957 | Pontecorvo hypothesises neutrino oscillations for the first time [Pon57]. |
| 1962 | Maki, Nakagawa and Sakata introduce neutrino flavour mixing and flavour oscillations [MNS62]. |
| 1962 | Discovery of the muon-neutrino by Lederman, Schwartz and Steinberger [Dan+62]. |
| 1965 | Bahcall and Davis discuss the feasibility of measuring solar neutrinos [BD64]. |
| 1965 | Oberservation of the first natural neutrinos by Reines et al. and Achar et al. simultaneously [Rei+65; Ach+65]. |
| 1968 | Observation of the first solar neutrinos by Davis et al [DHH68]. |
| 1975 | Discovery of the $\tau$-lepton, $\tau$-neutrino hypothesised [Per+75]. |
| 1985 | Observation of the atmospheric neutrino anomaly by IMB [Hai+86] and Kamiokande [Nak+86]. |
| 1986 | Kamiokande counts solar neutrinos, confirms solar neutrino deficit. |
| 1987 | Discovery of supernova neutrinos by Kamiokande [Hir+87] and IMB [Bio+87]. |
| 1989 | LEP-experiments (ALEPH [Dec+90], DELPHI [Aar+89], L3 [Ade+89], OPAL [Akr+89]) confirm: Only three light neutrino species exist. |
| 1998 | Super-Kamiokande finds neutrino oscillations in atmospheric neutrinos and thus neutrino masses [Fuk+98]. |
| 2000 | Discovery of the $\tau$-neutrino by DONUT [Kod+01]. |
| 2001 | SNO provides evidence that neutrino-oscillations cause the solar neutrino problem [Ahm+01; Ahm+02]. |
| 2002 | For the first time, KamLAND observes neutrino oscillations with man-made neutrinos [Egu+03]. |
| 2013 | IceCube discovers neutrinos from beyond our galaxy [Aar+13]. |

Figure 2.5: Timeline of the neutrino's history. For more information see the included references. The selection of the depicted events is greatly inspired by [GLP16].

*β-Decay*

In 1914, JAMES CHADWICK measured a continuous β-decay spectrum. When a $\beta^-$-decay takes place,

$$X(A,Z) \longrightarrow Y(A,Z+1) + e^- + \bar{\nu}_e, \qquad (2.16)$$

a parent nucleon $X(A,Z)$ with $A$ nucleons (each nucleon containing $Z$ protons and $A - Z$ neutrons) decays into a daughter nucleon $Y(A, Z + 1)$ [Ric14]. Specifically, a neutron $n$ bound in $X$ decays into a proton $p$, an electron $e^-$, and an unobserved anti-neutrino $\bar{\nu}_e$:

$$n \longrightarrow p + e^- + \bar{\nu}_e. \qquad (2.17)$$

Note that a $\beta^+$ decay

$$p \longrightarrow n + e^+ + \nu_e \qquad (2.18)$$

can, in contrary to the $\beta^-$ decay, only take place with a bound proton due to $m_p < m_n$.

Consider the three body decay from equation (2.16). Assuming the parent nucleus $X$ is at rest, the energy $E_{e^-}$ of the electron has a continuous spectrum with $E_{e^-} \in [m_e, E_{max}]$. Here, $E_{max} = m_X - m_Y$ can be derived using the conservation of energy.

Without the existence of the anti neutrino $\bar{\nu}_e$, the $\beta^-$-decay from equation (2.16) would simply be a two body decay:

$$X(A,Z) \longrightarrow Y(A,Z+1) + e^-. \qquad (2.19)$$

In that case the electron would have a *fixed* energy $E = E_{max} = m_B - m_C$, assuming the law of energy conservation holds true. However, this did not concur with the experimental findings of James Chadwick in 1914. In order to solve this issue, Pauli introduced the hypothetical neutrino. Another reason to propose the neutrino lied within the conservation of momentum. A nucleus that has an even number of nuclei $A$ has an integral spin and follows the Bose-Einstein statistic, while an odd number of nuclei $A$ results in a half-integral spin and the nucleus following the Fermi-Dirac statistic. Considering equation (2.16), the parent and daughter nuclei follow the same statistic. Due to the conservation of momentum and the $e^\pm$ having a spin of $J = 1/2$ this can only be achieved, if another particle, the neutrino, with a half integral spin exists.

### 2.2.2 *Discovery of the neutrino (1954)*

The first experimental indications for neutrinos were found 38 years after Pauli's proposal in 1952 by Rodeback and Allen [RA52]. They used neutrino recoils following electron capture in $Ar^{37}$:

$$Ar^{37} + e^-_{K,L} \longrightarrow Cl^{37} + \nu + \mathcal{Q}, \qquad (2.20)$$

where $e^-_{K,L}$ is the captured orbital electron, $\nu$ the emitted neutrino (note that the idea of neutrino flavours was still unfamiliar at that time), and $\mathcal{Q}$ the disintegration energy that is given by the mass difference between Ar$^{37}$ and Cl$^{37}$ and was measured to be around 816 keV. Assuming all of the energy is dissipated via the Cl$^{37}$ and the neutrino, the energy distribution of the nuclear recoil should be centred sharply around 9.67eV which corresponds to a velocity for the Cl$^{37}$ of 0.71 cm µs$^{-1}$. This allowed measuring the recoil velocity by means of a delayed coincidence measurement started by the Auger electrons emitted after electron capture and stopped by detecting the recoiling nucleus. Indeed, the expected time delay and the measured time delay were in good agreement [All15; RA52; Zub11].

The first confirmed detection of a free neutrino was performed by REINES and COWAN in 1956 [Cow+56; RC59]. They utilised the inverse beta decay, often referred to as IBD, where an anti electron neutrino $\bar{\nu}_e$ interacts with a proton $p$ resulting in a neutron $n$ and a positron $e^+$:

$$\bar{\nu}_e + p \longrightarrow n + e^+. \tag{2.21}$$

The positron annihilates almost instantly with an electron, creating a pair of two 511 keV gammas:

$$e^+ e^- \longrightarrow \gamma + \gamma. \tag{2.22}$$

The neutron created by the inverse beta decay causes a delayed signal due to neutron proton capture. As a neutrino source they used nearby nuclear reactors (first Hanford, then Savannah River Plant), as during the nuclear fission of $^{235}$U, among others, elements are produced that emit neutrons in order to approach the valley of stability. The subsequent beta decay of these elements then creates anti electron neutrinos.

*Hanford site was a nuclear production complex in the state of Washington. The experiment was moved to the Savannah River Site, a nuclear reservation in South Carolina, due to improved shielding against cosmic rays.*

Based on that REINES and COWAN used a coincidence measurement to prove the existence of the $\bar{\nu}_e$. For the purpose of detecting the two gammas, hydrogenous liquid scintillator creating visible light as a response to the two gammas by means of Compton scattering was used. Photomultiplier tubes (PMTs) were then used to detect the visible light. The detection of the neutrons was ensured by Cadmium ($^{108}$Cd) that was dissolved in the scintillator. Cadmium, being a strong neutron absorber, can generate an excited state $^{109}$Cd$^*$ which in turn emits a gamma ray:

$$n + {}^{108}\text{Cd} \longrightarrow {}^{109}\text{Cd}^* \longrightarrow {}^{109}\text{Cd} + \gamma. \tag{2.23}$$

In their experiment they determined the cross section for reaction (2.21) to be in good agreement with the predicted cross section of $6.3 \times 10^{-44}$ cm$^2$. After several improvements were made to the detector, the cross section was determined to be $(11.0 \pm 2.6) \times 10^{-44}$ cm$^2$ per $\bar{\nu}$, agreeing with the theoretical value of $(10.0 \pm 1.6) \times 10^{-44}$ cm$^2$ per $\bar{\nu}$. In 1995 REINES was awarded the Nobel Price.

### 2.2.3  *Discovery of the muon neutrino (1964)*

In 1962 Leon Lederman, Melvin Schwartz, Jack Steinberger *et al.* [Dan+62] proved the existence of the muon neutrino by utilising the first source for highly energetic neutrinos, the synchrotron in Brookhaven. With this accelerator 15 GeV protons were shot at a Beryllium target in order to create high pion fluxes. These pions decay with a branching ratio of $(99.98770 \pm 0.00004)$ % into muons [Oli16]:

$$\pi^+ \longrightarrow \mu^+ \nu_\mu \tag{2.24}$$

$$\pi^- \longrightarrow \mu^- \bar{\nu}_\mu \tag{2.25}$$

The entire resulting flux was then passed through a 13.5 m thick iron layer segregating the neutrinos whose interactions were being observed in a 10 t aluminium spark chamber behind the iron layer.

Should there have only been a single neutrino type, i.e. if the $\nu_e$ and the $\nu_\mu$ would have been similar, then the following two reactions should have appeared with the same probability:

$$\nu_\mu + n \longrightarrow \mu^- + p, \tag{2.26}$$

$$\nu_e + n \longrightarrow e^- + p. \tag{2.27}$$

However, for different neutrino types, only reaction (2.26) should be observed as the neutrino beam almost entirely consisted of muon neutrinos. Indeed, Lederman *et al.* showed that muonic interactions were dominating. During a period of 25 days roughly $10^{14}$ neutrinos passed their spark chamber causing 51 events with muons in the final state. Later it has been shown at CERN that the ratio of produced electrons to muons amounts to $0.017 \pm 0.005$ [CD13].

### 2.2.4  *Detection of atmospheric neutrinos (1965)*

Cosmic rays hitting Earth's atmosphere interact with it creating secondary particles which can interact further or propagate directly to the earth's surface [GH02]. The flux of highly energetic neutrinos created in the decay of such secondary particles has already been calculated by Greisen [Gre61] and various others, however their detection was still pending. In 1960, Markov [Mar60] proposed to perform neutrino physics with atmospheric neutrinos using Cherenkov-light in the deep ocean. However, the first detection of atmospheric neutrinos was achieved in 1965 by two different experiments simultaneously.

Reines *et al.* [Rei+65] followed the idea of proving the existence of muons created in neutrino interactions in rock by means of an embedded detector array. As a location they chose the 3.2 km (8800 metre water equivalent, MWE) deep East Rand Proprietary Gold Mine near Johannesburg [Bee16], South Africa, where the background would be reduced by the overburden. They used a detector based on 110 m$^2$

mineral oil based liquid scintillator viewed by 5-inch photomultiplier tubes.

Achar *et al.* followed a very similar approach, they also designed an experiment for detecting muons produced in interaction of cosmic ray neutrinos [Ach+65]. Their detector was located in the Kolar gold mines in India at a depth of 2300 m (7500 MWE). It consisted of two telescopes, each made out of two $2\,\text{m} \times 3\,\text{m}$ walls of plastic scintillators with neon flash tubes and lead absorbers in-between that were read out by 5-inch PMTs.

### 2.2.5  *The Homestake experiment (1968)*

In 1968, Davis and Bahcall measured a deficit in the solar neutrino flux predicted by the Standard Model [DHH68]. The Homestake experiment was located in the Homestake gold mines in Lead, Lawrence County, South Dakota at a depth of 1478 m and consisted of a 615 t tank filled with $C_2Cl_4$-Tetrachloroethylene. When a $^{37}\text{Cl}$ atom in the tetrachloroethylene interacts with a neutrino, it transforms into a radioactive $^{37}\text{Ar}$ atom as per the reaction

$$\nu_e + {}^{37}\text{Cl} \longrightarrow {}^{37}\text{Ar} + e^-. \tag{2.28}$$
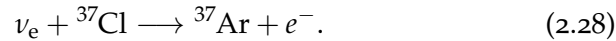
Due to the relatively low interaction threshold of 0.814 MeV the Homestake experiment was the first experiment capable of detecting solar neutrinos.

However, the reaction of the neutrino capture stated above cannot be measured directly. Hence, Davis and Bahcall used the fact that the radioactive $^{37}\text{Ar}$ isotopes decay back into an excited chlorine atoms after a half life of roughly three days. In order to detect this decay helium was bubbled through the tank to collect the $^{37}\text{Ar}$ isotopes. This way, the argon was collected, cleaned, and subsequently filled into gas counters, which were specially shielded due to the expectedly low counting rate.

The experiment showed that the electron neutrino flux was only about a third of the expected flux. For many years this posed a problem for the understanding of neutrino production in the sun, which is why the result of the Homestake experiment was called the 'solar neutrino problem'.

Even after the discovery of neutrino oscillations (see section 2.3.6) it was still debated whether these oscillations solved the solar neutrino problem. This is because various other experiments showed different deficits which could not be explained with neutrino oscillations. It was also argued that the deficit should not surpass 50 % since the observations should just be an average effect of the oscillation, and, lastly, the detection efficiency of the experiments was questioned [CH16]. Finally however, the solar neutrino problem could be explained using

the findings of the SNO experiment in 2002 – the same year Davis was awarded the nobel price for the Homestake experiment [AB19].

### 2.2.6   *Detection of supernova neutrinos (1987)*

On February 24, 1987 the supernova SN1987A was optically sighted [SDJ87]. Following this sighting the Kamiokande II detector conducted a search in the data taken on the same day. Kamiokande II consisted of an inner detector based on 2140 t of water viewed by 20-inch PMTs sorrounded by an outer water cherenkov detector. Neutrinos of different flavours were detected through the scattering reaction [Hir+87].

*Kamiokande stands for Kamioka Nucleon Decay Experiement, and should have originally been used to detect the hypothetical decay of a proton.*

$$\nu_e + e \rightarrow \nu_e + e \tag{2.29}$$

The Kamiokande II detector registered a corresponding pulse of eleven neutrinos within thirteen seconds with fitting time structure, energy distribution, and volume distribution. Similarly, a burst of eight neutrinos within six seconds has also been detected within the volume of the Irvine-Michigan-Brookhaven water Cherenkov detector [Bio+87] and a pulse of five neutrinos was detected by the INR Baksan underground scintillation telescope [Ale+88]. A pulse of five neutrinos detected by the Mont Blanc Underground Neutrino Observatory is believed to be uncorrelated with SN1987A [Arn+89]. A full report of SN1987A and its detection can be found in [Arn+89].

*Irvine-Michigan-Brookhaven is often just referred to as IMB.*

### 2.2.7   *Neutrino-oscillations (1998)*

After Gell-Mann and Pais experimentally proved the theory of $K^0 \rightleftharpoons \pi^+ + \pi^- \rightleftharpoons \bar{K}^0$ mixing and oscillations [GP55], Pontecorvo proposed the idea of neutrino oscillations, i.e. the phenomenon of spontaneous and periodic changes from one neutrino flavour to another [An+16], in 1957 [Pon57; Pon58]. Forty-one years later, in 1998, SuperKamiokande was able to provide experimental evidence for neutrino oscillations – and thus the fact that neutrinos are not massless – using atmospheric neutrinos.

SuperKamiokande is the updated version of Kamiokande II and was finished in 1996. It features a fiducial volume of 50 kt pure water, viewed by more than 11 000 20-inch PMTs at a depth of 1000 m. Atmospheric neutrinos are uniformly created, meaning that in theory the number of observed atmospheric neutrinos should be uniform and independent of the zenith angle. However, SuperKamiokande found that the number of muon neutrinos going upwards was just half the number of muon neutrinos going down. Moreover, it was found that the number of upwards going electron neutrinos was larger than expected.

The upwards going neutrinos originated in the atmosphere on the other side of Earth and have, upon reaching the detector, travelled

more than $13\,000\,\text{km}$ through it. During this path length the muon neutrinos must have lost their muonic properties and have changed into neutrinos of another flavour – an effect called neutrino oscillations.

### 2.2.8  *Discovery of the tau neutrino (2001)*

In 1975 MARTIN L. PERL *et al.* discovered the $\tau$-Lepton at SLAC's $e^+e^-$ colliding Ring SPEAR [Per+75]. The tau neutrino was proposed shortly after the discovery of the tau lepton. However, the first direct observation was only done 25 years after that in the year 2000 [Kod+01]. Physicist working at the DONUT (Direct Observation of Nu Tau) shot an $800\,\text{GeV}$ proton beam at a $1\,\text{m}$ long tungsten beam dump located $36\,\text{m}$ upstream on an emulsion target. The primary source for neutrinos was the decay of $D_\text{S}$ mesons into a $\tau$ and a $\bar{\nu}_\tau$, where in turn the $\tau$ decays into another $\bar{\nu}_\tau$. Other decay products from the proton – that is mostly muons – were absorbed by shielding devices or swept away via magnets.

### 2.2.9  *Solving the solar neutrino problem (2002)*

The Sudbury Neutrino Observatory (SNO) is a neutrino telescope located in the Creighton Mine in the city of Greater Sudbury, Ontario, Canada, at a depth of roughly $2\,\text{km}$. Its water Cherenkov detector features an acrylic vessel filled with $1\,\text{kt}$ of heavy water that is surrounded by approximately 9600 PMTs and was the first detector to be explicitly designed for searching electron, muon and tau neutrinos from the sun. The use of heavy water allowed SNO – in contrast to SuperKamiokande – to analyse three reactions at once.

*Heavy water, also called deuterium oxide, has the chemical formula $D_2O$.*

Firstly, the elastic scattering (ES) of electrons by neutrinos, which is sensitive to all flavours $\alpha \in \{e, \mu, \tau\}$:

$$\nu_\alpha + e^- \longrightarrow \nu_\alpha + e^-. \tag{2.30}$$

Secondly, a charged current (CC) interaction that is sensitive to electron neutrinos:

$$d + \nu_\text{e} \longrightarrow p + p + e^-. \tag{2.31}$$

Thirdly, a neutral current (NC) interaction sensitive to all flavours:

$$d + \nu_\alpha \longrightarrow \nu_\alpha + p + n. \tag{2.32}$$

The fluxes for each reaction are given by

$$\phi_\text{CC} = \phi_e, \tag{2.33}$$
$$\phi_\text{ES} = \phi_e + 0.1559\phi_{\mu\tau}, \tag{2.34}$$
$$\phi_\text{NC} = \phi_e + \phi_{\mu\tau}. \tag{2.35}$$

Measurements by SNO resulted in the following fluxes:

$$\phi_e = 1.76^{+0.05}_{-0.05}(\text{stat})^{+0.09}_{-0.09}(\text{syst}) \times 10^6 \text{ cm}^{-2}\text{s}^{-1}, \qquad (2.36)$$

$$\phi_{\mu\tau} = 3.41^{+0.45}_{-0.45}(\text{stat})^{+0.48}_{-0.45}(\text{syst}) \times 10^6 \text{ cm}^{-2}\text{s}^{-1}. \qquad (2.37)$$

The measured muon- and tau-neutrino rate was $5.3\sigma$ above zero, and $5.5\sigma$ including SuperKamiokande's data, providing very strong evidence for flavour transformation consistent with neutrino oscillations [Ahm+02]. Additionally, the total flux measured with the NC reaction was found to be

$$\phi_{\text{CC}} = 6.42^{+1.57}_{-1.57}(\text{stat})^{0.55}_{-0.58}(\text{syst}) \times 10^6 \text{ cm}^{-2}\text{s}^{-1}, \qquad (2.38)$$

and thus in good agreement with the standard solar model prediction of $\phi_{\text{SSM}} = 5.05^{+1.01}_{-0.81}$.

### 2.2.10    *KamLAND (2002-2005)*

KamLAND is a liquid scintillator antineutrino detector located at a depth of 2700 MWE near Kamioka, Japan. It is designed to search for reactor electron-antineutrinos from nuclear power plants. During the nuclear fission of $^{235}$U, $^{238}$U, $^{239}$Pu, and $^{241}$Pu in reactors, elements are produced which emit neutrons in order to approach the valley of stability. In average, the beta decay of these elements produces six electron-antineutrinos per fission [Kai16; LS05]. Via the inverse beta decay

$$\bar{\nu}_e + p \rightarrow e^+ + n \qquad (2.39)$$

these electron antineutrinos are detected using a large balloon filled with 1 kt of ultra-pure liquid scintillator viewed by roughly 1300 17-inch PMTs and around 550 20-inch PMTs.

From 2002 to 2004 KamLAND obtained evidence for reactor neutrino oscillations when the observed number of reactor anti neutrinos coming from near nuclear power plants was found to be only 0.6 % of the expected number [Egu+03]. In 2005, KamLAND, for the first time, examined the electron antineutrinos produced by natural radioactivity in the earth ($^{238}$U, $^{232}$Th decays) [Ara+05]. Over a time of $(749.0 \pm 0.5)$ days, a total of 152 events were recorded. Of these, $80.4 \pm 7.2$ came from reactor sources, $42 \pm 11$ from $^{13}$C$(\alpha, n)^{16}$O reactions and $2.38 \pm 0.01$ from accidental coincidences, resulting in a total background of $127 \pm 13$ events, leaving a total of $25^{+19}_{-18}$ geoneutrino events. This was consistent with reference earth models which predicted nineteen events [Suz06; Eno+07].

### 2.2.11    *IceCube (2013)*

IceCube is a water Cherenkov detector located in the antarctic ice. It consists of 5160 PMTs located at depths ranging from 1450 m to

2450 m, instrumenting a total of $1\,\text{km}^3$ ice. In 2013, IceCube found two neutrino events at energies exceeding $1\,\text{PeV}$, higher than one would expect of atmospheric background [Aar+13]. A follow up analysis of a 2-year data set was performed and showed 28 events with energies ranging from $30\,\text{eV}$ to $1200\,\text{eV}$, seven of which contained muon tracks and 21 were showerlike. This was the first indication of highly energetic neutrinos coming from cosmic accelerators outside the solar system.

Very recently IceCube found the first evidence for a source of these highly energetic comic neutrinos. One neutrino event was coincident in direction and time with a gamma ray flare from the blazar TXS 0506+056. A search within 9.5 years of data revealed an excess of high-energy neutrino events at the position of the blazar with a statistical significance of $3.5\sigma$ [Col18].

*Blazars are a subset of Active Galactic Nuclei (AGNs), which have a rapid, large-amplitude optical variability as well as a highly variable optical polarisation and radio emission – see [Pet97].*

## 2.3 PROPERTIES OF THE NEUTRINO

Neutrinos have several interesting properties which are outlined in this section. This includes the helicity and chirality of neutrinos as well as their behaviour under charge conjugation and parity transformation. This section also outlines the Dirac and Majorana formalism, the seesaw model, as well as neutrino oscillations and sterile neutrinos.

### 2.3.1 *Helicity and Chirality*

Begin with the relativistic wave equation of a spin $1/2$ particle, the Dirac equation. In its most compact form the Dirac equation is given by

$$(i\slashed{\partial} - m)\psi = 0. \tag{2.40}$$

Substituting $\slashed{\partial} = \gamma^\mu \partial_\mu$ (Feynman Slash notation) gives the following, slightly more prevalent form of the Dirac equation:

$$(i\gamma^\mu \partial_\mu - m)\psi = (i\gamma^0 \partial_0 - i\gamma^i \partial_i - m)\psi = 0, \quad i = 1, 2, 3, \tag{2.41}$$

*Note that in general, if A is covariant vector, $\slashed{A} := \gamma^\mu A_\mu$. This is done for convenience reasons.*

with $\partial_\mu = \partial/\partial x_\mu$, a 4-component spinor field $\psi$ and the hermitian Dirac $\gamma$-matrices

$$\gamma^0 = \begin{pmatrix} \mathbb{1} & 0 \\ 0 & -\mathbb{1} \end{pmatrix}, \qquad \gamma^i = \begin{pmatrix} 0 & \sigma^i \\ -\sigma^i & 0 \end{pmatrix}. \tag{2.42}$$

Here, $\sigma^i$ are the Pauli matrices given by

$$\sigma^1 = \begin{pmatrix} 0 & 1 \\ 1 & 0 \end{pmatrix}, \qquad \sigma^2 = \begin{pmatrix} 0 & -i \\ i & 0 \end{pmatrix}, \qquad \sigma^3 = \begin{pmatrix} 1 & 0 \\ 0 & -1 \end{pmatrix}. \tag{2.43}$$

The $\gamma^5$ matrix is given by

$$\gamma^5 = i\gamma^0 \gamma^1 \gamma^2 \gamma^3 = \begin{pmatrix} 0 & \mathbb{1} \\ \mathbb{1} & 0 \end{pmatrix}, \tag{2.44}$$

with $(\gamma^5)^2 = \mathbb{1}$. The $\gamma$-matrices fulfil the following anti-commutator relations:

$$\{\gamma^\mu, \gamma^\nu\} = 2\eta^{\mu\nu}\mathbb{1}, \tag{2.45}$$

$$\{\gamma^\mu, \gamma^5\} = 0. \tag{2.46}$$

Here, $\eta^{\mu\nu}$ is the Minkowski metric with signature $(+, -, -, -)$. Note that from equation (2.46) it follows that

$$\gamma^5\sigma^i = \sigma^i\gamma^5. \tag{2.47}$$

Multiplying the Dirac equation (2.41) from the left side with $\gamma^0$ yields using $\gamma^i = \gamma^0\gamma^5\sigma^i$

$$\left(\mathrm{i}(\gamma^0)^2\partial_0 - \mathrm{i}(\gamma^0)^2\gamma^5\sigma^i\partial_i - m\gamma^0\right)\psi = 0, \tag{2.48}$$

and further using $(\gamma^0)^2 = \mathbb{1}$:

$$(\mathrm{i}\partial_0 - \mathrm{i}\gamma^5\sigma^i\partial_i - m\gamma^0)\psi = 0. \tag{2.49}$$

Continuing by multiplying this equation from the left side, this time with $\gamma^5$, gives with equations (2.46) and (2.47)

$$(\mathrm{i}\partial_0\gamma^5 - \mathrm{i}\sigma^i\partial_i + m\gamma^0\gamma^5)\psi = 0. \tag{2.50}$$

Adding and subtracting equations (2.49) and (2.50) results in a two coupled equations:

$$\left[\mathrm{i}\partial_0(1 \pm \gamma^5) \mp \mathrm{i}\sigma^i\partial_i(1 \pm \gamma^5) - m\gamma^0(1 \mp \gamma^5)\right]\psi = 0. \tag{2.51}$$

Using $\gamma^5$ from equation (2.44) the so called *projection operators* $\mathcal{P}_\mathrm{L}$ and $\mathcal{P}_\mathrm{R}$ can be defined as

$$\mathcal{P}_\mathrm{L} = \frac{1 - \gamma^5}{2}, \qquad \mathcal{P}_\mathrm{R} = \frac{1 + \gamma^5}{2}. \tag{2.52}$$

As $\mathcal{P}_\mathrm{L}$ and $\mathcal{P}_\mathrm{R}$ are projectors, they are idempotent by definition, i.e.

$$\mathcal{P}_\mathrm{L}^2 = \mathcal{P}_\mathrm{L}, \qquad \mathcal{P}_\mathrm{R}^2 = \mathcal{P}_\mathrm{R}. \tag{2.53}$$

Moreover,

$$\mathcal{P}_\mathrm{L}\mathcal{P}_\mathrm{R} = \mathcal{P}_\mathrm{R}\mathcal{P}_\mathrm{L} = 0, \qquad \mathcal{P}_\mathrm{L} + \mathcal{P}_\mathrm{R} = 1. \tag{2.54}$$

In particular, the introduction of $\mathcal{P}_\mathrm{L}$ and $\mathcal{P}_\mathrm{R}$ motivates the decomposition of $\psi$ into left- and right-handed chiral components [Hen13]:

$$\psi = \begin{pmatrix} \psi_\mathrm{L} \\ \psi_\mathrm{R} \end{pmatrix}, \tag{2.55}$$

where

$$\psi_\mathrm{L} = \frac{1 - \gamma^5}{2}\psi = \mathcal{P}_\mathrm{L}\psi, \tag{2.56}$$

$$\psi_\mathrm{R} = \frac{1 + \gamma^5}{2}\psi = \mathcal{P}_\mathrm{R}\psi. \tag{2.57}$$

From these two equations it follows immediately that

$$\mathcal{P}_L\psi_R = \mathcal{P}_R\psi_L = 0. \tag{2.58}$$

By plugging in the projectors from equation (2.52) into equation (2.58) one can now easily find that the eigenvalues to $\gamma^5$ are given by $\pm 1$:

$$\gamma^5\psi_{L,R} = \pm 1 \cdot \psi_{L,R}. \tag{2.59}$$

These eigenvalues are called *chirality*, with $\psi_{L,R}$ being the left- and right handed chiral components of $\psi$ that are projected out via $\mathcal{P}_{L,R}$. Note that any arbitrary four component spinor $\psi$ can be written as the sum of the left- and right handed chiral projections:

$$\psi = \psi_L + \psi_R = \mathcal{P}_L\psi + \mathcal{P}_R\psi. \tag{2.60}$$

The chiral projections can now be used to write the two coupled equations (2.51) more compactly:

$$(i\partial_0 \mp i\sigma^i\partial_i)\psi_{R,L} = m\gamma^0\psi_{L,R}. \tag{2.61}$$

These coupled equations can be decoupled by assuming the mass $m$ is zero, resulting in

$$i\partial_0\psi_{R,L} = \pm i\sigma^i\partial_i\psi_{R,L}. \tag{2.62}$$

Since for a four-vector $x_0 = ct = t$ assuming natural units, $\partial_0$ is equal to $\partial_t$ and with $i\partial_t = E$ as well as $-i\partial_i = p_i$ equation (2.62) is simply the Schrödinger equation in momentum space:

$$E\psi_{L,R} = \pm\sigma^i p_i\psi_{L,R}, \tag{2.63}$$

or respectively

$$\psi_{L,R} = \pm\frac{\sigma^i p_i}{E}\psi_{L,R}. \tag{2.64}$$

Note that in the Dirac theory, $E = p$ for a particle and $E = -p$ for an antiparticle. Since the *helicity operator* $\mathcal{H}$ is defined by

$$\mathcal{H} = \frac{\sigma p}{|p|}, \tag{2.65}$$

equation (2.64) thus immediately implies that $\psi_L$ is an eigenspinor with helicity eigenvalues $\mathcal{H} = \pm 1$ for particles and antiparticles respectively. Similarly, $\psi_R$ is an eigenspinor with helicity eigenvalues $\mathcal{H} = \mp 1$ for particles and antiparticles respectively. This means that for a vanishing mass $m$ helicity and chirality are equal. For a non-vanishing mass $m$ decoupling the chirality eigenspinors $\psi_L$ and $\psi_R$ as done in equation (2.62) cannot be performed, meaning that they no longer describe particles which have a fixed helicity.

According to the *two-component theory* a neutrino spinor denoted by $\psi_\nu$ is in the weak interaction always of the following form:

$$\psi_\nu = \frac{1 - \gamma^5}{2}\psi = \psi_L. \tag{2.66}$$

Thus, $\psi_R = \mathcal{P}_R \psi = 0$ and an interacting neutrino is *always* left-handed with its antineutrino consequently being right-handed. Furthermore, the helicity for neutrino and antineutrino is *always* given by $\mathcal{H} = \mp 1$ respectively – assuming $m = 0$. For the proof that the $\psi_{L,R}$ only have two independent components, namely the 2-component Weyl spinors, refer to [Sch13].

### 2.3.2   *Charge conjugation*

Let $\phi$ denote a fermion with $\bar{\phi}$ being its corresponding antiparticle. Unlike with all fundamental fermions contained within the Standard Model, the distinction between particle and antiparticle via charge is not as evident for neutrinos. Should particle and antiparticle be not identical, i.e. $\phi \neq \bar{\phi}$, the fermion is called a Dirac particle. If however particle and antiparticle are equivalent ($\phi = \bar{\phi}$) then the fermion is referred to as a Majorana particle. This necessitates all of the fermions' additive quantum numbers to be neutral, implying the violation of lepton number conservation should neutrinos be Majorana particles.

Particles and antiparticles are connected via the Hermitian charge conjugation operator $\mathcal{C} = i\gamma_0\gamma_2$, which can be written in the Dirac-Pauli representation as:

$$\mathcal{C}\,|\phi(\boldsymbol{x},t)\rangle = \eta_c\,|\bar{\phi}(\boldsymbol{x},t)\rangle. \tag{2.67}$$

Here, the eigenvalue $\eta_c$, which is also referred to as the particle's charge parity, can take on the values $\eta_c = \pm 1$. Note that $\mathcal{C}$ has the following properties:

$$\mathcal{C}^{-1}\gamma_\alpha\mathcal{C} = -\gamma_\alpha^\mathsf{T}, \quad \mathcal{C}^{-1}\gamma_5\mathcal{C} = \gamma_5^\mathsf{T}, \quad \mathcal{C}^\dagger = \mathcal{C}^{-1} = \mathcal{C}^\mathsf{T} = -\mathcal{C}. \tag{2.68}$$

Additionally, the twofold application of $\mathcal{C}$ must return the particle to its original state.

Let $\psi(x)$ be the spinor field of a free neutrino that fulfils the Dirac equation (2.41). Then the associated charge conjugated field $\psi^c$ is given by

$$\psi \xrightarrow{\mathcal{C}} \psi^c = \mathcal{C}\psi\mathcal{C}^{-1} = \eta_c\mathcal{C}\bar{\psi}^\mathsf{T}. \tag{2.69}$$

Applying the projection operators $\mathcal{P}_{R,L}$ – recall equation (2.52) – to both sides gives

$$\mathcal{P}_{L,R}\psi = \psi_{L,R} \xrightarrow{\mathcal{C}} \mathcal{P}_{L,R}\psi^c = (\psi^c)_{R,L} = (\psi_{L,R})^c. \tag{2.70}$$

The last equality holds true since

$$(\psi_L)^c = (\mathcal{P}_L\psi)^c = \eta_c\mathcal{C}\overline{\mathcal{P}_L\psi}^\mathsf{T} = \eta_c\mathcal{P}_R\mathcal{C}\bar{\psi}^\mathsf{T} = \mathcal{P}_R\psi^c = (\psi^c)_R, \tag{2.71}$$

where equation (2.69) as well as $\overline{\mathcal{P}_L\psi}^\mathsf{T} = \mathcal{P}_R^\mathsf{T}\bar{\psi}^\mathsf{T}$ have been used. Equation (2.70) illustrates two aspects.

Firstly,

$$\psi_{\text{R,L}} \xrightarrow{\mathcal{C}} (\psi^c)_{\text{R,L}}, \tag{2.72}$$

which shows that $\mathcal{C}$ does indeed transform a left-handed particle into a right-handed one and vice versa. The helicity (chirality) remains unchanged unless an additional parity transformation is applied.

Secondly,

$$(\psi_{\text{L,R}})^c = (\psi^c)_{\text{R,L}}, \tag{2.73}$$

i.e. the operation (2.69) not only transforms a left-handed particle into a right-handed one (and vice versa), but also transform the helicity (chirality). To accommodate this fact, $\psi^c_{\text{L,R}}$ is commonly referred to as the $\mathcal{CP}$ conjugate with respect to $\psi_{\text{L,R}}$, instead of just charge conjugate. Note that $\mathcal{P}$ is referred to as *parity operator* and is not to be confused with the projectors $\mathcal{P}_{L,R}$.

### 2.3.3 *Parity transformation*

With the parity operator $\mathcal{P}$ a parity transformation is given by

$$\psi(\boldsymbol{x},t) \xrightarrow{\mathcal{P}} \mathcal{P}\psi(\boldsymbol{x},t)\mathcal{P}^{-1} = \eta_{\text{p}}\gamma^0\psi(-\boldsymbol{x},t), \tag{2.74}$$

where $\eta_{\text{p}} = \pm 1$ is the particle's inner parity. Using the relation (2.69) for the charge conjugated field $\psi^c$ results in

$$\psi^c = \eta_{\text{c}}\mathcal{C}\bar{\psi}^{\mathsf{T}} \xrightarrow{\mathcal{P}} \eta_{\text{c}}\eta_{\text{p}}^*\mathcal{C}(\gamma^0)^{\mathsf{T}}\bar{\psi}^{\mathsf{T}} = -\eta_{\text{p}}^*\gamma^0\psi^c. \tag{2.75}$$

This immediately implies two important aspects. Firstly, a fermion and its anti-fermion have opposite inner parities: If $\eta_{\text{p}} = \pm 1$, then $\eta_{\text{p}}^c = \mp 1$. Secondly, for a Majorana particle $\eta_{\text{p}}$ is equal to $-\eta_{\text{p}}^*$, since for Majorana fields $\psi^c_{\text{M}} = \pm\psi_{\text{M}}$ – see equation (2.78). Hence, a Majorana particle has an imaginary inner parity.

A Majorana field is given by

$$\tilde{\psi}_{\text{M}} = \frac{\tilde{\psi} + \eta_{\text{c}}\tilde{\psi}^c}{\sqrt{2}}, \tag{2.76}$$

where $\eta_{\text{c}} = \lambda_{\text{c}}\exp(2i\phi)$ with $\lambda_{\text{c}} = \pm 1$. Applying the phase transformation

$$\begin{aligned}
\tilde{\psi}_{\text{M}} \longrightarrow \tilde{\psi}_{\text{M}}\exp(-i\phi) &= \frac{\tilde{\psi}\exp(-i\phi) + \lambda_{\text{c}}\tilde{\psi}^c\exp(i\phi)}{\sqrt{2}} \\
&= \frac{\psi + \lambda_{\text{c}}\psi^c}{\sqrt{2}} \equiv \psi_{\text{M}}
\end{aligned} \tag{2.77}$$

results in the field $\psi_{\text{M}}$ being the eigenstate of the charge conjugation $\mathcal{C}$ with eigenvalues $\lambda_{\text{c}} = \pm 1$:

$$\psi^c_{\text{M}} = \frac{\psi^c + \lambda_{\text{c}}\psi}{\sqrt{2}} = \lambda_{\text{c}}\psi_{\text{M}}. \tag{2.78}$$

Due to the fact that $\psi_M$ and $\psi_M^c$ are indistinguishable, a Majorana particle is thus identical with its antiparticle. Regarding $\mathcal{CP}$ it can be obtained that

$$\psi_M(\boldsymbol{x},t) \xrightarrow{\mathcal{C}} \psi_M^c = \lambda_c \psi_M \xrightarrow{\mathcal{P}} \frac{\lambda_c(\eta_P \gamma^0 \psi - \lambda_c \eta_P^* \gamma^0 \psi^c)}{\sqrt{2}} \tag{2.79}$$

$$= \lambda_c \eta_P \gamma^0 \psi_M \tag{2.80}$$

$$= \pm i \gamma^0 \psi_M(-\boldsymbol{x},t), \tag{2.81}$$

where $\eta_P^* = -\eta_P$ has been used. Thus, a Majorana particle has $\eta_{cp} = \pm 1$, if $\lambda_c = 1$.

Finally, it can be obtained from equation (2.77) that

$$(\gamma^5 \psi_M)^c = \eta_c \mathcal{C}(\bar{\gamma}^5 \bar{\psi}_M)^\mathsf{T} = -\eta_c \mathcal{C}(\gamma^5)^\mathsf{T} \bar{\psi}_M^\mathsf{T} = -\gamma^5 \psi_M^c$$
$$= -\lambda_c \gamma^5 \psi_M. \tag{2.82}$$

This, in combination with equation (2.70), implies that a certain state cannot simultaneously be an eigenstate to $\mathcal{C}$ and an eigenstate to chirality. Hence, a Majorana-neutrino does not have a fixed chirality. Note however, that $\psi_M$ will still fulfil the Dirac equation (2.41), since $\psi$ and $\psi^c$ do so.

### 2.3.4 *Dirac and Majorana formalism*

Consider the Lagrange density for a Dirac field

$$\mathcal{L} = \bar{\psi}(i\slashed{\partial} - m_D)\psi \tag{2.83}$$

where $m_D$ is the Dirac mass, $\bar{\psi} = \psi^\dagger \gamma^0$ the Dirac adjoint of the Dirac spinor $\psi$ and $\slashed{\partial} = \gamma^\mu \partial_\mu$ (Feynman slash notation). Hence,

$$\mathcal{L} = \bar{\psi}(i\gamma^\mu \partial_\mu - m_D)\psi \tag{2.84}$$

with $\partial_\mu = \partial/\partial x_\mu$ and the Dirac gamma matrices $\gamma^\mu$ as introduced in section 2.3.1 – see equations (2.42) and (2.43). The first term in equation (2.84) corresponds to the kinetic energy and the second term is the Dirac mass term:

$$\mathcal{L}_D = m_D \bar{\psi}\psi. \tag{2.85}$$

When requiring the Lagrangian $\mathcal{L}$ to be hermitian, the Hermitian adjoint Lagrangian $\mathcal{L}^\dagger$ defined by

$$\langle \psi | \mathcal{L} | \phi \rangle = \left( \langle \phi | \mathcal{L}^\dagger | \psi \rangle \right)^* \tag{2.86}$$

must be equal to the Lagrangian. Therefore

$$\mathcal{L} = \mathcal{L}^\dagger. \tag{2.87}$$

This implies that $m_D$ from equation (2.85) must be real.

For two arbitrary spinors $\phi$ and $\psi$ the following relations hold true:

$$\bar{\psi}_L \phi_L = \bar{\psi} P_R P_L \phi = 0 \tag{2.88}$$

$$\bar{\psi}_R \phi_R = 0. \tag{2.89}$$

Hence,

$$\bar{\psi}\phi = (\bar{\psi}_L + \bar{\psi}_R)(\phi_L + \phi_R) = \bar{\psi}_L \phi_R + \bar{\psi}_R \phi_L. \tag{2.90}$$

Thus, the Dirac term can be written as

$$\mathcal{L}_D = m_D(\bar{\psi}_L \psi_R + \bar{\psi}_R \psi_L), \tag{2.91}$$

where

$$\bar{\psi}_R \psi_L = (\bar{\psi}_L \psi_R)^\dagger. \tag{2.92}$$

One can easily see that the Dirac mass term requires left handed as well as right handed Neutrinos. However, the Standard Model only contains left handed neutrinos. This is the reason why in the Standard Model neutrinos do remain massless.

In a more general treatment including $\psi^c$ three other Lorentz scalars exist beside $\bar{\psi}\psi$, viz. $\bar{\psi}^c \psi^c$, $\bar{\psi}\psi^c$ and $\bar{\psi}^c \psi^c$. Similar to $\bar{\psi}\psi$, $\bar{\psi}^c \psi^c$ is hermitian and hence equivalent to $\bar{\psi}\psi$. The Lorentz scalars $\bar{\psi}\psi^c$ and $\bar{\psi}^c \psi^c$ are hermitian conjugates because for two spinors it holds that

$$(\bar{\psi}\phi)^\dagger = (\psi^\dagger \gamma_0 \phi)^\dagger = \phi^\dagger \gamma_4 \psi = \bar{\phi}\psi. \tag{2.93}$$

This results in another hermitian mass term besides $\mathcal{L}_D$, the so called Majorana mass term:

$$\mathcal{L}_M = \frac{1}{2}\left(m_M \bar{\psi}\psi^c + m_M^* \bar{\psi}^c \psi\right) = \frac{1}{2} m_M \bar{\psi}\psi^c + \text{h.c.} \tag{2.94}$$

Here, $m_M$ is the Majorana mass and h.c. a Hermitian conjugate term. Utilising the chiral projection with the notation

$$\psi_{L,R}^c = (\psi^c)_{R,L} = (\psi_{R,L})^c, \tag{2.95}$$

two hermitian Majorana mass terms can be acquired:

$$\mathcal{L}_M = \mathcal{L}_M^L + \mathcal{L}_M^R. \tag{2.96}$$

Here,

$$\mathcal{L}^L = \frac{1}{2} m_L \left(\bar{\psi}_L \psi_R^c + \bar{\psi}_R^c \psi_L\right) = \frac{1}{2} m_L \bar{\psi}_L \psi_R^c + \text{h.c.} \tag{2.97}$$

$$\mathcal{L}^R = \frac{1}{2} m_R \left(\bar{\psi}_R \psi_L^c + \bar{\psi}_L^c \psi_R\right) = \frac{1}{2} m_R \bar{\psi}_L^c \psi_R + \text{h.c.} \tag{2.98}$$

Note that since the mass term is required to be hermitian, $m_L$ and $m_R$ are real Majorana masses.

Now, the Dirac-Majorana mass term – which is the most general mass term – can be written as a combination of the Dirac- and the Majorana mass term:

$$2\mathcal{L} = \bar{\Psi}_L M \Psi_R^c + \bar{\Psi}_R^c M \psi_L. \tag{2.99}$$

Here, $M$ is given by

$$M = \begin{pmatrix} m_L & m_D \\ m_D & m_R \end{pmatrix} \tag{2.100}$$

and the fields are given by

$$\Psi_L = \begin{pmatrix} \psi_L \\ \psi_L^c \end{pmatrix} = \begin{pmatrix} \psi_L \\ (\psi_R)^c \end{pmatrix} \tag{2.101}$$

$$(\Psi_L)^c, = \begin{pmatrix} (\psi_L)^c \\ \psi_R \end{pmatrix} = \begin{pmatrix} \psi_R^c \\ \psi_R \end{pmatrix} = \Psi_R^c. \tag{2.102}$$

The elements of $M$ are real under the prerequisite of CP conservation. So far, experiments have shown that for interactions of real neutrinos only the two fields $\psi_L$ and $\psi_R^c$ are present. They are thus often denoted as *active neutrinos*, while the two non interacting fields $\psi_R$ and $\psi_L^c$ are referred to as *sterile neutrinos*. It is customary to denote the latter ones with an $N$ and the active neutrinos with the letter $\nu$, resulting in:

$$\psi_L = \nu_L, \quad \psi_L^c = N_L^c, \tag{2.103}$$

$$\psi_R = N_R, \quad \psi_R^c = \nu_R^c. \tag{2.104}$$

Utilising these relations the Dirac-Majorana mass term from equation (2.99) can be written as

$$2\mathcal{L} = m_D \left( \bar{\nu}_L N_R + \bar{N}_L^c \nu_R^c \right) + m_L \bar{\nu}_L \nu_R^c + m_R \bar{N}_L^c N_R + \text{h.c.}, \tag{2.105}$$

which is equivalent to

$$
\begin{aligned}
2\mathcal{L} &= (\bar{\nu}_L, \bar{N}_L^c) \begin{pmatrix} m_L & m_D \\ m_D & m_R \end{pmatrix} \begin{pmatrix} \nu_R^c \\ N_R \end{pmatrix} + \text{h.c.} \\
&= (\bar{\nu}_L, \bar{N}_L^c) \, M \begin{pmatrix} \nu_R^c \\ N_R \end{pmatrix} + \text{h.c.}
\end{aligned}
\tag{2.106}
$$

where

$$M = \begin{pmatrix} m_L & m_D \\ m_D & m_R \end{pmatrix}. \tag{2.107}$$

Diagonalising the matrix $M$ gives the following mass eigenstates:

$$\psi_{1L} = \cos\theta \cdot \psi_L - \sin\theta \cdot \psi_L^c, \quad \psi_{1R}^c = \cos\theta \cdot \psi_R^c - \sin\theta \cdot \psi_R, \tag{2.108}$$

$$\psi_{2L} = \sin\theta \cdot \psi_L + \cos\theta \cdot \psi_L^c, \quad \psi_{2R}^c = \sin\theta \cdot \psi_R^c + \cos\theta \cdot \psi_R. \tag{2.109}$$

Here, $\theta$ is the mixing angle given by

$$\tan 2\theta = \frac{2m_D}{m_R - m_L}. \tag{2.110}$$

Solving the equation $\det(M - \lambda_m) = 0$ gives the two eigenvalues

$$\lambda_{m_{1,2}} = \frac{1}{2} \left[ (m_L + m_R) \pm \sqrt{(m_L - m_R)^2 + 4m_D^2} \right]. \tag{2.111}$$

Assuming that the left handed, sterile neutrino does not participate in the weak interaction, i.e. $m_L = 0$, and $m_R \gg m_D$ the following special case for the mass eigenstates arises:

$$m_\nu \equiv m_1 = \frac{m_D^2}{m_R}, \quad m_N \equiv m_2 = m_R \left( 1 + \frac{m_D^2}{m_R^2} \right) \approx m_R. \qquad (2.112)$$

This corresponds to the Seesaw model, which is outlined in the next section.

### 2.3.5 *Seesaw model*

The Seesaw model extends the Standard model by introducing right handed Majorana neutrinos $N_R$ besides the light ($m_L \approx 0$), left handed neutrinos $\nu_L$. Note that the introduced $N_R$ must have a high mass ($m_R \gg m_D$) as they would have otherwise already been experimentally detected. In this scenario, the mass matrix $M$ in the Lagrange density from equations (2.106) and (2.107) is of the form

$$M = \begin{pmatrix} 0 & m_D \\ m_D & m_R \end{pmatrix}. \qquad (2.113)$$

Diagonalising this matrix results in a light neutrino $\nu$ and a heavy Majorana neutrino $N$ as mass eigenstates with

$$m_\nu = \frac{m_D^2}{m_R^2} \ll m_D, \qquad m_N \approx m_R. \qquad (2.114)$$

Equation (2.114) illustrates one important aspect. Let $m_D$ be fixed. Then the mass of the light neutrino $m_\nu$ decreases as the mass of the heavy Majorana neutrino increases and vice versa. This gives the seesaw mechanism its name; it is said that the seesaw mechanism 'creates' the mass $m_\nu$.

In order to apply equation (2.114) on three families of fermions the simple assumption can be made that $m_R$ is similar for all three families and $m_D = m_{q_{2/3}}$ with $q_{2/3} \in \{$up, charge, top$\}$. These assumptions, which are suggested by Grand-Unified-Theory (GUT) models, result in the quadratic seesaw prediction where the neutrino masses scale quadratically with the quark masses:

$$m_{\nu_e} : m_{\nu_\mu} : m_{\nu_\tau} \sim m_u^2 : m_c^2 : m_t^2. \qquad (2.115)$$

In the same way

$$m_{\nu_e} : m_{\nu_\mu} : m_{\nu_\tau} \sim m_e^2 : m_\mu^2 : m_\tau^2 \qquad (2.116)$$

if $m_D = m_\ell$ with $\ell \in \{e, \mu, \tau\}$. In an alternative version of the model $m_R \propto m_D$ is assumed, which results in the linear seesaw prediction. Note that the seesaw predictions are highly model-dependent. For

example, the ratio of the three neutrino masses for the SUSY-GUT model and the SO(10)-GUT model is, according to [BKL92], given by:

$$m_1 : m_2 : m_3 = \begin{cases} 0.05m_u^2 : 0.09m_c^2 : 0.38m_t^2 & \text{for SUSY} \\ 0.05m_u^2 : 0.07m_c^2 : 0.18m_t^2 & \text{for SO(10).} \end{cases} \tag{2.117}$$

### 2.3.6  *Neutrino Oscillations*

The fact that neutrinos can periodically change from one flavour to another is called neutrino oscillations. As outlined in section 2.2, neutrino oscillations were hypothesised in 1957 by Bruno Pontecorvo [Pon57]. The model used today to describe neutrino oscillations was then developed by Ziro Maki, Masami Nakagawa and Shoichi Sakata in 1962 [MNS62], although at that point no experimental evidence for neutrino oscillations was available. The discovery of neutrino oscillations, which is attributed to Kamiokande in 1998, also confirmed that neutrinos are indeed massive [Fuk+98].

*Oscillation formalism in vacuo*

Figure 2.6 schematically shows a neutrino oscillation experiment, where a neutrino source creates a charged lepton $\bar{\ell}_\alpha$ of flavour $\alpha$ and an accompanying neutrino $\nu_\alpha$ via $W$ exchange. The $\nu_\alpha$ then hits a target, for example a detector, after having travelled a distance $L$ in vacuo. There it interacts through another $W$ exchange, creating another charged lepton $\ell_\beta$ of flavour $\beta$, meaning that at the time of it's interaction in the target the neutrino is a $\nu_\beta$. If the flavours $\alpha$ and $\beta$ are different, the neutrino has changed its flavour and has undergone a neutrino oscillation [Kay08].
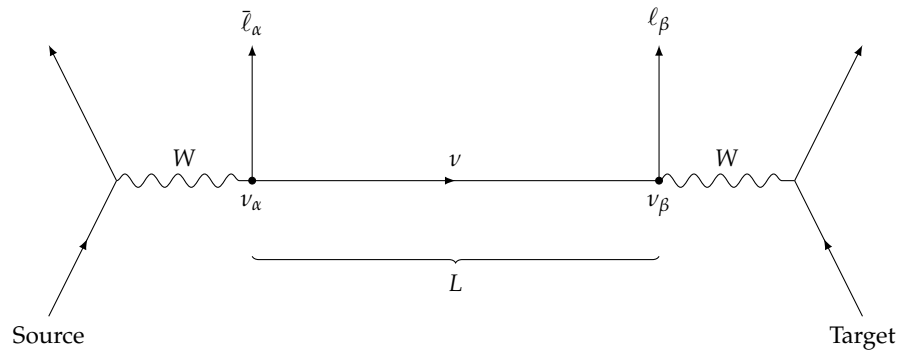


Figure 2.6: Schematical representation of a neutrino oscillation experiment. Via $W$ exchange, a neutrino source creates a charged lepton $\bar{\ell}_\alpha$ and a neutrino $\nu_\alpha$ which travels a distance $L$ until interacting in a target, where it creates a charged lepton $\ell_\beta$ and a $\nu_\beta$ of flavour $\beta$. If $\alpha \neq \beta$, the neutrino has oscillated. Representation adapted from [Kay08].

First, the general formalism of neutrino oscillations for $N$ flavours will be derived 'the normal way'. Whilst highly sophisticated derivations can be done using quantum field theory (see e.g. [Kay81; GS96; AS09; Dvo11]), the following way of deriving the oscillation formalism has become standard within the neutrino community, especially as it results in correct equations nevertheless. Note that the following approach is highly based on [Tim17].

For massive neutrinos there exists a set of mass eigenstates $|\nu_i\rangle$ which describes the space and time evolution of the neutrinos. Furthermore, there is a set of flavour eigenstates $|\nu_\ell\rangle$ describing the interactions of neutrinos with matter. These flavour eigenstates are connected to the mass eigenstates as per

$$|\nu_\ell\rangle = \sum_i U_{\ell i}^* |\nu_i\rangle, \tag{2.118}$$

where $U_{\ell i}$ are the entries of a rotation matrix $\mathbf{U}$. This unitary matrix (i.e $\mathbf{U}^\intercal \mathbf{U} = \mathbf{U}\mathbf{U}^\intercal = \mathbf{1}$) is referred to as Pontecorvo-Maki-Nakagawa-Sakata (PMNS) matrix and is the analogue to the Cabibbo-Kobayashi-Maskawa (CKM) quark mixing matrix. Note that the same can be done for the anti particles, where

$$|\bar{\nu}_\ell\rangle = \sum_i U_{\ell i} |\bar{\nu}_i\rangle. \tag{2.119}$$

*Evidently, the difference between the treatment of neutrinos and anti-neutrinos is just the complex conjugation of $\mathbf{U}$. It is thus sufficient to only discuss the neutrinos further.*

The mass eigenstates $|\nu_\ell\rangle$ evolve with time as they propagate:

$$|\nu_\ell(t)\rangle = \sum_i U_{\ell i}^* \exp\left(-\mathrm{i} p_i x\right) \tag{2.120}$$

with the four-vector position $x$ of the neutrino and the four-vector momentum $p_i$ of its mass state $i$. The time-dependent transition amplitude for a flavour conversion is given by

$$A(\ell \to \beta)(t) = \langle \nu_\beta | \nu_\ell(t)\rangle, \tag{2.121}$$

where

$$\langle \nu_\beta | = \sum_j U_{\beta j} \langle \nu_j |. \tag{2.122}$$

Hence,

$$A(\ell \to \beta)(t) = \left(\sum_j U_{\beta j} \langle \nu_j |\right) \left(\sum_i U_{\ell i}^* \exp(-\mathrm{i} p_i x) |\nu_i\rangle\right) \tag{2.123}$$

$$= \sum_i \sum_j U_{\beta j} U_{\ell i}^* \langle \nu_j | \nu_i\rangle \exp(-\mathrm{i} p_i x) \tag{2.124}$$

$$= \sum_i U_{\beta i} U_{\ell i}^* \exp(-\mathrm{i} p_i x). \tag{2.125}$$

Note that in the second step $\langle \nu_j | \nu_i\rangle = \delta_{ij}$ was used where $\delta_{ij}$ is the Kronecker symbol. Consider the exponent term in equation (2.125),

which, using $m_i$ and $E_i$ for the mass and energy of the $i^{\text{th}}$ mass eigenstate, can be expressed as

$$p_i x = E_i t - \boldsymbol{p} x. \tag{2.126}$$

Using $E_i = \sqrt{|\boldsymbol{p}|^2 + m_i^2}$ for $m_i \ll E_i$ and $ct = t = x = L$ as well as $\boldsymbol{p} x = |\boldsymbol{p}| L$ where $L$ is the distance between source and detector the exponent term can be binomially expanded:

$$p_i x = E_i t - \boldsymbol{p} x \tag{2.127}$$

$$\simeq |\boldsymbol{p}| L \left( 1 + \frac{m_i^2}{2|\boldsymbol{p}|^2} - |\boldsymbol{p}| L \right) \tag{2.128}$$

$$\simeq \frac{m_i^2 L}{2E}. \tag{2.129}$$

Hence, equation (2.125) now reads

$$A(\ell \to \beta)(t) = A(\ell \to \beta)(L) = \sum_i U_{\beta i} U_{\ell i}^* \exp\left( -\mathrm{i} \frac{m_i^2}{2} \frac{L}{E} \right). \tag{2.130}$$

The transition probability can now be obtained from the transition amplitude:

$$P(\ell \to \beta)(L) = |A(\ell \to \beta)(L)|^2 =$$

$$= \left( \sum_i U_{\beta i}^* U_{\alpha i} \exp\left[ -\mathrm{i} \frac{m_i^2}{2} \frac{L}{E} \right] \right) \left( \sum_j U_{\beta j} U_{\ell j}^* \exp\left[ -\mathrm{i} \frac{m_j^2}{2} \frac{L}{E} \right] \right)$$

$$= \sum_i \sum_j U_{\beta i}^* U_{\ell i} U_{\beta j} U_{\ell j}^* \exp\left[ -\mathrm{i} \frac{m_i^2 - m_j^2}{2} \frac{L}{E} \right]$$

$$= \sum_i \sum_j U_{\beta i}^* U_{\ell i} U_{\beta j} U_{\ell j}^* \exp\left[ -\mathrm{i} \frac{\Delta m_{ij}^2}{2} \frac{L}{E} \right]$$

$$+ \left( \sum_i \sum_j U_{\beta j}^* U_{\beta i} U_{\ell i}^* U_{\ell j} - \sum_i \sum_j U_{\beta j}^* U_{\beta i} U_{\ell i}^* U_{\ell j} \right) \tag{2.131}$$

with $\Delta m_{ij}^2 = m_i^2 - m_j^2$. In the last step a zero is added through the term in brackets, such that the transition amplitude can be rewritten as

$$P(\ell \to \beta)(L) = \sum_i \sum_j U_{\beta j}^* U_{\beta i} U_{\ell i}^* U_{\ell j} \left( \exp\left[ -\mathrm{i} \frac{\Delta m_{ij}^2}{2} \frac{L}{E} \right] - 1 \right)$$

$$+ \sum_i \sum_j U_{\beta j}^* U_{\beta i} U_{\ell i}^* U_{\alpha j}$$

$$= \sum_i \sum_j \Lambda_{ij} + \sum_i \sum_j \Xi_{ij}, \tag{2.132}$$

where

$$\Xi_{ij} = U^*_{\beta j} U_{\beta i} U^*_{\ell i} U_{\alpha j}, \tag{2.133}$$

$$\Lambda_{ij} = \Xi_{ij} \left( \exp\left[ -i \frac{\Delta m^2_{ij}}{2} \frac{L}{E} \right] - 1 \right). \tag{2.134}$$

Consider the sum over $\Xi_{ij}$. Using $U^* = (U^\dagger)^\mathsf{T}$ one finds that

$$\sum_i \sum_j \Xi_{ij} = \sum_i U_{\beta i} U^*_{\ell i} \sum_j U^*_{\beta j} U_{\alpha j}$$

$$= \sum_i U_{\beta i} U^\dagger_{i\ell} \sum_j U^\dagger_{j\beta} U_{\alpha j}$$

$$= \delta_{\ell\beta}. \tag{2.135}$$

Now consider $\Lambda_{ij}$. For $i = j$, $\Delta m^2_{ij} = \Delta m^2_{ii} = 0$ and hence $\Lambda_{ii} = 0$. If $i \neq j$, then $\Delta m^2_{ij} = -\Delta m^2_{ji}$ and one finds that $\Lambda_{ij} = \Lambda_{ji}^*$. Hence, $2\Re(\Lambda_{ij}) = \Lambda_{ij} + \Lambda_{ji}^*$. Altogether this means that the $i = j$ terms can be removed and equation (2.132) now reads

$$P(\ell \to \beta)(L) =$$
$$= \delta_{\ell\beta} + 2 \sum_{i>j} \sum_j \Re\left( \Lambda_{ij} \right)$$

$$= \delta_{\ell\beta} + 2 \sum_{i>j} \sum_j \Re\left( \Xi_{ij} \left( \exp\left[ -i \frac{\Delta m^2_{ij}}{2} \frac{L}{E} \right] \right) - 1 \right). \tag{2.136}$$

With Euler's formula $\exp(-ix) = \cos(x) - i\sin(x)$ as well as $1 - \cos(x) = 2\sin^2(x/2)$ gives

$$P(\ell \to \beta)(L) = \delta_{\ell\beta} + 2 \sum_{i>j} \sum_j \Im\left( \Xi_{ij} \sin\left[ \frac{\Delta m^2_{ij}}{2} \frac{L}{E} \right] \right)$$

$$- 4 \sum_{i>j} \sum_j \Re\left( \Xi_{ij} \sin^2\left[ \frac{\Delta m^2_{ij}}{4} \frac{L}{E} \right] \right). \tag{2.137}$$

Equation (2.137) is the most general expression for $N$ neutrinos oscillating in vacuum. It makes clear that oscillations between flavour eigenstates do indeed occur, frequencies depending on $1/E$ as well as $\Delta m^2_{ij}$ and with amplitudes determined by the elements of $U$. Moreover, equation (2.137) also highlights that at least some values for $\Delta m^2_{ij}$ must be non-zero, as otherwise no oscillations would occur.

*Three-flavour framework and mass hierarchy*

In the standard three-flavour framework there are three mass eigenstates

$$|\nu_i\rangle, \ i \in \{1, 2, 3\} \tag{2.138}$$

and three flavour eigenstates

$$|\nu_\ell\rangle, \; \ell \in \{e, \mu, \tau\} \tag{2.139}$$

which are connected via equation (2.118). The behaviour of neutrino oscillations is then determined by six free parameter, two independent mass differences, three mixing angles and a single CP-violating phase. The PMNS matrix can be parametrised in terms of the mixing angles $\theta_{ij}$ with $ij \in \{12, , 13, 23\}$ and the CP-violating phase $\delta$ as follows:

$$U = \begin{pmatrix} U_{e1} & U_{e2} & U_{e3} \\ U_{\mu 1} & U_{\mu 2} & U_{\mu 3} \\ U_{\tau 1} & U_{\tau 2} & U_{\tau 3} \end{pmatrix} \tag{2.140}$$

$$= U_{12}^{\text{solar}} \cdot U_{23} \cdot U_{13}^{\text{atmospheric}}$$

$$= \begin{pmatrix} c_{12} & s_{12} & 0 \\ -s_{12} & c_{12} & 0 \\ 0 & 0 & 1 \end{pmatrix} \begin{pmatrix} c_{13} & 0 & s_{13}e^{-i\delta} \\ 0 & 1 & 0 \\ -s_{13}e^{i\delta} & 0 & c_{13} \end{pmatrix} \begin{pmatrix} 1 & 0 & 0 \\ 0 & c_{23} & s_{23} \\ 0 & -s_{23} & c_{23} \end{pmatrix}$$

$$= \begin{pmatrix} c_{12}c_{13} & s_{12}c_{13} & s_{13}e^{-i\delta} \\ -s_{12}c_{23} - c_{12}s_{13}s_{23}e^{i\delta} & c_{12}c_{23} - s_{12}s_{13}s_{23}e^{i\delta} & c_{13}s_{23} \\ s_{12}s_{23} - c_{12}s_{13}c_{23}e^{i\delta} & -c_{12}s_{23} - s_{12}s_{13}c_{23}e^{i\delta} & c_{13}c_{23} \end{pmatrix}$$

Here, $c_{ij} = \cos\theta_{ij}$ and $s_{ij} = \sin\theta_{ij}$. The solar term $U_{12}^{\text{solar}}$ and the atmospheric term $U^{\text{atmospheric}}$ contain the solar neutrino oscillation angle $\theta_{12}$ and the atmospheric neutrino oscillation angle $\theta_{23}$ respectively. The remaining term contains the angle $\theta_{13}$, sometimes also referred to as reactor oscillation angle, as well as the unmeasured CP violating phase. In the three-flavour framework the energy-dependence of neutrino oscillations is governed by the two mass differences $\Delta m_{31}^2$ and $\Delta m_{21}^2$. While the absolute values for both of these mass differences are known, the exact sign of $|\Delta m_{31}^2|$ still remains to be measured. For an overview of the values for the six three-flavour neutrino oscillation parameters see table 2.1.

Table 2.1: The best fit values as well as the $1\sigma$ intervals for the six three-flavour neutrino oscillation parameters. The data is based on an evaluation of current experimental data performed by [Cap+14]. See also: [An+16].

| PARAMETER | NORMAL HIERARCHY | | INVERTED HIERARCHY | |
|---|---|---|---|---|
| | Best fit | $1\sigma$ range | Best fit | $1\sigma$ range |
| $\Delta m_{21}^2 / 10^{-5}\,\text{eV}^2$ | 7.54 | 7.32−7.80 | 7.54 | 7.32−7.80 |
| $\Delta m_{31}^2 / 10^{-3}\,\text{eV}^2$ | 2.47 | 2.41−2.53 | 2.42 | 2.36−2.48 |
| $\sin^2\theta_{12} / 10^{-2}$ | 3.08 | 2.91−3.25 | 3.08 | 2.91−3.25 |
| $\sin^2\theta_{13} / 10^{-2}$ | 2.34 | 2.15−2.54 | 2.40 | 2.18−2.59 |
| $\sin^2\theta_{23} / 10^{-1}$ | 4.37 | 4.14−4.70 | 4.55 | 4.24−4.94 |
| $\delta / 180°$ | 1.39 | 1.22−1.77 | 1.31 | 0.98−1.60 |

Note that it is important to emphasise that the absolute masses are unknown. This, in combination with fact that the sign of $|\Delta m_{31}^2|$ was

not yet measured, gives rise to two possibilities of ordering the mass eigenstates. Either,

$$m_1 < m_2 < m_3, \tag{2.141}$$

or

$$m_3 < m_1 < m_2. \tag{2.142}$$

This is called the mass hierarchy, as illustrated in figure 2.7. In case of relation (2.141) neutrinos follow the normal hierarchy (NH in short), whereas for neutrinos following the inverted hierarchy (IH in short) would follow relation (2.142). Current experiments aimed at determining the mass hierarchy include the JUNO detector in China, which is described in more detail in [Kai16].
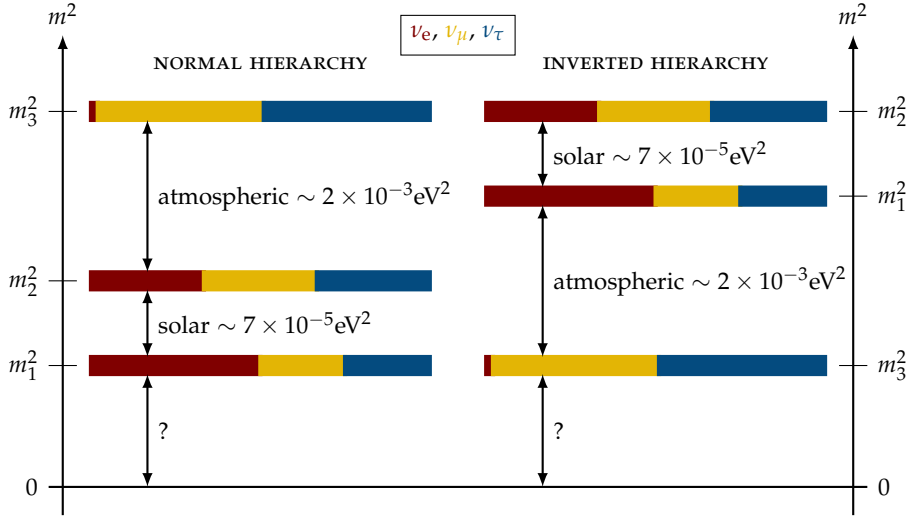


Figure 2.7: The ordering of the neutrino mass eigenstates for the normal and inverted mass hierarchies. The colours indicate the proportion of the different neutrino flavours in each mass eigenstate. Representation adapted from [An+16].

*Neutrino oscillations in matter*

So far only neutrino oscillations in vacuo were discussed. In 1978 however, LINCOLN WOLFENSTEIN adverted to changes in the physics of neutrino oscillations if they occur in matter [Wol78]. At the present day these changes are explained by the corresponding MIKHEYEV-SMIRNOV-WOLFENSTEIN (MSW) effect [MS86].

The MSW effect consists of two parts, namely a resonance amplification of the oscillation and (partially) adiabatic neutrino conversion – although the latter effect is negligible in most cases. In matter, the neutrino undergoes scattering and absorption processes. At low energies elastic forward scattering is the main process and inelastic scattering can be neglected [Wol78]. It is described by a potential $V$, given as the difference of the potentials $V_e$ and $V_a$ of different neutrinos $\nu_e$ and $\nu_a$:

$$V = V_e - V_a = \sqrt{2} G_F n_e. \tag{2.143}$$

Here, $G_F$ is the Fermi constant and $n_e$ the electron density. The effective hamiltonian in matter is then no longer the hamiltonian in vacuo $H_0$ but changes as follows:

$$H_0 \longrightarrow H = H_0 + V. \tag{2.144}$$

As a consequence, the effective mixing angle $\theta_m$ in matter is related to the vacuum mixing angle $\theta$ in the following way [Lor16; Akhoo]:

$$\sin^2 2\theta_m = \frac{\left(\frac{\Delta m^2}{2E}\right)^2 \sin^2 2\theta}{\left(\frac{\Delta m^2}{2E}\cos 2\theta - \sqrt{2}G_F n_e\right)^2 + \left(\frac{\Delta m^2}{2E}\right)^2 \sin^2 2\theta}. \tag{2.145}$$

This oscillation amplitude has a typical resonance form. The maximum ($\sin^2 2\theta = 1$) is obtained if the MSW resonance condition is satisfied:

$$\sqrt{2}G_F n_e = \frac{\Delta m^2}{2E}\cos 2\theta. \tag{2.146}$$

If this is indeed the case, mixing in matter is maximised regardless of the vacuum mixing angle.

### 2.3.7  *Sterile neutrinos*

The three-flavour framework of neutrino oscillations as described at the end of the previous section 2.3.6 is experimentally well established. However, it is incompatible with a handful of observed anomalies, which would require at least a single additional mass difference [Giu16].

*Anomalies in electron-flavoured neutrino appearance experiments*

Reactor neutrino experiments provided spectra for $^{235}$U, $^{238}$U, $^{239}$Pu and $^{241}$Pu. A calculation of the ratio $R$ between observed and expected $\bar{\nu}_e$ events gave $R = 0.943 \pm 0.023$ [Men+11]. This deficit, which has a statistical significance of roughly $2.8\sigma$, is called the reactor antineutrino anomaly.

*GALLEX and SAGE stand for 'Gallium Experiment' and 'Soviet-American Gallium Experiment'. The ratios given here for GALLEX are not the ones initially published but originate from a retrospective update [Kae+10] of the initial results.*

Another anomaly is the gallium neutrino anomaly. The GALLEX [Ham+98; Kae+10] and SAGE [Abd+96; Abd+06] experiments measured the cross sections of electron neutrinos emitted by radioactive $^{51}$Cr and $^{37}$Ar sources. For GALLEX, the ratios of measured cross sections to the expected cross sections were found to be $R_{G,1}(^{51}\text{Cr}) = 0.953 \pm 0.110$ and $R_{G,2}(^{51}\text{Ce}) = 0.812^{+0.10}_{-0.11}$. The SAGE experiment found ratios of $R_{S,1}(^{51}\text{Cr}) = 0.95 \pm 0.12$ and $R_{S,2}(^{37}\text{Ar}) = 0.79^{+0.09}_{-0.10}$. In total, the global statistical significance of both findings combined was found to be around $3\sigma$ [GL11].

Moreover, an anomaly was detected by LSND, an experiment in the United States of America designed to search for $\bar{\nu}_\mu \to \bar{\nu}_e$ oscillations. LSND detected a total $\bar{\nu}_e$ excess of $87.9 \pm 22.4$ (stat.) $\pm 6.0$ (syst.)

[Agu+01]. This corresponds to a deviation from the three-flavour model of $3.8\sigma$ [Tim17].

Furthermore in 2013, MiniBooNE, an experiment designed to measure $\nu_\mu \to \nu_e$ and $\bar{\nu}_\mu \to \bar{\nu}_e$ oscillations at Fermilab, performed two analyses for both oscillations separately. For the $\nu_e$ an excess of $162.0 \pm 47.8$, corresponding to $3.4\sigma$ and for the $\bar{\nu}_e$ an excess of $78.4 \pm 28.5$, corresponding to $2.8\sigma$ was observed [Agu+13]. Very recently in early 2018, MiniBooNE published further observations of an excess in both neutrino and antineutrino running modes of $(460.0 \pm 95.8)$ events with a statistical significance of $4.8\sigma$ [Agu+18]. Combined with the results of LSND the statistical significance of the excesses is $6.1\sigma$. The Fermilab Short-Baseline Neutrino Program [Acc+15] will further continue investigating this excess.

*Model of sterile neutrinos*

The absolute simplest sterile neutrino model is the '3+1-model' containing the three known neutrino flavours $\nu_e, \nu_\mu$ and $\nu_\tau$ accompanied by an additional flavour $\nu_s$. This extends the PMNS matrix from equation (2.140) such that

$$U = \begin{pmatrix} U_{e1} & U_{e2} & U_{e3} & U_{e4} \\ U_{\mu 1} & U_{\mu 2} & U_{\mu 3} & U_{\mu 4} \\ U_{\tau 1} & U_{\tau 2} & U_{\tau 3} & U_{\tau 4} \\ U_{s1} & U_{s2} & U_{s3} & U_{s4} \end{pmatrix} \tag{2.147}$$

Naturally, the elements $U_{\ell i}$, with $\ell \in \{e, \mu, \tau, s\}$ and $i \in \{1, 2, 3, 4\}$ get longer and more complicated, especially to derive. Hence, they are omitted within this work, but can be looked up in [Tim17]. Evidently, the PMNS matrix gets even more complicated if more flavours have to be added.

Indeed, there are arguments that this is the case. As was discussed in section 2.3.6, the mass scales $\Delta m^2_{31} = \Delta m^2_{\mathrm{atm}}$ and $\Delta m^2_{21} = \Delta m^2_{\mathrm{sol}}$ were confirmed by several experiments. These two mass scales require at least two massive states of active neutrinos whose mass eigenvalues are different. Therefore, the number of right-handed sterile neutrinos must be at least two, $\mathcal{N} \geqslant 2$, where for $\mathcal{N} = 2$ the lightest active neutrino mass vanishes. In order to explain the baryon asymmetry, the smallness of neutrino masses and the existence of dark matter, the number of right-handed sterile neutrinos required is $\mathcal{N} \geqslant 3$ [Ale+16]. The minimal choice of $\mathcal{N} = 3$ certainly seems reasonable since it remains within the Standard Model's 'three-type nature'. Figure 2.8 shows the Standard Model extended by three right-chiral sterile neutrinos as counterparts of the 'normal' neutrinos. This is called the Neutrino Minimal Standard Model, or $\nu$MSM in short. Note that in the $\nu$MSM the number of introduced sterile neutrinos is not limited to $\mathcal{N} = 3$ but can rather be chosen.

Figure 2.8: The three generations of fermions (including their masses and charges taken from [Tan+18]) as a part of the Standard Model. In this case, three right-chiral sterile neutrinos $N_1, N_2$ and $N_3$ (shaded in blue) are added accompanying the traditional left-chiral neutrinos $\nu_e, \nu_\mu$ and $\nu_\tau$. Together with the four gauge bosons $\gamma, g, Z^0, W^\pm$ and the Higgs boson $H$ this extended case is one way of representing the Neutrino Minimal Standard Model (the $\nu$MSM is not limited to just three sterile Neutrinos).

# SHIP

SHiP is an apronym meaning '*Search for Hidden Particles*'. It is a proposed general purpose fixed target beam dump facility utilising the Super Proton Synchrotron at CERN. In general, SHiP is to set sail exploring the lands beyond the physics of the Standard Model – the so called BSM-physics. In particular, SHiP will search for heavy sterile neutrinos, which are often referred to as heavy neutral leptons (HNLs). SHiP will also allow to directly observe the tau-antineutrino $\bar{\nu}_\tau$ for the first time in history.

This chapter illustrates the SHiP experiment, beginning with section 3.1 outlining the limits of the Standard Model. Section 3.2 touches on the topic of the energy and intensity frontiers, two different approaches on exploring BSM-physics. Afterwards, section 3.3 describes various physics aspects which were not yet covered in chapter 2 such as the physical processes in the target. The subsequent sections are dedicated to the SHiP detector. Since the SHiP detector is quite complex, section 3.4 provides a brief summary of the detector listing its individual components and touching upon their purposes (some readers may thus find it useful to read the introduction to the detector before reading the prior section dealing with SHiP's physics.). The individual components of the detector are then described individually and in much more detail in the sections afterwards, starting with the proton target in section 3.5 and finally concluding with the Hidden Sector Detector in section 3.8. Note that these sections are mainly based on the Technical Proposal [Ane+15] and thus subject to change. An updated publication is planned to be published end of 2019.

## 3.1 MOTIVATION

After the discovery of the Higgs-Boson in 2012 [Aad+12] the Standard Model is considered to be complete. However, the Standard Model still seems to be an incomplete description of nature as some questions can currently not be answered with it. For example, the existence and nature of dark matter, which, in contrast to the visible matter, does not interact via the electromagnetic force and is thus hard to detect and has only been shown experimentally by its gravitational effects on visible matter, can not be explained with the Standard Model

[CER12]. Furthermore, the Standard Model is incapable of providing an explanation for the baryonic asymmetry problem (also referred to as matter-antimatter asymmetry problem), which is the observed imbalance between baryonic and antibaryonic matter. Moreover, non-zero neutrino masses are inexplicable within the Standard Model. Finally, there is also no consensus view on a mechanism accounting for cosmic inflation [Ane+15]. It is thus pretty clear that there is physics beyond the Standard Model and eventually several particles still need to be discovered.

## 3.2 ENERGY AND INTENSITY FRONTIER

There are currently two approaches for revealing yet undiscovered particles – see figure 3.1. One possibility is that the undiscovered particles have high masses and thus require energies way beyond of what current collider experiments are capable of delivering. Newer prospective accelerators and colliders crossing the so called 'energy frontier' can create and discover these particles, reveal their interactions, and investigate fundamental forces [Cra11].
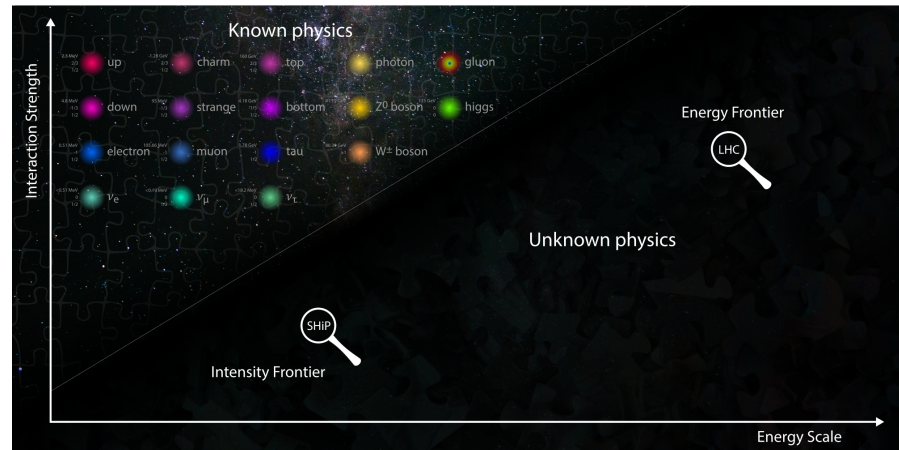


Figure 3.1: Illustration of the known (top left third) and unknown parts of physics (bottom right thirds) and how to explore physics beyond the Standard Model. The values for masses, charges and spins of the SM-particles shown in the top left third were taken from [Tan+18]. On the energy frontier high energy scales can be discovered using future colliders such as the proposed FCC. Small interaction strengths can be explored using experiments with very high intensities at the intensity frontier.

Another way to reveal undiscovered particles is to use experiments that cross the 'intensity frontier.' This approach covers the possibility that the particles' large masses are not the key for their discovery but rather their minuscule interactions. In that case, experiments with very high intensities are required. Intense particle beams and highly sensitive detectors can be used to investigate fundamental forces and

particle interactions by studying events that only occur rarely in nature [Cra11]. This is the approach that the SHiP experiment – and other experiments aimed at exploring BSM physics – follow. Table 3.1 shows a comparison between the properties of the SHiP detector with the properties of past experiments, viz. PS191 [Ber+86; Ber+88; Van08], NuTeV [Vai+99] and CHARM [Dor+86].

Table 3.1: Comparison between key properties of SHiP and the ones of past experiments aimed at searching heavy neutral leptons, viz. PS191, NuTeV and CHARM. The data was taken from [Ane+15].

| Experiment | PS191 | NuTeV | CHARM | SHiP |
|---|---|---|---|---|
| Proton energy $\cdot$ GeV$^{-1}$ | 19.2 | 800 | 400 | 400 |
| Protons on target $\cdot$ $10^{19}$ | 8.86 | 0.25 | 0.24 | 20 |
| Decay volume $\cdot$ m$^{-3}$ | 360 | 1100 | 315 | 1780 |
| Decay volume pressure $\cdot$ bar$^{-1}$ | 1 (He) | 1 (He) | 1 (air) | $10^{-6}$ (air) |
| Distance to target $\cdot$ m$^{-1}$ | 128 | 1400 | 480 | 80...90 |
| Off beam axis $\cdot$ mrad$^{-1}$ | 40 | 0 | 0 | 0 |

## 3.3 PHYSICS

This section outlines SHiP-related physics aspects which were not yet covered in chapter 2. In particular, the production of neutrinos – especially $\tau$ neutrinos – and heavy neutral leptons after proton interactions in SHiP's target are elucidated.

### 3.3.1 *Neutrino production*

The SHiP experiment will utilise CERN's SPS beam with an energy of 400 GeV. When this beam strikes the proton target, whose technical design is outlined in section 3.5, there are two major ways of producing tau neutrinos. Firstly, $D_s^{\pm}$ mesons can be produced in primary proton interactions. As has been shown in [Abr+13], the corresponding branching ratio is given by

$$f_{D_s} = (7.7 \pm 0.6^{-0.5}_{-0.4}) \, \%.$$ (3.1)

Note that due to the chosen target material the production of $D_s^{\pm}$ is symmetrical, i.e. $D_s^+, D_s^-$ are produced in the same amount. The decays of these $D_s^{\pm}$ can then result in the production of $\tau$ leptons and $\tau$ neutrinos:

$$D_s^+ \longrightarrow \tau^+ + \nu_\tau$$ (3.2)

$$D_s^- \longrightarrow \tau^- + \bar{\nu}_\tau.$$ (3.3)

The branching ratios for these decays is given by

$$\mathrm{Br}(D_s \to \tau) = (5.48 \pm 0.23) \, \%,$$ (3.4)

respectively [Tan+18]. Secondly, the created $\tau$ leptons subsequently decay through the weak interaction, as shown in table 3.2. An example

Table 3.2: Top six decays of the $\tau^\pm$ lepton, which account for more than 95 % of all $\tau^\pm$ decays. The branching ratios were taken from [Tan+18].

| Decay modes for $\tau^\pm$ | | Branching ratios in % |
|---|---|---|
| $\tau^+ \to \pi^+ \pi^0 \bar{\nu}_\tau$ | $\tau^- \to \pi^- \pi^0 \nu_\tau$ | $25.4940 \pm 0.0893$ |
| $\tau^+ \to e^+ \nu_e \bar{\nu}_\tau$ | $\tau^- \to e^- \bar{\nu}_e \nu_\tau$ | $17.8174 \pm 0.0399$ |
| $\tau^+ \to \pi^+ \bar{\nu}_\tau$ | $\tau^- \to \pi^- \nu_\tau$ | $17.8165 \pm 0.0512$ |
| $\tau^+ \to \mu^+ \nu_\mu \bar{\nu}_\tau$ | $\tau^- \to \mu^- \bar{\nu}_\mu \nu_\tau$ | $17.3936 \pm 0.0384$ |
| $\tau^+ \to \pi^+ 2\pi^0 \bar{\nu}_\tau$ | $\tau^- \to \pi^- 2\pi^0 \nu_\tau$ | $9.2595 \pm 0.0964$ |
| $\tau^+ \to \pi^+ \pi^+ \pi^- \bar{\nu}_\tau$ | $\tau^- \to \pi^- \pi^- \pi^+ \nu_\tau$ | $8.9870 \pm 0.0514$ |

for a possible $D_s^+$ decay chain is shown in figure 3.2. Note that a $\tau$ neutrino is always created during the decay of a $\tau$ lepton due to lepton number conservation. However, the decays of $D_s$ mesons into a $\tau$ and a $\nu_\tau$ and the decay of $\tau$ leptons are kinematically different. Thus, the
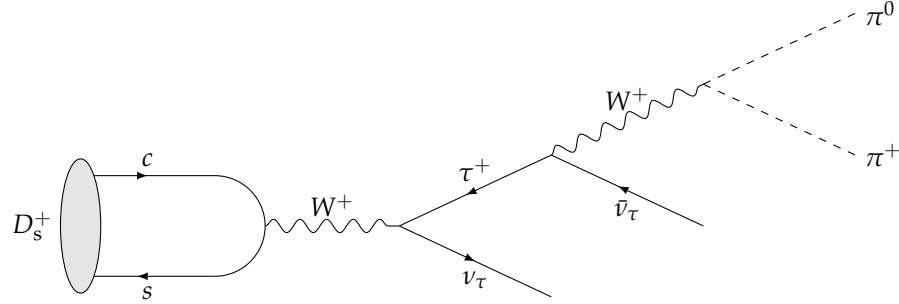


Figure 3.2: $D_s$ decay chain for a $D_s^+ \to \tau^+ + \nu_\tau$ decay with a subsequent $\tau^+ \to \pi^+ + \pi^0 + \bar{\nu}_\tau$ decay. The branching ratio of the complete chain is given by $5.48\% \cdot 25.49\% \simeq 1.4\%$. Adapted from [Ale+16; Hab15].

momentum distributions of the neutrinos created in the two different processes vary distinctly. As can be seen in figure 3.3, the spectrum for $\tau$ neutrinos created directly due to decaying $D_s$ mesons is much softer than that of $\tau$ neutrinos created during the decay of a $\tau$ lepton.

Using equations (3.1) and (3.4), the total number of tau neutrinos ($\nu_\tau$ and $\bar{\nu}_\tau$) emanating from the proton target can be approximated using the following formula:

$$N_{\nu_\tau + \bar{\nu}_\tau} = 4N_p \frac{\sigma_{c\bar{c}}}{\sigma_{pN}} f_{D_s} \mathrm{Br}(D_s \to \tau) \tag{3.5}$$

$$= 2.86 \times 10^{-5} N_p \tag{3.6}$$

$$= 5.71 \times 10^{15}. \tag{3.7}$$

Here, $N_p = 2 \times 10^{20}$ is the expected number of incoming protons interacting with the target over a runtime of five years, $\sigma_{c\bar{c}} = (18.1 \pm 1.7)\,\mu b$
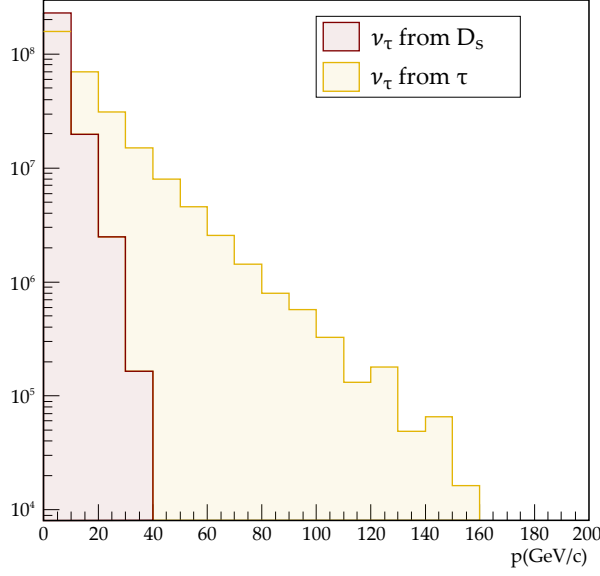
Figure 3.3: Momentum distributions of tau neutrinos produced directly in $D_s$ decays and and in $\tau$-lepton decays. Due to kinematical differences between the decay processes the $\nu_\tau$ spectrum from $D_s$ decays is much softer. Adapted from [Ane+15].

is the charm production per nucleon [LW06] and $\sigma_{pN} = 10.7\,\text{mb}$ the hadronic cross section per nucleon in the molybdenum target.

However, not only $\tau$ neutrinos are produced. Besides the decay of $\tau$ leptons as shown in table 3.2, many other processes can produce electron and muon neutrinos. In particular, secondary proton interactions result in pions and kaons, whose decays induce the production of electron and muon neutrinos. With a branching ratio of $(99.987\,70 \pm 0.000\,04)\,\%$ charged $\pi$-mesons decay with a vast majority into a muon and a muon neutrino:

$$\pi^+ \longrightarrow \mu^+ + \nu_\mu \tag{3.8}$$

$$\pi^- \longrightarrow \mu^- + \bar{\nu}_\mu. \tag{3.9}$$

The decay of kaons as shown in table 3.3 further induces the production of electron and muon neutrinos. Figure 3.4 shows the momentum

Table 3.3: Top six decay modes of the $K^\pm$ meson, accounting for more than 99 % of all $K^\pm$ decay modes. For the further decay of the charged pions refer to equations (3.8) and (3.9). Values taken from [Tan+18].

| Decay modes for $K^\pm$ | | Branching ratios in % |
|---|---|---|
| $K^+ \to \mu^+ \nu_\mu$ | $K^- \to \mu^- \bar{\nu}_\mu$ | $63.550 \pm 0.110$ |
| $K^+ \to \pi^+ \pi^0$ | $K^- \to \pi^- \pi^0$ | $20.660 \pm 0.080$ |
| $K^+ \to \pi^+ \pi^+ \pi^-$ | $K^- \to \pi^- \pi^- \pi^+$ | $5.590 \pm 0.040$ |
| $K^+ \to \pi^0 e^+ \nu_e$ | $K^- \to \pi^0 e^- \bar{\nu}_e$ | $5.070 \pm 0.040$ |
| $K^+ \to \pi^0 \mu^+ \nu_\mu$ | $K^- \to \pi^0 \mu^- \bar{\nu}_\mu$ | $3.353 \pm 0.034$ |
| $K^+ \to \pi^+ \pi^0 \pi^0$ | $K^- \to \pi^- \pi^0 \pi^0$ | $1.761 \pm 0.022$ |

spectra of neutrinos and antineutrinos combined for all three flavours in the proton target and the neutrino target. The spectra have been obtained by a Geant4 based simulation. The neutrino yield for $10 \times 10^{20}$ protons on target in the proton target, the neutrino detector and their charged current interactions is shown in table 3.4.
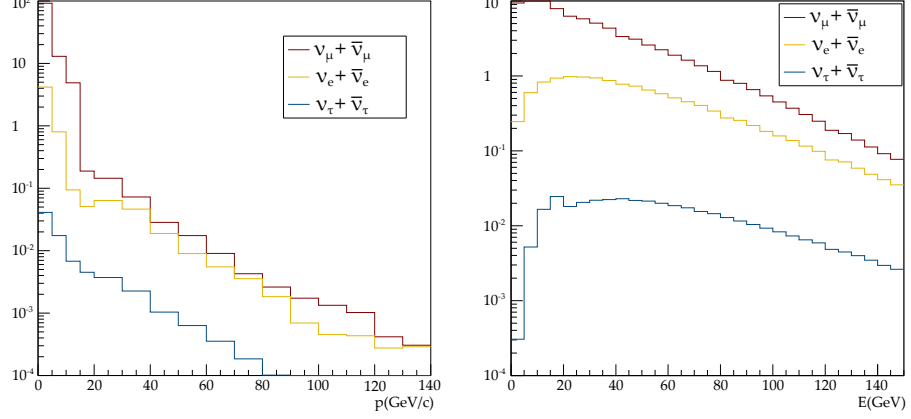


Figure 3.4: Simulation results of the spectra of the three neutrino flavours in the proton target (left side) and the neutrino target (right side). A 0.5 GeV cut was applied for $\nu_\mu$ and $\nu_e$ and the total number of neutrinos was normalised to 100. Adapted from [Ane+15].

Table 3.4: Integrated neutrino yield for $2 \times 10^{20}$ protons on target for different neutrino flavours including the corresponding mean energies at the target and the neutrino detector as well as their charged current deep inelastic scattering (CC DIS) interactions. Reproduced from [Buo17].

| Flavour | $\langle E \rangle$ | $p$-target | $\langle E \rangle$ | $\nu$-detector | $\langle E \rangle$ | CC DIS |
|---|---|---|---|---|---|---|
| $\nu_\mu$ | 1.5 | $3.4 \times 10^{18}$ | 10.7 | $4.4 \times 10^{16}$ | 31 | $2.3 \times 10^6$ |
| $\nu_e$ | 4.1 | $2.2 \times 10^{17}$ | 29.5 | $5.7 \times 10^{15}$ | 50 | $6.3 \times 10^5$ |
| $\nu_\tau$ | 7.4 | $1.1 \times 10^{16}$ | 22.3 | $4.7 \times 10^{14}$ | 45 | $2.6 \times 10^4$ |
| $\bar{\nu}_\mu$ | 1.6 | $2.1 \times 10^{18}$ | 8.6 | $3.5 \times 10^{16}$ | 26 | $8.6 \times 10^5$ |
| $\bar{\nu}_\mu$ | 4.7 | $1.8 \times 10^{17}$ | 21.6 | $5.2 \times 10^{15}$ | 38 | $2.2 \times 10^5$ |
| $\bar{\nu}_\tau$ | 8.1 | $1.1 \times 10^{16}$ | 30.7 | $4.7 \times 10^{14}$ | 58 | $1.9 \times 10^4$ |

### 3.3.2 *Heavy Neutral Leptons*

In fixed target experiments – and thus SHiP – heavy neutral leptons can be created in various different ways, viz.

- Production from hadrons' decays

- Production from Deep Inelastic Scattering $p$-nucleus interactions

- Production from the coherent proton-nuclear scattering.

However, the first way – i.e. the production from hadron's decays, in particular the production via (semi)-leptonic decays of the lightest charmed and beauty-mesons which is shown in figure 3.5 – is the main contributor to the HNL production [Bon+18].
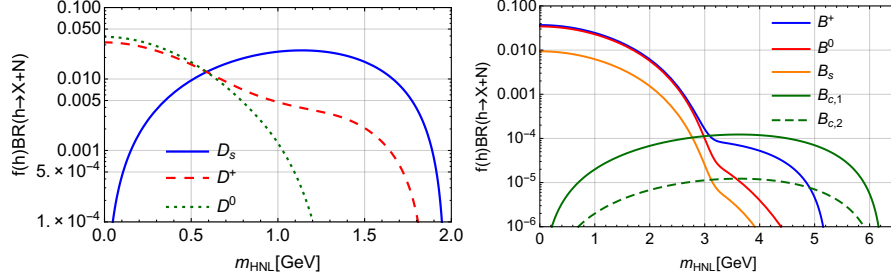


Figure 3.5: The product of the branching ratio and the production fraction for HNL creation in SHiP based on charmed meson decays (left) and beauty meson decays (right). Both images are taken from [Bon+18].

Figure 3.6 is a Feynman-diagram-like representation of the production and decay of a heavy neutral lepton $N$. Here, a $D_s$ meson decays into a muon and a muon-neutrino with a branching ratio of $\mathrm{Br}(D_s \to \mu + \nu_\mu) = (5.90 \pm 0.33) \times 10^{-3}$ [Ber+12]. This muon neutrino changes into a heavy neutral lepton. Note that the production of this sterile neutrino is suppressed by a factor $\theta_\mu$ with respect to the production of an active neutrino. In the decay the sterile neutrino changes back into a muon neutrino. Via the decay products $\pi$ and $\mu$ information about the HNL can be inferred. Since the nature and production of heavy neutral leptons is a very wide topic it will not be covered further within this thesis. For a full review of the phenomenology of GeV-scale heavy neutral leptons see [Bon+18].
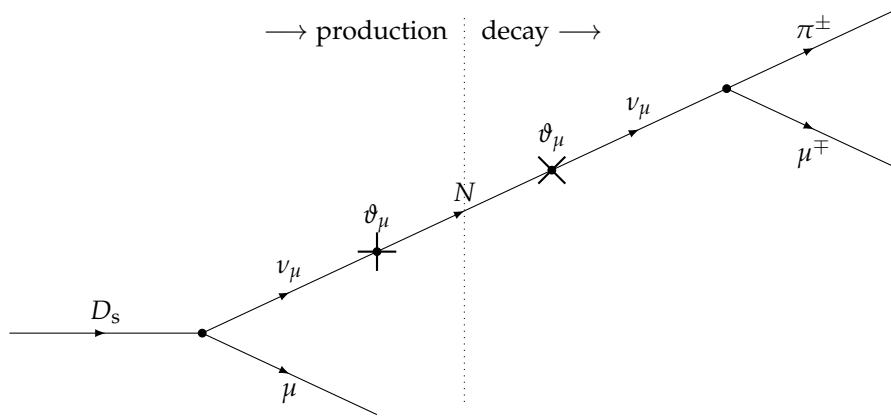


Figure 3.6: The production (left) and the decay (right) of a heavy neutral lepton $N$. The production of $N$ is suppressed by a factor $\vartheta_\mu$ with respect to the production of an active neutrino.

## 3.4 OUTLINE OF THE DETECTOR AND EXPERIMENT SITE

This section briefly outlines the SHiP site and the SHiP detector for quick reference purposes. Each individual part of the SHiP detector mentioned in this section is described in detail in sections 3.5 ff.

### 3.4.1 *Experiment site*

The SHiP facility will use the Super Proton Synchrotron (SPS) at CERN. The SPS is a synchrotron with a circumference of 6.9 km that is used as a preaccelerator for the Large Hadron Collider (LHC). The operational requirements for SHiP are based on minimal modifications to the SPS complex as well as best reusability of already existing beam and transfer lines – although new beam transfer lines are planned. Figure 3.7 gives an overview of the SPS accelerator complex. Here, the SHiP facility is located on the North area at the CERN Prevessin site.
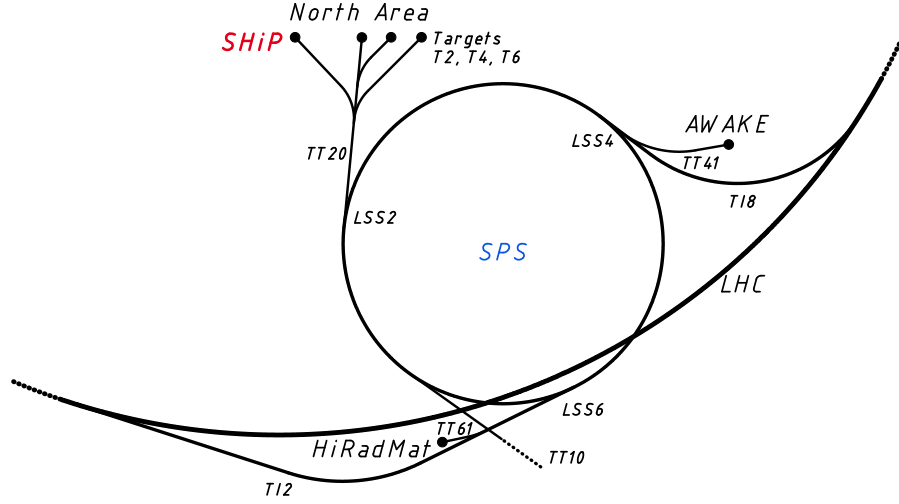


Figure 3.7: Schematic overview of the SPS accelerator complex. SHiP will be located at CERN's north area and will use 400 GeV protons accelerated by the SPS. The SPS itself can be used as a preaccelerator for the LHC. The image is not to scale.

### 3.4.2 *SHiP detector*

Figure 3.8 shows the preliminary layout of the SHiP detector. A proton beam coming from the SPS hits a Molybdenum-Tungsten *proton target* (see section 3.5), resulting in an estimated $2 \times 10^{20}$ protons on target collisions over five years. After the proton target a *hadron stopper* (see section 3.6) stops $\pi^{\pm}$ and $K$ mesons before decaying. Additionally, an *active muon shield* (see ibid.) removes muons from the decay volume. The *neutrino detector* (see section 3.7) is placed downstream the muon shield and consists of an OPERA-like [Aga+18]
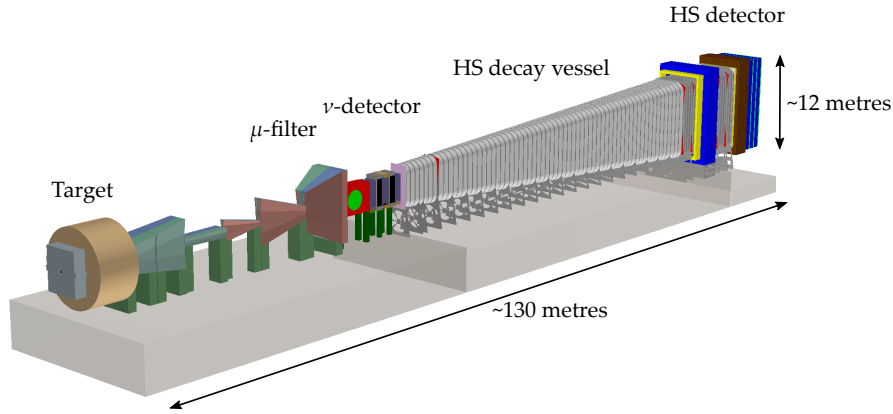
Figure 3.8: Layout of the SHiP experiment. The protons collide with a target which is followed by a muon filter and a neutrino detector. Hidden particles decay in the HS decay vessel and the resulting decay products are detected in the HS detector. Adapted from [Gra19].

emulsion tracker in a magnetic field. Here, charged particles produced in charged current neutrino interactions are measured and identified. A target tracker provides time stamps for reconstructed events. It is followed by a *muon magnetic spectrometer* (see section 3.7.3) which identifies muons created in neutrino interactions and $\tau$ decays as well as vetoes charged particles produced outside the main decay vessel. The main *vacuum decay vessel* is a fifty metre long frustum of a pyramid and the first part of the *Hidden Sector Detector* (see section 3.8). The hidden sector detector also incorporates the spectrometer straw tracker, where the masses and tracks of the hidden particles' decay products are reconstructed. Finally, the hidden sector detector also has *electromagnetic and hadronic calorimeters* which form the particle identification system whose task is to identify the decay products.

## 3.5 PROTON TARGET

The super proton synchrotron beam has an intensity of 400 GeV, resulting in an instantaneous beam power of roughly 5.56 MW per spill and an average beam power of around 355 kW over consecutive spills. This makes the design of the target, especially its radiological protection and its cooling particularly complicated.

*A spill is a particle bunch which is delivered to the target.*

Due to the physics scope of the experiment, the SHiP proton target is on the one hand designed to maximise the production of heavy mesons such as $B$ and $D$ mesons and on the other hand designed to minimise the production of muons and neutrinos which are created in the decays of pion, kaons and short-lived meson resonances resulting from proton interactions. In order to achieve this, the pions and kaons have to be stopped as soon as possible before decaying. Thus, the

target has to be large enough to contain the full proton shower and has to be made out of a material with a high atomic mass and an interaction length as small as possible.

Currently, the design foresees a longitudinally segmented hybrid target, as shown in figure 3.9. The first half of the target will consist out of several blocks of tantalum-alloy clad titanium-zirconium doped molybdenum (TZM) with a cumulative length of four interaction lengths (one interaction length is 58 cm). The second half of the target will be made out of pure tungsten blocks with a total length of six interaction lengths. Between the different blocks 16 slits with a width of 5 mm will be used for watercooling the target. Their locations as well as the widths of the TZM and tungsten blocks are optimised to make the energy deposition in the target to be as uniform as possible. Computations show that this design limits the peak power density per spill in the target to less than $850\,\mathrm{J\,cm^{-3}}$.

The target will be situated in a double walled vessel. While the inner vessel ensures the pressurised water cooling of the target, the outer, gas filled vessel acts as a safety hull containing possible leaks from the inner vessel and avoiding corrosion. The double walled vessel itself is located in a target complex designed to be remotely manageable.

Downstream the proton target a 5 m thick proximity shielding acting as a hadron stopper is planned. The main task of the hadron stopper is to absorb secondary hadrons and non-interacting protons which escape the target. It will also reduce the radiative exposure of the muon shield significantly.
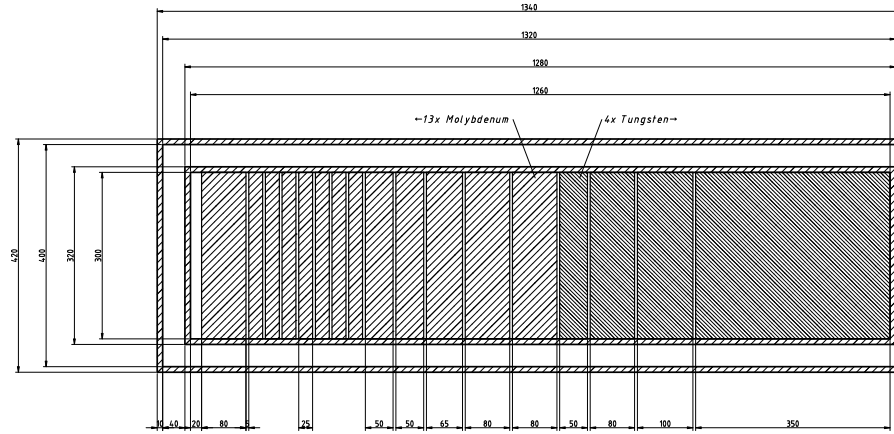


Figure 3.9: A cut through the proton target. The target will consist of molybdenum and tungsten blocks interleaved with watercooling slits. Adapted from [Ane+15].

## 3.6 ACTIVE MUON SHIELD

Per second of spill duration, a total flux of $\mathcal{O}(10^{11})$ muons with a momentum exceeding $1\,\mathrm{GeV}\,c_0{}^{-1}$ emanates from the proton target. These

muons pose a great challenge since they can cause fake decay vertices in the decay volume. Moreover, they can produce long-lived neutral particles in the immediate vicinity via deep inelastic scattering. Hence, the muon flux has to be reduced by several orders of magnitude. In order to maximise the acceptance the detector has to be as close to the proton target as possible, which in turn means that the muon shielding has to be as short as technically feasible. It is realised by a set of sweeping magnets.

## 3.7 THE τ NEUTRINO DETECTOR

The τ neutrino detector, which is illustrated in figure 3.10, consists of two subunits. The first subunit is the the Neutrino Emulsion Target (NET), which uses the Emulsion Cloud Chamber (ECC) technology. The second subunit is the muon magnetic spectrometer (MMS).
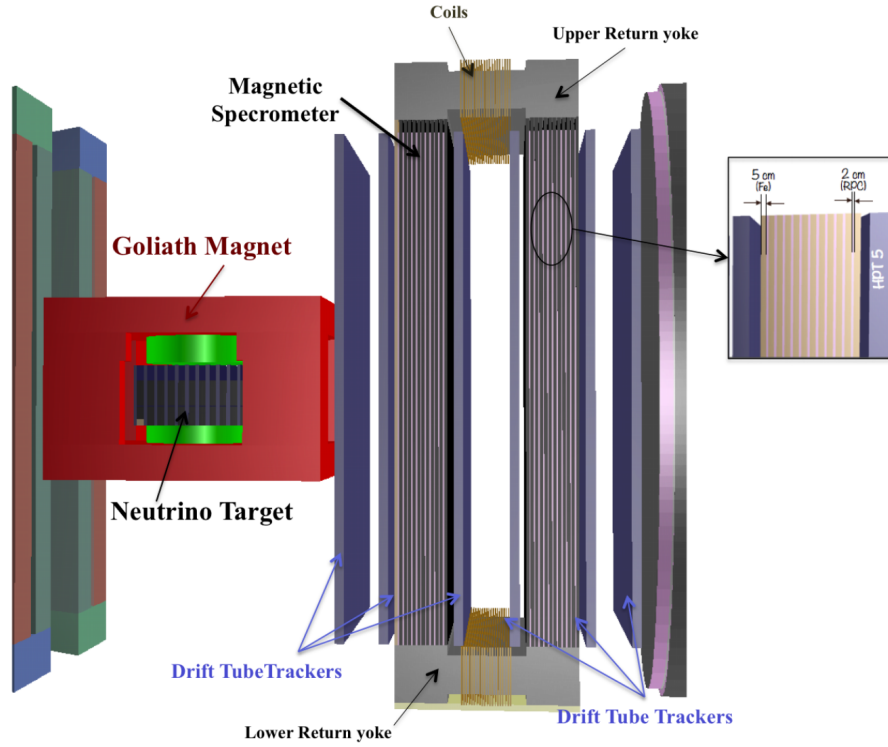


Figure 3.10: The tau neutrino detector of the SHiP experiment. It consists of two main parts, the neutrino target and the magnetic spectrometer. Taken from [Ane+15].

### 3.7.1  Neutrino Target

The neutrino target is made up of two parts. Firstly, the neutrino emulsion target (NET) is located inside the magnetic field of the Goliath magnet. The NET is followed by the second part, the muon target tracker (TT).

The neutrino target consists of eleven *walls* of $15 \times 7$ individual *bricks* and their corresponding *compact emulsion spectrometers* (CES), as shown in figure 3.11.
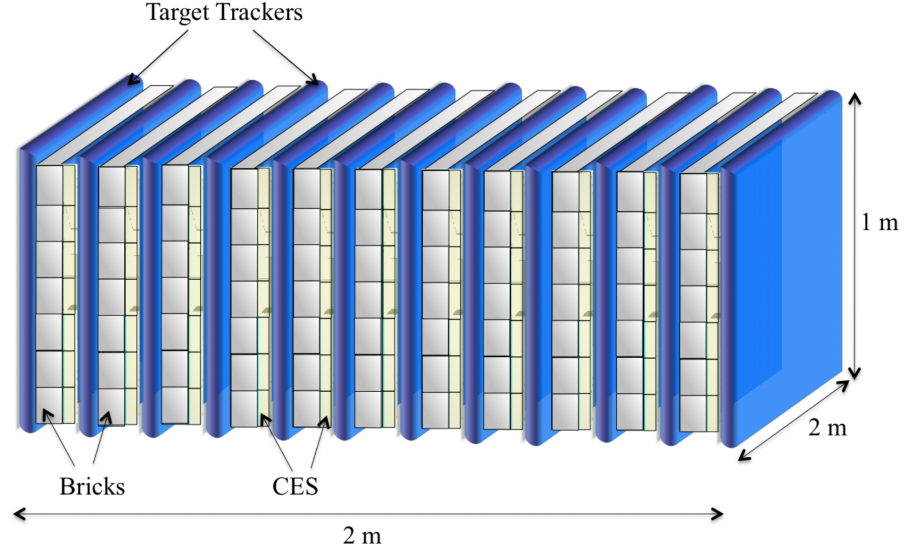


Figure 3.11: Schematic view of the $\tau$-neutrino target. It is the first part of the $\tau$-neutrino detector and consist of two parts, viz. the neutrino emulsion targets (NET) and the target trackers (TT). The neutrino emulsion targets consist of bricks and compact emulsion spectrometers (CES).

*Neutrino Emulsion Target*

The neutrino emulsion target is located in the magnetic field of the Goliath magnet and consists of OPERA-type modules employing the emulsion cloud chamber (ECC) technology. It is a modular design where each unit consist of bricks and a compact emulsion spectrometer. With the NET $\nu_\tau$ and $\bar{\nu}_\tau$ can be distinguished by measuring the properties of the $\tau$ leptons created by the $\nu_\tau$ and $\bar{\nu}_\tau$ in the target.

BRICKS    Each individual brick consists of alternating layers of emulsion films and lead plates. In total, 57 layers of $300\,\mu m$ thin emulsion film and 56 layers of $1\,mm$ thin lead plates will be used.

The emulsion film is made out of a transparent plastic base that has a sensitive layer on each side. Each sensitive layer consists of AgBr crystals in gelatin binder, which, in case of a scattering event, are sensitised along the particle's path creating *latent image centres*. These image centres can be made visible with an optical microscope via a chemical process called development. During the development, the growth of silver clusters with a diameter of $0.6\,\mu m$ at the latent image centres is induced. The path of the scattering particle can then be determined by connecting the two hits shown in the two sensitive layers. Note that the emulsion accumulates tracks over time, meaning

that the bricks must be replaceable as this track accumulation makes it increasingly different to match tracks.

Transversally, each brick has a size of 128 mm × 102 mm and longitudinally each brick is 79 mm long. The mass of a single brick is approximately 8.3 kg. The design of the bricks allows a complete event reconstruction due to the short lifetime of the $\tau$ lepton and the consequent neutrino interaction and $\tau$ lepton decay vertices lying in the same brick.

COMPACT EMULSION SPECTROMETERS     The $\tau$ lepton mostly decays into hadrons with a branching ratios of 49.5 % and 15.0 % for the $\tau^- \rightarrow h^- \nu_\tau(n\pi^0)$ and $\tau^- \longrightarrow h^- h^- h^- \nu_\tau(n\pi^0)$ processes respectively – see also table 3.2. Since hadrons have an interaction length that is about a third of the length of a brick, they are typically unable to leave the target. It is therefore necessary to determine their charge in order to distinguish between tau neutrinos and anti tau neutrinos. The decays of $\tau$-leptons can be classified into *short* and *long* decays. In a short decay, the decay of the $\tau$ lepton takes place in the same lead layer of the brick where the neutrino interaction occured. In this case, the selection of the $\tau$ candidates is performed by a measurement of the impact parameter with respect to the vertex of the decay's daughter particles. Conversely, long decays occur further downstream, where the selection of the $\tau$ candidates is based on a measurement of the kink angle between the $\tau$ track and the daughter track.

In order to perform charge measurements in the target, a compact emulsion spectrometer is situated after every brick. The CES consists of three 300 µm emulsion films interleaved with two 15 mm Rohacell layers. The Rohacell layers are passive material and act as spacers in order to diminish the effect of multiple coulomb scattering. With the CES, an efficiency of 90 % for the charge measurement of hadrons produced during the $\tau$ lepton decay can be achieved, assuming a magnetic field strength of 1 T. Additionally, the efficiency of determining muon tracks is improved by 20 % by the CES.

*Target Tracker (TT)*

In the $\nu_\tau$ target of the SHiP experiment, target trackers (TT) are placed in between two walls of neutrino emulsion targets with a gap of a few millimetres . With one target tracker being located upstream, this results in twelve TTs in total. Each target tracker has dimensions of 2 m × 1 m and a thickness of less than 5 cm. The task of the target trackers is to provide the time stamp for the events that are reconstructed in the emulsion. Moreover, they predict the target unit in which the neutrino interaction has occurred. The performance that has to be achieved by the target trackers for a magnetic field $1\,\text{T} \leqslant B \leqslant 1.5\,\text{T}$ is a position resolution of 100 µm and an efficiency of 99 % up to 1 rad. This is because tracks of the same interaction that originate

from different vertices have to be distinguished. Also, the muonic flux complicates the tracking in the compact emulsion spectrometers. The target trackers improve this situation by providing a muon veto.

### 3.7.2   *Goliath Magnet*

In order to be able to perform charge measurements, the neutrino target has to be magnetised. Since the target volume of a few cubic metres has to experience a Tesla field along the vertical axis, the magnetisation of the $\nu_\tau$ target is planned to be accomplished using the Goliath magnet. The Goliath magnet, which has been manufactured in 1976, has external dimensions of $4.5\,\text{m} \times 3.6\,\text{m} \times 2.79\,\text{m}$ [Gai69] and features side windows enabling the change of the bricks. Based on a map obtained by the NA57 experiment [Vir01] the behaviour of the magnetic field has been derived in the past [Ane+15]. It was found that the magnetic field has cylindrically symmetrical and has a constant strength of about 1.5 T in the centre.

### 3.7.3   *Muon Magnetic Spectrometer*

The main task of the muon spectrometer is the precise identification of the charge signs and the momenta of the muons created in neutrino interactions and $\tau$ decays. It consists of three main components, namely the magnet, resistance plate chambers and drift tubes, whose design is heavily based on the experience gained during the OPERA experiment.

#### *Magnet*

The task of the magnet is to bend charged particles' tracks so that their charge can be measured. The design of the magnet is depicted in figure 3.12. It consists of two iron walls consisting of four slabs each. Each slab consists of twelve 5 cm thick iron layers with 2 cm thick air gaps in between that are reserved for resistance plate chambers. The iron walls are connected via top and bottom iron yokes, resulting in a height of 10 m and a width of 4 m. The magnetisation is achieved by two coils around the top and bottom yokes. The coils have twenty windings and are operated at a nominal current of 1.6 kA, resulting in a magnetic field strength of approximately 1.57 T with a reported non uniformity along the height of less than five percent.

#### *Resistive Plate Chambers*

Resistive plate chambers (RPCs) are gas-based detectors which are generally used for identifying charged particles via their flight time. Figure 3.13 schematically shows the construction of an RPC. It consists of two resistive electrode plates made of 2cm thick Bakelite$^{\circledR}$ which
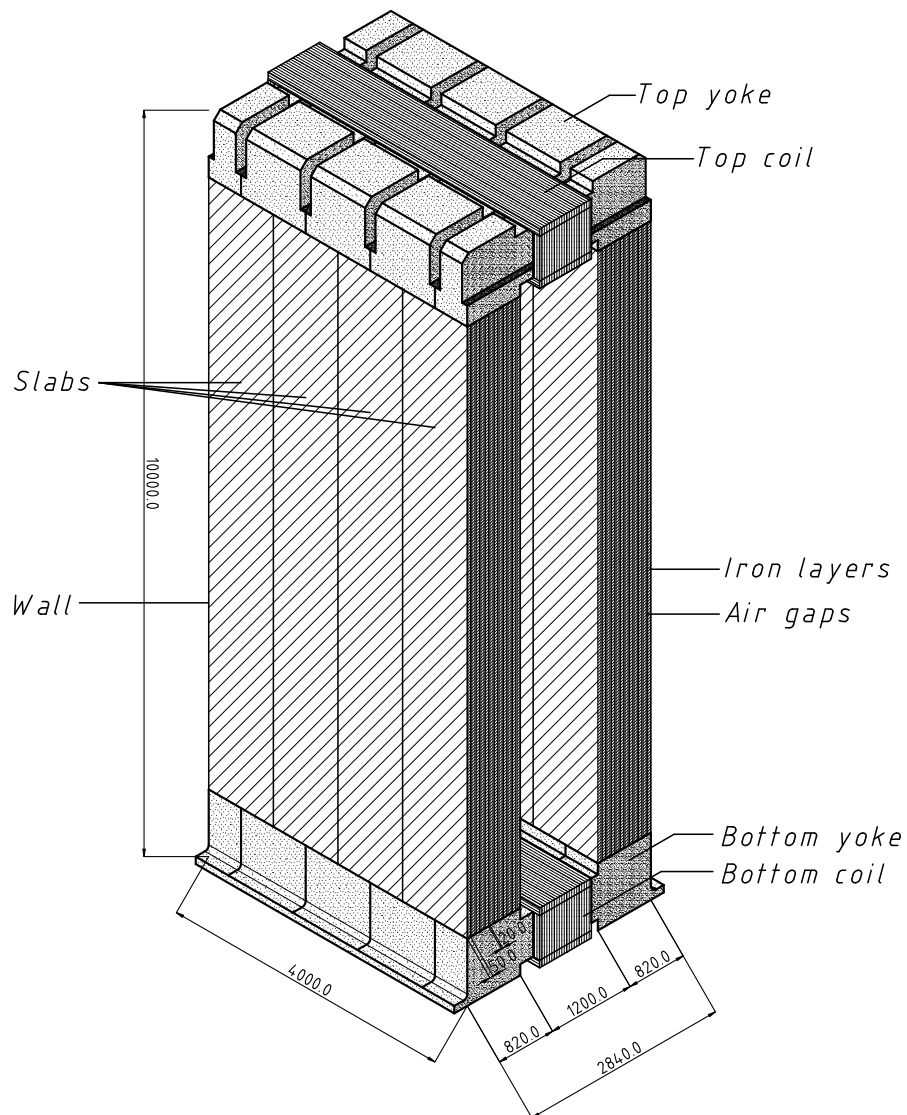
Figure 3.12: A sketch of the muon magnetic spectrometer's magnet. The magnet consist of two iron walls made up of four slabs each. Adapted from [Ane+15].

enclose a gas volume of usually 2 cm and whose outsides are coated with graphite. The graphite layers act as electrodes between which a high voltage is applied creating a homogeneous electric field within the gas volume. Thus, the ionisation of gas atoms caused by the passage of a charged particle produces an electron avalanche and consequently a spark that is quenched by the resistance of the electrodes. The spark induces a signal which can be read out by means of copper strips that are separated from the graphite layers through 200 µm polyethylene terephthalate (PET) films.

In SHiP, the RPCs are used to track particles within the magnetised iron walls with a resolution of 1 cm. In each of the 22 gaps between the iron layers one 2 cm plane of RPCs is used. Each plane has dimensions of 4 m × 8 m (width × height) and is subdivided into 14 RPC chambers each measuring 2 m in width and 1.1 m in height. The readout of each row of RPCs is performed using 32 orthogonal strip panels.
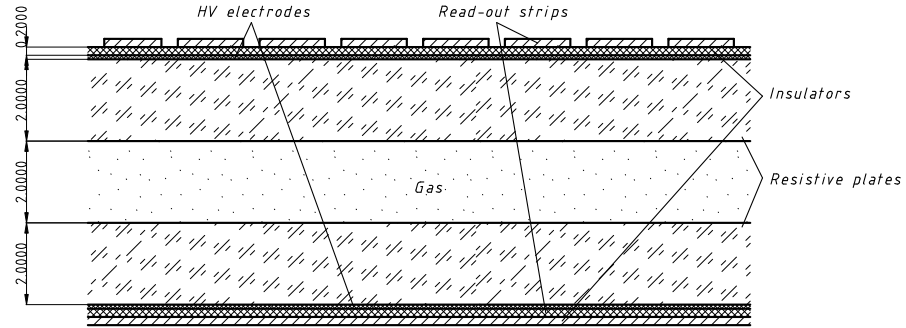


Figure 3.13: Schematic representation of a resistive plate chamber (RPC). RPCs are gas-based detectors which, in SHiP, are used to track particles within the walls of the MMS magnet.

*Drift tube tracking system*

The drift tube tracking system used in SHiP has the task to measure the charge and the momenta of the muons created in neutrino interactions in the emulsion target. In order to further improve the efficiency, the iron yoke of the Goliath magnet is used as a muon filter. In order to conduct a full three-dimensional reconstruction of the muon track, a pair of drift tube stations is located between the Goliath magnet and the spectrometer. These stations are rotated by ±3.6° around the beam axis in order to ensure optimal reusability of the OPERA drift tube stations. For the charge and momentum measurement by the spectrometer, two drift tube stations will each be located inside the magnet and on the outer, downstream side of the magnet resulting in a total of ten planes. In SHiP, the drift tube modules of the OPERA experiment are being reused, eight of which form one of the ten drift tube stations in SHiP. Each module consists of 48 aluminium tubes which are arranged in an array of 12 × 4 tubes. Every tube has a length

of 7926 mm, an outer diameter of 38 mm and an inner diameter of 37.15 mm. The central sense wire is made out of gold plated tungsten.

Unlike in the OPERA experiment where the drift tubes were operated with a $ArCO_2$ mixture at a ratio of 80 % to 20 %, SHiP will use a $ArCO_2N_2$ gas mixture. The addition of nitrogen reduces the drift time and thus results in quicker collection times. The electronics are another part where OPERA's setup differs from SHiP, which will use newly designed electronics. The main difference is the utilisation of a continuous triggerless readout process. Here, the drift time as well as the time over threshold are measured. Measuring the latter is considered as being useful for rejecting electrical noise as well as X-ray hits. In order to ensure a highly accurate track reconstruction, the drift time needs to have an accuracy of 2 ns root mean square (RMS). Therefore, not only the timestamp of the target tracker is considered, but also a redundant time stamp provided by a layer of scintillator tiles located between the Goliath magnet and the first station of drift tubes.

## 3.8 HIDDEN SECTOR DETECTOR

The hidden sector detector consists of four main parts, a vacuum decay vessel including a veto, a spectrometer tracker, an electromagnetic/hadronic calorimeter and a muon detector.

### 3.8.1 *Vacuum decay vessel*

Deep inelastic neutrino-nucleon scattering creates neutral strange particles such as $K_L^0, K_S^0, \Lambda$, also referred to as $V^0$ particles. The decay of these particles mimics the decay of hidden particles thus creating a considerable background. The performance of SHiP is directly associated with the rejection of such background. In order to bring the background rejection to the required level, the fiducial volume is contained in a vacuum decay vessel. The vacuum vessel is a frustum of a pyramid with a length of approximately 50 m. It consists of S355J0(J2/K2)W COR-TEN™ steel and is evacuated to $\mathcal{O}(10^{-3}\,\text{bar})$. Upstream its dimensions are 2.4 m × 4.5 m enlarging up to 5 m × 10 m downstream.

The veto capabilities of the vacuum decay vessel are provided by a background tagger. Possibly, the background tagger will also permit to decide offline, whether or not activity in the tracking and calorimeter detectors comes from outside particles. Currently, two different implementations of the background tagger are being evaluated, one based on liquid scintillator and one on plastic scintillator. While the first one will be directly integrated in the decay volume, the latter one is planned to be attached directly to the structure.

### 3.8.2    *Spectrometer straw tracker*

The spectrometer straw tracker is located downstream the vacuum decay vessel. Its objective is to reconstruct the tracks of charged particles created during the decay of hidden particles, to determine the track momentum and to reject background events. It will be implemented as a magnetic spectrometer using a large aperture dipole magnet in combination with two tracking telescopes. Straw tubes will be used for the spectrometer tracker since, among other aspects, a high spacial resolution is required. The spectrometer tracker will also utilise a timing detector which will provide time stamp so that particles in the spectrometer can be measured coincidingly. This required coincidence allows to differentiate spurious signals caused by background muons crossing the vessel within the vertex reconstruction resolution from authentic events. It is currently being investigated whether plastic scintillators or multi gap resistive plate chambers (MRPCs) are best suited for the timing tracker.

### 3.8.3    *Electromagnetic and hadronic calorimeter*

The calorimeters are located downstream the spectrometer tracker. They both utilise the Shashlik-technique, i.e. they consist of alternating layers of absorber material and scintillator material, which are read out via wavelength shifting (WLS) fibres.

The objective of the electromagnetic calorimeter (ECAL) is the identification of electrons, pions and photons in order to discern decays of heavy neutral leptons from kaon decays. It will also provide timing information on signals at the nanosecond level.

The purpose of the hadronic calorimeter (HCAL) is to separate pions from muons, in particular for particles with momenta less than $5\,\mathrm{GeV}\,c_0{}^{-1}$. Moreover, the HCAL will tag neutral hadrons which have not yet been observed by any other detector and, similar to the ECAL, provide timing information on the signals at the nanosecond level.

### 3.8.4    *Muon detector*

The main goal of the muon detector, which is located downstream the two calorimeters, is to detect muons as efficiently as possible. In order to do so, the muon detector is planned to consist of four active modules, also called stations. Each station is $6\,\mathrm{m} \times 12\,\mathrm{m}$ (width $\times$ height) in dimensions and consists of two layers of plastic scintillator bars and the accompanying aluminium support structure. The plastic scintillators will be read out via wavelength shifting fibres. Between the stations $60\,\mathrm{cm}$ iron walls will be located acting as muon filters.

# STRAW TUBES

> ' ... In the fabrication and operation of a chamber people seem to use a mixture of competence, technical skill and magic rites, of the kind "I do not know what I'm doing but somebody told me to do so". '
>
> — Fabio Sauli, *Principles of operation of multiwire proportional and drift chambers*

A straw tube is a gaseous ionisation detector and is used for the detection of fast, charged or ionising particles in high energy physics experiments [Tok90]. In nearly all cases a straw tube is not used singularly, but multiple arrays of parallel straw tubes form a straw detector. The benefit of straw detectors are their simple design and thus their affordability as well as their high spatial resolution [Kuc+17].

## 4.1 WORKING PRINCIPLE

The layout and basic working principle of a straw tube are illustrated in figure 4.1. A straw tube consists of a conductively coated foil rolled up to form a cylindrical tube with an inner radius $r_t$. This tube is filled with a suitable gas or a gas mixture – for more information about the effect of different gas mixture see section 4.2.4. In its middle a conductive wire with a radius $r_w$ is placed. An electrical potential is applied between the two parts such that the foil's conductive coating acts as a cathode while the wire forms the anode. The applied high voltage results in a radially symmetric electrical field, which is derived in section 4.1.2.

*Typical values are $r_t = 1\,\mathrm{cm}$ and $r_w = 22.5\,\mu\mathrm{m}$.*

If a charged ionising particle passes through the tube, it interacts with the gas atoms mainly via the Coulomb interaction creating clusters of electron-ion-pairs along its way. This process is called *primary ionisation*. The number of clusters created follows a Poisson distribution. If *n* denotes the *average* number of primary ionisations, then

$$P_n(k) = \frac{n^k}{k!} \exp(-n) \tag{4.1}$$

describes the probability for *k actual* primary ionisations to happen. The theoretical efficiency $\eta$ for this process is given by

$$\eta = \sum_{k=1}^{\infty} P_n(k) = 1 - P_0(k) = 1 - \exp(-n \cdot 1\,\mathrm{cm}), \tag{4.2}$$

which, for a typical value of $n = 30$ for 1 cm results in an inefficiency of $1 \times 10^{15}$ [Sew06; Sau77]. The number of electrons and ions created

per cluster varies with the energy transferred during the ionisation event. Assuming the absence of a magnetic field, the electric field inside the straw tube makes the electrons drift along the electric field lines towards the wire while the ions drift towards the foil. Since the electrons are highly mobile, they can further ionise gas atoms along their way, especially near the anode wire where the field strength is particularly large – see equation (4.16) or figure 4.3. This process, also referred to as *secondary ionisation*, results in an avalanche, multiplying the initial charge by a factor called the *gas gain* [Dub11]. The secondary ionisation is the major contributor to the electric signal which can be read out using special electronic equipment and then be further processed. The leading edge of the measured signal corresponds to those electrons which arrived first and were thus nearest to the wire. This shortest distance is called *drift radius.* The time it takes the electrons to travel the drift radius is called *drift time* and depends on several factors such as the tube's geometry, the used gas mixture and pressure, the applied high voltage, or the temperature.

An important aspect of a straw tube is its detection efficiency. Assume a straw tube detector consists of various tubes arranged in $n$ layers through which a particle passes. By means of software algorithms the track of the particle can then be reconstructed. After a track which passed the particular straw tube is reconstructed it is checked whether or not the straw tube has *fired*, i.e. given a signal. Then, the *single tube hit detection efficiency* $\eta$ can be defined as the ratio of 'fired to not fired' straw tubes:

$$\eta = \frac{N_{\text{fired}}}{N_{\neg\text{fired}}},\tag{4.3}$$

with a standard deviation of

$$\sigma_\eta = \sqrt{\frac{\eta(1-\eta)}{N_{\neg\text{fired}}}}.\tag{4.4}$$

Another important characteristic is the *single tube track efficiency* $\tilde{\eta}$ which can be written as the product of the single tube hit efficiency and the probability $\eta$ that the hit gives the correct value for the drift radius [Zim+05]:

$$\tilde{\eta} = \eta\varepsilon.\tag{4.5}$$

### 4.1.1 *Ionisation*

The differential energy loss per unit length of the particles crossing a straw tube is given by the Bethe-Bloch-formula [Bet30; Bet32]:

$$-\frac{\mathrm{d}E}{\mathrm{d}x} = \frac{4\pi r_e^2 m_e c_0^2 N_A Z \varrho z^2}{A\beta^2}\left[\ln\left(\frac{2m_e c_0^2\beta^2}{I(1-\beta^2)}\right) - \beta^2 - \frac{\delta(\beta)}{2}\right].\tag{4.6}$$

Here,
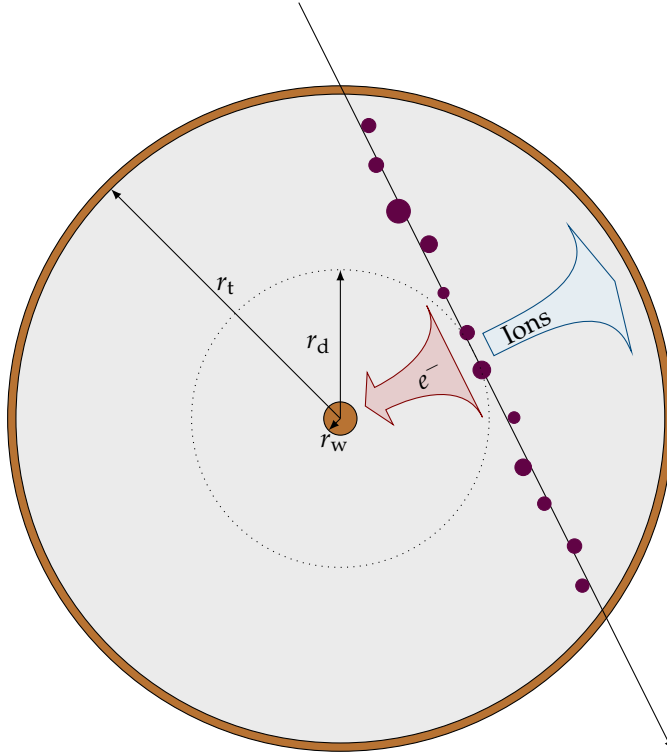
Figure 4.1: Schematic cross section of a gas-filled straw tube with a radius $r_t$. An electrical field is applied between the tube and the anode wire, which has a radius of $r_w$. An ionising particle passing through the straw tube creates clusters of electron-ion-pairs along its way (ionisation clusters, purple). Electrons (red) drift quickly towards the anode wire creating further electron-ion-pairs through the avalanche effect, ions (blue) drift slowly towards the tube resulting in an electrical signal, whose leading edge corresponds to the electrons which were nearest to the anode wire. This minimum distance is called the drift radius $r_d$.

$$
\begin{aligned}
E &= \text{energy of the particle} \\
x &= \text{path length} \\
r_e &= \text{electron radius, } r_e = 2.818\,\text{fm [Kuc14]} \\
m_e &= \text{electron mass, } m_e = 9.109 \times 10^{-31}\,\text{kg [Kuc14; Tan+18]} \\
z &= \text{charge of the particle} \\
c_0 &= \text{speed of light, } c_0 = 2.997\,924\,58 \times 10^8\,\text{m s}^{-1}\,\text{[Kuc14]} \\
v &= \text{velocity of the particle} \\
\beta &= \text{relativistic velocity, } \beta = v/c \\
N_A &= \text{Avogadro number, } N_A = 6.022 \times 10^{23}\,\text{mol}^{-1}\,\text{[Kuc14]} \\
Z &= \text{atomic number of the absorber} \\
A &= \text{mass number of the absorber} \\
\varrho &= \text{density of the absorber} \\
I &= \text{mean excitation potential of the absorber} \\
\delta(\beta) &= \text{density effect}
\end{aligned}
$$

For many materials the ratio $Z/A$ can be assumed as constant. Thus, the energy loss can be considered as being solely dependent on the density $\varrho$ and and the mean excitation potential $I$ of the absorber. The latter one has to be measured for each material, however the assumption that $I = I_0 Z$ with $I_0 = 12\,\text{eV}$ often suffices. In general the energy loss first decreases with increasing energy with $1/v^2$. A minimum is reached at momenta of roughly $\beta\gamma = p/mc \approx 3$. Particles with energies that lie in this minimum are often referred to as *minimum ionising particles*. For higher energies the energy loss increases again. This increase is described by the logarithmic term in the Bethe-Bloch equation [Sew06].

*Minimum ionising particles are often just referred to as 'MIPs'.*

### 4.1.2 *Electrical field*

The derivation of the electrical field inside a straw tube begins with Maxwell's first equation – Gaus's law. It states that

$$
\operatorname{div} \boldsymbol{E} = \frac{\varrho}{\epsilon_0}, \tag{4.7}
$$

or, in its integral form,

$$
\int_V \operatorname{div} \boldsymbol{E} \, \mathrm{d}V = \frac{1}{\epsilon_0} \int_V \varrho \, \mathrm{d}V = \oint_{A=\partial V} \boldsymbol{E} \, \mathrm{d}\boldsymbol{A}. \tag{4.8}
$$

Here, $\varrho$ denotes the charge density, $\epsilon_0 = 8.85 \times 10^{-12}\,\text{A s V}^{-1}\,\text{m}^{-1}$ [Kuc14] the vacuum permittivity and $\partial V$ the closure of the volume $V$. Using cylindrical coordinates where $\mathrm{d}\boldsymbol{A} = r\,\mathrm{d}\phi\,\mathrm{d}z$ then gives

$$
\oint_{\partial V} \boldsymbol{E} \, \mathrm{d}\boldsymbol{A} = \int_0^{\Delta z} \int_0^{2\pi} E(r)\, r \, \mathrm{d}\phi \, \mathrm{d}z = 2\pi r \Delta z E(r). \tag{4.9}
$$

Moreover,

$$
\frac{1}{\epsilon_0} \int_V \rho \, \mathrm{d}V = \frac{\Delta Q}{\epsilon_0} \tag{4.10}
$$
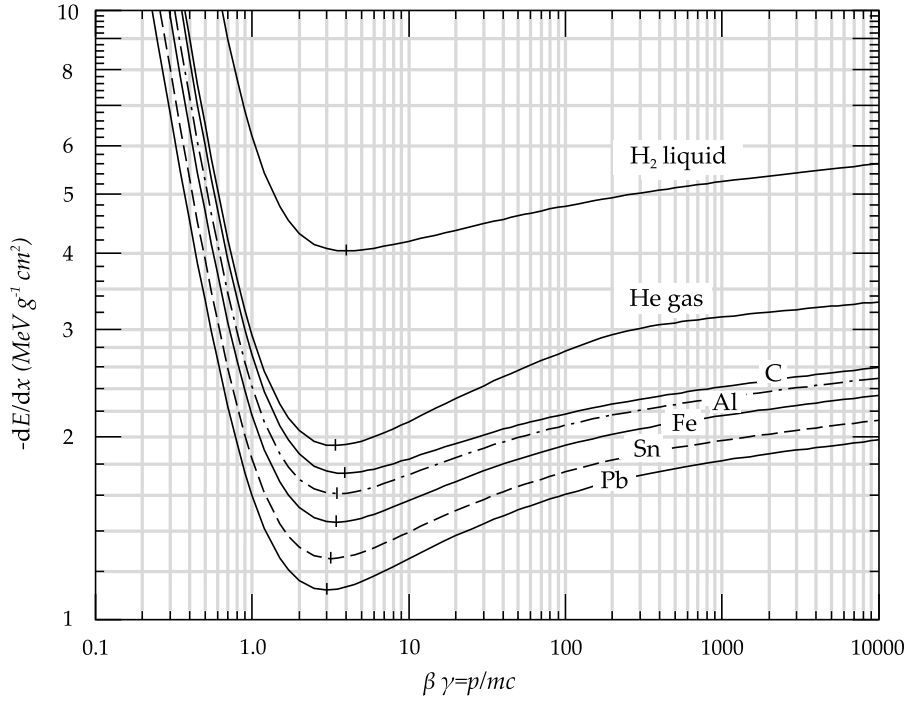
Figure 4.2: Mean energy loss in hydrogen, helium, carbon, aluminium, iron, tin and lead. Taken from [Ams+08].

with $\Delta Q$ denoting the charges contained within a length $\Delta z$ of the anode wire. From equation (4.8) it thus follows that

$$2\pi r \Delta z E(r) = \frac{\Delta Q}{\epsilon_0}. \tag{4.11}$$

In order to simplify the treatment edge effects can be neglected. This can be done by introducing the assumption that the total length $l$ of the anode wire is much larger than the radius $r_t$ of the straw tube ($l \gg r$). Then the charge density per length of the anode wire can be seen as constant:

$$\frac{Q}{z} = \frac{\mathrm{d}Q}{\mathrm{d}z} = \text{const.} \tag{4.12}$$

Hence, equation (4.11) gives

$$E(r) = \frac{1}{2\pi r \epsilon_0} \frac{\mathrm{d}Q}{\mathrm{d}z}. \tag{4.13}$$

This electric field is created by a high voltage $U$, given by

$$U = \int_{r_w}^{r_t} E(r)\,\mathrm{d}r = \frac{1}{2\pi\epsilon_0}\frac{\mathrm{d}Q}{\mathrm{d}z}\int_{r_w}^{r_t} r^{-1}\,\mathrm{d}r = \frac{1}{2\pi\epsilon_0}\ln\left(\frac{r_t}{r_w}\right)\frac{\mathrm{d}Q}{\mathrm{d}z}. \tag{4.14}$$

*Note that this can be done as the electric field is a conservative field.*

Solving for $\mathrm{d}Q/\mathrm{d}z$ gives

$$\frac{\mathrm{d}Q}{\mathrm{d}z} = \frac{2\pi\epsilon_0 U}{\ln\left(\frac{r_t}{r_w}\right)} \tag{4.15}$$

and plugging this into equation (4.14) finally yields

$$E(r) = \frac{U}{r \ln\left(\frac{r_t}{r_w}\right)}. \tag{4.16}$$
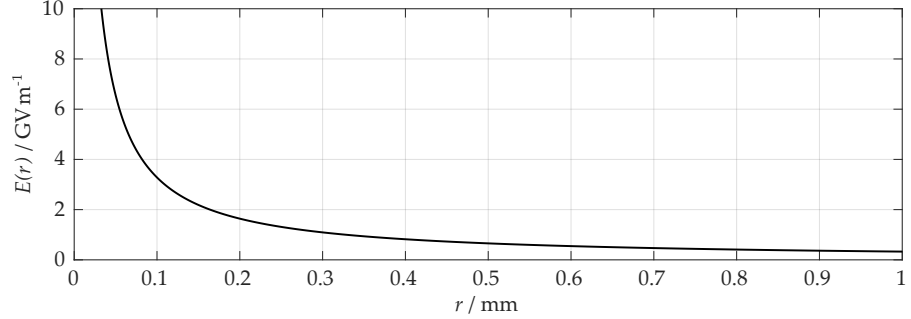


Figure 4.3: The electrical field $E$ inside a straw tube as a function of the radius $r$ – see equation (4.16) – for typical values of $r_t = 1\,\text{cm}, r_w = 22.5\,\mu\text{m}$ and $U = 2\,\text{kV}$.

### 4.1.3    Gas gain

Consider an electron drifting in the electric field inside a straw tube. If this electron has gained sufficient energy an ionisation event can occur. Such ionisation events via collision are the basis for avalanche multiplication. The mean free path length $\lambda$ for ionisation events is given by the average distance an electron has to travel before it gets the chance to become involved in an ionisation event. The inverse of the mean free path length is referred to as the *first Townsend coefficient* $\alpha$, which describes the number of ion pairs that are created over a certain length

*The Townsend coefficient is named after Sir John Sealy Edward Townsend who discovered the phenomenon of the elctron avalance.*

$$\frac{1}{\lambda} = \alpha\left(\frac{E}{\varrho}, \varrho\right). \tag{4.17}$$

The Townsend coefficient has to be measured for every gas as no analytical expression for it exists. However, the coefficient increases with the energy $E$ as the ionisation cross section increases with increasing collision energy. Moreover, assuming $E/\varrho$ fixed, $\alpha$ scales with the density, as all linear dimensions in a gas scale with the mean free path length $\lambda$ which is proportional to $\varrho$ [Fer06; RRB08]. Let $N$ be the number of electrons. Then, the increase of N per path d$r$ can be written with $\alpha$ as

*The term $E/\varrho$ is sometimes referred to as 'reduced field strength'.*

$$\mathrm{d}N = N\alpha\,\mathrm{d}r. \tag{4.18}$$

Integrating equation (4.18) from the radius $r_{\min}$ where the avalanche starts to the radius $r_w$ of the anode wire gives

$$N_{\text{final}} = N_{\text{initial}} \exp\left(\int_{r_{\min}}^{r_w} \alpha(r)\,\mathrm{d}r\right), \tag{4.19}$$

where $N_{\text{final}}$ and $N_{\text{initial}}$ are the final and initial number of electrons in the avalanche. Rearranging this equation gives the gas gain $G$

$$G = \frac{N_{\text{final}}}{N_{\text{initial}}} = \exp\left(\int_{r_{\text{min}}}^{r_{\text{w}}} \alpha(r)\, dr\right) = \exp\left(\int_{E(r_{\text{min}})}^{E(r_{\text{w}})} \frac{\alpha(E)}{\frac{dE}{dr}}\, dE\right). \quad (4.20)$$

Substituting the electric field from equation (4.16) gives

$$G = \exp\left(\frac{U}{\ln\left(\frac{r_{\text{t}}}{r_{\text{w}}}\right)} \int_{E(r_{\text{min}})}^{E(r_{\text{w}})} \frac{\alpha(E)}{E^2}\, dE\right). \quad (4.21)$$

Diethorn [Die56] parametrised the Townsend coefficient as $\alpha = \beta E$, i.e. as linearly dependent on the energy, which is especially true in noble gases. It can be shown that equation (4.21) can then be written as [RRB08]:

$$\ln G = \frac{\ln 2}{\ln\left(\frac{r_{\text{t}}}{r_{\text{w}}}\right)} \frac{U}{\Delta U} \ln \frac{U}{\ln\left(\frac{r_{\text{t}}}{r_{\text{w}}}\right) r_{\text{w}} E(r_{\text{min}}, \varrho_0)\frac{\varrho}{\varrho_0}}. \quad (4.22)$$

This equation is called *Diethorn formula*. Here, $\varrho_0$ is the normal gas density and $\Delta U$ the potential that has to be passed by the electrons in order to be able to perform another ionisation. Applying the Diethorn parametrisation can also be used to determine the dependence of the gain on the gas density. It can be derived that

$$\frac{dG}{G} = -\frac{q_r \ln 2}{2\pi\epsilon_0 \Delta U} \frac{d\varrho}{\rho} \quad (4.23)$$

where $q_r$ is the charge per unit length and $\epsilon_0$ the vacuum permittivity. In practical scenarios the factor of $d\varrho/\varrho$ ranges from five to eight, meaning that changes in gas pressure cause five- to eight-fold variations in gain. For more detailed derivations see [Die56; RRB08].

### 4.1.4  *Drift radius and drift time*

The drift radius $r_{\text{d}}$ is the shortest distance between the track of ionised particles and the anode wire – see figure 4.1. The time it takes the electrons to drift along $r_{\text{d}}$ is called the drift time $t_{\text{d}}$. The drift time from some radius $r \leqslant r_{\text{t}}$ to the anode is given by

$$t_{\text{d}} = t(r) = \int_{t_0}^{t} dt' = \int_{0}^{r(t)} \frac{dt'}{dr'}\, dr' = \int_{0}^{r(t)} \frac{1}{v_{\text{d}}}\, dr'. \quad (4.24)$$

Here,

$$v_{\text{d}} = \frac{dr}{dt} \quad (4.25)$$

is the drift velocity. Rearranging equation (4.24) gives the *rt-relation*:

$$r(t) = \int_{t_0}^{t} v_{\text{d}}\, dt'. \quad (4.26)$$

A spatial resolution that is mostly independent of the drift radius requires a linear *rt*-relation:

$$r(t) = v_{\mathrm{d}}(t - t_0).\tag{4.27}$$

This results in a box-shaped drift time spectrum spectrum, as shown in the left side of figure 4.4. In most cases however, the drift velocity is not independent of the electric field – i.e. non-linear – and drift time spectra are skewed towards shorter times, as illustrated on the right side of figure 4.4. This is due to the fact that, from a technical standpoint, the implementation of a large detector with a linear *rt*-relation requires a uniform electric field and thus uncomfortably large working voltages and results in very long drift times [Sau77]. Using the assumption that the particle tracks are distributed homogeneously with respect to $r_{\mathrm{t}}$, the number of tracks d$N$ passing through the tube in an interval $[r, \mathrm{d}r]$ over d$r$ can be written as [Bie16]:

$$\frac{\mathrm{d}N}{\mathrm{d}r} = \frac{N_{\mathrm{tot}}}{r_{\mathrm{t}}}.\tag{4.28}$$

Here, $N_{\mathrm{tot}}$ is the total number of tracks inside the straw tube. Using this relation the drift velocity from equation (4.25) can be written as

$$v_{\mathrm{D}} = \frac{\mathrm{d}r}{\mathrm{d}t} = \frac{\mathrm{d}r}{\mathrm{d}N}\frac{\mathrm{d}N}{\mathrm{d}t} = \frac{r_{\mathrm{t}}}{N_{\mathrm{tot}}}\frac{\mathrm{d}N}{\mathrm{d}t}.\tag{4.29}$$

Plugging this into the rt-relation (4.26) gives:

$$r(t) = \frac{r_{\mathrm{t}}}{N_{\mathrm{tot}}}\int_{t_0}^{t} \frac{\mathrm{d}N}{\mathrm{d}t'}\,\mathrm{d}t'.\tag{4.30}$$

### 4.1.5  *Signal creation*

Moving charges in a straw tube create electrical signals on the cathodes which can be amplified and then read out. The signal consists of two parts, one from the electrons created in the avalanche near the wire and one from the drifting ions. The cause of the signal is the reduction of the electric field inside the straw tube. A drifting charge $q$ causes a reduction of the electric field given by

$$\Delta \varepsilon = q \int_{r_1}^{r_2} \boldsymbol{E}(\boldsymbol{r})\,\mathrm{d}\boldsymbol{r} = q(\Phi_{r_1} - \Phi_{r_2}),\tag{4.31}$$

where $\Phi_{r_i}$ is the electrical potential at the radius $r_i$. The electron avalanche happens largely near the anode wire. Assuming that the avalanche consists of successive doublings of electron-ion pairs, half of the charge carriers are created within a distance $\lambda_e$ from the anode wire – $\lambda_e$ being the mean free path length of an electron. This results in the electrons having only a small potential difference of $\overline{\Delta\Phi_e} \approx 2\Delta U$,
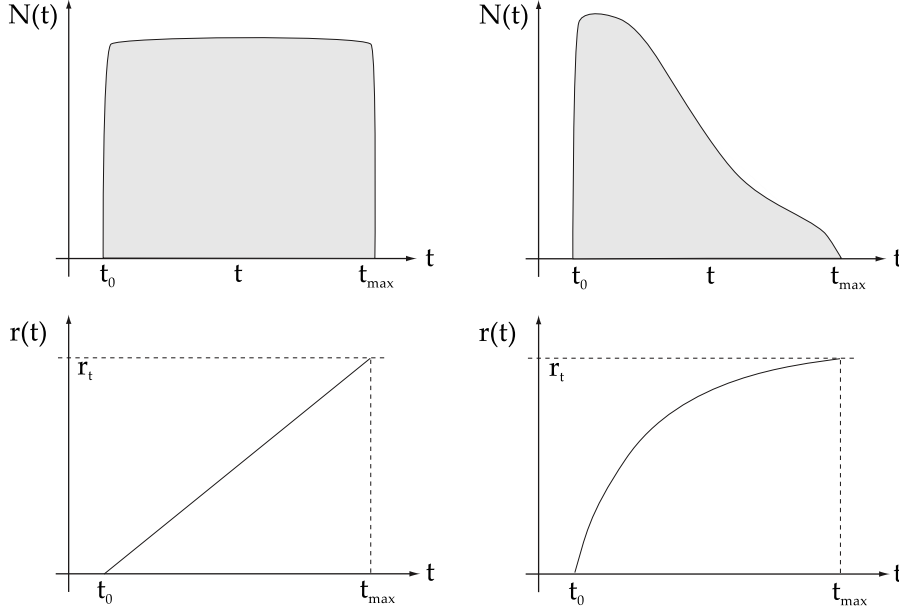
Figure 4.4: Schematical representation of drift time spectra and *rt*-relations. Left side: A box shaped drift time spectrum (top) resulting from a linear *rt*-relation (bottom). Right side: A TDC spectrum skewed towards shorter times (top) resulting from a non-linear *rt*-relation. Darstellung nach [KW16].

whereas the positive ions undergo a potential difference of $\overline{\Delta\Phi_{I^+}} \approx \Phi_{\text{tot}} - 2\Delta U$. For practical applications $\overline{\Delta\Phi_{I^+}} \gg \overline{\Delta\Phi_e}$, meaning that the signal of the electrons is negligable. More specifically, it can be shown that the ratio of charge induced by the electrons is given by [RRB08]

$$\frac{Q_e^{\text{ind}}}{Q_{\text{tot}}^{\text{ind}}} \approx \frac{\Delta U}{U \ln 2}. \qquad (4.32)$$

For typical values of $U$ and $\Delta U$ equation (4.32) gives $Q_e^{\text{ind}}/Q_{\text{tot}}^{\text{ind}} \approx 1\,\%$ to $2\,\%$.

## 4.2 EFFECTS ON DETECTOR PERFORMANCE

Even though straw tubes are relatively simple detectors there is a plethora of physical and chemical effects that influence their performance. Naturally, not all of these effects can be covered in detail within this work. The effects that are described in the following sections include the displacement of the anode wire, the influence of the drift gas, diffusion and ageing of the detector. Note that the description of these effects closely follow [RRB08; KW16], and, to some extent [Sau77; Bie16].

### 4.2.1    *Presence of a magnetic field*

The presence of a magnetic field can change the drift properties significantly as affected particles then travel on circular trajectories between collisions due to the Lorentz force. This results in a changed energy distribution and a change in drift velocity. In 1998, a study [Agu+98] investigated the effect of magnetic stray fields of 0.4 T to 0.8 T on the drift tubes for the barrel muon chambers of the CMS detector at the LHC. According to this study the modified drift velocity is given by

*CMS is an acronym for Compact Muon Solenoid.*

$$v_\mathrm{d} = \frac{e}{m_e} \tau |\boldsymbol{E}| \frac{1}{1 + (\omega\tau)^2} \left\{ \tilde{\boldsymbol{E}} + \omega\tau [\tilde{\boldsymbol{E}} \times \tilde{\boldsymbol{B}}] + (\omega\tau)^2 (\tilde{\boldsymbol{E}}\tilde{\boldsymbol{B}}) \tilde{\boldsymbol{B}} \right\}. \quad (4.33)$$

Here, $\omega$ is the cyclotron frequency, $\tau$ the electron frequency and $\tilde{\boldsymbol{E}}, \tilde{\boldsymbol{B}}$ the normal field vectors. This equation simplifies in case of orthogonal fields to

$$v_\mathrm{d}(E, B) = v_\mathrm{d}(E, 0) \cos\left(\alpha_\mathrm{L}(E, B)\right). \quad (4.34)$$

The Lorentz angle $\alpha_L$ has to be measured for every electric field strength, magnetic field strength and for every gas composition. In case of a gas mixture of $ArCO_2$ in a 85 %/15 % mixing ratio with $E = 2\,\mathrm{kV\,cm^{-1}}$ and $B = 0.5\,\mathrm{T}$ a Lorentz angle of $\alpha = 12°$ was found, resulting in an increase of the drift velocity of roughly 8 ns. Note that the drift tubes for CMS's barrel muon detector are not cylindrical but rectangular.

### 4.2.2    *Wire displacement*

In case of a perfect detector, the electric field derived in section 4.1.2 (see equation (4.16)) holds true. In reality however, the wire may be displaced from the centre. Let the wire be displaced from the centre of the tube in the $y$-direction by the distance $d$ as shown in figure 4.5. Since the wire defines the centre of the coordinate system, one boundary condition for the electric potential $\Phi$ is

$$\Phi(r_\mathrm{w}) = U. \quad (4.35)$$

Writing the radius vector $r$ as a function of $\phi$ gives the second boundary condition

$$r = d \sin\phi + r_\mathrm{t} \sqrt{\left(1 - \left(\frac{d}{r_\mathrm{t}}\right)^2\right)(1 - \sin^2\phi)}. \quad (4.36)$$

Using these boundary conditions the electrostatic problem can be solved, albeit quite a tedious calculation. Hence, the derivation is omitted here, although it is described in detail in [RRB08]. There, it
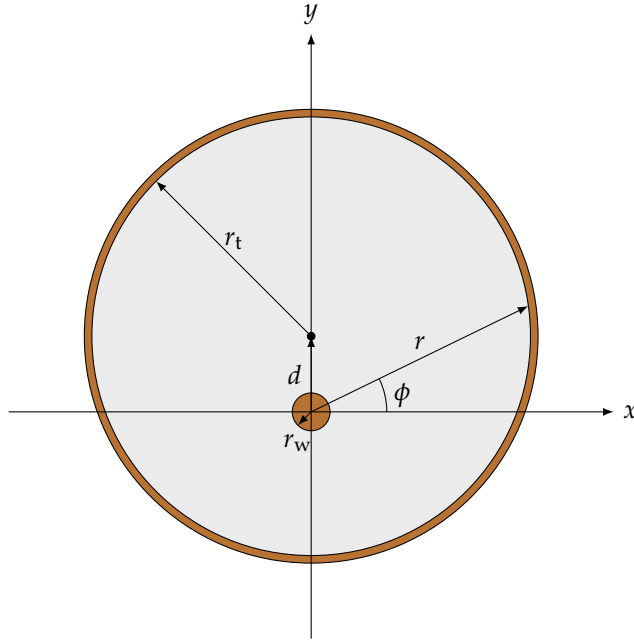
Figure 4.5: Schematic cross section of a straw tube with a radius $r_t$ and an anode wire radius $r_w$. The wire is displaced by a distance $d$ in the negative $y$-direction.

is shown that the boundary conditions (4.35) and (4.36) lead to field perturbations given by

$$E|_y = -\frac{U}{\ln\left(\frac{r_t}{r_w}\right)}\frac{d}{r_t^2},$$  (4.37)

$$E|_x = E|_z = 0.$$  (4.38)

This corresponds to a constant electric field in the negative $y$-direction with a $d/r_t$-fold magnitude compared to the undisplaced electric field $E(r_t)$ from equation (4.16). For the electrostatic force on the wire it can be shown that

$$\overline{E(r_w)|_y} = -\frac{U}{\ln\left(\frac{r_t}{r_w}\right)}\frac{d}{r_t^2}.$$  (4.39)

Thus, the average extra field on the wire surface is equal to the field perturbation from equations (4.37) and (4.38) [RRB08].

Another type of wire displacement is gravitational sag caused by the weight of the wire. Although the wires in most straw tubes are tensioned with a pulling force $F_p$ close to their maximum pulling force $F_{p,crit}$ they still experience a considerable gravitational sag, especially in long straw tubes. Let $\rho_w$ be the density of the wire, $\sigma_w$ its cross section, $L_w$ its length and $g = 9.81\,\mathrm{m\,s^{-2}}$ the gravitational acceleration. Then, the weight of the wire per length element $dx$ is given by $\rho_w g \sigma_w\,dx$ and the point of maximum gravitational sag, the sagitta, is given by

*As before, see [RRB08] for a detailed derivation.*

$$s = \frac{\rho_w g \sigma_w L_w^2}{8T} = \frac{CL_w^2}{8},$$  (4.40)

where $T$ is the force with which the wire is tensioned and $C = \rho_w g \sigma_w / T$. The electrostatic force changes this sagitta, resulting in

$$s' = \frac{C}{k^2} \left( \frac{1}{\cos \frac{kL_w}{2}} - 1 \right). \tag{4.41}$$

Here, $k = {}^{2\pi\epsilon_0 E^2(r_t)}/_T$. By dividing equations (4.41) and (4.40) it emerges that the electrostatic force increases the sagitta by a factor $\alpha$ given by

$$\alpha = \frac{s'}{s} = \frac{2}{q} \left( \frac{1}{\cos q} - 1 \right), \tag{4.42}$$

where $q = {}^{kL_w}/_2$.

### 4.2.3 Diffusion

Assume that an ionisation event produces several charges within a straw tube. According to the kinetic gas theory in thermodynamics, the average thermal energy can then be written as

*This equation can also be applied to 1 mol, in which case $E = \frac{3}{2}RT$ with the gas constant R.*

$$E_{th} = \frac{3}{2} k_B T \approx 0.04 \, \text{eV}, \tag{4.43}$$

where $k_B = 1.381 \times 10^{-23} \, \text{J K}^{-1}$ [Kuc14] is the Boltzmann constant and for the temperature $T$ normal room conditions were assumed. Maxwell's probability distribution of the energies is given by [Sau77]:

$$F(E) = C\sqrt{E} \exp\left(-\frac{E}{k_B T}\right). \tag{4.44}$$

When these charges drift inside the straw tube they are scattered on the gas molecules, leading, in the simplest case, to isotropic diffusion. If the drift starts at a time $t = 0$, then after a time $t$ the charges follow a Gaussian density distribution [RRB08]:

$$n = \frac{1}{(4\pi Dt)^{3/2}} \exp\left(-\frac{r^2}{4Dt}\right). \tag{4.45}$$

*In literature, this relation is sometimes called 'Nernst–Townsend formula', or 'Einstein formula'.*

Here, $D$ is the diffusion coefficient for which

$$\frac{D}{\mu} = \frac{k_B T}{e}, \tag{4.46}$$

where $\mu$ is the mobility and $e$ the elementary electric charge. After a point-like charge cloud has travelled a distance $L$ in a time $t$, the diffusion width $\sigma_x$ is given by

$$\sigma_x = \sqrt{2Dt} = \sqrt{\frac{2DL}{\mu E}} = \sqrt{\frac{4E_{th}L}{3eE}}. \tag{4.47}$$

Note that increased diffusion also broadens the distribution of arrival times, negatively affecting spatial resolution. Equation (4.47) illustrates that small thermal energies and large drift fields, or, in general, small diffusion coefficients are beneficial for detector performance.

### 4.2.4 *Drift gas composition*

The choice and composition of the gas within straw tubes can severly affect their performance. This section closely follows [KW16], where it is described that in general the following aspects have to be considered when choosing a gas composition:

- High ionisation density
- Low charge loss
- Low voltage at the required gain
- Stable operation
- Low Diffusion
- Adequate drift velocity
- Achieve low effect of space charge
- Radiation resistance
- Cost and security
- Proportional relationship between signal and ionisation

*Ionisation and charge loss*

The ionisation density, which should preferrably be as large as possible, is the number of primary ionisations per length and thus describes the total number of created electron-ion-pairs per unit length. Concerning different gases, this ionisation density is, among others, high for Argon, $CO_2$ and hydrocarbons except methane. However, the best ionisation density is achieved by the noble gases Krypton and Xenon although these gases are the most cost-intensive. Electronegative gases such as Oxygen are unfit for use as a main component in a drift gas due to their high charge loss. Charge loss is caused by electrons recombining with positive ions or through accretion to electronegative components in the gas.

*Voltage and gain*

The voltage required to achieve the required gain should be as low as possible to prevent leakage currents and flashovers. Here, the noble gases Helium, Neon, Argon, Krypton and Xenon are prime candidates. However, Helium and Neon have a comparatively small ionisation density. Nevertheless, they are partly used in detectors for low impulse particles due to their radiation length. Krypton and Xenon have the disadvantage of having a short radiation length, making them generally unsuitable for use in track detectors. Another disadvantage is, as before mentioned, their cost. This makes Argon an often used gas in straw tubes, albeit only in mixtures with other supplementary gases due to pure Argon's immense diffusion and instable behaviour during gas gain.

*Note that the noble gas Radon is unsuitable due to its inherent radioactivity.*

*Photo-absorption and quenching gases*

During gas gain atoms and molecules are excited or ionised. Consider Argon as main gas in a straw tube. An excited Argon atom is de-excited via the emission of a photon with an energy of $11.6\,\text{eV}$. However, the ionisation potential of the cathode material – often copper – is only $7.7\,\text{eV}$. Hence, a photon hitting the cathode can create a photo-electron due to the photoeffect, which may, in turn, create a new avalanche. This effect can lead to delayed avalanches or, in extreme cases, to permanent discharge. Since pure noble gases have only few excitation levels, they are unable to absorb photons and are thus instable during gas gain. This problem can be solved by adding *quenching gases* to the gas mixture. These contain molecules with a large number of rotational and vibrational states which can be excited via photons but are mainly de-excited in non-radiative processes. Examples for quenching gases are the hydrocarbons $CH_4$-Methane and $C_4H_{10}$-Isobutane, as well as $CO_2$, although the quenching abilities of $CO_2$ are significantly worse. Also, $CO_2$ is instable at very high gas gains. The disadvantages of $CO_2$ are often remedied by adding a third gas to the mix. The issue with using hydrocarbons as quenching gases is that they can create deposits of polymerisations on cathode and anode, limiting the lifetime of the detector. While alcohols such as $C_3H_8O$-Propanol or $C_3H_8O_2$-Dimethoxymethane do not tend to cause polymerisational deposits, they have a low saturation vapour pressure at room temperature, meaning only low concentrations are achievable. It has to be noted however, that already small concentrations of alcohols in the promille region can positively affect the lifetime of the detector. Another way to reduce the impact of polymerisation is to increase their conductivity. This can be achieved by adding a small amount of water to the gas by guiding the gas through a water bottle, a so called *bubbler*.

$C_3H_8O_2$ *is also more commonly referred to as Methylal or Formaldehyde dimethyl ether.*

*Diffusion and drift velocity*

Another effect of the quenching gases is that they reduce the thermal heating of anode and cathode caused by the electric field. This is because they absorb energy in inelastic collisions and redistribute it non-radiatively to other molecules in the gas. A large cross-section with a high inelasticity leads to a small characteristic energy and low diffusion. The drift velocity can be adjusted with the relative amount of the quenching gas. In general, it increases with larger field strengths until a maximum is reached after which the drift time decreases again. This saturation can be used to make the drift velocity robust against fluctuations of the field strength, pressure and temperature. The mixing ratio is thus an important optimisation parameter.

*Electronegative additives*

Electronegative gases such as $CBrF_3$-Bromotrifluoromethane, $C_2H_5Br$-Bromoethane or $SF_4$-Sulfur tetrafluoride may be added to the gas mixture at high gas gains in order to prevent possible secondary discharges. These molecules turn into ions by accumulating electrons but do not contribute to the gain due to their low mobility. Note that such additives cannot be used in detectors with larger drift radii since they may reduce the efficiency of particle detection.

### 4.2.5 *Drift gas pressure*

Besides the composition of the gas, another factor that influences the performance of a straw tube is the gas pressure. In fact, the gas pressure is one of the first aspects that have to be considered during the design of a straw tube since it largely affects the overall construction. While, in general, most performance characteristics, especially the spatial resolution, improve with increasing gas pressure, it has to be noted that in particularly large detectors (e.g. SHiP's muon magnetic spectrometer) high pressures cannot be achieved due to security reasons. Hence, the gas pressure has to compromise between safe detector operation and spatial resolution. Table 4.1 shows how the gas pressure influences several characteristics of a straw tube. Refer also to section 4.1.3, where the influence of the gas pressure on the gas gain is outlined.

Table 4.1: Influence on a few selected parameters relevant for a straw tube. A change of gas pressure by a factor $\Delta p$ results in the parameter changing by the indicated factor. Taken from [RRB08], a more extensive table can be found ibidem.

| Parameter | Change |
| --- | --- |
| Mean free path between collisions | $1/\Delta p$ |
| Mean free time between collisions | $1/\Delta p$ |
| Diffusion constant | $1/\Delta p$ |
| Electric field | $\Delta p$ |
| Magnetic field | $\Delta p$ |
| Mean distance between clusters | $1/\Delta p$ |
| Total ionisation | $\Delta p$ |
| Gain | $\Delta p$ |

### 4.2.6 *Ageing effects*

After a certain time a straw tube based detector will start to malfunction. Typical indications are an increase in dark current due to the Malter effect [Mal36] accompanied by a reduction in gain and resolution. This is caused by ageing effects which are mostly caused

*The Malter effect is also referred to as 'thin-field emission effect'.*

by chemical changes in the used materials. Mainly, the anode wire accumulates contaminants such as deposits of metals or oxidation since it accumulates charge during its operation. Note that adding Oxygen or $H_2O$ to the drift gas mixture may further encourage the build-up of contaminants and reduce the lifetime of the detector. A study [Ake+03] examined the ageing of the sense wires of the transition radiation tracker [CA+08a] of the ATLAS experiment [CA+08b]. They investigated the anode wire using a scanning electron microscope and energy dispersive X-ray methods. Figure 4.6 shows several pictures of amourphous deposits, crystalline deposits and other damages to an anode wire. Note that even though such studies exist, there is still no fundamental understanding of ageing straw tubes.

*ATLAS is an acronym for 'A Toroidal Lhc Apparatus'.*
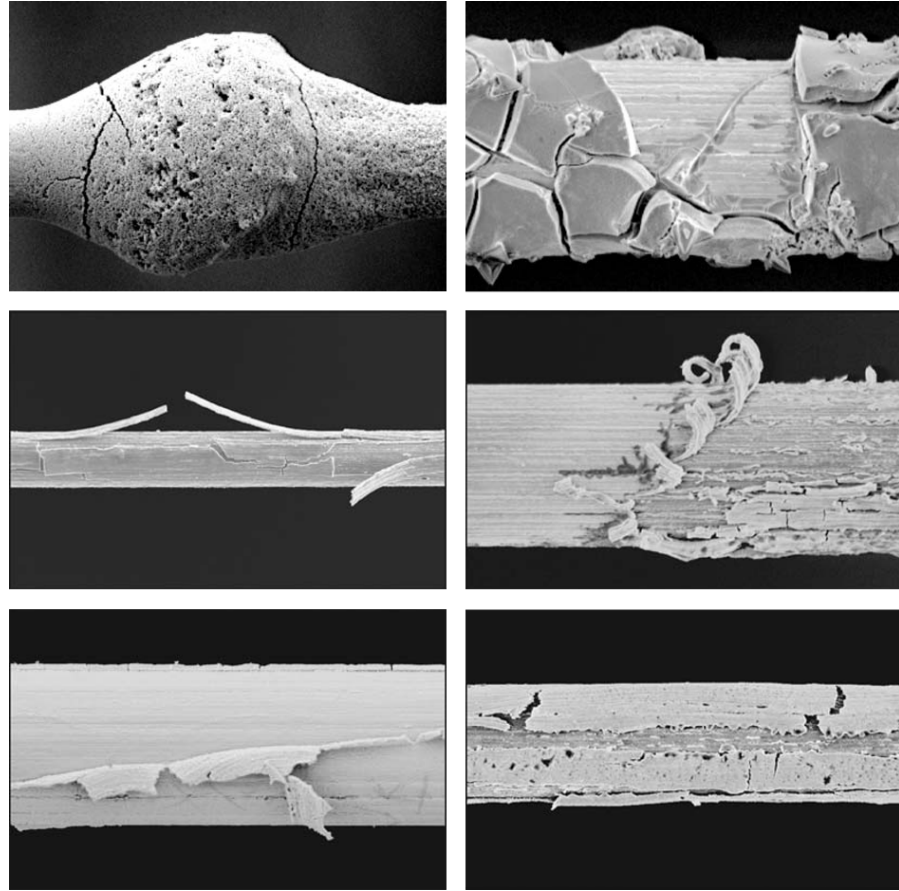


Figure 4.6: Various ageing effects observed on anode wires with a $0.5\,\mathrm{C\,cm^{-1}}$ accumulated charge using a $XeCF_4CO_2$ gas mixture at a mixing ratio of $70\,\%, 20\,\%, 10\,\%$. Top left image: Amorphous tungsten-oxide (WO) deposit observed on an anode wire after the addition of $1.2\,\%$ water and $1.5\,\%$ oxygen to the gas mixture. Top right image: Similar to the top left image, except this time crystalline tungsten-oxide deposits can be observed. Bottom four images: Damages to gold plating on an anode wire after $2\,\mathrm{C\,cm^{-1}}$ to $6\,\mathrm{C\,cm^{-1}}$ accumulated charge. Images taken from [Ake+03].

# Part II

## SST PROTOTYPING

Within this thesis crucial prototyping for the design of the Spectrometer Straw Tracker is performed. This prototyping is covered in this part. Here, chapter 5 covers the development of a simple functional model consisting of a single straw tube. After that the more advanced quad-straw prototype with which the proposed mechanical design for the SST is tested is explained in chapter 6. In chapter 7, surface analyses of the straws' conductive coating after being subjected to mechanical stress are outlined. Finally, chapter 8 presents the current status of the large-scale integration into modules will be mounted in large steel frames.

# SINGLE-STRAW FUNCTIONAL MODEL

'Omnium enim rerum principia parva sunt...'

*'All things are small in their first beginnings...'*

— M. T. Cicero, *De finibus bonorum et malorum*, Book V, Verse XXI, as translated by H. Rackham. Loeb Classical Library 40. Cambridge, MA: Harvard University Press

The research and development performed within this thesis began with the construction of a functional model for the SST. A functional model is a setup which uses – at least partially – non standardised parts, but, nevertheless, demonstrates the basic functionality of the final setup. The stage of development after the functional model is the design of a prototype and described in chapter 6.

## 5.1 DESIGN

The single-tube functional model consists of eleven individual parts, amounting to 21 parts in total. A cross-section of the parts is shown in figure 5.1. On both ends of the straw ④ Polyoxymethylene (POM)
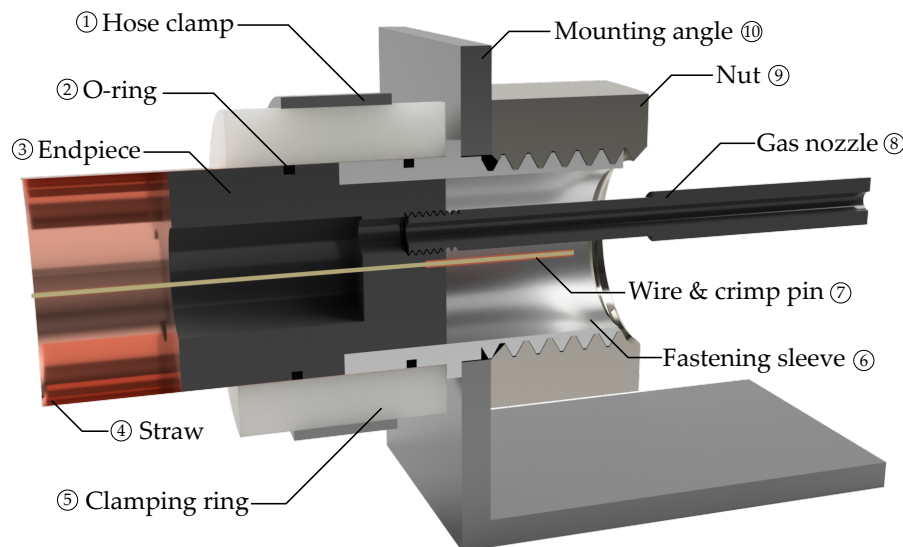


Figure 5.1: A cut through the mounting hardware of the single-straw functional model. A clamping ring distributes the force of a hose clamp to press a straw tube onto a straw endpiece and a fastening sleeve. Using a nut the fastening sleeve is attached to a mounting angle. A gas nozzle is used to supply the straw with gas. The anode wire is held in using a crimp pin.

end-pieces ③ with an O-ring ② are each inserted into the straw tube. The POM end-pieces are 25 mm long and have two sections with outer

diameters of 20 mm and 16 mm respectively. Each end-piece is hollow with an inner diameter of 10 mm, an M4 threaded section, and a small section with an inner diameter of 0.45 mm. The anode wire passes through this small bore and is securely fastened using a crimp-pin ⑦. The 16 mm outer sections of the end-pieces are slid into aluminium fastening sleeves ⑥. These fastening sleeves are 28 mm long with an outer diameter of 20 mm and an inner diameter of 16 mm. The outer sections of the fastening sleeves are partly threaded with a regular M20 thread. Similar to the end-pieces the fastening sleeves have a groove for an O-ring. A 1.5 mm wide and 1.5 mm high protruding retention ring is located on the outside of the fastening sleeves. A 14 mm long POM gas nozzle ⑧ with outer diameters of 4 mm and 5 mm and an inner diameter of 2 mm passes through the aluminium fastening sleeves and is screwed into the end-pieces. The different outer diameters ensure adequate clearance between the nozzle and the crimp pin. Using this gas nozzle the counting gas is supplied to the straw tube. The straw tube is pushed onto the end-pieces and the fastening sleeves by a hose-clamp ①. Using buffering POM clamping rings ⑤ distributing the force exerted by the hose clamps the straw is held on the end-pieces and fastening sleeves. Via M20 nuts ⑨ the fastening sleeves and thus the straws are fixed to mounting angles. Using these mounting angles the complete setup can be securely mounted to a frame.

## 5.2   commissioning

The commissioning of the single-straw functional model was done in three steps. First, the parts were assembled and the single-straw prototype was mounted on a mounting frame. Secondly the prototype was connected to a very simple, yet effective gas system. Finally, the electronics required for the read-out of the signals were commissioned and calibrated.

### 5.2.1   *Assembly*

First, a tungsten anode wire with a diameter of 45 μm was pulled through the straw using a magnetic nut and a magnet. In hindsight, this process caused significant damage to the straw tube – see also section 6.4.1 and chapter 7. Afterwards, the parts of the single-straw functional model were assembled as planned and outlined in section 5.2. The gas nozzle was only installed on one side. The mounting angles were then installed on a mounting frame consisting of various 60 mm × 60 mm aluminium profiles laid across two adjustable tables. Afterwards, the straw tube with its mounting hardware was attached to the mounting angles on both sides using the nuts. The straw was then tensioned using a weight of 5 kg to minimise sagging. Similarly,

the wire was tensioned using a weight of 180 g, the same weight that was used for OPERA's drift-tube detector. In figure C.1 the assembled single-straw functional model is shown.

### 5.2.2  *Gas System*

For the single-straw functional model a very simple gas system was implemented. The schematic of the gas system is shown in figure 5.3. The gas is stored in a gas bottle which can be opened using a main valve. A pressure reducer reduces the gas pressure to a set amount. Using two manometres before and after the pressure reducer the corresponding gas pressures are indicated. By means of a Swagelok quick connect coupling the pressure reducer is connected to an adjustable flow metre. At the flow metre the gas flow in litres per hour can be set within a range of $1 \mathrm{l h}^{-1}$ to $10 \mathrm{l h}^{-1}$. Using a second Swagelok quick-connect coupling the gas then enters the straw tube on one side. After flowing through the straw tube it is exhausted into the ambient air on the other side of the straw.

### 5.2.3  *Electronics*

A special set of electronics is required to read out a straw tube's signals. This includes a preamplifier, since the voltage signals created by an ionising particle passing through the straw tube are only in the order of micro-volts. The preamplified signal is then read out using a Flash Analogue to Digital Converter.

*The Preamplifier*

The preamplifier chosen for the use in the single-straw functional model is the L3 preamplifier. It is a hybrid linear amplifier originally designed for the muon detector in the LEP L3 experiment. Although this particular amplifier does have some known issues, such as subpar crosstalk properties, it was used successfully in various other experiments such as OPERA. Also, the L3 is used for the drift-tube setups used for practical courses at the University of Hamburg. In fact, the preamplifier – as well as the high voltage circuitry – used for the single-straw functional model were taken from one of the drift-tube setups. The preamplifier stage is housed in an aluminium box for security and shielding purposes. The box has four connectors. Via a single BNC connector the high voltage is supplied to the anode wire. Three LEMO connectors are used for the preamplifier's low voltage supply and for the positive and negative output signals. The actual preamplifier and the electric circuits are located on a veroboard inside the aluminium box. In figure 5.4 the schematics of the electrical circuit are shown.
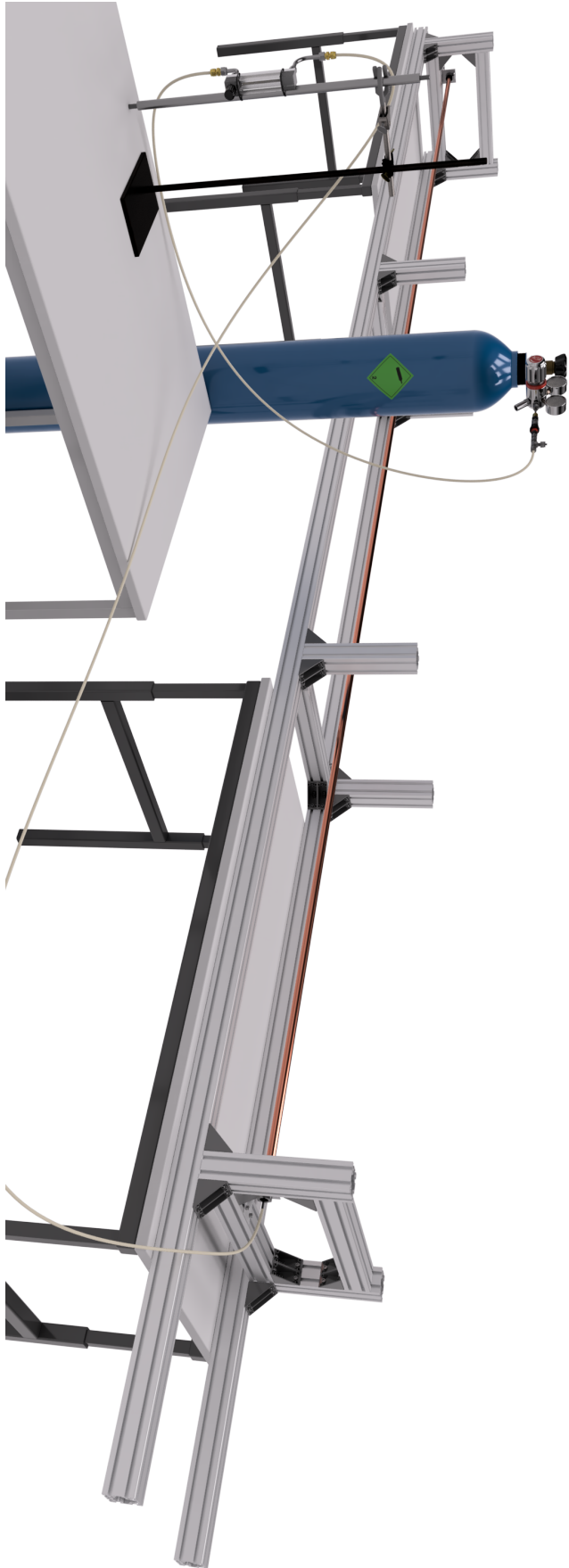
Figure 5.2: The assembled single-straw functional model mounted on the mounting frame consisting of aluminium profiles laid across two height-adjustable tables. In the foreground the gas system consisting of a gas bottle and a flow-metre is depicted.
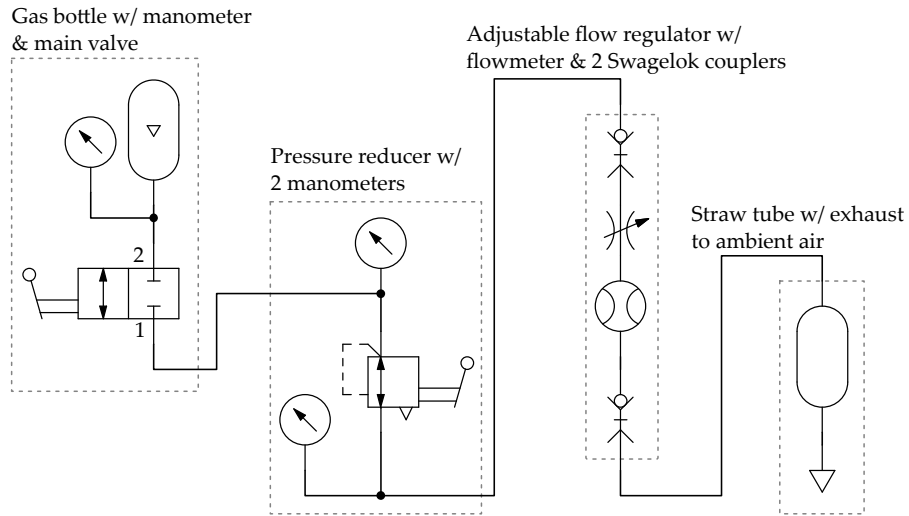
Figure 5.3: Schematic depiction of the gas system for the single-straw functional model using hydraulic/pneumatic symbols. Gas stored in a gas bottle flows through a pressure reducer and flow regulator into the straw and is afterwards exhausted into the ambient air.
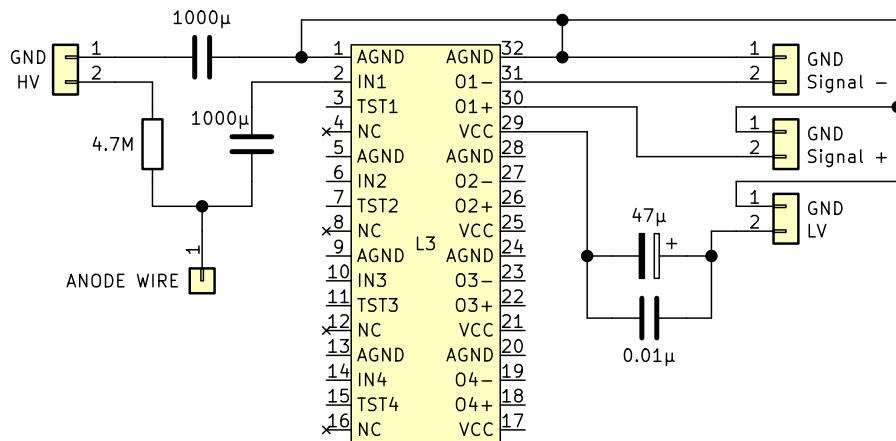


Figure 5.4: The electrical circuit used to supply the anode wire with high voltage and preamplify the signals. As an amplifier the L3 preamplifier was chosen.

*The Flash Analogue to Digital Converter (FADC)*

To convert the amplified analogue voltages to a digital signal a Flash Analogue to Digital Converter – FADC in short – is used. In this case, a CAEN Mod. V1720 FADC in combination with a CAEN Mod. V1718 USB VMEbus bridge handling the USB data transfer to a laboratory computer were chosen. The V1720 features a sampling rate of 250 MHz which results in a 4 ns time resolution. The FADC returns the input signal $V_{\text{input}}$ in arbitrary FADC units $V_{\text{FADC}} \in [0, 4096]$. A conversion from $V_{\text{FADC}}$ to the original input voltage can be performed via the following equation:

$$V_{\text{input}} = \aleph V_{\text{FADC}} + \chi. \tag{5.1}$$

Here, $\chi$ is an adjustable offset and $\aleph$ is a device-specific calibration constant.

To measure the calibration constant, and in particular the FADC's linearity, a function generator (Model: SONY Tektronix AFG320) was used to create different sine waves with a frequency of 500 kHz and peak-to-peak amplitudes ranging from 0.1 V to 2 V in 0.1 V steps. The output of the function generator was visualised using a digital oscilloscope (Model: Tektronix DPO7254) and also connected to the FADC. Figure 5.5 shows a screen capture of the digital oscilloscope for a 1 V peak-to-peak amplitude signal. The outputs of the function

*VMEbus stands for 'Versa Module Eurocard-bus' and is a computer bus standard originally developed by Motorola.*
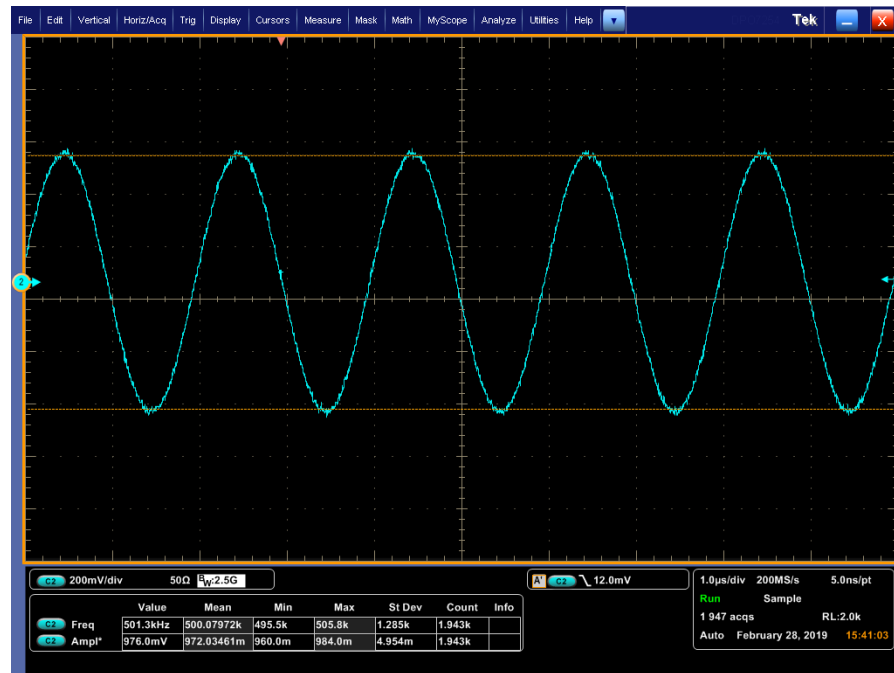


Figure 5.5: A screen capture of the oscilloscope during the FADC calibration. The sine wave with a set peak-to-peak amplitude of 1 V and a frequency of 500 kHz is clearly visible. The oscilloscope's measurement function shows an average amplitude of 972.03 mV and a frequency of 500.08 kHz.

generator were cross-checked with the oscilloscope and were found to be in good agreement with the set values. According to the oscilloscope's measurement function the peak-to-peak amplitude of the signal amounts to $(972.03 \pm 4.95)$ mV in average, differing from the set value of 1000 mV by roughly 2.8 %. The measured average frequency of $(500.09 \pm 1.29)$ kHz differs from the set value by less than 0.2 %. The differences are within the accuracy ranges of the oscilloscope and the function generator.

The signals of the FADC were acquired via CAEN's Wavedump software. A signal for a set voltage of 1 V is shown in figure 5.6. Here, the period amounts to $T = 2000$ ns resulting in a frequency of
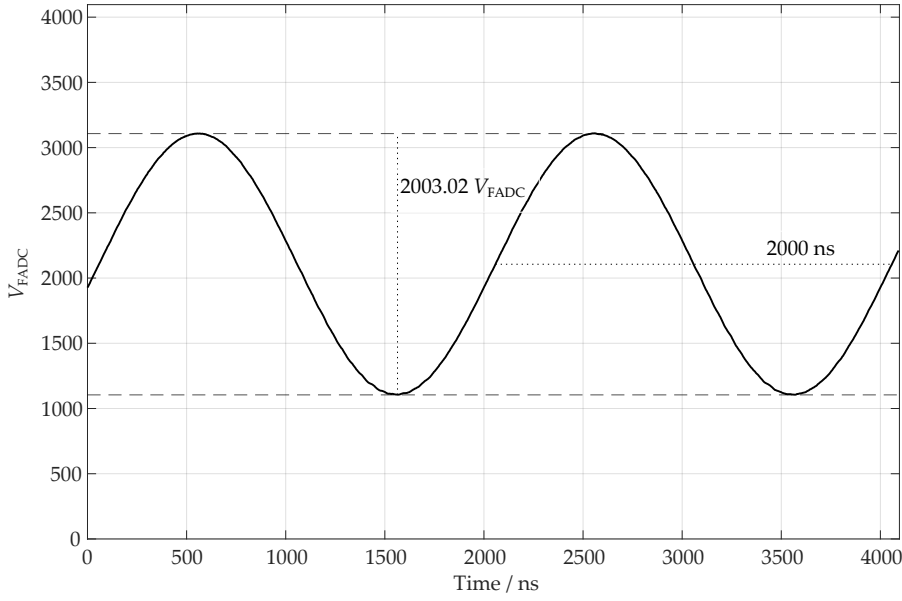


Figure 5.6: A voltage signal acquired by Wavedump during the calibration. The set voltage of 1 V corresponds to 2003.02 $V_{\mathrm{ADC}}$. The period is given by 2000 ns precisely matching the set value.

$f = 1/T = 500$ kHz matching the set frequency exactly. The average peak-to-peak amplitude in FADC units amounts to 2003.02 $V_{\mathrm{FADC}}$. This amplitude was determined for all input voltages. The results are depicted in figure 5.7. The plot clearly shows a linear relationship between the FADC units and the input voltage. A linear fit to the data results in

$$V_{\mathrm{FADC}} = 2005.83 \pm 1.02 \ V_{\mathrm{input}}. \tag{5.2}$$

Hence, the $V_{\mathrm{FADC}} = 4096$ FADC units correspond to $V_{\mathrm{input}} = 2.04$ V, meaning the calibration factor from equation (5.2) is given by

$$\aleph = \frac{2.04 \text{ V}}{4096}. \tag{5.3}$$
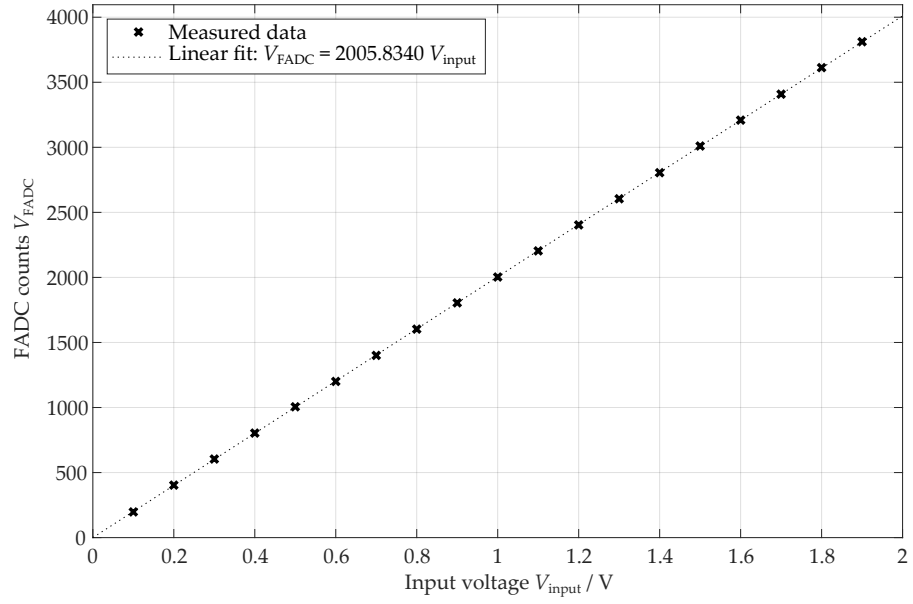
Figure 5.7: The calibration curve of the FADC. A linear fit results in $V_{\mathrm{FADC}} = 2005.83 \pm 1.02\, V_{\mathrm{input}}$, meaning that 4096 FADC counts correspond to a voltage of 2.04 V.

## 5.3   MEASUREMENTS

After the successful assembly of the single-straw prototype and the calibration of the FADC measurements were immediately conducted. These measurements included drift-time spectra as well as the signal attenuation along the straw. Furthermore, noise was also measured.

### 5.3.1   *Drift times*

The first measurements performed with the single-straw functional model were the measurement of drift-times. For this purpose, the signals of cosmic muons were used.

*Electronic setup*

Measuring cosmic muons requires an electronic trigger. This trigger was implemented by using two plastic scintillators with a length of around 300 mm and a width of 37 mm. These were mounted to the frame at a convenient location using a mounting bracket with one scintillator being above the straw tube and the other one below it. Note that the scintillators were deliberately placed away from the straw tube's end in order to rule out edge effects. Right at the straw tube's ends the electric field is no longer given by equation (4.16) but is rather radially asymmetric possibly leading to increased drift times. Both scintillators were equipped with identical models of Photomultiplier Tubes (PMTs). The setup is shown in figure 5.8. Special care was taken
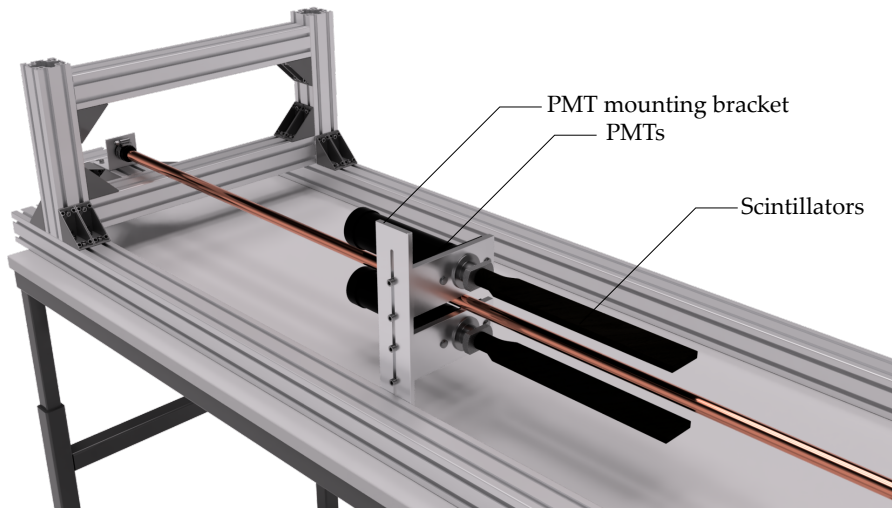
Figure 5.8: Placement of the two photomultiplier tubes during the drift-time measurements. The PMTs are mounted to the mounting frame using a special bracket. Each PMT is equipped with a scintillator. They were deliberately placed away from the straw's end to alleviate edge effects. The readout electronics are not shown.

to minimise the distance between the scintillators to the straw. That way, the probability that a muon which has passed both scintillators will also have passed the straw tube is greatly increased. Due to the short distance between the scintillators and the high velocity of the cosmic muons – approximately the speed of light – the time of flight of the muons is less than one nanosecond. This is below the time resolution of the used readout electronics and thus not of concern.

*Note that wrong triggers can still occur, since the scintillators are wider than the straw tube.*

The photomultiplier tubes were connected to their high voltage power supply (Oltronix HIGHPAC A2K5-20HR), as well as to a discriminator unit (CAEN Mod. N844). Here, special care was taken to use cables of the same length so that no signal delays are induced. The discrimination of the PMT signals is necessary to create logical $-800\,\text{mV}$ NIM signals with an adjustable temporal length. After passing the discriminator both signals were, again using cables with the same length, fed into a CAEN Mod. N405 three-fold coincidence logic unit. This unit was set to the AND mode resulting in NIM output signals showing a coincidence of both photomultiplier tubes. This signal was then used as an external trigger for the FADC. Concerning the signal coming from the straws, the negative output of the L3 amplifier was connected to the signal input port of the FADC. Using this electronic setup the tube's signals are acquired by the FADC if and only if the output of the trigger electronics is a logical 1. For the wire's high voltage supply a CAEN Mod. SY127 power supply was used. In figure 5.9 a schematic drawing of the readout electronics is shown.

*NIM stands for Nuclear Instrumentation Module. It was the first standard that defines mechanical and electrical specifications for electronic apparatuses and modules used in nuclear and high energy physics. See [Le094].*
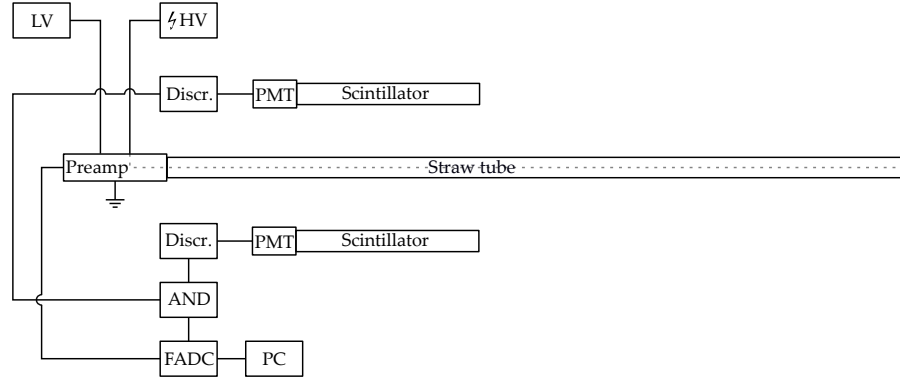
Figure 5.9: Schematic drawing of the readout electronics used during the drift-time measurement. The signals coming from two PMTs are discriminated and fed into an AND-gate thus acting as a trigger. The signal from the straw tube is taken by an FADC when the trigger is a logical 1. The gas system and the HV supply for the PMTs are not shown.

*Pulse shape*

A dataset of 16 680 signals coming from the single-straw functional model was taken using a gas mixture of Argon and $CO_2$ at an 80 % to 20 % mixing ratio and a high voltage of 2150 V. An exemplary straw tube pulse can be seen in figure 5.10. This pulse – see the continuous black line – shows the typical properties of a straw tube signal. First, the signal fluctuates around the baseline level $V_{base}$ which is shown as a dashed horizontal line. The baseline level is given by the average of the first entries of all events of the dataset. At around 750 ns a sharp peak with an absolute height of 0.8 V can be seen. After that, the voltage signal has several more peaks but climbs back to above the baseline level which it subsequently begins to approach. The fact that the first peak is the highest can easily be explained: From a geometrical consideration it follows that the number of ionisation clusters per time unit which reach the anode wire is larger for smaller drift times resulting in the first peak being statistically the highest one. The effect that the signal exceeds the baseline after the main pulse is physically caused by the conservation of charge.

*The trigger is located exactly at 20 % of the FADC's measurement time span.*

Using this pulse the drift time can easily be determined. Firstly, the trigger, whose position is at roughly 819 ns is marked by a vertical dashed line. Secondly, a threshold, shown as a dotted horizontal line, was determined. It is given by $V_{thr} = V_{base} - 5\sigma_{base}$, where $\sigma_{base}$ is the standard deviation of the baseline $V_{base}$. This baseline is indicated by a horizontal dashed line and given as the average of the zeroth bin of all signals. The drift time is then given by the time interval from the trigger position to the first time, where the pulse falls below the threshold. Note that the fact that signals are not distinguished from noise except by using the threshold is a possible source for errors.
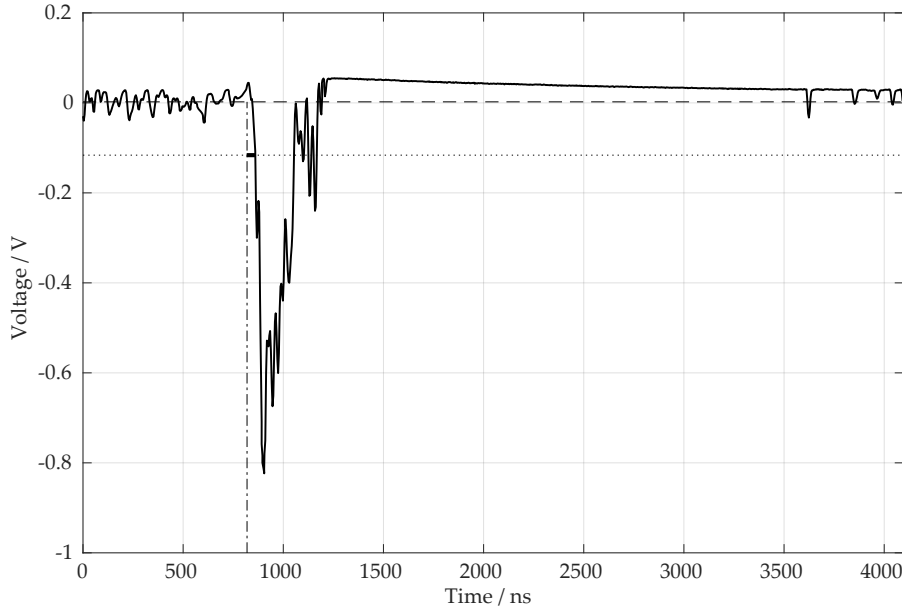
Figure 5.10: A typical pulse coming from a cosmic muon (solid black line). The horizontal dashed line is the baseline. The drift-time is given by the difference between the trigger position, shown as a vertical dashed-dotted line and the first time the signal exceeds the threshold (horizontal dotted line).

*Drift-time spectra*

The drift-times of all events were calculated, resulting in the drift-time spectrum shown in figure 5.11. This spectrum shows the expected form – at least for this specific gas mixture and for the used high voltage – with a sharp peak for low drift-times that is followed by a decline which terminates in a knee. The knee is a result of the finite size of the straw tube. In total, the drift-time spectrum has a length of 700 ns to 800 ns. At the OPERA experiment 8 m long tubes were used with a radius of 18.15 mm resulting in roughly 1350 ns long drift-time spectra [Zim+05]. The functional model's straw tube has a radius of 10 mm, which is about 54 % less than the radius of OPERA's tubes. To get a very rough approximation for the expected length of the straw's drift-time spectrum it then suffices to take 54 % of 1350 ns, resulting in approximately 730 ns. Thus, the length of the measured drift-time spectrum is within the expected range. Note that this is only a rough estimation as the electric field at the radius of the straw is in reality not equal to the electric field at the drift tube's radius as the potential at the wall is always zero; $E(r = r_{\text{straw}}) \neq E(r = r_{\text{DT}})$.

However, many of the drift-time spectra showed an unexpected behaviour. An example can be seen in figure 5.12. While this drift-time spectrum still has a clear peak at low drift-times, it has an unexpectedly long tail of more than 3000 ns. This is an effect caused by high noise levels. The noise is further investigated in section 5.3.2.
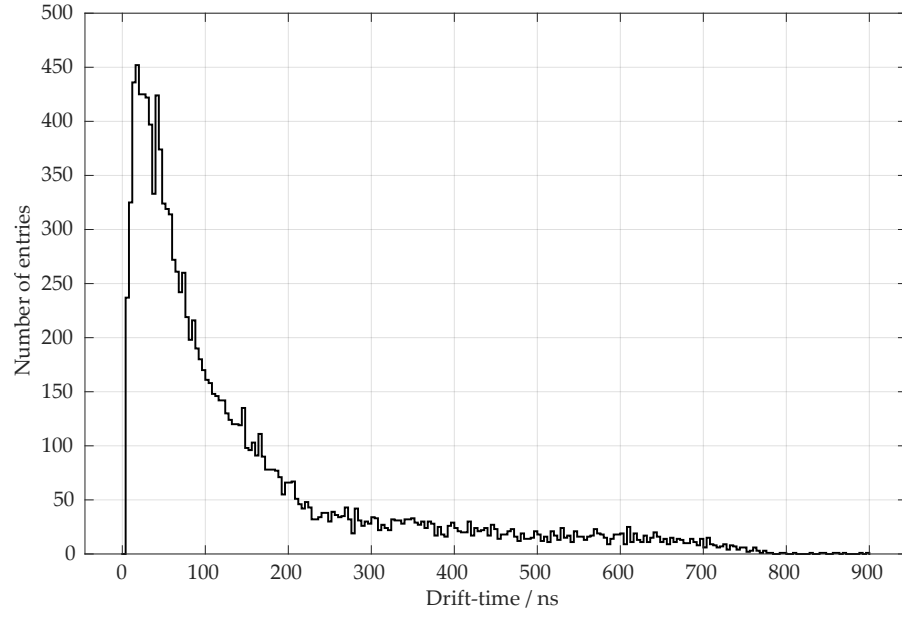
Figure 5.11: Drift-time spectrum for cosmic muons measured with the single-straw functional model at a high voltage of 2150 V. For the used parameters the spectrum shows the expected form with a length between 700 ns to 800 ns.
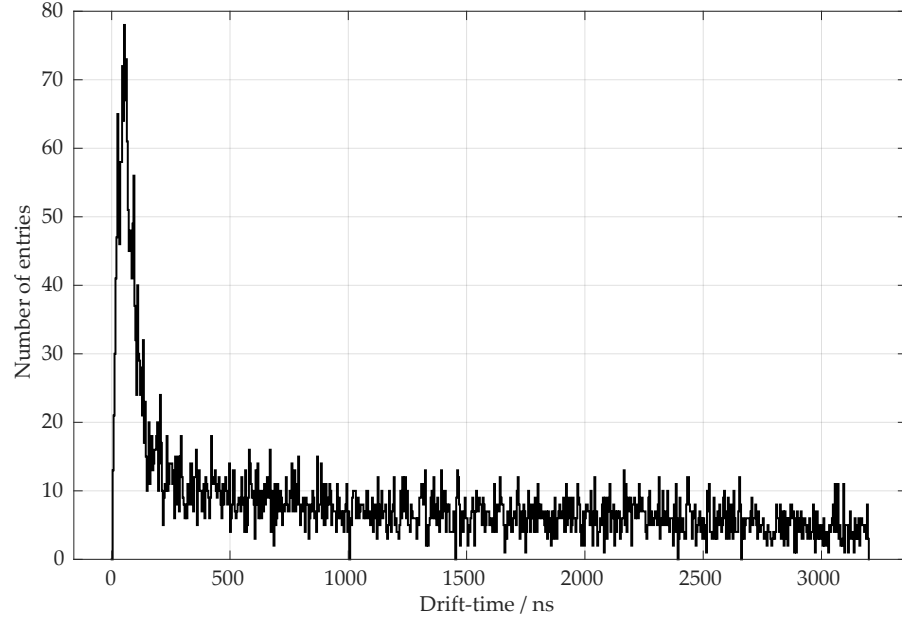


Figure 5.12: Noisy drift-time spectrum for cosmic muons measured with the single-straw functional model at a high voltage of 2150 V. The spectrum shows not the expected form with a length of more than 3000 ns. This behaviour is caused by noise.

*Outline of error sources*

The measurement of the drift-time spectra is subject to multiple sources of error. For example, the decision of whether or not a signal is actually counted as a signal depends on the setting of the discriminator's threshold which can be set arbitrarily. Here, a well chosen threshold can increase the efficiency of the straw tube. Another possible improvement could be the use of a full pulse form analysis, where for example the time over threshold of a pulse can be used to identify true signals more accurately. Furthermore, the used FADC only has a sampling rate of 250 MHz resulting in an improvable time resolution of 4 ns. A better time resolution would also improve the accuracy of future pulse form analyses. Other sources of errors are physical influences on the tube such as the gas mixture, the gas pressure or the gas flow.

### 5.3.2   *Noise*

During the measurement of the drift-times high noise levels were occasionally observed. The analysis of this noise is outlined in this section.

*Effect of voltage settings*

An early suspect for creating noise signals were the high voltage (HV) power supply of the anode wire and the low voltage (LV) power supply of the L3 preamplifier. To test this hypothesis the FADC was operated in the self-triggering mode. Here, all input signals exceeding a certain threshold are saved. The photomultiplier tubes required for measuring the drift-time spectra were not used. In total, 5000 pulses were each saved at different high voltages ranging from 0 V to 2300 V. This process was repeated for low voltages of 3 V, 4 V and 5 V. Additionally, at each low voltage setting a measurement was taken with the high voltage power supply on the 'disabled' setting and with it completely turned off. For each high voltage and each low voltage setting the standard deviation of the first bin of each signal was calculated. The measurement results are depicted in figure 5.13.

It can clearly be seen that with an increasing low voltage the noise levels increase linearly. This is expected, as an increased low voltage leads to a higher amplification and thus higher noise levels. At each low voltage setting the noise levels stay relatively constant in the range from 0 V to 2100 V for the HV. The average noise levels in this range are given by

$$\sigma_{3V} = (28.03 \pm 0.36)\,\text{mV}, \tag{5.4}$$

$$\sigma_{4V} = (29.91 \pm 0.53)\,\text{mV}, \tag{5.5}$$

$$\sigma_{5V} = (31.80 \pm 0.41)\,\text{mV}. \tag{5.6}$$
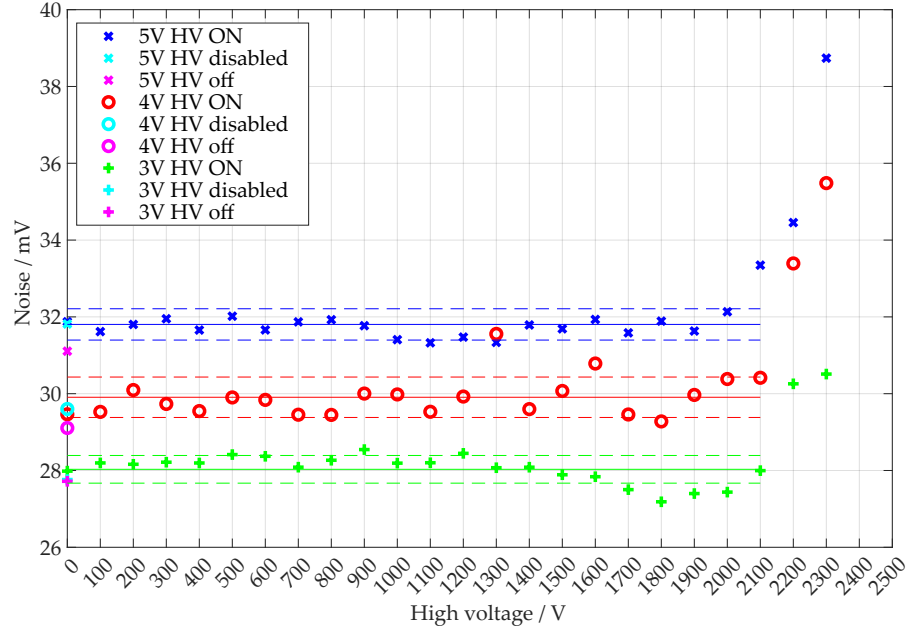
Figure 5.13: Effect of the low and high voltage on the noise. An increase in the low voltage results in more noise due to higher amplification. For the high voltage no increase of noise can be seen between 0 V to 2100 V. Above 2100 V the noise increases up to 15 % with respect to the average noise levels below 2100 V. These are shown as continuous horizontal lines, the dashed horizontal lines are the corresponding standard deviation.

In the range of 2100 V to 2300 V the noise levels increase significantly by 10 % to 15 % with respect to the corresponding average value. The noise with the high voltage power supply completely turned off is for all LV settings lower than the noise with the HV supply disabled and with the HV supply set to 0 V. Except for the LV = 3 V setting the noise levels with the HV completely disabled are the lowest values overall – although only by a very small margin and still within the $1\sigma$ or $2\sigma$ error intervals. In total, a significant increase of the noise can be seen with increasing low voltage and with high voltages larger than 2100 V – although this is not critical with regard to signals with pulse heights of around 800 mV as the one shown in figure 5.10.

*Noise due to improper grounding*

During the measurement process with the single-straw prototype much more prominent noise than the one observed for high voltages larger than 2100 V was observed. This noise manifested itself in a sudden increase of the event rate by an order of $\mathcal{O}(10^6)$ Hz. This noise occurred and remained after touching the mounting frame by hand. After turning the low voltage power supply of the L3 preamplifier off and on again the event rate reduced to a negligible amount – at least some of the times and only until the frame was touched again.

Sometimes, the observed noise all had the same form, consisting of several peaks with a periodic envelope. This can be seen in figure 5.14 which shows the average of 3000 noise recordings. Sometimes,
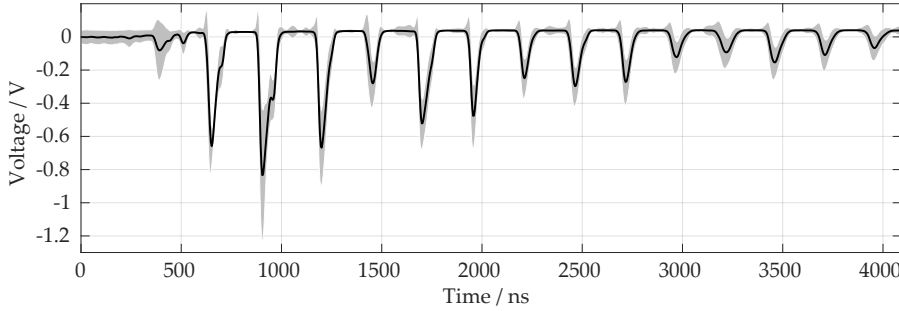


Figure 5.14: Average of noise recordings observed after touching the mounting frame. The standard deviation is shown in light grey. These signals occurred at a frequency of $\mathcal{O}(10^6 \text{ Hz})$. An envelope can be seen clearly. These signals were likely caused by a grounding problem such as a ground loop.

touching the mounting frame shifted the peaks to the left. Other times touching the mounting frame resulted in the signals no longer looking similar but rather resulted in seemingly random looking signals. It is highly likely that the observed noise and its behaviour were caused by a grounding issue such as a ground loop.

To fix this problem the grounding of the single-straw functional model and the L3 preamplifier in its box were reconsidered. Initially the single-straw functional model and the mounting frame were grounded by connecting them to the housing of the L3 preamplifier. This housing was grounded via the connected high- and low-voltage power supplies – which were on the same ground level – as well as the FADC. To minimise the noise the connection between the amplifier housing and the mounting frame was improved, in particular by scraping off the anodised layer of the extruded aluminium profiles at the points where the amplifier housing was attached to the frame. Most importantly however, a direct connection between the mounting angle of the single-straw prototype and a ground pin on the L3 preamplifier (pin 1, see figure 5.4) was established. This was done by soldering one end of a wire directly to the grounding pin on the L3 and jamming the other end between the mounting angle and the nut – confer figure 5.1. After that the observed signal rate was around 100 Hz. A 100 Hz signal rate is acceptable especially for measurements with the Fe-55 source where signal rates larger than 4000 Hz are expected. Further modifications to the grounding yielded no improvements.

*Long-term noise*

In order to test the baseline noise of the preliminary prototype a long-term measurement of the event rate over ten days from April 23, 2019

13:26:35 UTC to May 2, 2019 13:17:18 UTC, was performed. During the measurement, neither gas nor high voltage were supplied to the setup. The FADC's internal trigger threshold was set to 1000 $V_{ADC}$, corresponding to roughly 0.5 V absolute and 0.5 V with respect to the baseline at 2048 $V_{ADC}$. Note that this is a very high threshold – see figure 5.10 where a pulse has a height of 0.8 V.

The result is shown in figure 5.15, which, for reasons of clarity is split in two parts. It can be observed that the measurement consists of
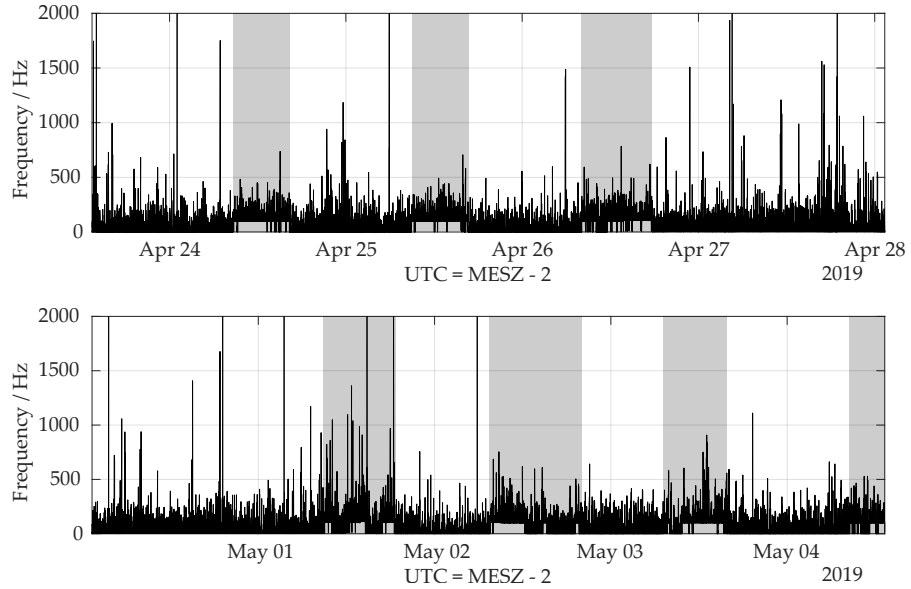


Figure 5.15: Noise signal frequency measured over several days spanned over two plots for reasons of readability. For the same reason both $y$ axes are capped at 2000 Hz. The measurement shows clear zones where the base noise is increased by roughly 100 Hz. These zones correspond with local working hours, indicating noise coming from electromagnetic pickup likely caused by some device operated only during daytime.

different regions with varying baseline levels. These baseline levels can be seen well in figure 5.16 showing the frequencies' occurrence in a histogram.

Here, two distinct peaks at 0 Hz and 100 Hz are visible, with two smaller peaks at around 10 Hz and 110 Hz representing the different baseline levels of the signal shown in figure 5.15. The time spans in which the observed signal rate is clearly increased, in the following referred to as regions of interest – ROIs in short, are shaded grey in figure 5.15. The accurate values are given in table 5.1.

In these regions of interest the baseline of the signal is in the range of roughly 100 Hz to 115 Hz. These regions occur on a per-day basis, with the 27th and 28th of April 2019 – Saturday and Sunday – being an exception. This, together with the nature of their times of occurrence strongly indicates a correlation with local working hours – although
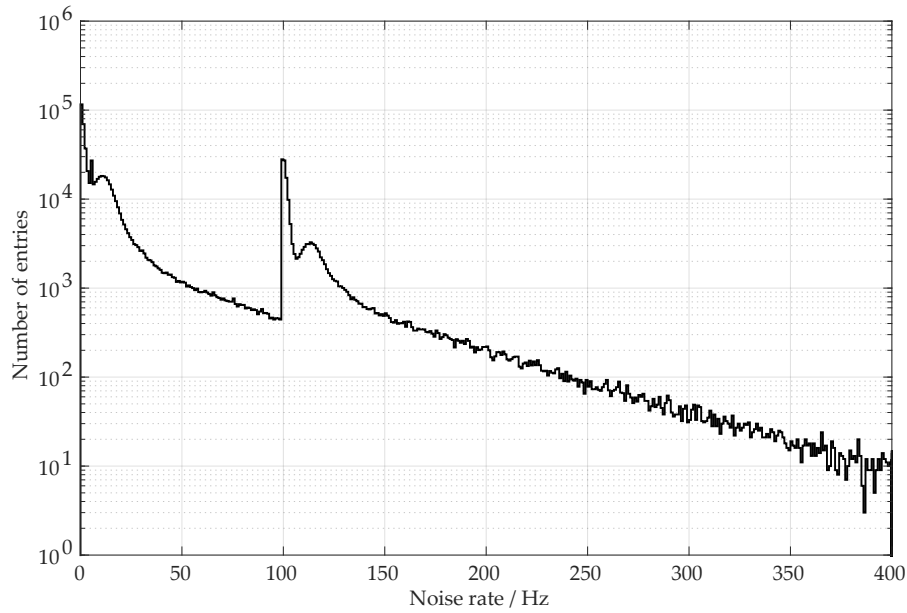
Figure 5.16: Logarithmic histogram of the noise frequencies from figure 5.15. Two peaks at $0\,\mathrm{Hz}$ and $100\,\mathrm{Hz}$ can be seen with smaller subsequent peaks at $10\,\mathrm{Hz}$ and $110\,\mathrm{Hz}$. The increased noise levels could be observed during working hours.

Table 5.1: Regions of interest with increased noise levels broken down by day, date and time. Clearly, increased noise is visible only during working hours. On weekend, no increased noise levels could be observed, although on Monday, May 1st – a local break holiday – increased noise was indeed observed.

| Day | Date | Time |
|-----|------|------|
| Wednesday | Apr. 24 | $08:40 - 16:20$ |
| Thursday | Apr. 25 | $08:50 - 16:40$ |
| Friday | Apr. 26 | $08:00 - 17:40$ |
| Saturday | Apr. 27 | — none — |
| Sunday | Apr. 28 | — none — |
| Monday* | May 01 | $09:00 - 18:30$ |
| Tuesday | May 02 | $07:30 - 19:50$ |
| Wednesday | May 03 | $07:10 - 15:45$ |
| Thursday | May 04 | $08:30 - $ .......... |

an ROI can be observed on the 1ˢᵗ of May, a local break holiday. In the appendix *A.1* a closer look on these regions of interests is taken.

### 5.3.3    *Attenuation*

In the functional model and later in the final SST the readout electronics are placed on one side of the straw tubes. This means that the signal of a particle which traverses through the straw tubes has, at least in the worst case, to travel five metres through the tube until it reaches the readout electronics. Due to this long signal path the signal is attenuated. In this section, a measurement of the signal attenuation is described.

*Methodology*

To measure the attenuation a radioactive Fe-55 gamma source was placed at 25 different locations along the straw tube. This was done by placing the source on a small, height adjustable laboratory lifting table as shown in figure 5.17. The setup was placed in such a way that the distance between the radioactive source and the straw tube was in the order of few millimetres. Also, special care was taken that the centre of the source was in line with the centre of the straw tube.

Power-wise, the straw's high voltage power supply was set to 2.2 kV and the L3 preamplfier was supplied with 4 V. Readout-wise, the negative output signal of the L3 preamplifier was connected to the FADC. The FADC was operated in the self-triggering mode, meaning that *all* signals exceeding a certain threshold were registered and saved. The measurement was repeated for four different threshold levels, viz. 500 $V_{\mathrm{FADC}} \simeq$ 0.25 V to 1250 $V_{\mathrm{FADC}} \simeq$ 0.62 V in equal steps. Note that these thresholds are absolute values and can be converted into 'real' voltages using the calibration from section 5.2.3. Furthermore, the FADC was configured in such a way that each internal trigger was put out at its 'Trigger Out' port. This port was connected to a 4 MHz counter. All measurements were performed using CAEN's Wavedump software and were run until the counter indicated more than 20 000 events.

*Measurement results*

For each of the pulses at each of the locations the pulse height was first determined using a Matlab script. For a threshold of 1000 $V_{\mathrm{FADC}} \simeq$ 0.49 V the results can be seen in figure 5.18 which shows the absolute signal height distribution in a 2D histogram. This representation was chosen to show especially the widths of the distributions at the different locations along the straw. The images for the other three thresholds all show the same behaviour.
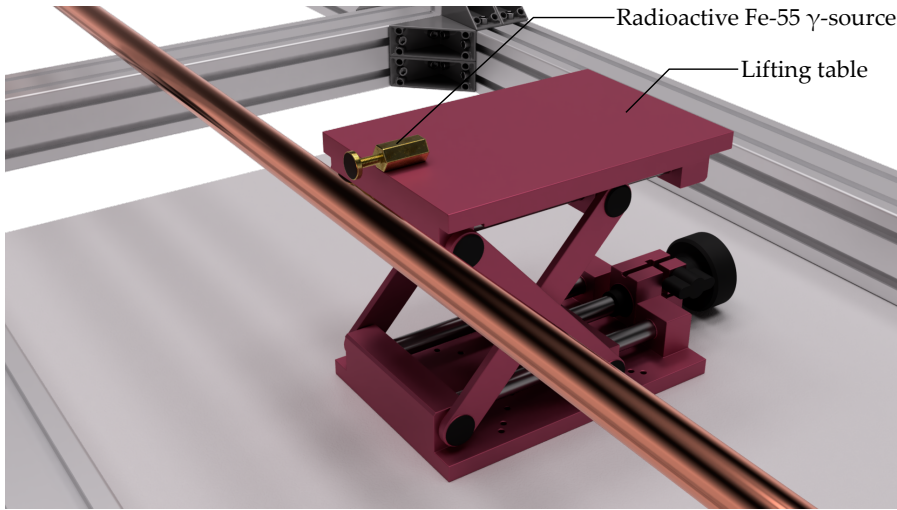
Figure 5.17: The setup used to measure the signal attenuation along the straw. A radioactive Fe-55 $\gamma$ source was placed on a lifting table. At 21 different locations at least 20 000 signals were acquired.

At the first three locations the signal height distribution is washed out with an absolute average signal height ranging between 875 mV and 880 mV. Beginning at a distance of 100 cm from the preamplifier the signal height distribution starts to get sharper with most signals having a height of around 930 mV. The signal height continues to increase and reaches its maximum at a distance of 200 cm where the majority of signals have heights of roughly 935 mV. Afterwards the signal height steadily decreases. At a distance of 500 cm away from the preamplifier most pulses have a height of approximately 920 mV. However, no clear exponential decrease is visible. The bottom plot in figure 5.18 shows the normalised average signal height and indicates that the signal at the last position is attenuated by

$$\delta_{\text{pulse-height}} \approx 1\,\% \qquad (5.7)$$

with respect to the maximum value. The fact that the signal height has a maximum in the middle of the straw can be explained by the sagging of the straw and the wire. While both the wire and the straw sag down in the middle the sagging of the straw is larger than the sagging of the wire. This causes the anode wire, especially in the middle of the straw, to be nearer to the straw's walls. This, according to equation (4.16), results in a larger electric field inside the straw tube and thus a larger signal. Strikingly, the maximum absolute signal height is not located in the middle, which may be caused by the straw not being mounted straight within the mounting frame. However, this does not explain the smeared pulse height distributions at the first three locations. These may have been caused by contaminations inside the straw tube or issues with the gas supply, especially as on this side the gas exhaust is located.
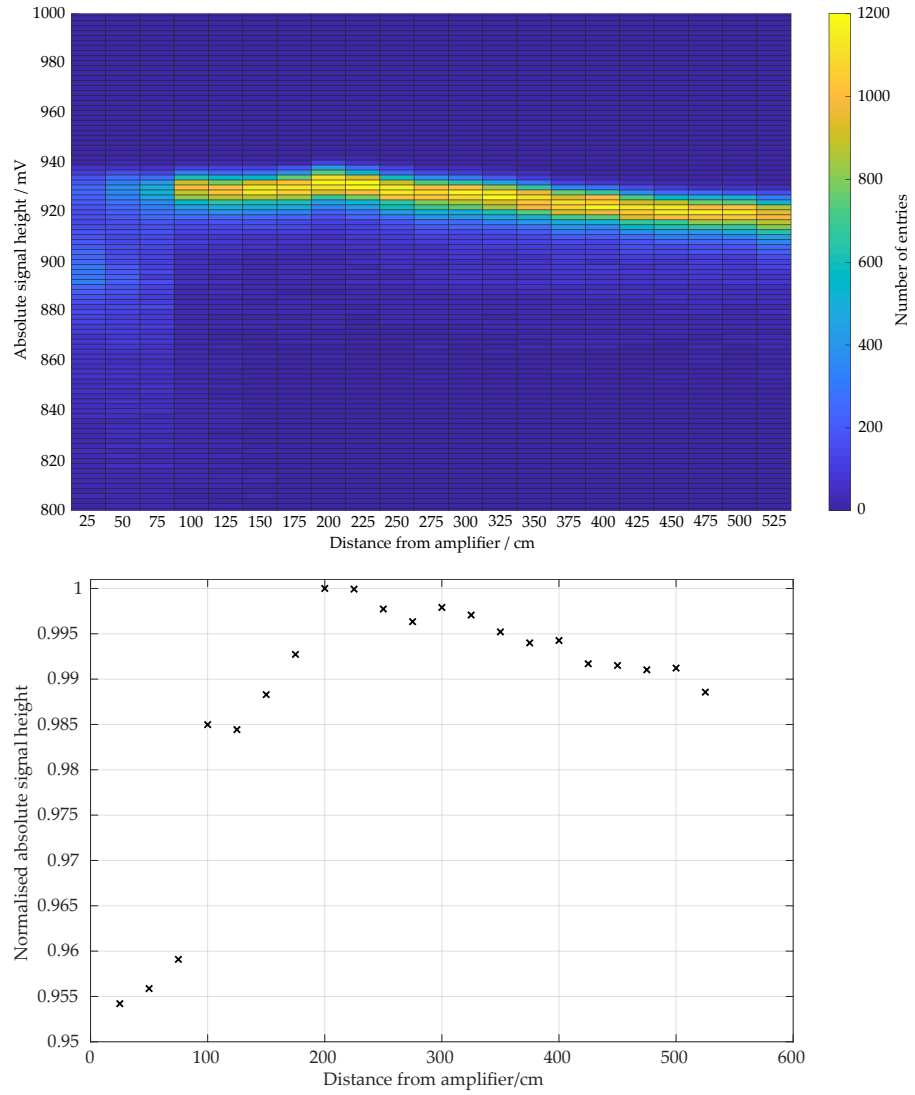
Figure 5.18: Signal attenuation along the straw tube using the signal height. The absolute signal height distribution is shown in the top image with a 0.2 mV binning. In the bottom image the normalised absolute signal height is shown. Note that errors are not depicted for reasons of clarity.
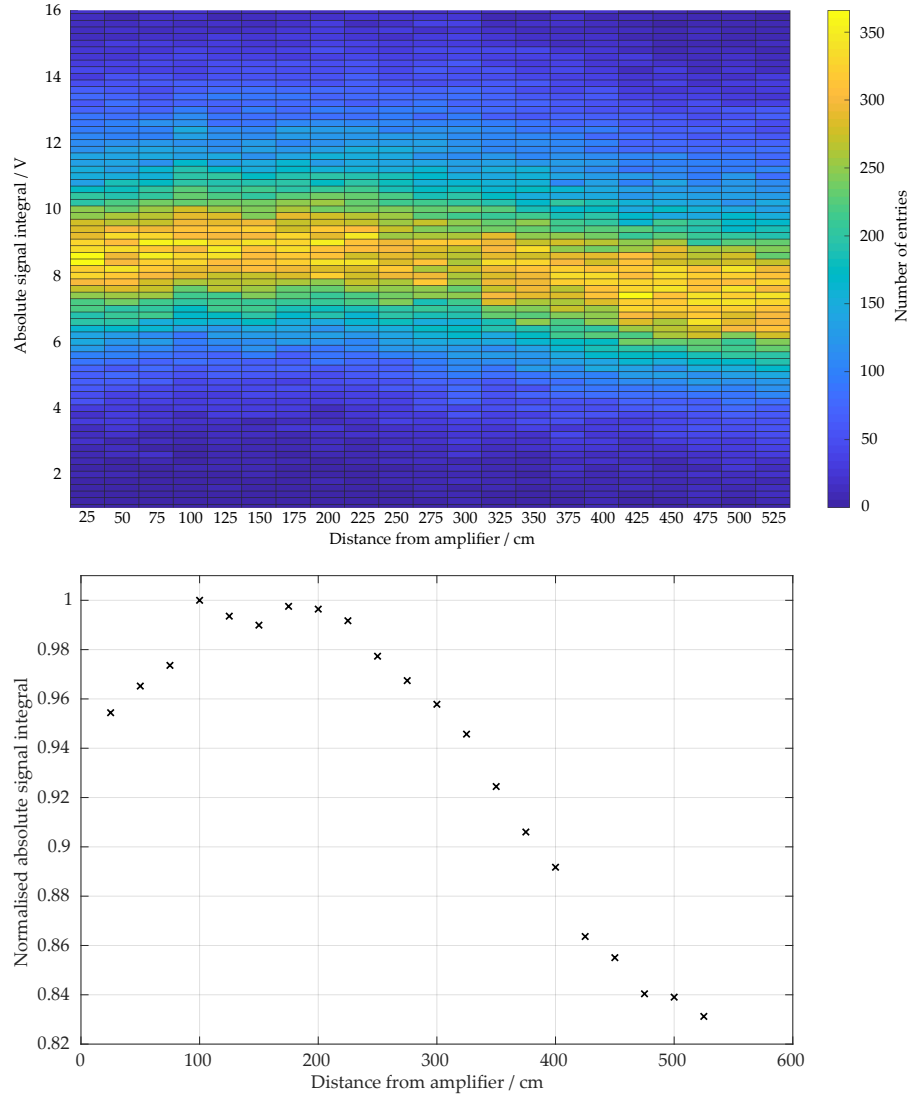
Figure 5.19: Signal attenuation along the straw tube using the signal integral. The absolute signal integral distribution is shown in the top image with a 0.2 V binning. In the bottom image the normalised absolute signal integral is shown. Note that errors are not depicted for reasons of clarity.

Another method to analyse the signals is not to use the signal height but rather the signal integral. The advantage of this method is that, in theory, random noise should cancel itself out. In figure 5.19 the signal integral distribution is shown for the same dataset taken at a threshold of 1000 $V_{\mathrm{FADC}}$. Similar to the pulse height distribution, the signal integral distributions at the other thresholds look very similar.

In general, the signal integral distribution shows the same behaviour as the pulse height distribution. The minimum of the signal is located in the area of 175 cm distance from the amplifier. Here, most integrals have approximately −9 V. From 175 cm to 525 cm the signal integral decreases steadily to roughly −8 V in average. Similarly, the signal integral decreases to circa −8.5 V in the range from 175 cm to 20 cm distance from the amplifier. The normalised average signal integral is shown in the bottom image of figure 5.19. It shows that the attenuation is given by

$$\delta_{\mathrm{integral}} \approx 17\,\% \tag{5.8}$$

This seems much more realistic than the previously acquired 1 %, as previous measurements of the attenuation in OPERA drift-tubes showed a signal attenuation of 36 % over a length of 8 m.

## 5.4    SUMMARY AND OUTLOOK

The goal of the single-straw functional model was to commission and test a single five metre long straw tube under regular laboratory conditions. To do so, a simple mounting mechanism was designed that allowed the straw to be mounted to a large aluminium frame. The mounting solution proved to be suitable for this specific application, although inappropriate for a large scale integration. A very simple gas system where, basically, gas stored in a gas bottle flows through the straw and is afterwards exhausted to the ambient air, was implemented. Electronics-wise, an L3-based preamplifier setup was taken off of an existing drift-tube setup. A flash analogue to digital converter (FADC) was used to read-out the signals of the straw tube after it was successfully calibrated using a function generator. Both the gas system and the electronic setup proved to be sufficiently suitable for the use in the single-straw functional model.

Using the single-straw functional model drift-time spectra of cosmic muons were determined. Some drift time spectra showed the expected form with lengths just shy of 800 ns, corresponding well with the expected length. However, several drift time spectra with an unexpected behaviour were observed. These spectra were distinguishable by their long tail, with lengths of more than 3000 ns and caused by noise.

Several noise effects were observed, including a slight noise increase for high voltages above 2100 V. Most importantly however, a severe grounding issue was detected where touching the mounting frame increased the noise rate to an order of $\mathcal{O}(10^6)$ Hz. This grounding

issue was mostly resolved by establishing a direct connection between the functional model's mounting angle and a ground pin on the L3 preamplifier. The base level-noise was determined to be significantly lower during night than day. This is an effect likely caused by electromagnetic pickup, which may be filtered out using software algorithms in future. Hardware-wise, an electromagnetic shielding is currently being developed which consists of two aluminium U-profiles which are placed around the functional model. It is also being investigated whether or not the functional model can be decoupled from the mounting frame to further help prevent the issues with the grounding. Once these measures are taken more precise measurements of the drift-times and, in particular, of the signal attenuation can be performed.

The signal attenuation along the straw tube, which, in theory, is expected to be exponential, was determined using two ways. Both ways relied on the same data taken using a Fe-55 source located at different positions along the straw. The first way relied on measuring the heights of the pulses. This yielded a rather low attenuation of roughly 1 %. Additionally, the signal height distributions at three points near the gas outlet were found to be much wider than at the other points. This may be caused by the gas outlet or a contamination within the straw. To narrow down the cause of this effect the measurement may be repeated in future with the straw turned the other way round. Also, a bubbler may be attached to the gas outlet. In the second method to measure the attenuation the integrals of the signals were used which resulted in an attenuation of about 17 %. Given OPERA's signal attenuation of 36 % over a length of 8 m the latter value seems much more realistic. However, both measurements did not indicate an exponential attenuation. Rather, the largest signals were found to come from the middle area of the straw and not the one closest to the preamplifier. This effect is likely caused by sagging, which cannot easily be corrected in the single-straw functional model. It is thus planned to re-measure the signal attenuation using the quad-straw prototype, which is designed to actively counteract the sagging and is described in the following chapter.

# QUAD-STRAW PROTOTYPE

The main goal of the single-straw functional model described in the previous chapter was to commission and test a single straw tube with an unprecedented length of approximately 5 m under laboratory conditions. The functional model meets the basic functional requirements needed in the later detector, however, it uses only a single straw tube and a highly simplified mechanical design. In the design process, the next step after designing and testing a functional model is to design a prototype.

Generally, the construction of a prototype has several advantages. Most importantly, it allows to evaluate and test the proposed design in a real-world object so that possible faults or required changes in manufacturing techniques can be detected early. While this early detection of faults also reduces cost, the small-scale nature of a prototype also means that possible changes can be applied faster, thus making the design process more efficient. In this chapter the design of a small prototype for the SHiP Spectrometer Straw Tracker is described.

## 6.1 SCOPE

A major challenge is the mechanical design of the SST, specifically the mounting of the anode wires as well as the straw tubes and their supports. The proposed setup for the mechanical design of the SHiP SST is based on the design of OPERA's drift-tube detector. Testing this proposed mechanical design is the main goal of the quad-straw prototype, which, as the name implies, uses four instead of only a single straw. Before manufacturing, all parts of the quad-straw prototype were 3D-modelled in Fusion 360 and a complete digital assembly of the prototype was made.

## 6.2 DESIGN OUTLINE

The Mylar straw tubes used for SHiP have a diameter of 20 mm and a wall thickness of 36 μm. Combined with the fact that each straw has an unprecedented length of 5 m this means that each straw underlies

significant gravitational sagging. Naturally, the anode wires also underlie sagging, however their sagging behaviour differs from the one of the straws due to their different geometry, material and tensioning. In total, this causes a net wire displacement, changing the electric field inside the straw tube and thus changing the signal characteristics. Furthermore, a wire displacement can promote sparkovers, which have the potential to damage the detector. To ensure that the anode wire is always centred with respect to the straw, several detector and prototypes designs were under consideration. The current design is a hybrid design which relies on straw tensioning, self-support of multiple straws by means of gluing packs of straws together and an external suspension using a carbon fibre tow.

*Note however that this effect could be corrected for in data post-processing, assuming the effect is quantitatively fully understood.*

The proposed technique has parallels with the design of a suspension bridge. Firstly, the straws are pulled straight by tensioning them up to their elastic limit. This is necessary as the Mylar is known to flow over time – meaning that the initial tension will halve itself over the course of 10 years. Additionally, sagging is mitigated by a strong, but small and highly tensioned carbon fibre tow. Each tow will hold two straws at certain suspension points. That way, the sagging of the straw tubes is controlled by the sagging of the carbon fibre tow. Furthermore, the straws are glued together at the suspension points, giving them an at least partially self-supporting property. The main advantage of this design is that both the carbon-fibre for the two straws as well as the two anode wires are anchored in the direct vicinity of each other in the mounting frame. Thus, movements of the mounting frame – caused for example by thermal effects or the evacuation of the vessel – likewise affect both the anode wires and the carbon fibre tow.

The carbon tow chosen for this purpose is the Carbon Roving NF-3 with 3000 filaments and a yarn count of 200 tex. Table 6.1 shows the technical specification of the carbon fibre tow.

Table 6.1: Technical data of the Carbon Roving NF-3. Taken from [KG10].

| Property | Value |
| --- | --- |
| Number of filaments | 3000 |
| Filament diameter | $7\,\mu m$ |
| Yarn count | 200 tex |
| Tensile strength | $3950\,N\,mm^{-2}$ |
| Elastic modulus | $238\,000\,N\,mm^{-2}$ |
| Elongation at rupture | $1.5\,\%$ |
| Density | $1.77\,g\,cm^{-3}$ |
| Specific electrical resistance | $1.6 \times 10^{-9}\,\Omega\,cm$ |
| Thermal conductivity | $17\,W\,mK^{-1}$ |

## 6.3 MECHANICAL PARTS

The quad-straw prototype was designed to operate with four straws. All of these four straws are installed to their respective mounting hardware allowing the straws to be attached to their endplates, which are on either sides of the straws. Additionally, the straws are supported using carbon fibre tows to compensate sagging. These carbon fibres are also mounted in the endplates. In the following sections each part of the prototype, which is shown as a 3D render in figure 6.1, is explained – beginning with the main parts of the mechanical structure, the endplates.
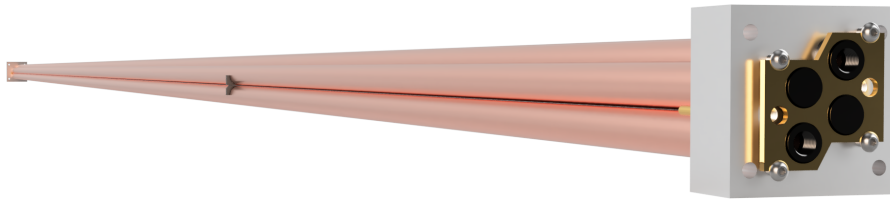


Figure 6.1: A rendered image of the quad-straw prototype. The straw tubes are, together with the anode wires and the supporting carbon fibre tows, attached to aluminium endplates on either side.

### 6.3.1 Endplates

The endplates are the core parts of the mechanical construction as both the straw tubes and the carbon fibres are attached to an endplate on either side. There are two different types of endplates. On one side the gas endplate is located. Here, the gas enters the prototype on a single input port and leaves the prototype using a similar output port. On the other side, the electrical endplate, the anode wires are supplied with high voltage and the signals can be read out using special readout electronics – see section 6.4.3. While both endplates have slight mechanical differences concerning the gas distribution, their main design features are identical.

Figure 6.2 shows a 3D rendered image of the endplate on the gas side as well as a cut through the endplate. The endplate has two sides, which are in the following referred to as 'straw side' – the side where the straws are attached – and 'I/O side' – the sides where the input/outputs for the gas and electronics are located. For structural reasons it is machined out of a solid EN AW 5083 aluminium block and has outer dimensions of 70 mm × 70 mm × 30 mm (width × height × thickness). The main feature of this endplate are the several holes to mount the four straw tubes. Each hole is made up of different bores of different diameters and depths. The main bores go through the complete endplate and have a diameter of 12 mm. Two ∅16 mm bores are drilled in from the straw side and mounting side with a depth
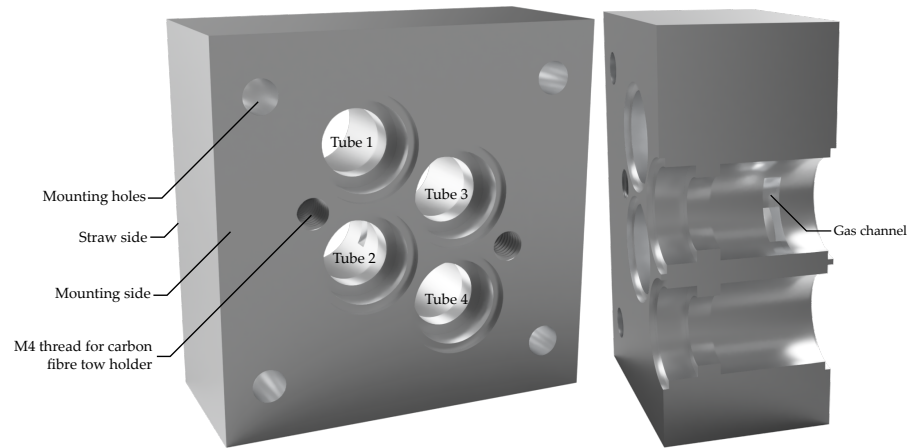
Figure 6.2: Images of the gas side endplate and of a cut through the endplate. The difference between the gas side endplate and the electrical side endplate are the internal gas channels. The endplates are the core parts of the mechanical construction.

of 6 mm and 20 mm respectively. Finally, on each side a ⌀19 mm bore with a depth of 1 mm is drilled into the endplate. This unique design creates several annuli which serve to properly seat and align the individual parts required to mount the straws and the anode wire to the endplates.

The endplate design also incorporates the gas distribution. This is done by milling a circular recess with a diameter of 13.5 mm and a depth of 3 mm into the sides of two of the bores so that there is a direct connection between them. On the gas side endplate this connects tubes two and three together, while on the electrical side endplate four milled recesses connect tubes one and two as well as tubes three and four together. That way, the gas enters tube one on the gas side endplate, flows through it, and is directed to tube two on the electrical side. After the gas has then arrived back at the gas side it flows via the gas channel towards tube three, flows through it, is directed towards tube four on the electrical side and completes its journey by arriving back on the gas side.

*Note that the gas can also flow in the opposite direction, i.e. tube 4 can be used as inlet and tube 1 as an outlet.*

Four 5 mm deep M4 tapped bores are located around the main bores on the straw side. Here, threaded rods can be screwed in such that a special hold-down plate securing the mounting hardware in place can be attached to the endplate. To mount the carbon fibres to the endplates, M6 tapped bores are located between tubes one and three as well as tubes two and four. These allow special carbon fibre holders to be screwed in and the fibres to be tensioned. Finally, each endplate has four ⌀6 mm holes in each corner so that it can be attached to a mounting frame using regular M6 bolts.

### 6.3.2  *Straw endpieces*

The straw endpieces, shown in figure 6.3, connect the straw tubes to the mounting hardware. A single endpiece is a hollow, turned tubular EN AW 5083 aluminium part with a total length of 34 mm and a mass of 12.4 g. It has a shorter section with a length of 6.2 mm and an outer diameter of 15.8 mm as well as a longer section with a length of 27.8 mm and an outer diameter of 19.8 mm that tapers in slightly to simplify the straw insertion process. The inner diameters are 12 mm and 34 mm respectively.



(a) The straw endpiece.



(b) A cut through the endplate and the straw endpiece.
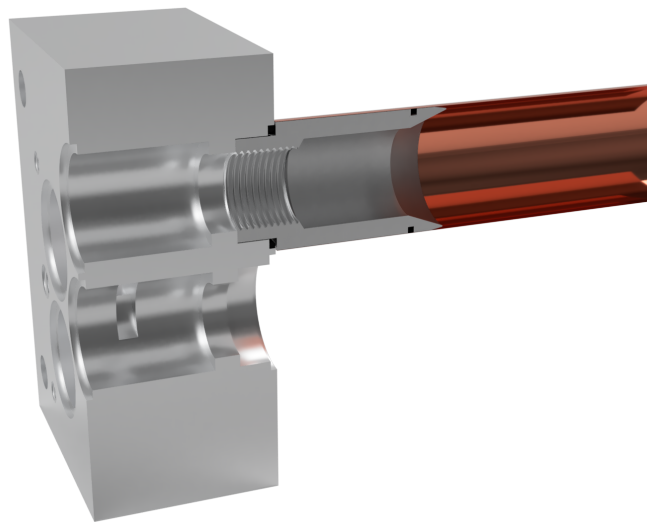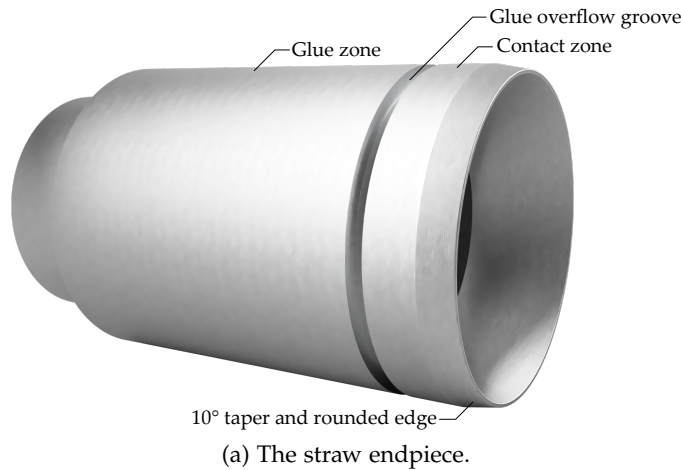
Figure 6.3: Images of a straw endpiece and a of a cut through the endplate and the endpiece showing the installation. The straw endpiece is a hollow aluminium part to which the straws is glued.

The large segments of the straw endpieces are slid into the straw tubes on either side so that the annulus between the smaller and the larger segment sits flush with the end of the straw tube. By means of glue the straws are bonded to the endpieces. To ensure the

electrical contact between the endpiece and the straw tube the long section is split into a larger glue zone and a smaller contact zone via a 1 mm wide and 1 mm deep ridge. The glue is only applied to the glue zone, while the electrical contact zone remains clean, ensuring electrical contact. The 1 mm ridge separating the two zones serves as an overflow basin preventing glue to enter the contact zone.

In the bottom image of figure 6.3 a cut through the endpiece shows the inner design. An ISO M12 × 1 fine inner thread is tapped into the narrower section of the endpiece. The inside of the larger section is plain, has an inner diameter of 14 mm, and tapers to a small rounded corner at the end. This rounded corner and the tapered construction are designed to minimise possible signal reflections which would occur on flat areas.

### 6.3.3    *Straw tensioning screws*

The straw endpieces explained in section 6.3.3 are attached to the endplates using the straw tensioning screws, shown in figure 6.4. These are special, custom made 12 × 14 mm screws with a slot drive equipped cylinder head of 6 mm length and a diameter of 15.5 mm. The shank of the straw tensioning screws has a length of 3 mm and the thread length is 11 mm. Here, an ISO M12 × 1 fine outside thread is used compatible with the thread used in the straw endpieces.

A key feature of the straw tensioning screws is that they are hollow. On the bottom image of figure 6.4 a cut through a tensioning screw is depicted. This hollowness allows gas to flow through the straw tensioning screws. The inner diameter of the screw amounts to 8 mm, leaving a wall thickness of about 1.4 mm.

Since the straw tensioning screws are – as their name implies – also used to tension the straws but only have rather small wall thickness, they are manufactured out of brass instead of the weaker – although lighter – aluminium. Also, brass is considered to have self-lubricating properties. The total mass of a single screw is 12.5 g.
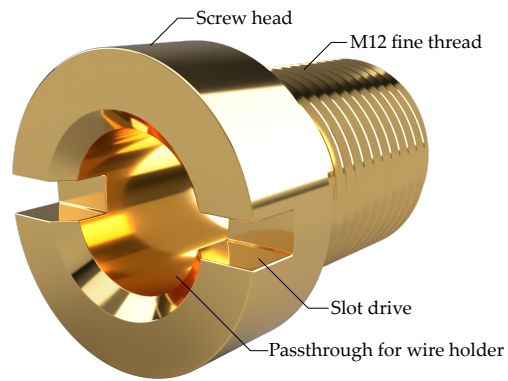
(a) The straw tensioning screw.
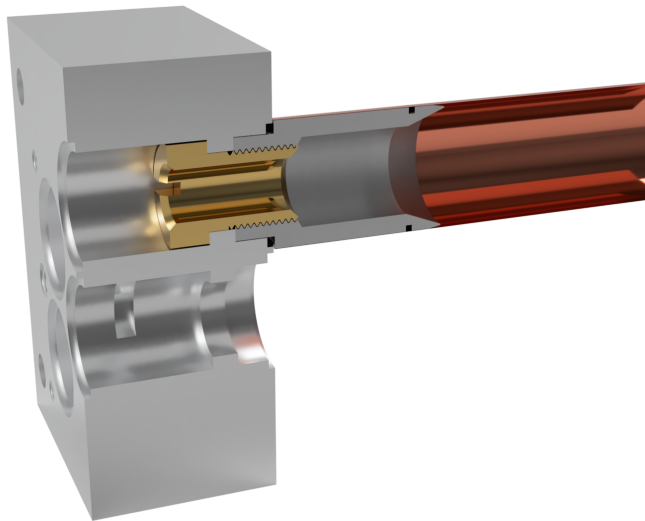


(b) A cut through the endplate and the straw tensioning screw.

Figure 6.4: Images of a straw tensioning screw and of a cut through the endplate and the straw tensioning screw showing the installation. The straw tensioning screw is a special hollow brass screw designed to attach the straw endpiece to the endplate.

### 6.3.4  *Sense wire holders*

The sense wire holders, shown in figure 6.5 attach the tungsten anode wires to the endplates. They consist of a 3 mm long head and a 52 mm long body, resulting in a total length of 55 mm. The head's outer diameter is 16 mm and the body's 6 mm. Similar to the straw endpieces and the straw tensioning screws from section 6.3.2 and 6.3.3 the sense wire holders are turned, hollow parts – although for reasons of electrical isolation they are manufactured out of POM. POM (Polyoxymethylene), also known as acetal, was chosen due to its high stiffness as well as excellent dimensional stability simplifying the required high-precision manufacturing process. A single sense wire holder has a mass of 2.1 g

The bottom image of figure 6.5 shows a cut through a sense wire holder, revealing multiple sections of different inner diameters. The anode wire is designed to run along the middle axis of the sense wire holder. Starting from the body, the wire enters a 43 mm long section with an inner diameter of 4 mm. The length of this section ensures that the wire is adequately isolated. Within 2 mm this section tapers down to 0.3 mm, creating the 1 mm long transition zone. This transition zone ultimately separates the wire's active measurement zone from its mounting zone. It is followed by a 5 mm long crimp-pin seating zone with an inner diameter of 0.8 mm. This zone is designed to seat a crimp pin – a hollow copper tube with an outer diameter of 0.7 mm which can be squeezed together to hold the anode wire which passes through it in place. Finally, in the sense wire holder's head, a 4 mm long crimp section with an inner diameter of 3 mm is located. The increased inner diameter is required to insert a special tool allowing to actually crimp the crimp pin.

The body of the sense wire holder is inserted through the hollow straw tensioning screw so that the head sits flush on the head of the tensioning screw. In order to make it easier to insert the 16 mm head into the 16 mm hole in the endplate the head features a 10° chamfer on one side. Through four holes with a diameter of 2 mm the gas can flow through the head of the sense wire holder into the straw tensioning screw.
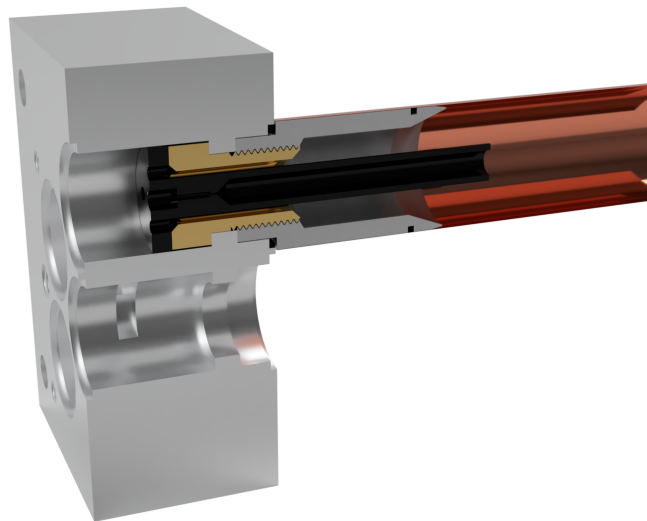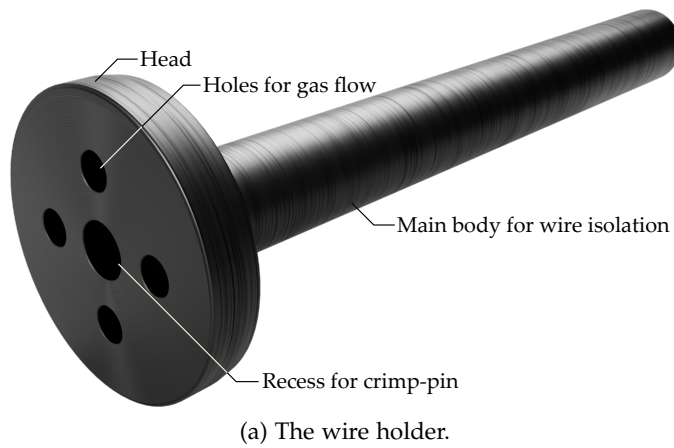
(a) The wire holder.



(b) A cut through the endplate and wire holder.

Figure 6.5: Images of a wire holder and of a cut through the endplate and the wire holder showing the installation. The wire holder is a special hollow POM part designed to attach the anode wire to the endplate. Via a crimp-pin the wire is held in the wire holder. Note that both the wire and the crimp pin are not shown in the image.

### 6.3.5 *Straw tube covers*

The straw tube covers in combination with an O-ring seal the gas filled volume of the quad-straw prototype off from the ambient air. Each straw tube cover is a turned Polyoxymethylene (POM) part consisting of two different sections with a total length of 13 mm as shown in figure 6.6. The insertion section has an outer diameter of 16 mm and a length of 6 mm. The last 3 mm of this section feature a 10° chamfer which allows the straw tube covers to fit in more easily into the 16 mm holes in the end plate.

The outside section of the straw tube covers consists of a 3 mm long section with a diameter of 19 mm and a slightly longer 4 mm section with a diameter of 14 mm. Due to the transition between the two sections of different diameter a 5 mm wide annulus is created.This area is used to firmly press the straw tube covers onto the O-ring and into the endplate using a hold-down plate (see the following section) and thus secure the covers in place. This is required, as the straw tube covers alone are just designed to be friction fit and proper, tight seating cannot be guaranteed, especially when gas pressure is applied to the prototype.

In total, the prototype requires eight straw tube covers in three different designs. For the gas inlet and outlet a special gas connector cover is used. This cover is hollow and has a 5 mm long section with an inner diameter of 12 mm common with all three cover types. The remaining inside section consists of a 3/8-inch 27 UNS thread into which a Swagelok gas connector can be screwed. The second cover is the electrical cover which has a special pass-through for the crimp pin. Four of these covers are required for the electrical side endplate. The final cover type is the blind cover. Unlike the gas connector type or the electrical type the blind type is not hollow and solely serves the purpose of plugging the endplate holes. Two of these blind covers are required for the prototype, both on the gas side.

*UNS stands for 'Unified Special Thread Series' and is a standardised American thread with special diameters and pitches for special purposes.*

Blind cover
Electrical cover
Gas cover
Outside section
Insertion section

Passthrough for crimp-pin
3/8" UNS thread
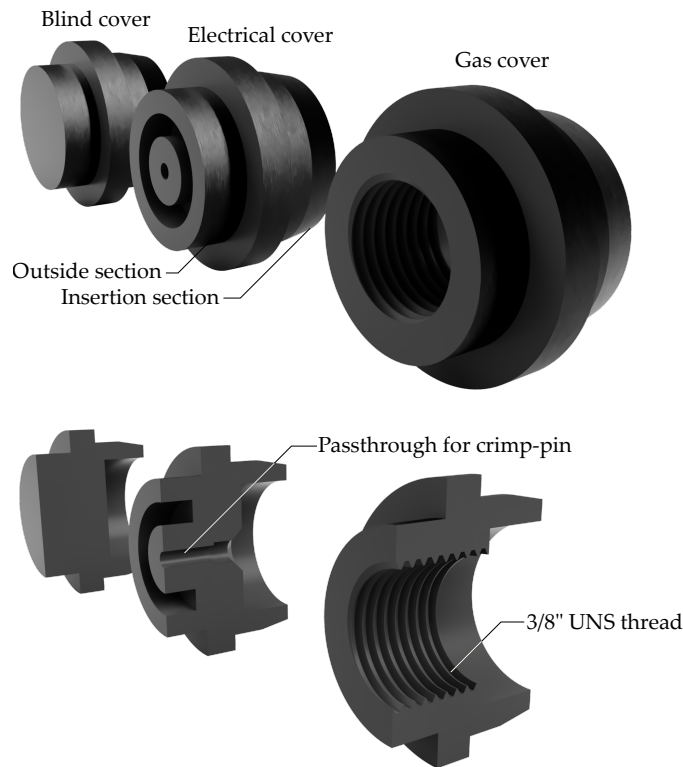
(a) Three versions of the straw tube covers and a cut through each of them.
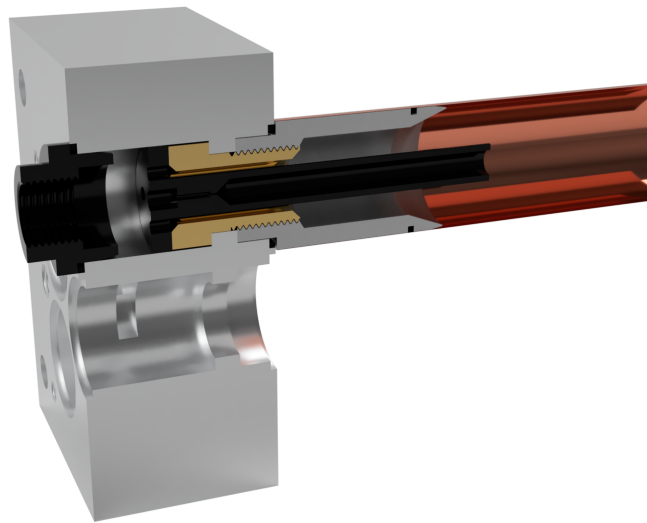


(b) A cut through the endplate and a gas cover.

Figure 6.6: Images of three types of straw tube covers and a of a cut through the endplate and a gas cover showing the installation. The different types are required for the gas I/O, for a passthrough for the crimp-pin and for a simple gas-tight plug. All covers are turned POM parts.

6.3.6   *Hold-down plates*

On each endplate a single hold-down plate is used to press the straw tube covers illustrated in section 6.3.5 firmly onto the O-rings and into the endplate. For that purpose, a hold-down plate is a 3 mm thick aluminium plate with outer dimensions of 50 mm × 49.31 mm. Each plate has four holes with a diameter of 15 mm designed to fit around the 14 mm outside sections of the straw tube covers and thus securely hold them in place. At the top and bottom edges of the endplate two half circularly shaped recesses with a radius of 2 mm are located. These recesses correspond spatially with the four M4 tapped bores in the endplate and are used to attach the hold-down plate to the endplate and to exert the required force onto it. The particular design allows for multiple hold-down plates to be attached seamlessly next to each other, as would be required for a larger prototype with more than four straw tubes. Two holes with a diameter of 7 mm spatially correspond with the holes in the endplate designed to hold the carbon fibre holders and allow these to be accessed. A hold-down plate is shown in figure 6.7.

Recess for mounting

Passthrough for covers

Passthrough for carbon
fibre tow holder
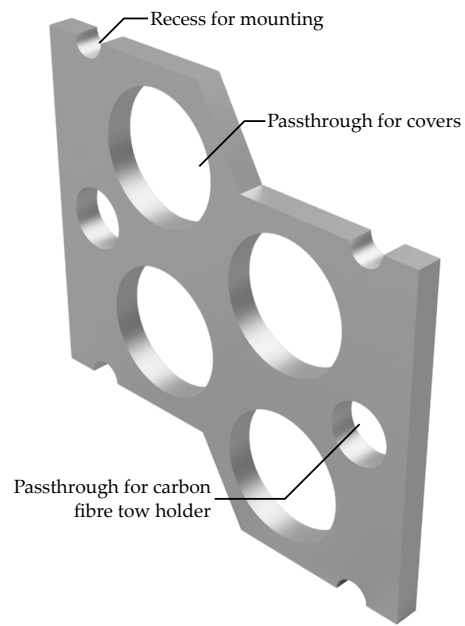
(a) The hold-down plate.
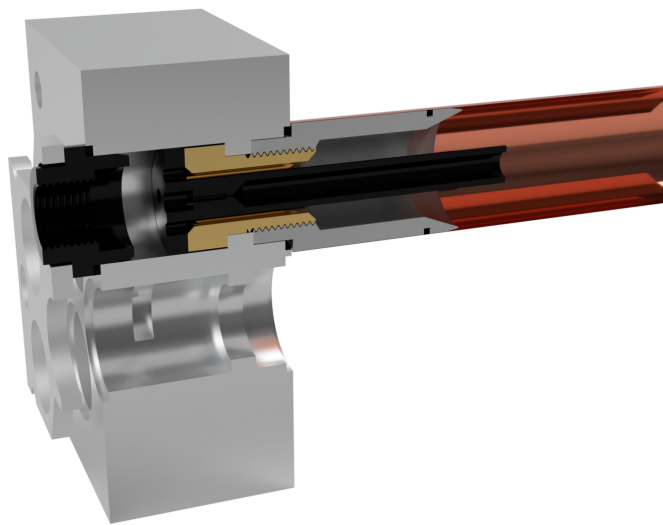


(b) A cut through the endplate and hold-down plate.

Figure 6.7: Images of a hold-down plate and of a cut through the endplate
and the hold-down plate showing the installation. The hold-down
plate is designed to push the friction-fit straw tube covers into the
endplate and secure them in place. Due to the special design of
the hold-down plate several of them can be installed seamlessly
next to each other. The hold-down plates also have several access
holes for the carbon fibre tow holders.

### 6.3.7   *Carbon fibre tow holders*

The carbon fibre tow holders serve the purpose of attaching the carbon fibre tows to the endplates. These carbon fibre tows are required to counteract the sagging of the straws. Each pair of straws is supported by a single carbon fibre. A carbon fibre holder is shown in figure 6.8 and has the same structure as a screw - except the other way round. Instead of a plain head and a threaded body, a carbon fibre holder
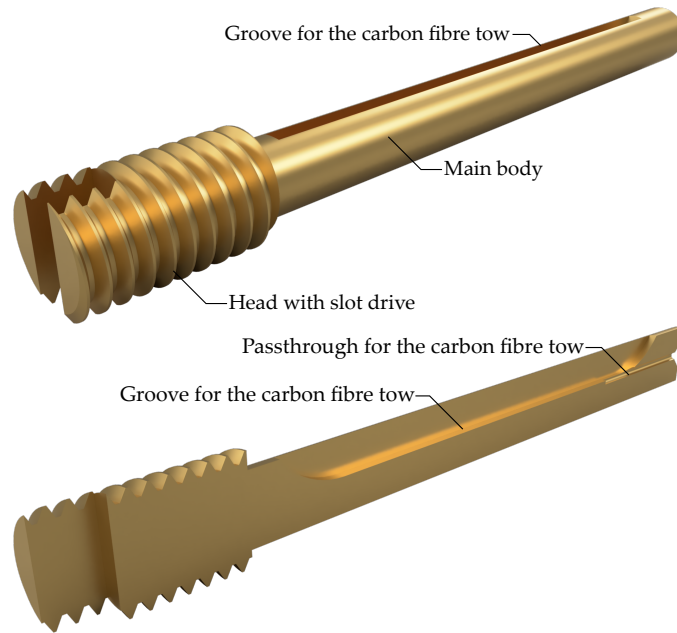


Figure 6.8: Images of a carbon fibre tow holder and a cut through it revealing the groove for the tow. The holder is required to mount the carbon fibre tow to the endplate. The tow itself is fixed in the groove by means of glue (not shown).

consists of a threaded head and a mostly plain body. The head is 10 mm long and has a standard M6 outer thread. It is driven using a 2 mm wide and 3 mm deep slot drive. The main body has a length of 40 mm, bringing the total length of a carbon fibre holder to 50 mm, and an outer diameter of 4 mm. The shaft of the carbon fibre holder has a 2 mm deep and 1 mm wide groove. This groove is cut into the holder using a circular mill, resulting in rounded groove ends. At the partly chamfered end of the shaft a 10 mm deep bore with a radius of 0.5 mm is located. Through this hole the carbon fibre tow is inserted into the holder. Afterwards, the tow is glued in securely by flooding the groove with epoxy. Similar to the straw tensioning screws the carbon fibre holders are turned out of brass. A single holder has a mass of 5.1 g.

6.3.8 *Straw supports*

The straw supports connect the straws to the carbon fibre. Specifically, each straw support is connected to two straws. That way, the sagging of the straw tubes can be controlled by the carbon fibre tow and the straw supports.

A straw support is a 20 mm high and 10 mm wide part. It has a thickness of 4 mm. On one side two large cut-outs in the shape of a quarter circle with a radius of 10 mm allow the straw support to sit flush against a pair of straw tubes. On the other side a 1 mm wide cut-out terminating in a half circle for the carbon fibre is located. The cut-out begins on the right edge of the part and runs into the holder at a 45° angle. The midpoint of the half circle is located (a) exactly 1.5 mm below the horizontal axis splitting the piece in halves and (b) exactly 2 mm away from the left edge of the piece. At least this is the case for the 'outer' spacer. Over the length of the straw tube multiple supports are required. The sagging occurring especially in the middle of the straws requires the need for different spacers near the centre – the 'inner' spacers. Compared to their 'outer' counterparts they are structurally identical except for a slight difference concerning the cut-out for the carbon fibre. Here, the midpoint of the half-circle is located 2.25 mm below the horizontal axis halving the piece, instead of only 1.5 mm. This ensures that the inner straw supports sit higher than the outer ones, counteracting the sagging of the straws.

Material-wise two options are currently under study. Firstly, the straw supports could be manufactured out of Rohacell®, Evonik Industries AG's trading name for Polymethacrylimid (PMI). Rohacell has the advantage of being very light with a density of around $32 \, \text{kg} \, \text{m}^{-3}$ [Gmb19a], meaning that a single Rohacell straw support has a mass of only around 0.01 g. Early tests have shown that the straw supports can indeed be made out of Rohacell with the required accuracy using a water jet cutter. However, a compulsory requirement for all parts that are used in the SST is their vacuum stability. The effect of a vacuum on the open-pored structure of Rohacell is currently not sufficiently tested to make Rohacell viable for the use as straw supports – at least yet.

*Rohacell is most commonly used in the aerospace and automotive industry for, amongst other applications, lightweight sandwich components. To cover these different use-case scenarios it comes in various different specifications with densities ranging from 32 to 100 kilos per cubic metre.*

For this reason another option under consideration is to 3D print the straw supports. To compensate for the increased mass of the 3D printer's filament the design is slightly different from the one explained above – although very similar. While all the outer dimensions for both the inner and outer supports are untouched the complete part is shelled leaving a wall thickness of 0.25 mm – the printer's minimum setting. The parts were successfully 3D-printed using black polylactide (PLA) filament with a density of $1.24 \, \text{g} \, \text{mm}^{-3}$, resulting in a total mass of 0.107 g per straw support. While vacuum stable, the print process

is time consuming and the suitability for mass production still needs to be discussed. Both types of straw supports are shown in figure 6.9.
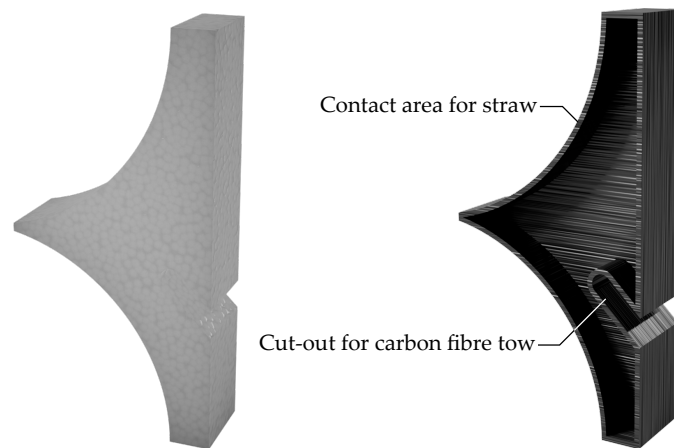


Figure 6.9: Two different versions of the straw supports designed to connect the carbon fibre tow to two straws. The left image shows the part made out of Rohacell, the right image shows a shelled, 3D printed version. The carbon fibre tow is designed to sit in the narrow cut-out on the right side of the support, the round surfaces on the left side are designed to be glued to the straws.

6.3.9 *Straw support applicator*

The straw support applicators are temporary parts designed to be used during the installation of the straw supports from section 6.3.8. A single straw support applicator is a 30 mm thick aluminium plate with outer dimensions of $66 \times 58.66$ mm (height $\times$ width). On the right side, the part features two circular cutouts with a radius of 10 mm for the straw tubes. Additionally, a 4 mm wide cutout for a straw support is located between the cutouts for the straw tubes. The straw support applicator is designed to be used with another applicator – rotated by $180°$ – on the other side. Due to the outer dimensions and the location of the cutouts they then perfectly imitate the layout of the straw tubes.

The straw supports are planned to be temporarily attached in their respective cutouts on the applicators by means of weak adhesive tape. The frontal area of the straw supports will be coated with a thin layer of glue. Afterwards the straw support applicators will, from both sides, be slid on a 60 mm $\times$ 60 mm aluminium profile against the straw tubes. After the glue has bonded the straw supports to the straws, they will be released from the applicators and the carbon fibre tow can be attached.

Cut-out for the spacer
Cut-out for the straw
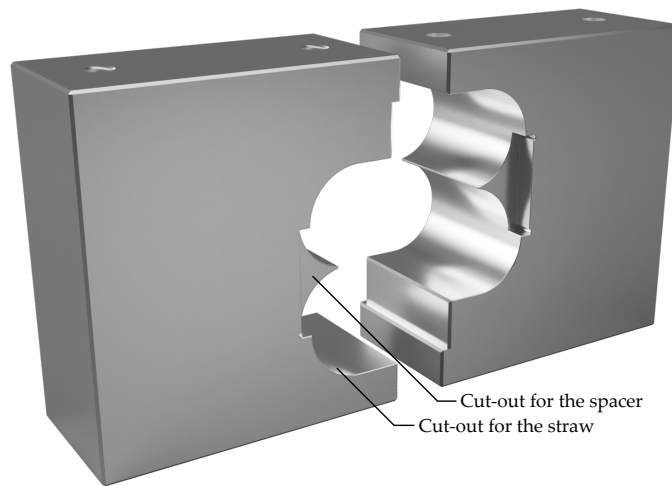
Figure 6.10: Image of two support applicators. They are used to apply the straw supports to the straws by means of glue. To do so accurately, they have a precise cut-out where the supports can be seated in. The cut-outs for the straws are designed to have the same layout as the four straws.

## 6.4 COMMISSIONING

The parts explained in section 6.3 were manufactured and afterwards the quad-straw prototype was assembled. During assembly, some issues became apparent and minor revisions to some parts were necessary. These, together with the gas system and the electronics design are outlined in this section.

### 6.4.1 *Assembly*

The quad-straw prototype was installed next to the single-straw functional model on the mounting frame, as shown in figure 6.11. The assembly of the quad-straw prototype was performed as follows. To begin, the first few centimetres of either end of the straws were cut off to make them straight and to remove damaged ends. Afterwards, the straws were glued onto the straw endpieces using a strong, low viscosity Loctite EA 9483 2-component epoxy. Since early tests indicated that this method may be problematic for the electrical contact between the straw and the endpiece the design of the endpiece received a minor revision. Instead of the first groove serving as an overflow basin for glue it was slightly enlarged and used to hold a section of a spiral spring. For this purpose, a Spira Manufacturing Quickshield NI-03 spiral was chosen. This spring is held in the groove using a fine, single-strand wire whose ends are twisted around each other and then pressed into the groove. Additional wider, but less deep grooves serving as glue basins were also added to the endpieces. A modified endpiece is shown in figure 6.12.

*Originally, the Quickshield NI-03 is intended to be used as a low cost EMI gasket solution.*

Figure 6.11: The assembled quad-straw prototype next to the single-straw functional model on the mounting frame. For the quad-straw prototype the ends of the straw tubes were cut off, resulting in the quad-straw prototype being slightly shorter than the single-straw functional model. Thus, one end of the quad-straw prototype is mounted to an additional, offset aluminium profile. The carbon fibre tows as well as the carbon spacers were not yet installed. The electronics and gas system are not depicted in this image.
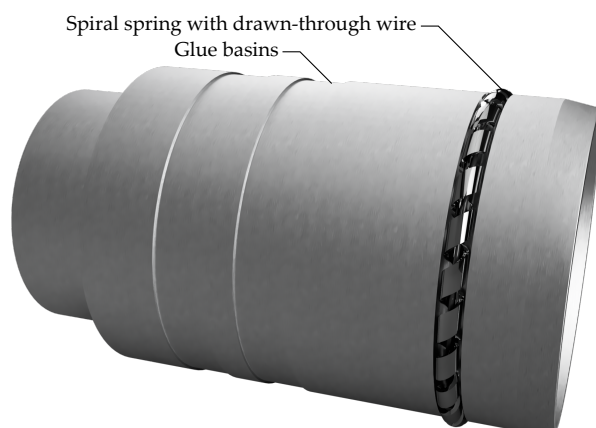
Figure 6.12: Modified design of the straw endpieces. To ensure adequate electrical contact a spiral spring is held in by a wire in the groove originally designed as a glue overflow basin. Two additional glue basis are added.

The endplates were attached to right-angular aluminium brackets via four bolts. Note that only the first few threads of these bolts were used in the beginning. The mounting brackets were then attached to the main frame at a distance 24 mm larger than the length of the straw tubes. Afterwards, the straw tubes were installed by threading the first few threads of the straw tensioning screws into the straw endpieces. After that the straw tensioning screws as well as the bolts connecting the endplates and the mounting bracket were fully tensioned and thus the straws were tensioned and elongated by 24 mm. This corresponds to about 60 N tension per straw.

After the straws were installed and tensioned the anode wires were mounted. It is currently discussed whether wires with a diameter of 30 μm or a diameter of 45 μm will be used for the Spectrometer Straw Tracker. Thus, straws one and two were equipped with the thinner wire and the other two straws with the thicker wire. To do so, the wire was threaded through the short piece of the anode wire holder and attached to a magnetic nut. Using a whiteboard magnet held against the outside of the straw tube the wire was then pulled through the straw. Utilising a small wire hook the nut, and thus the wire, were fished out of the straw tube and through the straw endpiece on the other side. Repeated attempts to thread the anode wire through the long part of the second anode wire holder remained unsuccessful. This was due to the fact that the manufacturing process left small grooves in the material on which the anode wire repeatedly got stuck. Furthermore, the manufacturing process left some burrs on the inside of the part which proved highly difficult to remove. Hence, a thicker single-strand wire was threaded through the wire holder from the short side, to which the anode wire was then attached and afterwards pulled through the wire holder.

After the wires were mounted on the first side using a crimp pin, they were tensioned using two different methods. For the thicker wire a deflection pulley and the standard OPERA-used tensioning weight with a mass – or pulling force – of $T_{45} = 180\,\mathrm{g}$ were used for tensioning. Due to the lower mechanical strength this weight could not be used for the thinner wire. Instead, a weight was chosen such that the sagging of the 30 μm wire is equal to the sagging of the 45 μm wire. For a pulling force $T_{45}$ the sagging of the 45 μm wire is given by

$$s_{45} = \frac{g\rho\pi r_{45}^2 L_0^2}{8T_{45}},\tag{6.1}$$

where g is the gravitational acceleration and $r_{45}$ the radius of the wire with the length $L_0$ and the density $\rho$ – see also equation 6.4. Since the thinner wire has a radius of $r_{30} = 2/3 \cdot r_{45}$, its sagging is given by

$$s_{30} = \frac{g\rho\pi r_{45}^2 L_0^2}{18T_{30}}.\tag{6.2}$$

The requirement that both wires should have the same sagging, $s_{45} = s_{30}$, then gives the following condition for the required pulling force:

$$T_{30} = \frac{4}{9}T_{45} = 80\,\mathrm{g}.\tag{6.3}$$

This pulling force was then implemented by using a digital spring scale mounted on a threaded rod. Afterwards, a second set of crimp-pins was used to finally secure the tensioned wires in place. Finally, the other remaining parts, i.e. the O-rings, the different covers and the holddown plates were attached to both endplates. Note that the hold-down plates from section 6.3.6 had to be cut back slightly in order to accommodate the mounting angle. The straw supports, carbon fibre holders, and the carbon fibre itself were not installed in the prototype, as the development of these parts is currently still ongoing.

### 6.4.2 Gas System

The gas system for the quad-straw prototype was slightly changed from the setup of the single-straw functional model. Instead of exhausting the gas into the surrounding air, the outflowing gas of the quad-straw prototype is flowing through a bubbler, which is simultaneously utilised by a drifttube setup used for practical courses at Hamburg University.

The gas is stored in a gas bottle. If the bottle is opened using a valve the gas passes through a pressure reducer, where the gas pressure before and after are measured using two manometers. After a Swagelok quick-lock coupling allowing the complete setup to be removed quickly two manually operated inflow valves A and D can be set to allow the gas to flow through either the quad-straw prototype or

the drift-tube setup. Before flowing through either setup an adjustable flowmetre is installed, where the flow of the gas was adjusted to $1 \, \mathrm{l}\,\mathrm{h}^{-1}$ during normal operation. Two outflow valves B and C are used to block the gas entering either measurement setup from the back side. A single bubbler, attached via another Swagelok quick-lock coupling, is then used for both apparatuses. The gas system is schematically shown in figure 6.13.
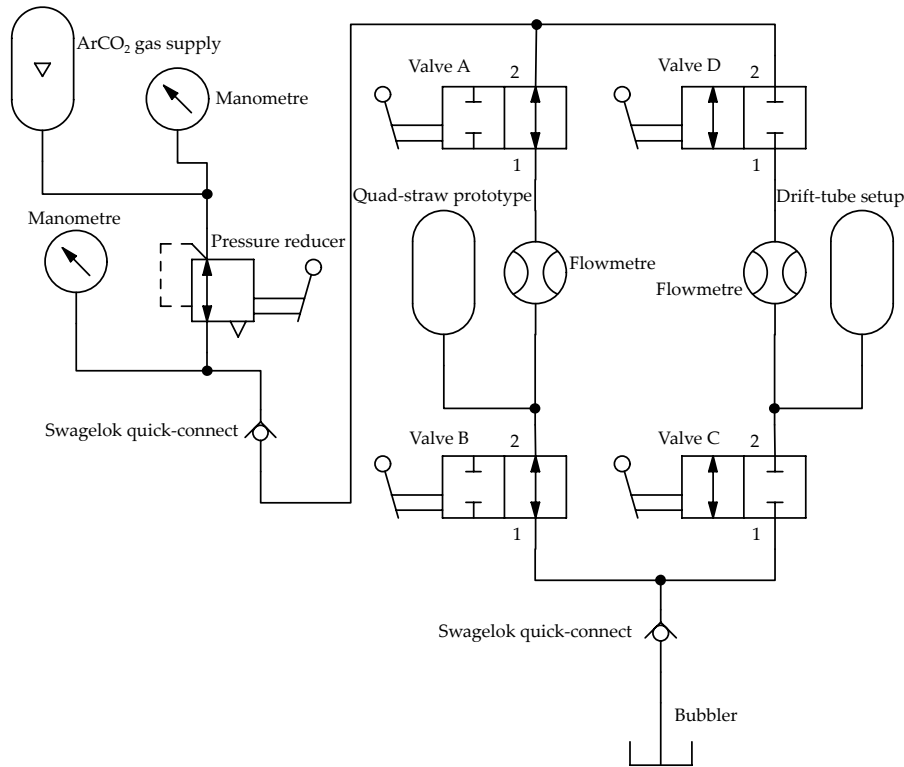


Figure 6.13: The gas system implemented for the quad-straw prototype. The quad-straw prototype shares the gas system with a drift-tube setup. Gas stored in a gas bottle flows through a pressure reducer and a flow regulator. Using four valves the gas can be set to flow through either of the two experiment setups. Afterwards, the gas is exhausted via a bubbler.

### 6.4.3 Electronics

The straw tubes of the quad-straw prototype will be read out using four separate L3 amplifiers – i.e. one amplifier per tube – to minimise potential cross talk. To design a suitable printed circuit board (PCB) the scheme of the existing readout electronics of the single-straw functional model were taken and adapted. Figure 6.14 shows the circuit diagram of the read-out electronics for the quad-straw prototype This schematic was used to design a PCB using SPRINT Layout 6.0 and KiCad – for more information about these programs see addendum B.5 and B.6. While the L3 amplifier is JEDEC conforming due to

*The 'JEDEC Solid State Technology Association' is a US based organisation for standardising semiconductors.*
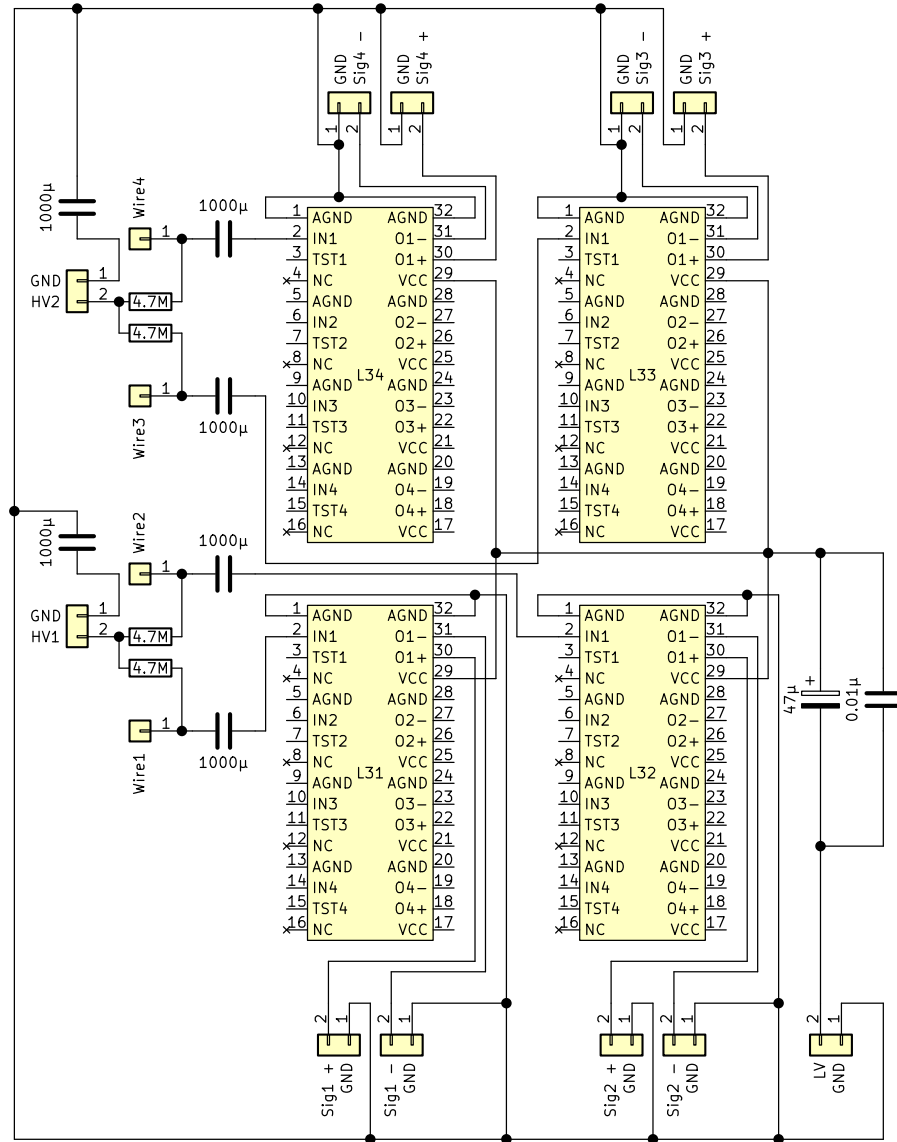
Figure 6.14: Circuit diagram of the complete preamplification circuit for the quad-straw prototype. Four separate L3 chips are used to mitigate cross-talk. To accommodate two different wire diameters two separate high voltage connectors are implemented. Due to the size of the L3 chips the circuit was later implemented on two separate boards.

it's 2.54 mm (0.1 inches) pin spacing with 16 pins in total, it has an unusually large width of 35.56 mm (1.4 inches). Since the readout electronics will have to fit inside a pair of aluminium profiles which are planned to shield to the straw tubes, the PCB needs to have a width of less than 8 cm to fit within the shielding. Due to the large size of the amplifiers this means that four chips on a single PCB would either result in a narrow but very long PCB or in a large number of vias. While this is not an issue for a commercially produced PCB, it can be a challenge for a manually soldered circuit on veroboard. Thus, a stacked layout was designed, where two PCBs are mounted on top of each other and are interconnected using male and female headers and sockets. Figure 6.15 shows rendered images of the bottom and top PCB, where top-layer tracks can bee seen in a golden hue.

*In electronics, a via is an electrical connection between two or more adjacent layers in a multi-layer PCB.*
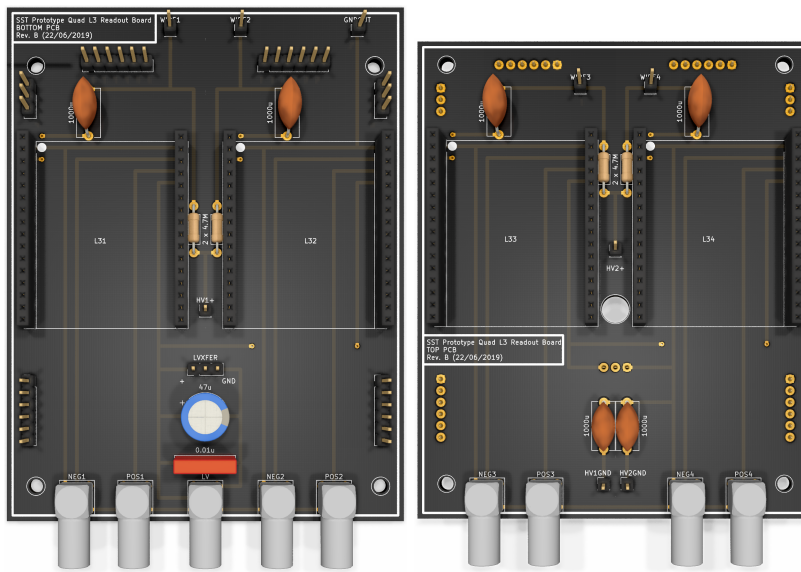


Figure 6.15: The two PCBs designed for the preamplification and HV supply for the quad-straw prototype's signals. For each straw tube an individual L3 amplifier is used. To minimise the overall footprint of the design two seperate PCBs are designed to be stackable. The bottom PCB is shown on the left side, the top one on the right. Each PCB can be supplied with a different high voltage.

On the bottom of both PCBs the output signals of the L3 amplifiers are located with one inverted (NEG) and one positive (POS) output per chip. The bottom board additionally features the connector for the low voltage (LV) with which all four chips are supplied. This low voltage, as well as the common ground, are transferred to the top PCB using the LV-transfer (LVXFER) pin headers. Both PCBs feature individual high voltage connectors so that the different anode wires (two wires with a 45 μm diameter and two with a 35 μm diameter) can be supplied with different high voltages in the quad-straw prototype. The connectors for these high voltages are located in the middle of each board between the two chips (marked HV1+ and HV2+). On

the top circuit board the HV2+ connector is slightly shifted, so that the cable connecting HV1+ can be passed through a drilled hole on the top PCB to the bottom PCB. The common ground connections for both high voltages are located near the top edge PCB. The connections for the four anode wires are located near the top edge of the PCBs (connectors WIRE1 - WIRE4). Additionally, the bottom board features an auxiliary common ground connector. The different lengths of the bottom and top PCBs allow for an easy connection of the anode wire cables.

Due to time constraints as well as relatively high costs for the production of two different PCBs the readout electronics were manually soldered on veroboards. The final stack of circuit boards is shown in figure 6.16.
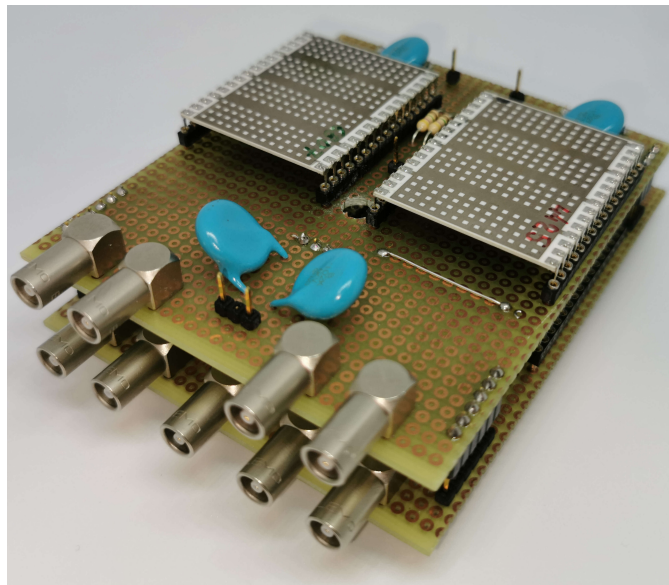


Figure 6.16: Electronics for the preamplification of the quad-straw prototype's signals. The design of the PCBs from figure 6.15 was soldered on two veroboards to save time and cost.

## 6.5 SAGGING OF THE STRAWS

Both the straw tubes and the anode wire sag down in the middle due to gravity. Due to their different geometries and materials their sagging behaviour differs from each other, causing a net wire displacement. This displacement changes the electric field in the straw tube and thus affects the detector's performance, although this effect can be corrected mathematically – assuming it is understood quantitatively. However, the net wire displacement can also cause sparks, which can damage the straw tube irreversibly and thus diminish the performance of the detector. It is thus highly important to understand and measure the sagging of the straw tubes.

### 6.5.1 *Expected sagging*

The theoretical sagging $s$ is given by

$$s = \frac{\rho g \sigma L_0^2}{8T}. \tag{6.4}$$

This equation was derived in section 4.2.2 – see equation (4.40). Here, $g = 9.81 \, \text{m s}^{-2}$ is the gravitational acceleration, $\rho = 1.39 \, \text{g cm}^{-3}$ is the density of Mylar [Fil03] and $L_0 = 533.6 \, \text{cm}$ the length of a tube which was determined using a measuring tape. The cross section of a straw is in good approximation given by $\sigma \simeq 2\pi \cdot 10 \, \text{mm} \cdot 0.036 \, \text{mm} \simeq 2.3 \, \text{mm}^3$. The pulling force for a straw is indicated by $T$. It can be calculated as

$$T = k\Delta L = E\sigma \frac{\Delta L}{L_0}, \tag{6.5}$$

where $k = {E\sigma}/{L_0}$ is the spring constant with $E = 4500 \, \text{N mm}^{-2}$ being the modulus of elasticity of a straw [Fil03]. The elongation of 24 mm is denoted by $\Delta L$. Plugging equation (6.5) into equation (6.4) gives

$$s = \frac{\rho g \sigma L_0^2}{8k\Delta L} = \frac{g}{8} \frac{\rho}{E} \frac{L_0^3}{\Delta L}. \tag{6.6}$$

In total, this gives for the expected, initial sagging

$$s \simeq 2.40 \, \text{mm}. \tag{6.7}$$

However, this is assuming that the modulus of elasticity of a straw tube is indeed given by $4500 \, \text{N mm}^{-2}$. To cross-validate this, the spring constant $k$ of a straw tube was determined experimentally. For this purpose, a straw tube was attached to the frame on one side, while the other side was attached to a spring scale on a threaded rod, allowing it to be moved. Using this spring scale the elongation of the tube depending on the required force was then determined. The results are shown in figure 6.17. A linear fit indicates that $(240.68 \pm 2.97) \, \text{g}$ are
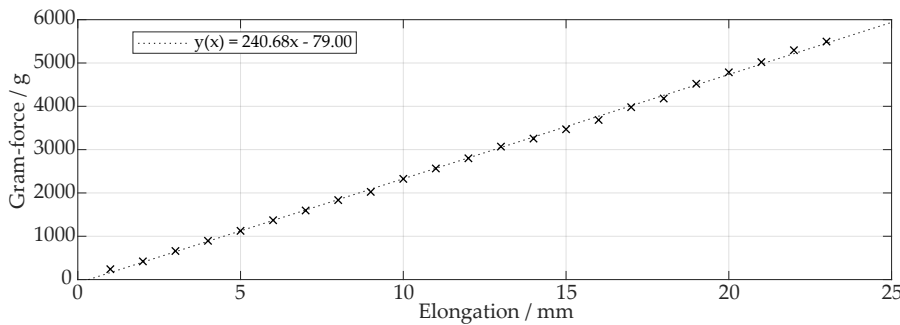


Figure 6.17: Measurement results for a straw's spring constant. A straw was elongated using an adjustable spring scale and the required gram-force was measured. A linear fit of the form $y(x) = 240.68x - 79$ indicates a spring constant of $2.36 \, \text{N mm}^{-1}$.

required for an elongation of 1 mm, meaning the spring constant of a straw tube is given by

$$k \simeq (2.36 \pm 0.03) \, \mathrm{N \, mm}^{-1}. \tag{6.8}$$

This results in a much stronger modulus of elasticity of

$$E_{\mathrm{measured}} \simeq (5475.2 \pm 69.6) \, \mathrm{N \, mm}^{-2}. \tag{6.9}$$

Using this value, the expected sagging is given by

$$s \simeq (1.97 \pm 0.16) \, \mathrm{mm}. \tag{6.10}$$

### 6.5.2  *Measurement of the sagging*

To measure the sagging of the straws a NIKON AC-2S optical level was used. It features a short focusing distance, a 24-fold magnification and automatic levelling through an automatic air-dampened compensator [05]. It also allows to measure angles using a horizontal circle. In figure 6.18 a view through the optical level's telescope is shown. The image was taken using a tripod mounted smartphone. It also illustrates the small field of view of the optical level, at least over relatively short distances – in this case the coin was placed about 3 m away from the optical level. The view through the scope reveals several lines, most importantly the main cross-hair allowing to accurately aim the optical level as well as centre the view. Moreover, two shorter lines are located above and below the horizontal line of the cross hair. These lines are called stadia lines and can be used to measure distances. The distance between the optical level and any given object is given by the distance between the two stadia lines times a factor of 100.
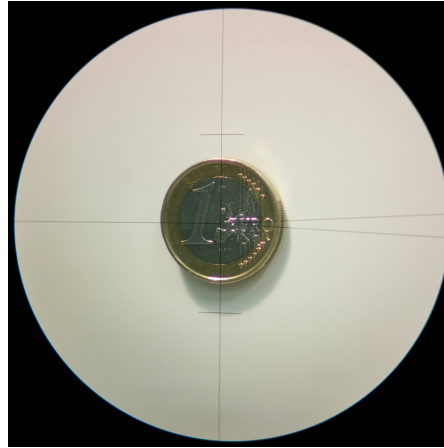


Figure 6.18: View at a one Euro coin through the optical level's telescope. The coins was placed roughly 3 m away from the level. The images shows the cross-hair as well as the stadia lines which can be used to measure distances.

The optical level was placed at a convenient location in the laboratory, as far away from the quad-straw prototype as possible. Figure 6.19

illustrates the location of the optical level in relation to the quad-straw prototype. The location was determined by measuring the distance from the optical level to the two endplates using the stadia lines and the enclosed angle using the horizontal circle. Via the law of cosines the length of the straw tubes was cross-checked to be 5360 mm – a value also determined using a regular measuring tape. The minimum distance to the straw tube setup, important to gauge later errors in measurement, was calculated to be 1920 mm.
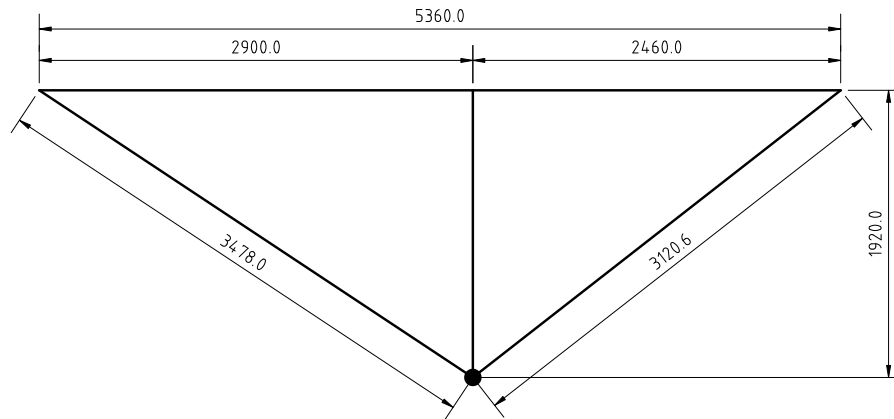


Figure 6.19: Location of the optical level with respect to the quad-straw prototype. The location was determined using the level itself.

During the determination of the optical level's location an inclination of the mounting frame became apparent. An inclined mounting frame can be problematic since even small inclinations can lead to the straws no longer being within the field of view towards either end of the quad-straw prototype. Thus, the mounting frame was levelled. For this purpose, a section of an aluminium profile was equipped with a ruler and placed at different locations on the horizontal beams of the mounting frame. The value on the ruler was then accurately read out using the optical level. In figure 6.20 images of the four corners of the mounting frame are shown. The evaluation of the data indicated that one side of the mounting frame was located approximately 13 mm higher than the other side. To level the mounting frame a hydraulic jack was used to lift and adjust the legs of the table on which the mounting frame is situated.

After the frame of the prototype was levelled to an acceptable level the sagging of the bottom front straw tube was measured. Since all four straws have the same length and were tensioned using the same force the same sagging behaviour is assumed for all four tubes. In order to measure the sagging at a certain point another aluminium cross brace was added to the mounting frame. On top of this cross brace a smaller 2 cm × 2 cm aluminium profile, equipped with a strip of millimetre paper was placed, as shown in figure 6.21. Afterwards, the height of the optical level was adjusted such that (a) the aiming point of the reticle was located between the bottom of the lower front
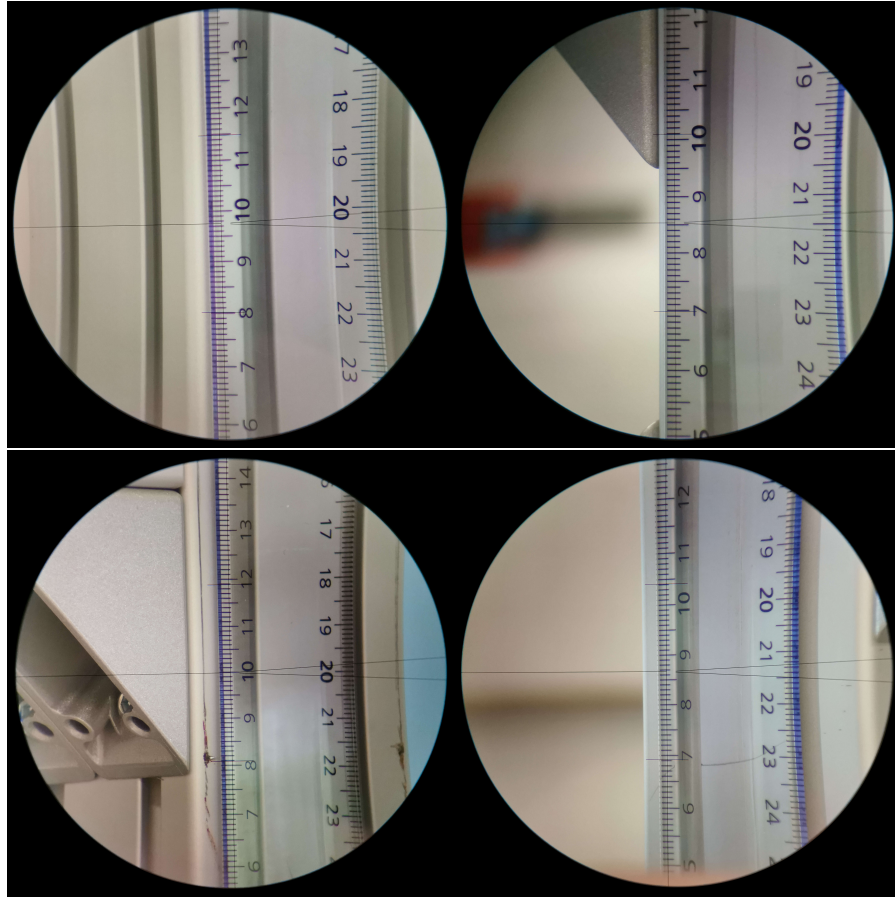
Figure 6.20: Views through the optical level's telescope at the four outermost corners of the mounting frame. The images indicate that the left side is approximately 1.3 cm lower than the right side.
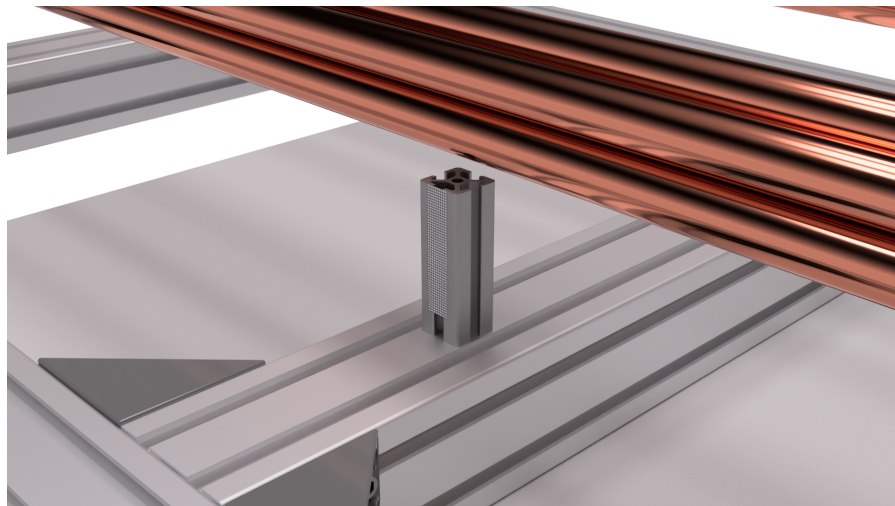


Figure 6.21: Image of the millimetre rod used in conjunction with the optical level to measure the sagging of the bottom front straw tube.

straw and the top of the measuring rod and (b) at least 20 mm were clearly visible on the measuring rod. Then, a picture through the optical level's telescope was taken using a smartphone camera and the measurement was repeated at different locations along the straw. In figure 6.22 the view through the telescope at the straw and the measuring rod is shown.
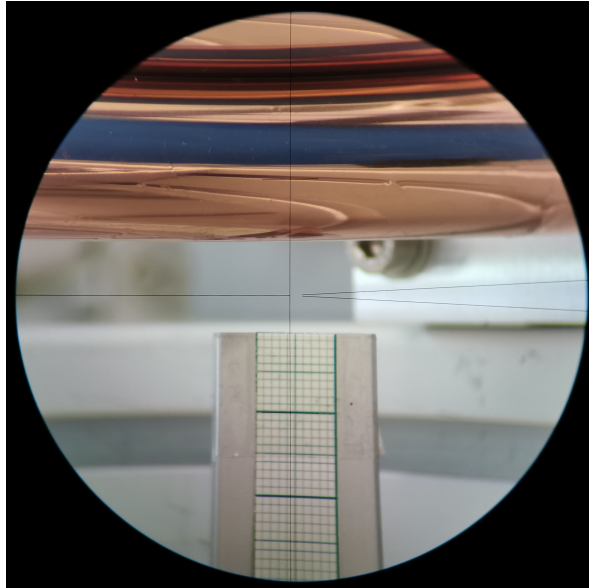


Figure 6.22: View through the optical level's telescope at the millimetre rod and the front bottom straw to measure the sagging.

To analyse the data the open source software package Fiji was used. It is an image analysis package based on ImageJ. More information about Fiji can be found in the addendum B.1. In Fiji, the image was first converted to greyscale, which makes determining the image intensity easier. Afterwards, the grey value was taken along a horizontal line, starting from slightly above the edge of the straw tube to slightly below the 20 mm mark on the measuring rod. In figure 6.23 the greyscale image with the vertical line can be seen, the corresponding grey value profile is depicted in figure 6.24. The grey value profile was exported from Fiji and imported in Matlab for further processing.

Beginning at zero pixels the grey value slightly increases to roughly 156, then sharply decreases to around 130 at 11 pixels before quickly rising to around 174 at 15 pixels. A close inspection shows that these three peaks are caused by reflections on the straw's surface. After these peaks the grey value plateaus at a grey level of approximately 163. The plateau is interrupted by a set of sharp peaks at 249 pixels, where the grey value drops to roughly 33. The beginning of this plateau corresponds to the end of the straw tube, the interrupting peak is caused by the horizontal crosshair of the reticle. After the plateau ends at around 300 pixels the grey value decreases slightly and afterwards peaks to its highest value of 215 at 400 pixels. This

*Fiji stands for 'Fiji is just ImageJ'.*

*In a greyscale image each pixel only carries information about light intensity. In an 8-bit greyscale image this intensity is described by an integer between 0 (black) and 255 (white), also called grey value.*
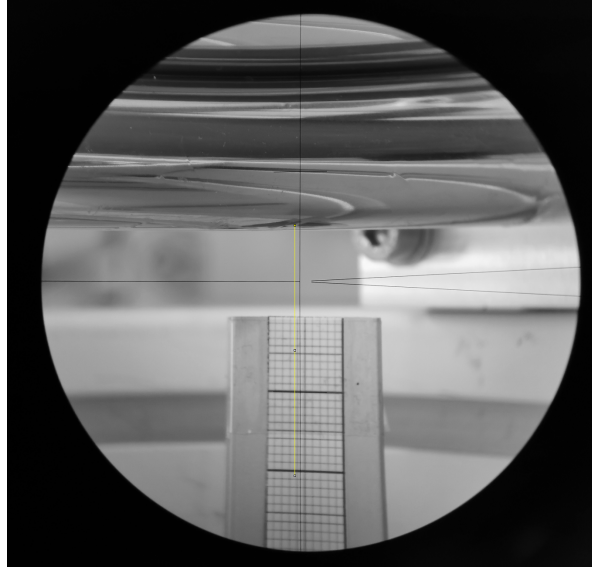
Figure 6.23: The image from figure 6.22 converted to greyscale with the vertical line (yellow) along which the grey value profile was determined using Fiji.
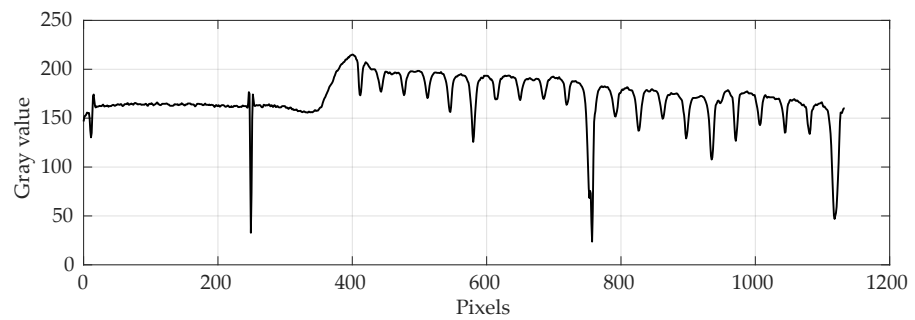


Figure 6.24: The grey value along the vertical line shown in figure 6.23 from top to bottom. The first major peak corresponds to the end of the straw. The second peak is a result of the crosshair's horizontal line. Subsequent peaks are caused by the markings on the millimetre rod.

behaviour is caused by lighter background objects, specifically an aluminium profile behind the measuring rod. Finally, the grey value profile shows 21 equidistant peaks of different heights. Clearly, these peaks correspond to the millimetre markings on the measuring rod. Different peak heights can be explained by uneven line widths and line intensities of the millimetre markings. Over the course of the 21 peaks the average grey value slightly decreases. This is probably caused by the ambient lighting being lower the closer to the bottom of the measuring rod, or it may be caused by shadows.

Making use of Matlab's `peakfind` algorithm the locations of the end of the straw $p_s$, of the horizontal cross-hair, $p_h$, of the zeroth millimetre marking $p_0$ and of the 20$^{th}$ millimetre marking $p_{20}$ were found. The difference $\Delta p_{20-0} = p_{20} - p_0$ corresponds to the pixel equivalent of 20 mm. Using the rule of three, the pixel distance $\Delta p_{s-h} = p_s - p_h$ between the straw and the cross-hair was then converted into a distance in millimetres.

For example, the following peaks were found in figure 6.24: $p_s = 18$ px, $p_h = 249$ px, $p_0 = 412$ px and $p_{20} = 1118$ px. Hence, 20 mm correspond to $\Delta p_{20-0} = 1118$ px $- 412$ px $= 706$ px and thus 1 px $\widehat{=}$ $20/706$ mm. The distance between the straw and the crosshair's horizontal reference line is given by $\Delta p_{s-h} = 249$ px $- 18$ px $= 231$ px. This can now easily be converted into millimetres using the millimetre equivalent of one pixel: 231 px $\widehat{=}$ $231 \cdot 20/706$ mm $\simeq 6.544$ mm.

The same procedure was used for all images that were taken. The results for the distance between the horizontal reticule and the straw are depicted in figure 6.25 with a '×' sign. As expected, the distance between the straw and the horizontal reticule is larger in the middle and smaller at either ends of the straw tube. However, a slight asymmetry can be seen. Whereas the distance between the straw and the cross-hair is approximately 5.54 mm at 50 cm, it is around 6.54 mm at 503.7 cm. This is caused by the right side of the straw being slightly higher than the left side of the straw – most likely due to the mounting frame being not perfectly levelled.

To calculate the sagging of the straw tube its theoretical behaviour without sagging was calculated. This is simply given by a straight line through the two points nearest to the endplates, i.e the ones at 50 cm and 503.7 cm. This line was calculated to approximately have the form $y(x) = 1.89 \cdot 10^{-4}\, x + 5.53$ where $y(x)$ is the distance between the straw and the reticule at the position $x$ along the straw. It is shown in figure 6.25 as a dashed line. The sagging can then be determined by calculating the difference between the value of this linear equation and the measured distance between straw and crosshair at each position along the straw. In figure 6.25 this is depicted as vertical dotted lines. The corresponding values for the sagging are given to the right of each line.
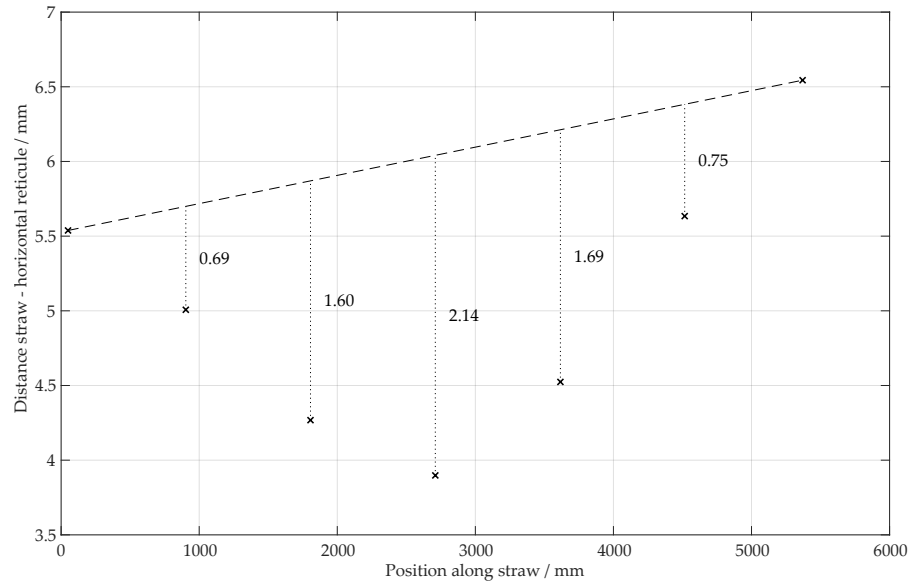
Figure 6.25: The distance between the straw and the horizontal line of the cross-hair at seven different locations. The dashed line through the first and last point shows the location of the straw without sagging. The differences between the measurement and this line, shown as vertical dotted lines, is the straw sagging. It is given as a number to the right of each dotted line. The maximum sagging of 2.1 mm is in good agreement with the expected value.

The sagging follows the expected behaviour. The maximum sagging of 2.14 mm is located in the middle of the straw. It is around 12.4 % larger than the expected sagging assuming the literary value for the modulus of elasticity and around 7.5 percent less than the expected sagging assuming the measured modulus of elasticity – see section 6.6.1. Towards either side of the straw the sagging decreases as expected. All in all, the measurement of the straw's sagging shows the expected form and gives values that are within the expected range.

One major source of error in this measurement is the fact that it heavily relies on images that are taken through the level's telescope using a smartphone camera. This process of image taking can distort and thus adulterate the measurement results. Naturally, the optics of the level themselves can also cause distortions although this effect is basically negligible due to the optic's high quality. Furthermore, this measurement relies on the millimetre paper, where imperfections can also falsify the results. Moreover, the location of the millimetre rod under the straws has to be considered. The nearer the millimetre rod is towards the optical level, the larger it appears and thus each millimetre is equivalent to a larger number of pixels. Assuming a 20 mm section of the millimetre rod placed under the straw is located roughly 5 mm nearer to the level and using the minimum distance between the level and the straws of 1920 mm from figure 6.19, a simple calculation using the theorem of intersecting lines indicates that the

20 mm would then appear as 20.05 mm – an effect of 0.25 %. Lastly, it has to be noted that determining the sagging relies on the line fitted through the first and last points. Ideally these points would have to be exactly at the endplates, however no measurements could be taken right next to the endplate due to parts of the mounting frame being within the line of sight of the optical level. Thus, they are 50 mm away from the endplates which introduces a small systematic error.

## 6.6 SAGGING OF THE WIRES

To gain knowledge about the net wire displacement not only the sagging of the straws but also the sagging of the wires has to be measured. However, measuring the wire's sagging is much more difficult as it is located inside the straw tube and thus not directly visible. A non-optical method to measure the wire sagging is to use sophisticated resonance systems where the wire is made to oscillate. The resulting oscillation displays a resonance at the wire's natural frequency from which the sagging can be derived. General information about this method can be found in [Sau18; RRB08] and in particular in [Gar+19]. However, a different technique was used within this thesis. At CERN, the wire of a straw tube was successfully determined using an optical method – see [Daniil'sPaper]. Since straw tubes are only made of 36 μm thick Mylar they can appear translucent – assuming a strong enough light source is placed behind them. At CERN, a straw's anode wire sagging was measured using a set of LEDs placed behind a straw tube and an optical microscope placed in front of the straw. This and another method were used to measure the wire sagging within this thesis and are described in this section after a brief outline of the expected sagging and the design of the required LED system.

### 6.6.1 *Expected sagging*

The formula for the wire sagging $s$ was originally introduced in section 4.2.2 – see equation (4.40). For a wire with a 45 μm radius, a length of $L_0 = 5.36$ m, a density $\rho = 19\,250$ kg m$^{-3}$ and a cross-section of $\sigma = 3.18 \times 10^{-9}$ m$^2$ the sagging is given by

$$s = \frac{\rho g \sigma L_0^2}{8T} \tag{6.11}$$

Here, $T = 1.77$ N is the tensioning force equivalent to a mass of 180 g. This gives for the expected sagging:

$$s = 0.61 \text{ mm}. \tag{6.12}$$

For the thinner ∅30 μm wire the expected sagging is similar, since the tensioning force was adapted accordingly – see section 6.4.1.

### 6.6.2  *Design of the LED system*

The LEDs are required to shine enough light through the straw tubes so that the wire becomes clearly visible. To do so, the main requirements for the LEDs were their maximum brightness, form factor and their cost. While high-power LEDs with more than 9000 lm such as Cree's XLamp CXA3070 [Inc18] are becoming increasingly available on the market, they are larger than a single straw in form factor with a package size of 27.35 mm × 27.35 mm meaning that some of the light may shine around the straw tube directly into the microscope, perhaps leading to overexposure of certain image parts or other artefacts caused by reflections on the straws. The LEDs that were chosen are five of OSRAM's DURIS S10 (type GWP7LM32.EM-QTRP-XX57-1) series surface mount (SMD) LEDs [18] on a preassembled PCB (called 'PowerStar') manufactured by Intelligent LED Solutions (ILS) [ILS16]. This alleviates the need and cost required for a custom-made PCB. These LEDs each have a luminous flux of 1210 lm and come in a small package with a 7 mm × 7 mm footprint. More technical specifications are given in table 6.2.

Table 6.2: Technical specifications of the used DURIS S10 series LEDs. The data is taken from [18].

| Parameter | Symbol | Value | Unit |
|---|---|---|---|
| Luminous flux | $\Phi_V$ | 1210 | °C |
| Colour temperature | $C$ | 3000 | K |
| Operating temperature | $T_{op}$ | −40...110 | °C |
| Junction temperature | $T_j$ | 125 | °C |
| Forward voltage (typ.) | $V_F$ | 28.4 | V |
| Forward current at $V_F$ | $I_F$ | 0.3 | A |

While, according to ILS's datasheet, the PowerStars ensure that the LEDs operate under the recommended maximum junction temperature $T_{j,max}$ early tests indicated that additional cooling may be required as after a few minutes smoke started to develop with the back side of the PowerStars reaching up to 115 °C (measured with an infrared thermometer). Closer investigations revealed that the smoke development was caused by melting solder flux and not the LED itself – for security reasons however, a cooling solution was designed.

*Heat sink choice*

The exact analytical determination of a required heat sink is a highly complex topic depending, amongst other factors, on the required power dissipation, the heat sink's type, its material and orientation, thermal transfer materials and operating conditions – for example the ambient air temperature – as well as active or passive air flow. Due to

this complexity the analytical determination of the LED heat sink was only done roughly within this thesis.

In order to determine the required heat sink its required key characteristic, the thermal resistance, has to be determined. The thermal resistance given in Kelvin per Watt is a heat property and describes an object's resistance to heat flow across a temperature gradient. In analogy to Ohm's law, it is defined by

$$R_\theta = \frac{\Delta T}{q} \tag{6.13}$$

where $\Delta T$ denotes the temperature difference and $q$ the heat flux. To determine the required $R_\theta$ of the heat sink the thermal model shown in figure 6.26 is assumed. Here, the LED junction – the part
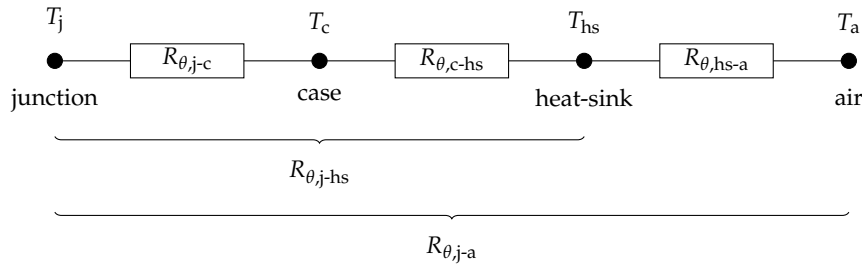


Figure 6.26: The thermal model assumed for heat sink calculation. It consist of the junction connected to the case which dissipates the heat via a heat-sink to the air. Between each entity the heat transfer is affected by thermal resistance $R_\theta$.

creating the heat – with temperature $T_j$ is connected to its casing with temperature $T_c$ – the PowerStar – which is then connected to the heat sink with temperature $T_{hs}$ dissipating the heat to the air of temperature $T_a$. Between the junction and the case there is a thermal resistance of $R_{\theta,\text{j-c}}$, given by the manufacturer of the LED. Similarly, $R_{\theta,\text{c-hs}}$ is the resistance between the case and the heat sink, and $R_{\theta,\text{hs-a}}$ is the resistance between the heat sink and the air, which depends on the heat sink. This is the value that needs to be determined.

Let $R_{\theta,\text{j-a}}$ be the total resistance between the junction and the ambient air and $R_{\theta,\text{j-hs}}$ the resistance between the junction and the heat sink. Since the combination of thermal resistances follows the same laws as the combination of electrical resistances, the aforementioned total resistances are given by

$$R_{\theta,\text{j-a}} = R_{\theta,\text{j-hs}} + R_{\theta,\text{hs-a}}, \tag{6.14}$$

where

$$R_{\theta,\text{j-hs}} = R_{\theta,\text{j-c}} + R_{\theta,\text{c-hs}}. \tag{6.15}$$

Using the definition of the thermal resistance from equation (6.13), $R_{\theta,\text{j-a}}$ can also be written as

$$R_{\theta,\text{j-a}} = \frac{\Delta T}{P} = \frac{T_j - T_a}{P}, \tag{6.16}$$

where $P = \eta V_F I_F$ specifies the LEDs' power loss resulting from their efficiency $\eta < 1$. The quantities $V_F$ and $I_F$ are the forward voltage and current of the LED and are given in table 6.2. Substituting this relation into equation (6.14) and solving for $R_{\theta,hs\text{-}a}$ gives

$$R_{\theta,hs\text{-}a} = \frac{T_j - T_a}{P} - R_{\theta,j\text{-}hs}. \tag{6.17}$$

For multiple LEDs the resistance $R_{\theta,j\text{-}a}$ from equation (6.15) is a parallel circuit of resistances given by

$$\frac{1}{R_{\theta,j\text{-}a}} = \sum_i \frac{1}{R_{\theta,j\text{-}c,i} + R_{\theta,c\text{-}hs,i}}. \tag{6.18}$$

Assuming the same conditions and values for the five used LEDs, equation (6.17) finally reads

$$R_{\theta,hs\text{-}a} = \frac{T_j - T_a}{P} - \frac{R_{\theta,j\text{-}c} + R_{\theta,c\text{-}hs}}{5}. \tag{6.19}$$

The thermal resistance $R_{\theta,c-hs}$ depends on the thermal interface material – TIM in short – applied between the LEDs' cases and the heat sink. Assuming the layer of TIM is a homogeneous body with a thickness $d$ and a cross-section of $A$ the thermal resistance between the case and the heat sink can be calculated using

$$R_{\theta,c\text{-}hs} = \frac{d}{\lambda A}. \tag{6.20}$$

Here, $\lambda$ is the thermal conductivity and a material property. The thermal interface chosen was Electrolube's HTC (heat transfer compound), a silicon-free general-purpose thermal interface paste featuring a thermal conductivity of $0.9\,\mathrm{W\,m^{-1}\,K^{-1}}$ [Ele19]. Using the surface area of a single PowerStar of $A = 285\,\mathrm{mm^2}$ and assuming a typical value for the thickness of the TIM layer of $d = 0.05\,\mathrm{mm}$ gives

$$R_{\theta,c\text{-}hs} \simeq 0.19\,\mathrm{K\,W^{-1}}. \tag{6.21}$$

With $T_j = 125\,°\mathrm{C}$, $T_a = 40\,°\mathrm{C}$, $P = 35\,\mathrm{W}$ and $R_{\theta,j\text{-}c} = 1.4\,\mathrm{K\,W^{-1}}$ ultimately gives from equation (6.19):

$$R_{\theta,hs\text{-}a} \simeq 2.11\,\mathrm{K\,W^{-1}}. \tag{6.22}$$

Hence, the required heat sink needs to have a thermal resistance *lower* than $2.11\,\mathrm{K\,W^{-1}}$ to ensure adequate cooling performance.

The chosen heat sink is a pair of extruded aluminium heat sinks (type SK 48 75 SA) manufactured by Fischer Elektronik that are mainly designed to be used for SSR-3 and TO-3 packages. Each heat sink has outer dimensions of $75\,\mathrm{mm} \times 65\,\mathrm{mm} \times 20\,\mathrm{mm}$ (length $\times$ width $\times$ height) [19a]. The two heat sinks used together result in a total length of 150 mm, so that the thermal resistance – assuming a perfect connection between the two heat sinks – amounts to:

*SSR-3 is a standard for solid-state relays. TO-3 is a standardised metal semiconductor package often used for transistors.*

$$R_{\theta,hs\text{-}a} \simeq 2\,\mathrm{K\,W^{-1}}. \tag{6.23}$$

*Design, CAD-integration and simulation results*

To minimise potentially costly design changes a complete CAD model of the LED system was designed using Autodesk's Fusion 360 prior to construction. Figure 6.27 shows a 3D rendering of the CAD-model. The LEDs are mounted on a 2 mm thick aluminium base plate with
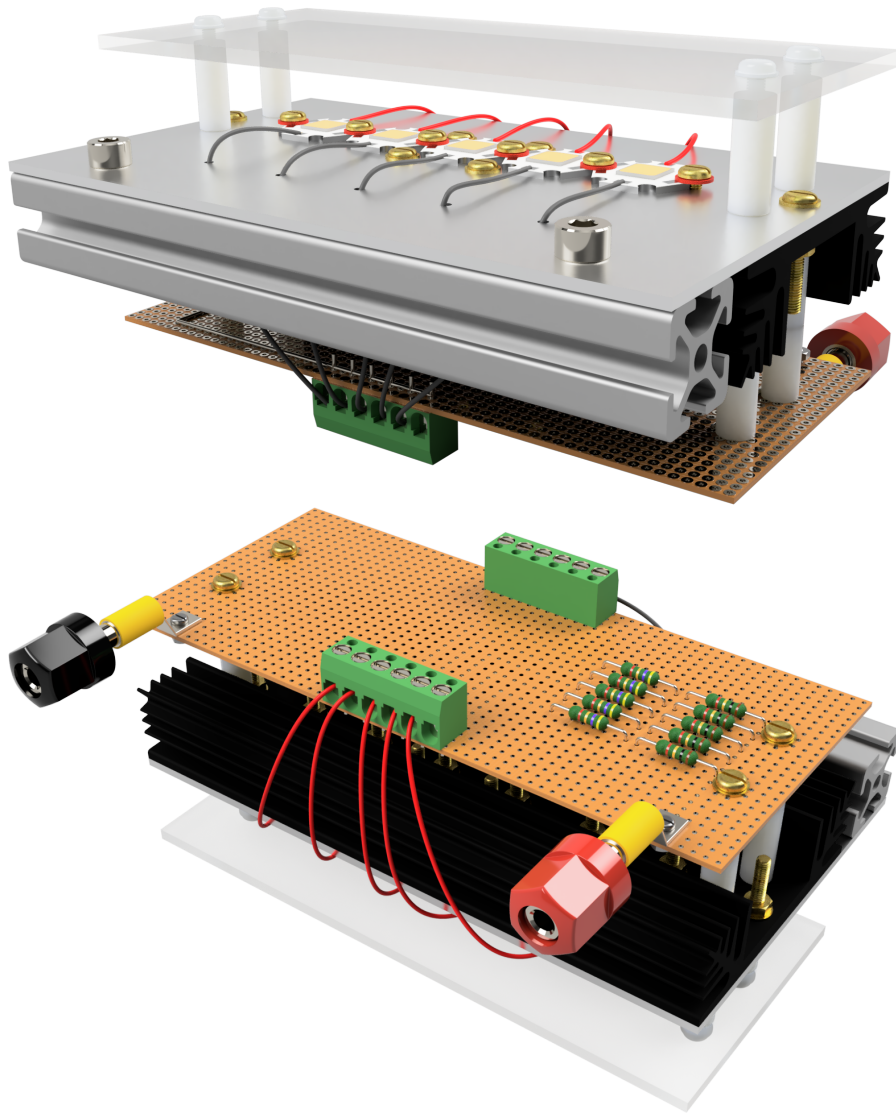


Figure 6.27: Renderings of the LED system from two sides. The LEDs are mounted on a base plate on which the heatsinks and a mounting rail are installed. The electric circuit is soldered to a veroboard mounted to the heatsink using nylon spacers. A diffuser plate diffuses the light of the LEDs.

outer dimension of 90 × 150 mm using regular M3 screws with heat-resistant paper washers. Six M3 bolts connect the two heat sinks to the base plate. An extruded aluminium profile acts as a mounting rail and is connected to the base-plate using M5 screws. Five small holes in the baseplate allow the power wires of the LEDs to pass through it.

The electronics for the LEDs are located on a PCB that is mounted to the heat sink using plastic standoffs. The circuit diagram of the LED system is shown in figure 6.28. Above the LEDs a plexiglass diffuser
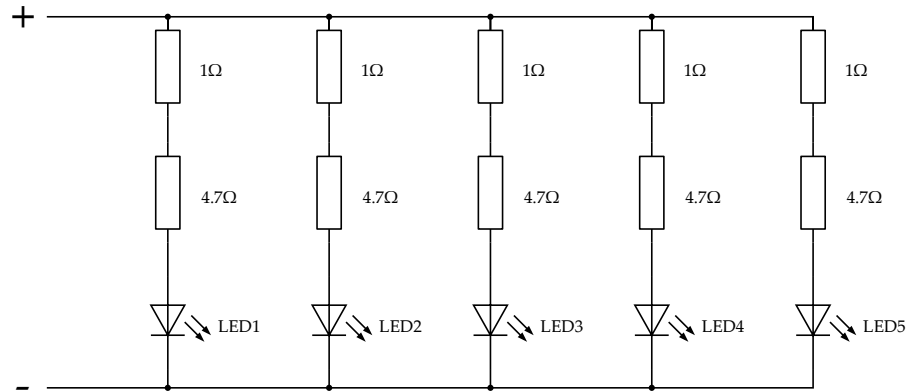


Figure 6.28: Circuit diagram of the LED system. Each of the LEDs has two dropping resistors with a total resistance of 5.7 Ω so that a 30 V power supply can be used.

*Plexiglass is a tradename for Poly(methyl methacrylate) – PMMA in short*

plate is mounted using nylon screws and standoffs. In the final LED system two different diffuser plates were used with a transparency of 92 % and 70 % respectively. While this reduces the total light output by 62 % this combination was found to diffuse the light sufficiently to alleviate overexposed spots on the microscope images. The LED system is powered using a Zentro Elektronik LA30/5GA adjustable power supply operated at 30 V.

Based on this CAD model thermal simulations using the finite element method were performed to validate the cooling system. To minimise computational cost the 3D model was simplified to only include the thermally relevant parts. In the simulation, each LED puts out 5 W of heat. The thermal resistances between the junction, case and heat sink were included in the simulation. The ambient temperature was assumed to be 20 °C. Figure 6.29 shows the results of the simulation. It shows that the hottest LED, the one in the middle, reaches a temperature of 62 °C with its PowerStar reaching temperatures between 53 °C to 59 °C. The aluminium baseplate and the heat sink reach temperatures between 52 °C to 54 °C. All values are much lower than the 115 °C measured earlier before the cooling system was installed.

To validate the simulation results a circuit for a single DS18B20 temperature sensor was added to the PCB for the LEDs and read out using an Arduino microcontroller. More information about the DS18B20 and Arduinos can be found in [Kai16]. The temperature sensor was attached to the heat sink using an adhesive thermal pad.
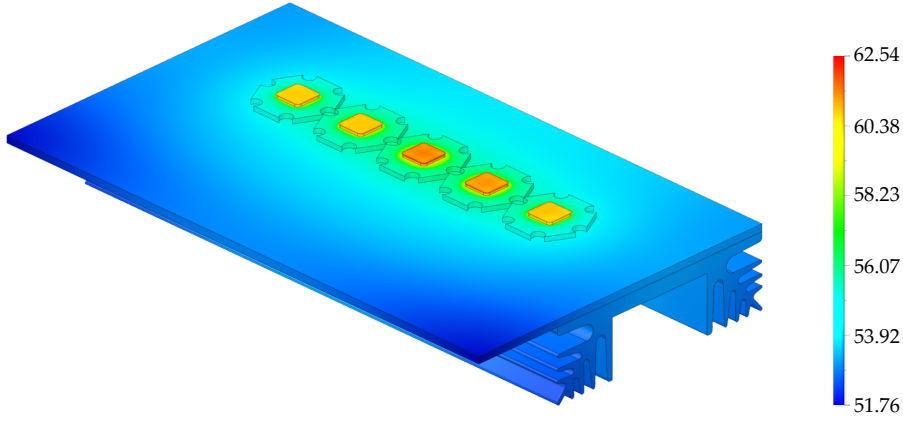
Figure 6.29: Results of a thermal FEM-analysis of the LEDs' cooling system. The colourscale indicates the temperature in degrees Celsius. To simplify the simulation only the LEDs on their PowerStars, the baseplate and the heatsink were considered. Each LED has a power loss of 5 W. In the simulation the hottest LED reaches a temperature of 62.5 °C, the heatsink reaches temperatures around 52 °C. The simulation is in good agreement with measurements.

The temperature curve is shown in figure 6.30. A fitted exponential function of the form $T(t) = T_{\mathrm{max}} - \Delta T \exp\left(-\frac{t}{\tau}\right)$ results in

$$T(t) = 55.63\,°\mathrm{C} - 34.23\,°\mathrm{C} \exp\left(\frac{-t}{344.83\,\mathrm{s}}\right). \qquad (6.24)$$

This indicates a maximum temperature of $(55.63 \pm 0.01)\,°\mathrm{C}$ after a temperature increase of $(34.23 \pm 0.04)\,°\mathrm{C}$. Thus, the ambient temperature lies at $(21.40 \pm 0.05)\,°\mathrm{C}$. Correcting the maximum temperature to an ambient temperature of 20 °C gives a maximum temperature of $(54.23 \pm 0.05)\,°\mathrm{C}$ on the heat sink. According to the simulation, the temperature of the heat sink at the point where the sensor was placed should have a temperature of 54.6 °C. The measured value deviates by less than 1 % from the simulation result. A direct measurement of the LED using the sensor was not performed since the LEDs are highly fragile. A measurement performed with an infrared thermometer was within 10 % simulation result.

### 6.6.3  *Microscope method*

Using the LED system described in the previous section the wire sagging was measured in two different ways. The first method was based on an optical microscope and done very similar to XXX (Daniils paper). The optical microscope was placed in front of the straws and used to take accurate images of the straw tube and the wire. For the microscope, the DINO-LITE AM7515MZT - Edge was chosen, featuring a resolution of five megapixels and an adjustable optical

*A resolution of five mega-pixels corresponds in this case to a 2592× 1944 pixel image*
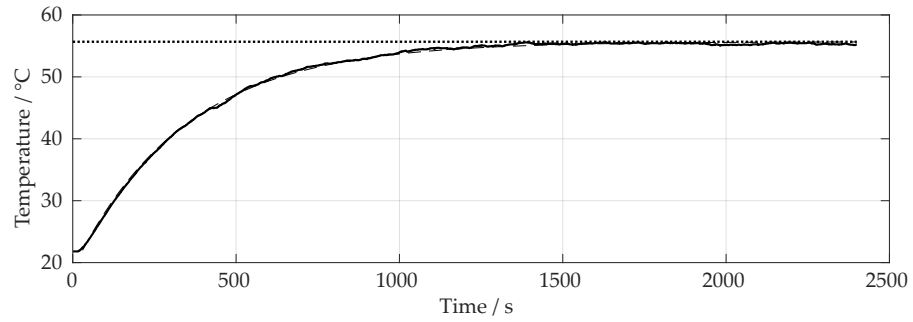
Figure 6.30: Temperature curve of the heat sink measured using a DS18B20 temperature sensor read out by an Arduino microcontroller. An exponential fit (dashed line) indicates a temperature increase by 34.23 °C up to a maximum temperature of 55.63 °C. The results are in good agreement with the simulation.

zoom from 20 to 220 times [19b]. Additionally the AM7515MZT has eight white LEDs built in, which, however, were not used in this setup.

*Measurement setup*

To measure the wire sagging the LED-system was mounted on two 2 cm × 2 cm aluminium profiles which were then installed on an additional aluminium profile which was added to the mounting frame. The LED system was placed as close to the straws as possible without touching them.

In order to mount the microscope a special microscope holder was designed. It is shown in figure 6.31.

This holder originally was planned to be a 2-axes holder for a radioactive source, but was re-purposed to hold the microscope with free adjustment capabilities in three axes (along the straw, in height and in distance to the straws). The holder consists of a base plate which allows it to be installed on the main mounting frame. A 15 cm long 5 cm × 5 cm vertical aluminium profile is screwed on to the top of the base plate. An M5 threaded rod runs inside one of the profile's notches and attaches an aluminium mounting angle to the profile. At the top, a knurled head thumb screw is fixed to the rod. Turning this screw allows the mounting angle to be adjusted in height. This mounting angle is equipped at the bottom with a small extension piece which was originally designed to hold a radioactive source, but is immaterial for the microscope. Instead, on top of the mounting angle half of a 15 cm long 5 cm × 5 cm long aluminium profile is located. Here, too, a knurled head thumb screw is fixed to an M5 threaded rod running inside the profile's groove. That way, a sledge, which is attached to the rod, can be moved towards and away from the straw tubes. This allows to adjust the focus of the microscope, although only very coarsely. The sledge has a thin aluminium mounting clip which holds the microscope securely in place. In order to prevent damage
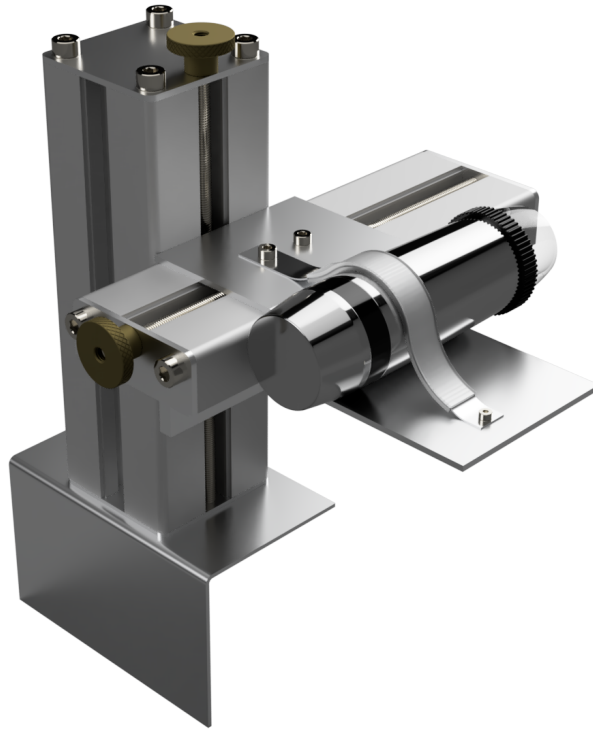
Figure 6.31: Three-axis holder for the DinoLite digital microscope. The micro-
scope can be moved up and down as well as towards and away
from the straw using thumb screws. The holder is designed to
be installed to the mounting frame so that it can be slid along
the straw.

to the microscope a piece of heat-shrink tubing was put over the clip
to provide some cushioning. The complete setup of the microscope
holder, the quad-straw prototype and the LED system is shown in
figure 6.32.

*Methodology*

First, the optical microscope was calibrated using its supplied auto-
calibration target. The LED system and the optical microscope were
placed at five different locations along the straw tube. At each loca-
tion an image of the bottom front (30 µm wire) and top back straw
(45 µm wire) was taken. An example image can be seen in figure
6.33 In order to be able to see the wires clearly the gaps between
the LEDs and the diffuser plate were taped with black masking tape.
Additionally, a special, non-reflective black cloth was placed on the
tables holding the main mounting frame (not shown in figure 6.32).
Also, the laboratory lights were turned off and the window blinds
closed. This reduced reflections on the straw tubes due to scattered
light significantly. Moreover, the shutter speed of the microscope was
manually adjusted to an appropriate level.
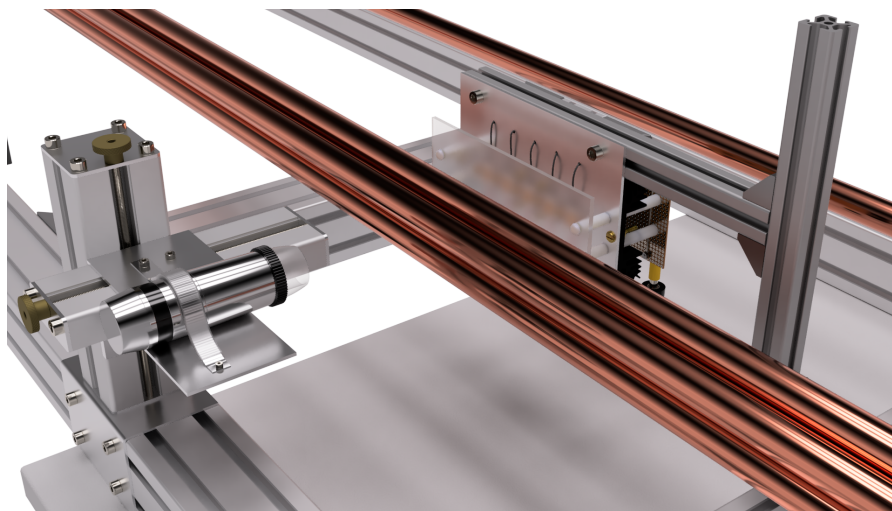
Figure 6.32: Image of the setup used to measure the wire's sagging with the microscope. The LED system is closely placed behind the straws. The microscope is mounted in the microscope holder and located in front of the straws.
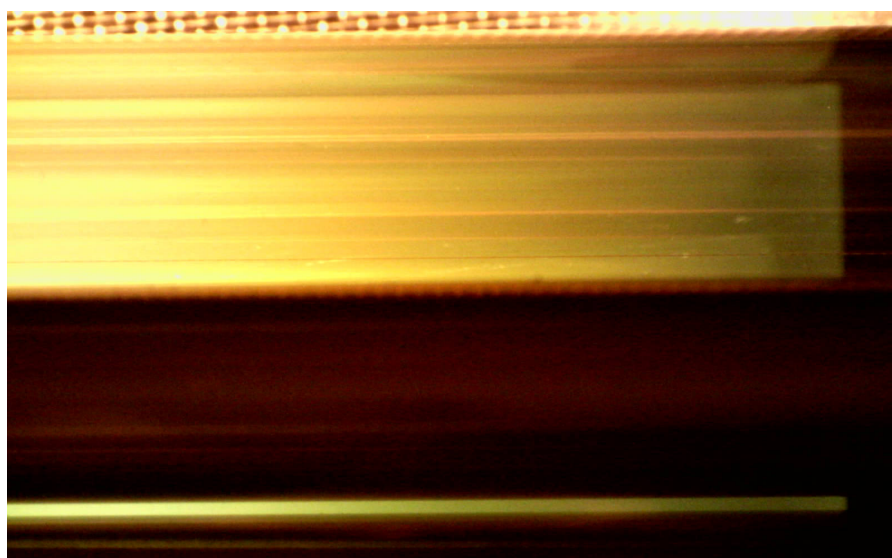


Figure 6.33: Image of the anode wire taken with the digital microscope. The wire can be seen in the middle of the image as a faint, black line.

Although these measures proved to be highly effective to increase the visibility of the anode wire, at some locations the wire still remained indiscernible. This was mostly due to the overlapping layout of the straw tubes. For example, the bottom front straw has an overlap with the lower half of the bottom back straw. In some cases, this overlap prevented the wire from being clearly visible. In these cases, the overlapping straws were slightly moved out of the way by hand. Special care was taken not to move the straw tube that was currently imaged.

Each image was afterwards analysed using the DinoLite software package. In theory, the distance between the wire and the straw tube's wall can be directly determined using this software package. However, this is only possible for a specific calibration profile that is only valid in a small range of magnification. Since the focus of the microscope is changed by adjusting the magnification, and for each measurement the focus had to be changed slightly, a new calibration would have been required for each single measurement. However, this could not be done because calibrating the microscope at exactly the correct magnification would have required a very precise mechanism allowing to accurately adjust the distance to the calibration target – and thus the focus. Hence, measuring the distance between the anode wire and the straw tube using the DinoLite software gave unrealistic results. For example, on one image the straw tube was measured to have a diameter of 27 mm instead of the expected 20 mm.

Thus, a similar method as described in section 6.5 using Fiji was used. First, the vertical grey value profile of the straw was determined. Afterwards, the distances in pixels between the wire to the bottom wall of the straw as well as the distance between the two walls of the straw tube were determined. Assuming that the latter distance in pixels corresponds to exactly 20 mm, the pixel distance between the wire and the wall can easily be converted into a distance in mm. To determine the sagging of the wire, the distances were then correlated with the results of the straw sagging from section 6.5.

*Results*

The methodology was applied to all five images that were taken per straw. The measurement results, which are illustrated in figure 6.34, show an unexpected behaviour. For the $\varnothing 30\,\mu m$ wire the maximum sagging is indeed located in the middle of the straw where it is expected. However, the value of around $-1.34\,mm$ is more than twice as high as the expected sagging. Moreover, the minimum sagging of around $-0.5\,mm$ is not located near the ends of the straw tube but rather at 1806 mm. At the ends of the straws the sagging lies between 0.7 mm on the one end and 0.9 mm at the other end.

The sagging behaviour of the $\varnothing 45\,\mu m$ also shows an unexpected behaviour. Here, the maximum sagging of $-1.78\,mm$ is located at the
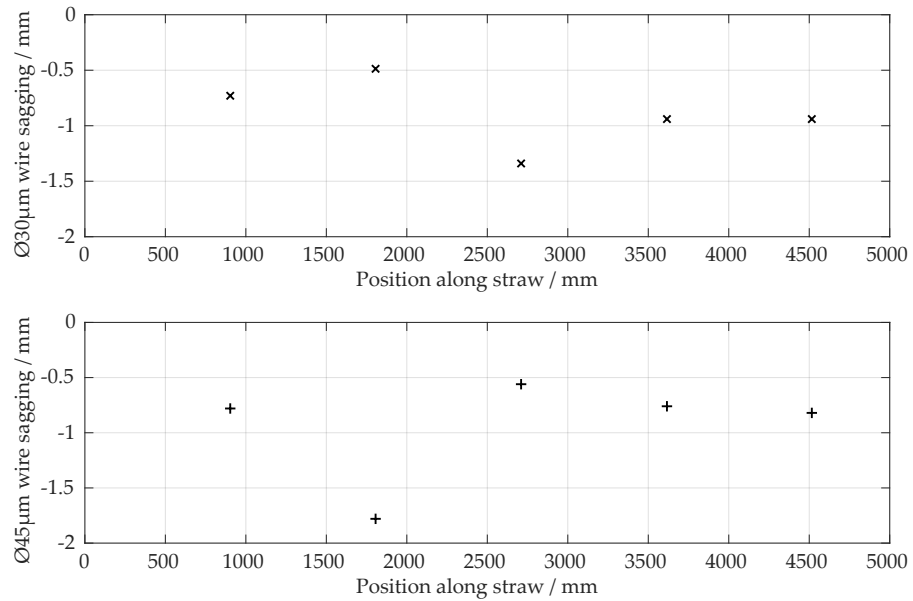
Figure 6.34: Measurement results for the sagging of two wires with diameters of 30 µm (top) and 45 µm (bottom). The images do not show the expected behaviour as no clear curve where the maximum sagging is in the middle of the straw can be seen.

1806 mm position and the minimum sagging of $-0.56$ mm is located exactly in the middle of the straw. The remaining values for the sagging range between 0.76 mm and 0.82 mm.

In general, both measurements do not show the expected sagging behaviour close to a catenary curve. Moreover, the maximum sagging values in both measurements are more than twice as high as expected. In fact, almost all values – except for the minimum ones in each measurement – are larger than the maximum expected sagging.

There are several reasons which may have caused this behaviour. First and foremost the possibility of a wrong feature identification – feature meaning the anode wire and the straw tube ends – on the microscope images are a source of error. Especially the identification of the straw tube ends was – at least in some cases – not as clear as necessary. This was mostly due to reflections and the resulting over- or underexposure of the images near the straw's ends. An imperfect focus, resulting in a blurry image, can further increase the error on the feature identification. Secondly, imperfect manufacturing of the microscope holder caused the microscope arm to have significant backlash. Due to this backlash the microscope could have been slightly angled in some cases which may have contributed to the errors. Thirdly, the method using the microscope relies heavily on the fact that the straw tube has at all positions a radius of exactly 20 mm. However, this is not the case as can be seen in figure 6.35. In theory, the outsides of the straw tubes should at all points touch each other due to the design of the endplates. Yet, figure 6.35 clearly shows a significant

distance between two straw tubes, indicating that the straws do not maintain a perfect circular cross section but are rather elliptical – at least at some points. This may be caused by the sagging of the straw or torsions which may have been induced during the installation of the straws to the endplates. These variable cross sections of the tubes are another source of error in the wire sagging measurement using the microscope. Lastly, at some locations the overlapping straws had to be supported to reduce the overlap and thus make the wire visible on the microscope. This process may have also affected the location and/or shape of the studied straw and thus induced another error.
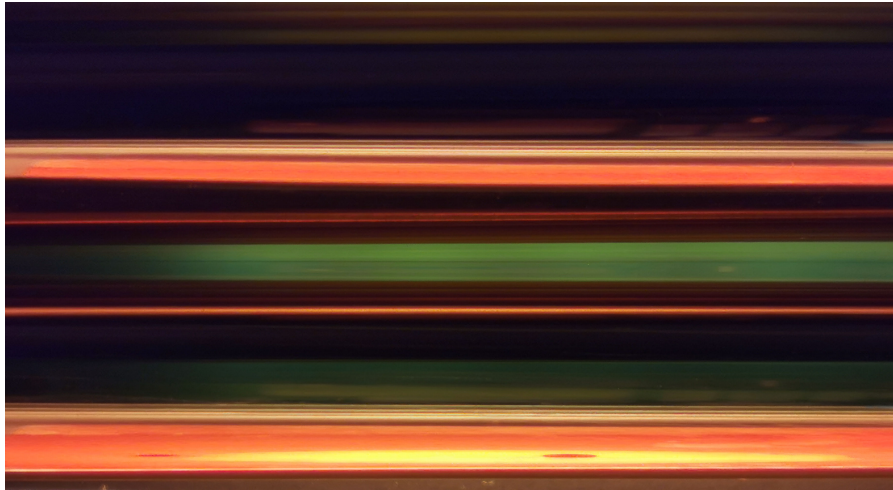


Figure 6.35: A microscope image showing a significant distance between two straw tubes (green area in the middle of the image). This is likely caused due to the straw tubes not having a perfect circular cross section all the way along the length. One reason for this may be a slight torsion that was induced during the installation of the straw.

### 6.6.4  *Optical level method*

The results obtained with the microscope proved to be inconsistent and unrealistic. Thus, the wire sagging was also determined using the Nikon AS-2C optical level.

*Methodology*

This method was very similar to the measurement of the sagging of the straw tubes but still utilised the LED system. Again, the LED system was placed behind the straws at a very small distance. Under the straws, another aluminium profile was installed as a cross brace. A short section of a $2\,\text{cm} \times 2\,\text{cm}$ aluminium profile with a millimetre scale was placed on the cross brace, similar to figure 6.21. Using the optical level introduced in section 6.5 the bottom front straw as

well as part of the millimetre scale were then observed. To make the wire clearly visible, similar measures to the ones described in the previous section were taken. Again, overlapping straws were carefully supported at certain locations to minimise the overlap.

At seven different locations images through the optical level's telescope were taken using a smartphone camera. An example image is shown in figure 6.36. Using Fiji the distance between the wire and the horizontal reticule was then calculated using the millimetre scale. This was done in precisely the same way used to measure the sagging of the straw tubes – see section 6.5.
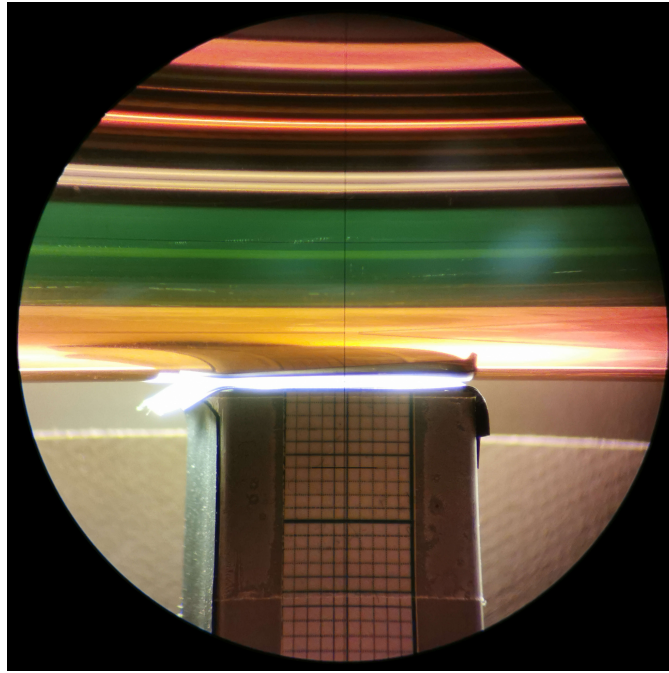


Figure 6.36: View through the optical level's telescope at the millimetre rod and the front bottom straw's wire to measure the sagging.

*Results*

The results of the measurement are shown in figure 6.37. The maximum sagging of 0.58 mm, which is 0.05 mm or roughly 8 % lower than the expected sagging, is located in the middle of the straw. Towards either end of the straw the sagging decreases continually, with one exception at the 4516 mm position where the sagging is lower than at both adjacent positions. In general though, the measurement using the optical level yields a clear catenary curve with results in the expected range. Possible sources of error in this measurement are similar to the ones outlined in section 6.5.
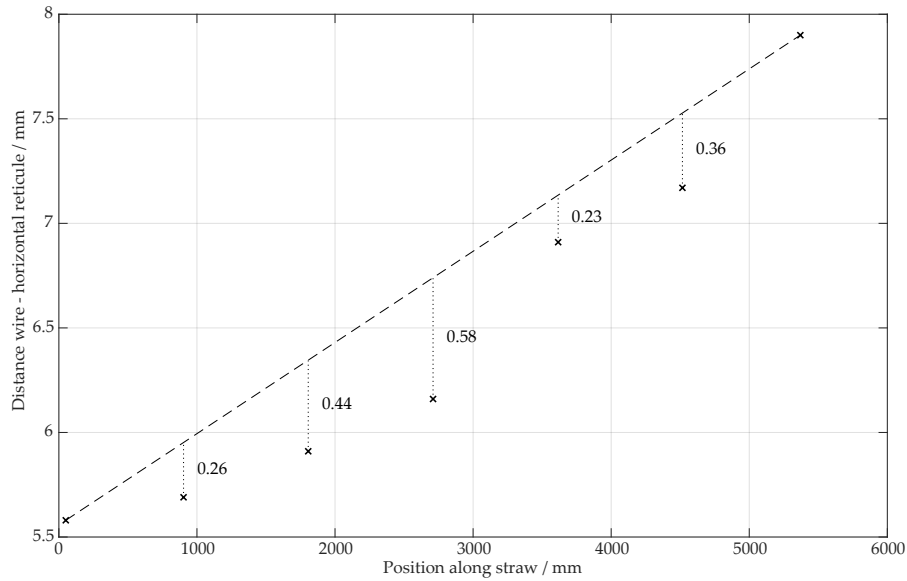
Figure 6.37: The distance between the $\varnothing 30\,\mu$m wire and the horizontal line of the cross-hair at seven different locations. The dashed line through the first and last point shows the location of the wire without sagging. The differences between the measurement and this line, shown as vertical dotted lines, is the wire sagging. It is given as a number to the right of each dotted line. The maximum sagging of 0.58 mm is in good agreement with the expected value.

## 6.7 SUMMARY AND OUTLOOK

The quad-straw prototype was designed to test the mechanical parts proposed for the SHiP Spectrometer Straw Tracker. It consists of several different parts which were outlined in section 6.3. Most of these parts were assembled successfully. However, during the assembly several minor, but considerable issues with the design became apparent.

Firstly, the straw endpieces, originally outlined in section 6.3.2 had to be modified to ensure an adequate electrical contact. To do so, a spiral spring was placed in the groove originally intended to serve as a glue barrier. The method of holding the spiral spring in the groove using a wire inlay has to be reconsidered, as the sharp ends of the wire can severely damage, or, in the worst case, puncture the straw tube. Other methods of holding the spiral spring are currently under study. Furthermore, the groove for the spring has to be made slightly deeper, as the current dimensions lead to the springs protruding out of the groove and thus result in the straws bulging around the spring.

Another aspect that requires changes is the way in which the anode wires are installed in the straw tubes. In the assembly process the wires were fed through the straws after the straw endpieces were glued in. This meant that the wire had to be meticulously fished out of the straw

and through the endpieces using a small wire hook. By feeding the wires through the straws before installing the endpieces this process may be simplified significantly. Moreover, the method of feeding the wires through the straws has to be reconsidered. During the assembly, this was done by using a magnet and a magnetic nut to which the wire was tied. This process resulted in considerable visible damage to the straws' outside but also to their inner coatings – see also chapter 7. Other methods of feeding the wires through the straws must be considered. One way could be to attach the wire to a special chute and then use air pressure to blow the chute – and thus the wire – through the straw. This technique was used for OPERA's drift-tubes, however its suitability for straw tubes is not yet determined. Another option could be to stand the straws up vertically and afterwards feed the wires through them using gravity. However, the process of positioning the straw vertically may cause kinks and requires a clean room with a height of more than 5 m. One other viable option could be to maintain the technique using the magnet but to wrap the magnet in a soft material such as cloth that is unlikely to cause significant scratches to the coating. In that case though, the possibility and effect of the wrapping leaving some residue such as lint inside the straw tube must be considered. Finally, a rolling sledge as shown in figure 6.38 might be used. It is a small, roughly 60 mm long part with two sets of six circularly arranged wheels at either end. These wheels consist of soft, readily available 4 mm × 1.5 mm precision O-rings. They are located so that the whole sledge has a diameter of 20 mm and fits snugly into a straw tube. The base of the sledge consists of various identical parts that are circularly arranged, held together by small, glued in metal studs, and designed to be easily 3D-printable. The complete sledge is hollow in the middle so that the wire can be fed through it and be attached at the front of the sledge. Using a magnetic ring the sledge can the be pulled through the straw tube. The fact that the sledge has wheels means that, in theory, no damages due to scraping should occur.

Furthermore, the anode wire holders from section 6.3.4 need a revision. Due to their design they fit quite loosely inside the endplates, although this is much improved after the wire is installed due to the pulling force. Furthermore, feeding the wire through these parts proved to be a mechanical puzzle, mostly due to the manufacturing process and imperfections left by it. This may be resolved by either polishing the inside of the parts or by changing the manufacturing process to injection moulding. Alternatively, the part may be made out of two halves which are somehow bonded together after the wire is fed through. Possible changes to this part are currently investigated. In any case the manufacturing process of all the parts has to be reconsidered for the final SST due to the large number of parts required.
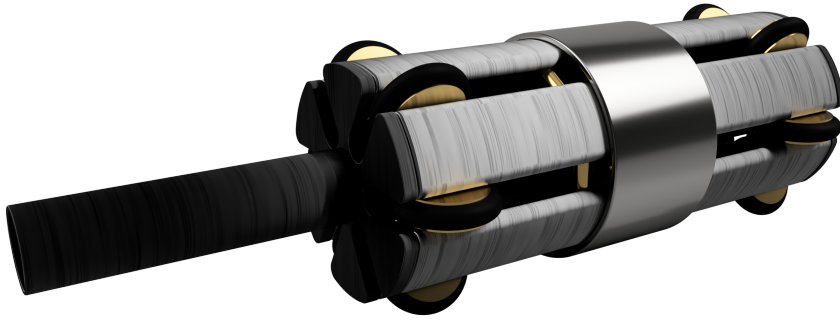
Figure 6.38: Proposed design of a wire sledge designed to pull the anode wire through the straw during installation. It is 40 mm long and 20 mm in diameter. Six wheels at the front and the back allow the sledge to roll through the straw. The sledge has a steel ring so that it can be pulled through the straw with a magnet. A long extraction nose allows the part to be extracted from the straw easily.

The straw supports as well as the carbon fibre holders and the carbon fibre were not yet installed during the assembly process. This was mainly due to the still ongoing design process. In particular it is currently discussed whether or not a compression spring holding the carbon fibre holders is required. This spring is necessary in the current design of the large-scale SST stations – see chapter 8. However, the implementation of such springs would require a significant change to the endplate design and thus a complete rebuild of the current prototype, or a new, second quad-straw prototype.

The sagging of the straws without the carbon fibres was successfully measured in section 6.5 using an optical level. The maximum sagging of 2.14 mm lies in the expected region. For the wire, the sagging was measured in two different ways. Both ways relied on a set of LEDs which were shining light through the straw tubes. The used LED system is a custom design utilising five Osram Duris S10 series LEDs. Due to their heat production and close proximity to each other as well as to the straw tubes a passive cooling solution was necessary. This cooling solution was successfully implemented and the temperature results correspond well with simulation results obtained during the design stage of the LED system. The LED system was used for both measurement methods.

The first method to measure the wire sagging was based on an optical microscope. This method gave mostly inconclusive results with maximum sagging values over two times larger than expected. Main causes for this behaviour were reflections and a loose microscope holder. To increase the accuracy of this method the LED system may be equipped with a highly absorbing light guide that directs the light only through the straws and thus minimises reflections.

Furthermore, the microscope holder needs to be redesigned to allow for much more precise operation. A possible redesign, together with the aforementioned light guide for the LED system is shown in figure 6.39. In the newly proposed microscope holder the microscope is
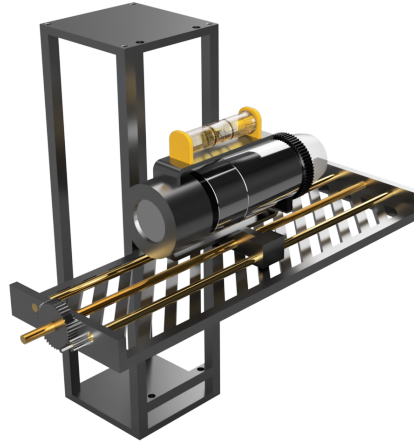


Figure 6.39: Proposed re-design of the microscopy holder. The microscope is mounted on a custom-built sled which can be moved accurately by using a transmission. The height adjustment is also utilising a transmission. Possible inclinations can be checked using spirit levels.

placed in a holder whose design is adapted to the exact design of the microscope. Using a spirit level the inclination of the microscope can be checked directly. Furthermore, the vertical and horizontal sledges to adjust the position of the microscope are guided by two additional brass rails. The sledges are still moved using a threaded rod, but instead of a coarse thread a fine thread can be used to improve accuracy. A set of gears acting as a transmission achieves a further increase in accuracy. With such an improved and more accurate holder the microscope may be operated at a constant calibration and the height of the straw tubes can be measured. The height of the tubes was found to be inconsistent along the length.

The second method to measure the wire sagging was based on the optical level and was performed similar to the measurement of the straw sagging. This method gave good results with the maximum sagging of 0.58 mm being within 10 % of the expected value.

What remains to be done in future is to first install the straw supports and afterwards the carbon fibre tows. Also, the straws must be glued together to form a partially self-supporting pack. Then, the straw sagging can be re-measured and the effectiveness of the suspension-bridge design can be verified. Furthermore it is necessary to successfully perform measurements such as the measurement of drift-time spectra or a re-measurement of the signal attenuation from section 5.3.3 with the quad-straw prototype. Efforts to capture

meaningful signals from the quad-straw prototype remained without results. After the installation of the quad-straw prototype to the main mounting frame both, the single-straw functional model as well as the quad-straw prototype only gave noise signals at a rate in the order of $\mathcal{O}(10^6)$MHz. This is very likely a grounding issue caused by the frame, as turning off all electronic devices within the laboratory had only a small effect on the noise rate. Touching the frame by hand significantly impacted the noise rate. Connecting a working drift-tube setup to the mounting frame caused the drift-tubes to have a similarly high noise rate. Currently, it is investigated how the quad-straw prototype can be decoupled completely from the mounting frame. Moreover, an electromagnetic shielding is planned which aims to further reduce the noise. This shielding is achieved by a set of U-profiles which are placed around the prototype.

# 7

# SURFACE ANALYSES OF THE STRAWS

The straw tubes experience several types of mechanical stress not only during, but also before and after the assembly. During installation the straw tubes must be fitted with the straw endpieces and afterwards be mounted to the endplates. Due to the straw's fragile nature small kinks or slightly excessive torsions are unavoidable during this process. While these effects can also cause the physical form of the straw tubes to change, they also affect the electrical coating on the inside of the tubes. Additionally, pulling the anode wire through the straw by means of a magnetic nut and a magnet caused significant abrasions on the outside but, most importantly, on the the inside of the straw. The tension of the tubes also affects the electrical coating. In this chapter, a surface analysis of this coating is presented using a scanning electron microscope (SEM).

## 7.1 SCRATCHES

In both the single-straw functional model from chapter 5 as well as the quad-straw prototype from chapter 6 the anode wire was pulled through the straw tubes by means of a magnetic nut and a magnet. This technique, while convenient and relatively easy, did cause visible damage to the straw tube – especially to the outside, i.e. the Mylar foil. From eye, damage to the inner conductive coating of the straw was hard to see. For the SEM analysis scratches were reproduced by sliding a nut along the coating once using a magnet. In figure 7.1 the resulting scratches on the inside coating of the straw tubes are depicted. On the top image a 2060× magnification of three parallel scratches running in the movement direction of the nut can be seen. These scratches are roughly of the same width and, for the most part straight. While the scratches on the top and on the bottom are continuous, the one in the middle is interrupted for roughly 16 μm after continuing slightly narrower. Although the scratch is not fully prominent between the two interrupted sections, slight dragging marks can be discerned. The areas between the scratches looks mostly smooth with occasional bumps and surface irregularities – however, no visible or significant differences to a control sample's surface can be seen.

In the bottom image a $10650\times$ magnification of a single scratch can be seen. The scratch is approximately $2\,\mu m$ wide. It is clearly visible how pulling the nut through the straw has scraped the coating away and pushed parts of it to either side. The same pattern was discernible on all scratches. In total, roughly 10 of such scratches were produced per 2.4 mm, meaning that a single pass of an M3 nut with a width across corners of approximately 6 mm creates approximately 25 of these scratches. However, the number of scratches created in the prototypes' straw tubes is probably higher than that since during the installation the nut occasionally lost attraction to the magnet and was slightly pulled back due to the anode wire's tension. Hence, some parts of the straws were subjected to the nut more than once resulting in more scratches.

The damages shown in figure 7.1 are likely to cause considerable changes in the electric field inside the straw tubes. However, the impact of such effects on detector performance are not yet analysed. Furthermore, parts of the scraped off coating may hang into the straw and could possibly promote sparkovers which damage the detector. It is thus important to minimise scratches to the straws' coatings in future.

| 20 μm | EHT = 10.00 kV | Signal A = SE2 | Date :8 Aug 2019    Time :15:11:15 |
| Mag = 2.06 K X | Aperture = 30.00 μm | Collector Bias = 300 V | Stage X = 86.296 mm , Y = 81.224 mm |
| | I Probe = 213 pA | WD = 17.5 mm | T = 0.0 °    Tilt Corrn. = Off    0.0 ° |

| 2 μm | EHT = 10.00 kV | Signal A = SE2 | Date :8 Aug 2019    Time :15:09:44 |
| Mag = 10.65 K X | Aperture = 30.00 μm | Collector Bias = 300 V | Stage X = 86.297 mm , Y = 80.890 mm |
| | I Probe = 213 pA | WD = 17.6 mm | T = 0.0 °    Tilt Corrn. = Off    0.0 ° |
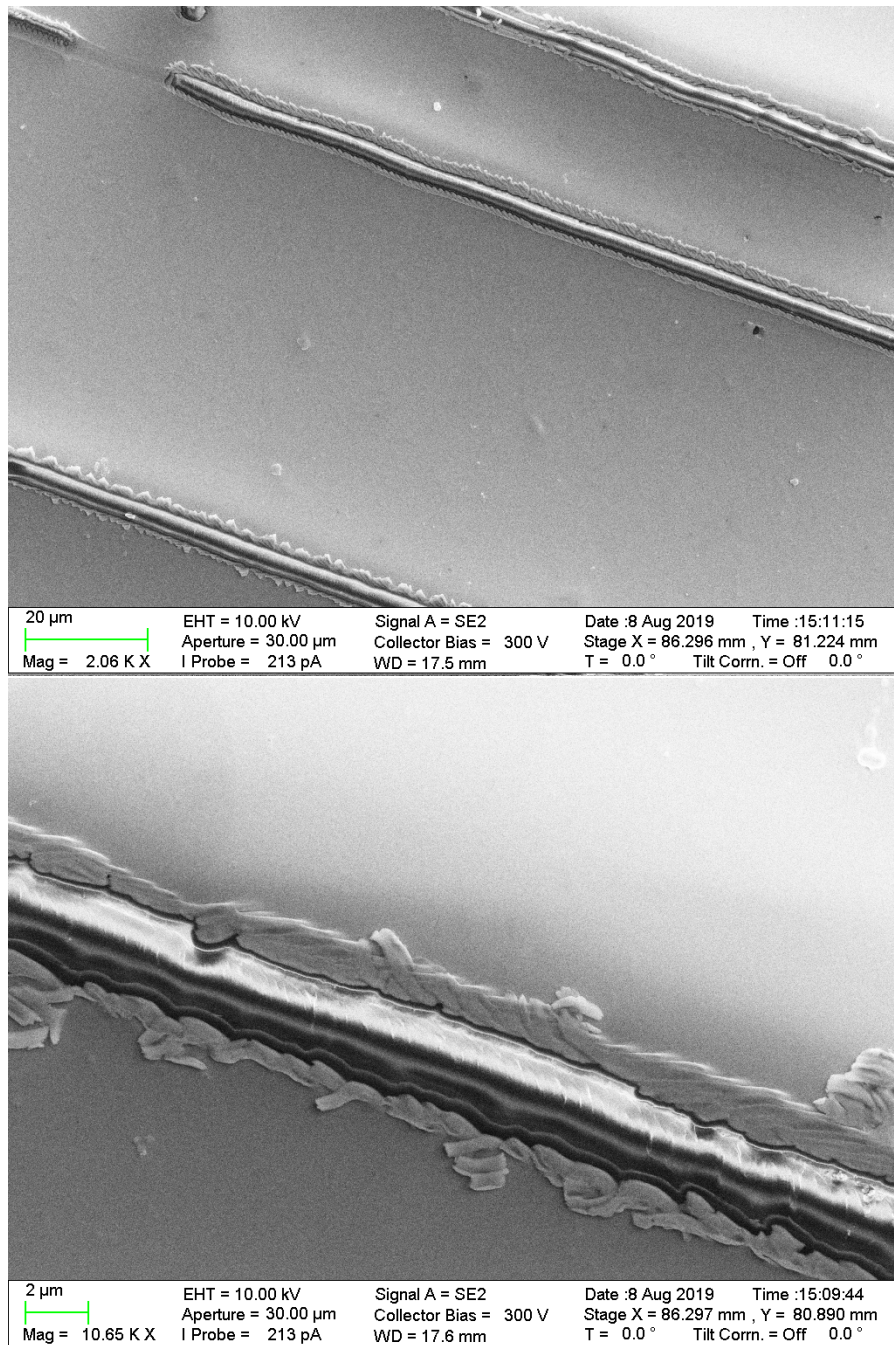
Figure 7.1: Damages on a straw tube's conductive coating caused by pulling a magnetic nut over the surface, as was done for the installation of the anode wire.

## 7.2   KINKS

During the installation process of the straws kinks are almost unavoidable. Especially when sliding the straws over the straw endpieces rotational movements are required which cause creases especially near the straws' ends. Also during the installation to the endplates kinks are likely to occur in the middle of the straws, mostly due to sagging. To test the effect of kinks on a straw tube's inner coating a sample was deliberately creased. In figure 7.2 SEM images of the kink are shown. Here, the kink fold runs diagonally from top to bottom.

In the top image the general area of the kink is shown under $1250\times$ magnification. Here, the damage to the surface coating is clearly visible. Multiple creases, cracks and areas where the coating has partially chipped off can be seen. The severity of these imperfections decreases with increasing distance from the kink fold. On average, a crack occurs roughly every 7 μm. While most cracks are parallel to the kink fold some finer cracks exist which run between the parallel cracks at an angle. In the direct vicinity of the fold the damages have a width of up to 6 μm.

The damages caused by kinks appear to be less severe than the ones caused by scratching the surface although they also may locally affect the electric field and thus the detector performance. However kinks are likely to occur much easier and more often than scratches – assuming a safe technique to pull the wire through the straw. Therefore it is important to minimise the possibility of creating kinks in the straw tube.
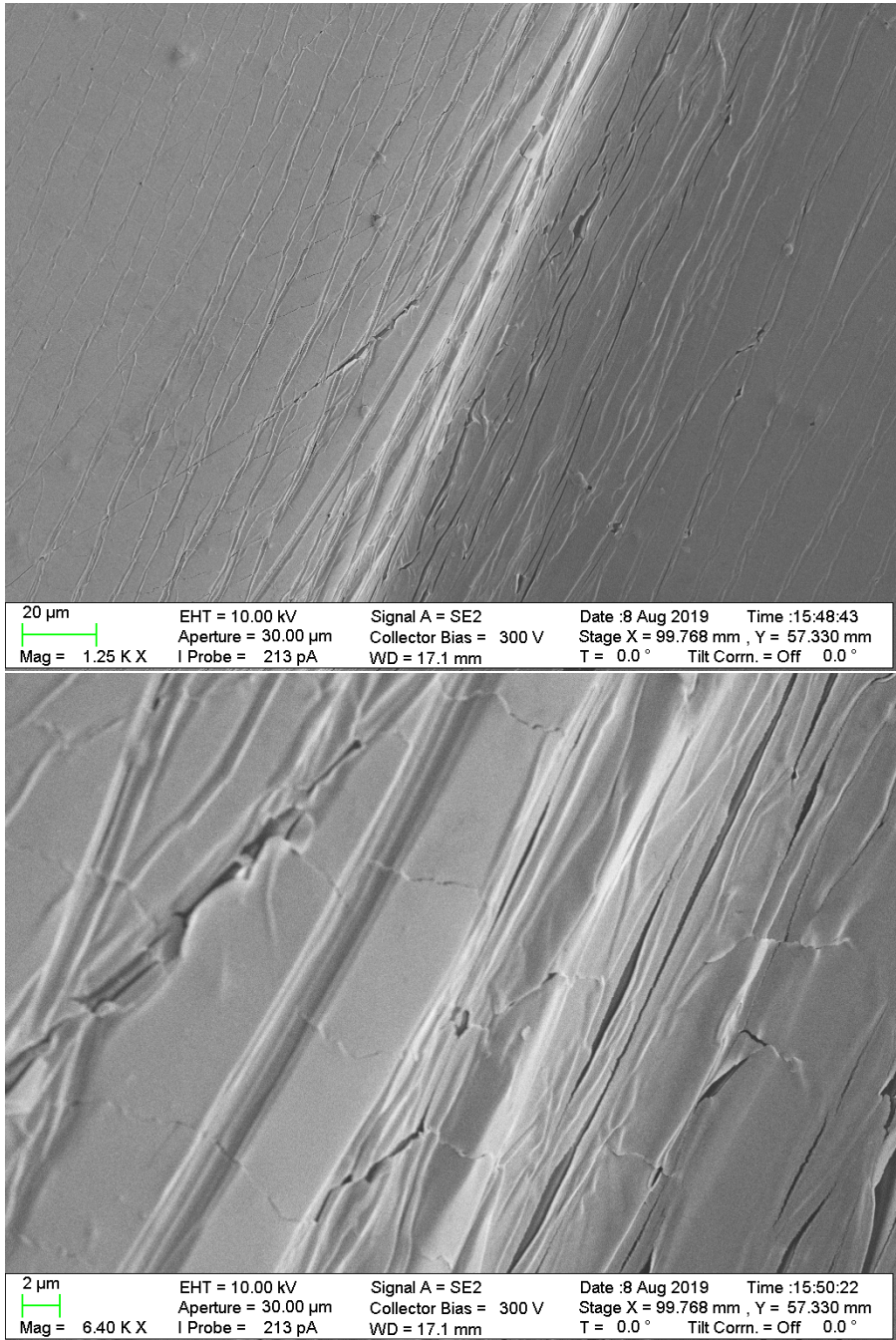
Figure 7.2: Damages on a straw tube's conductive coating caused by a kink. Such kinks can occur easily in a straw tube, especially during installation.

## 7.3   DAMAGE DUE TO ELONGATION

In the quad-straw prototype from chapter 6 the straws with a length of approximately 5 m are elongated by 24 mm, corresponding to an increase in length of roughly 0.5 %. To examine the elongation's effect on the straws' coating a section of a straw needs to be analysed in a scanning electron microscope while being in an elongated state. For the purpose of elongating a section of a straw a special tensioning device was designed. With the first design a medium accuracy was achieved, which is why the design was afterwards revised to improve the accuracy with which the elongation can be set.

### 7.3.1   *Medium accuracy measurement*

In figure 7.3 a 3D-render of the medium-accuracy tensioning device is shown. It was designed to be able to elongate two sections of a straw tube. It consists of a $50 \times 50 \times 8.5$ mm EN AW 5083 aluminium frame.
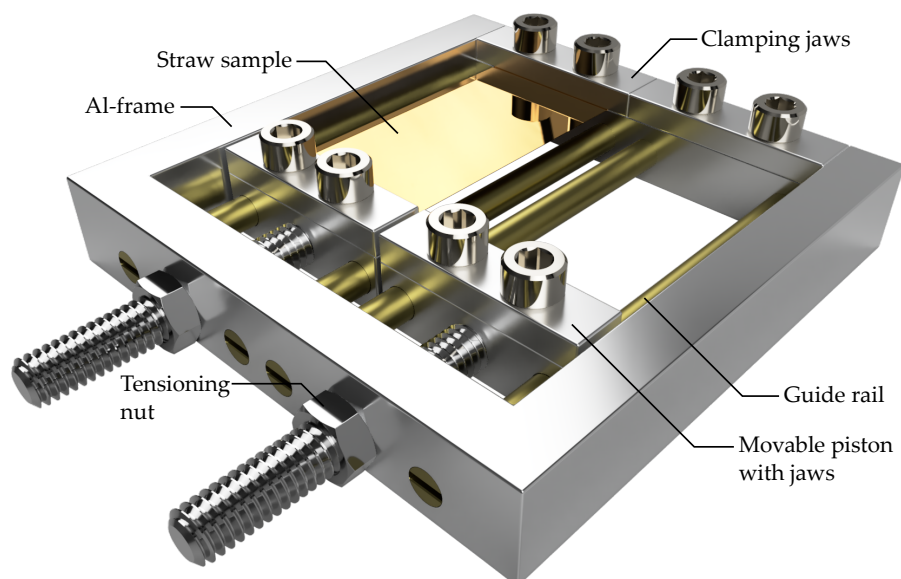


Figure 7.3: The first version of the tensioning device. It consist of an aluminium frame and pistons between which a section of a straw can be clamped in. Using a nut the piston can be moved and the sample elongated. The tensioning device can hold two samples, only one of which is shown.

On one side of the frame the height is reduced to 5 mm such that two 3.5 mm high clamping jaws can sit flush with the top of the frame. These clamping jaws are used to clamp one side of the straw sections to the frame and are securely held down using a pair of M3 screws per jaw. Two moving pistons allow the elongation to be set to different levels. Each piston consists of a lower and an upper clamping jaw between which the other side of the sample is held in, again using a pair of M3 screws. Since the pistons are moving parts, they are slightly

less wide (19.25 mm width) than the fixed clamping jaws on the other side (20 mm width). The pistons are guided by two brass guiding rails with 3 mm in diameter. These brass rails are 50 mm long slot-driven set screws screwed in to a thread in the frame. Brass was chosen due to its slight self-lubricating properties – external lubrications by means of oil or grease could not be used for this purpose since all materials placed inside the SEM must be vacuum resistant. An M4 screw is screwed into each piston and passes through a 4.1 mm hole in the frame. Using a tensioning nut, the screw and thus the piston can be moved and the straw stretched. To allow the the frame to sit flush with the ground special M3 nuts with an M4 thread were used as tensioning nuts. By using hardened stainless steel nuts the reduction of material was counterbalanced. Due to the fact that a regular M4 thread has a pitch of 0.7 mm, about 1.4 revolutions of the nut are required to tension the respective straw section by 1 mm.

*Technically, fluids can be used in a SEM, however it has to be preprocessed. This is often done for biological applications [Gol+16].*

To roughly estimate the forces acting on the tensioning device it is assumed that each section of a straw acts as a spring with a spring constant $k$. Then – assuming an elongation of $\Delta L$ – the force is given by Hooke's law:

$$F = k\Delta L. \tag{7.1}$$

The spring constant $k$ can be expressed in terms of the modulus of elasticity $E$, such that

$$F = \frac{EA\Delta L}{L_0}. \tag{7.2}$$

Here, $A = wh$ is the cross section (the product of the width $w$ and the height $h$) of the straw section and $L_0$ its initial length.

According to the datasheet [Fil03], the module of elasticity for Mylar is $4500\,\text{N}\,\text{mm}^{-2}$. Hence, for a $L_0 = 30\,\text{mm}$ long section with a width of 18 mm and a height of 36 μm the force for a single straw tube section streched by 0.5 % (corresponding to $\Delta L = 0.15\,\text{mm}$) is

$$F \simeq 12.5\,\text{N}. \tag{7.3}$$

To simulate a worst-case scenario, a very rough FEM-analysis of the tensioning device was performed for two straw sections assuming an elongation of 5 mm or 16.67 %, in which case $F(\Delta L = 5\,\text{mm}) = 486\,\text{N}$ per section. The results can be seen in figure 7.4. For this load case the frame would bend inwards by roughly 0.08 mm on the one side and by roughly 0.05 mm on the other side. Thus, the total bending is about 0.13 mm, resulting in a 2.6 % error on the exaggerated elongation of 5 mm. The error caused by the frame bending is negligible, especially since the brass guide rails, which were excluded in this FEM analysis, add to the structural rigidity of the tensioning device.

For the SEM-imaging, two 30 mm long and 18 mm wide sections of a straw tube were used. They were stretched by 0.15 mm and 0.5 mm, corresponding to an elongation of 25 mm and 83.3 mm on a 5 m long straw tube. Figure 7.5 shows the SEM images of the two

Figure 7.4: Results of a FEM analysis of the tensioning device. As a worst-case scenario it was assumed that two samples are elongated by 5 mm each. The total bending of the frame is given by negligible 0.13 mm. The colour-scale indicates the total displacement in millimetres.

measurements, the 0.15 mm elongated sample on the top and the 0.5 mm elongated one on the bottom. On both images some surface irregularities such as bumps are visible, however a similar number of irregularities was also observed on a control sample. On the top image no notable damages are discernible. This was the case for the whole sample except for the edges where, due to cutting, cracks in the coating could be seen. Similarly, the bottom image shows no clearly damaged areas, except for one very small crack on the hump shaped irregularity in the middle of the image. Upon closer inspection, this crack turned out to be around 5 μm long and $\mathcal{O}(10)$ nm wide. These cracks could be observed on other small irregularities. It is likely that these irregularities are weak spots which are damaged first by the elongation. On both samples at least four localised zones with significant damage were observed. These zones, one of which is shown in figure 7.6, are about $30 \times 30$ μm in size. They are characterised by various cracks in different directions creating differently sized and shaped scales of the coating material. These are likely to be caused by weakspots on the coating which already existed prior to elongating the samples.

Since no significant damage due to elongation was observed the elongation of the samples was increased to 1.0 mm and 1.4 mm, corresponding to 166.6 mm and 233.3 mm for a 5 m long straw tube. The results are shown in figure 7.7. The 1 mm elongated sample shows several fine, approximately 0.1 μm wide cracks. For an elongation of 1.4 mm the number as well as the width of the cracks increases significantly. Here, cracks with a width of roughly 0.5 μm can be seen consistently every few micrometres. While these cracks are likely to affect the detector performance in a considerable way the corresponding elongation of more than 200 mm for a 5 m long tube is way out of the operating range of a straw. In the SST the maximum elongation
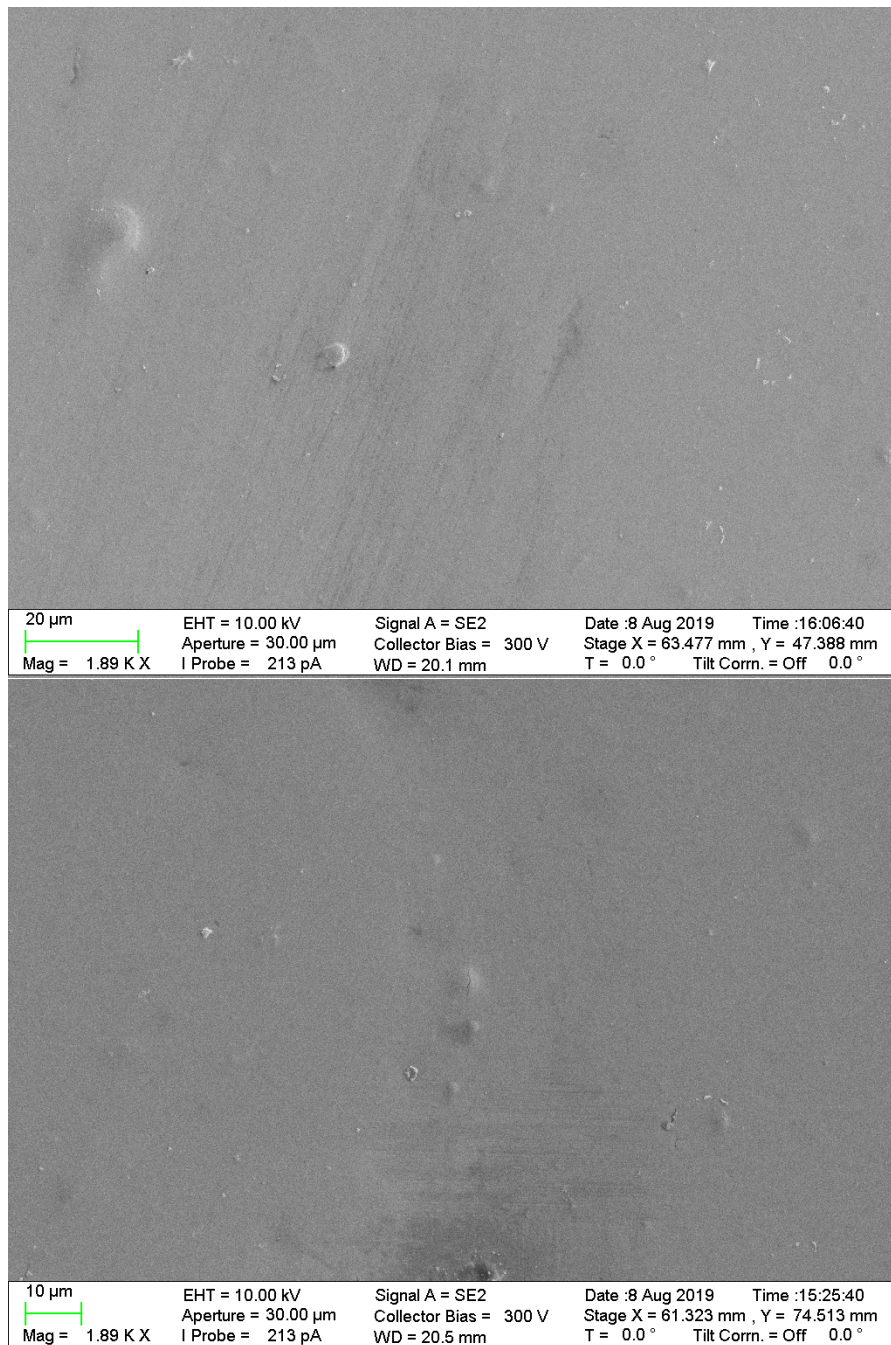
Figure 7.5: SEM images of two straw samples which were elongated by 0.15 mm (top image) and 0.7 mm (bottom image) in horizontal direction. No damage can be seen except for a miniscule crack on the bump in the centre of the bottom image.
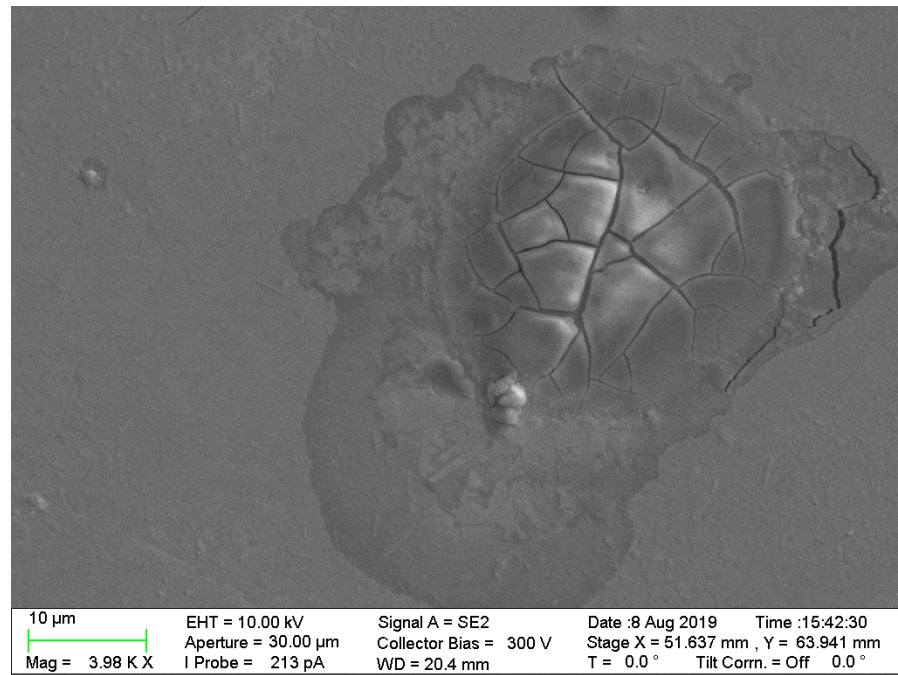
Figure 7.6: Localised damage observed on all elongated samples, but not on
a control sample.

of the straws is planned to be below 40 mm. For such elongations the
measurements indicate no significant damage to the straws' coatings.
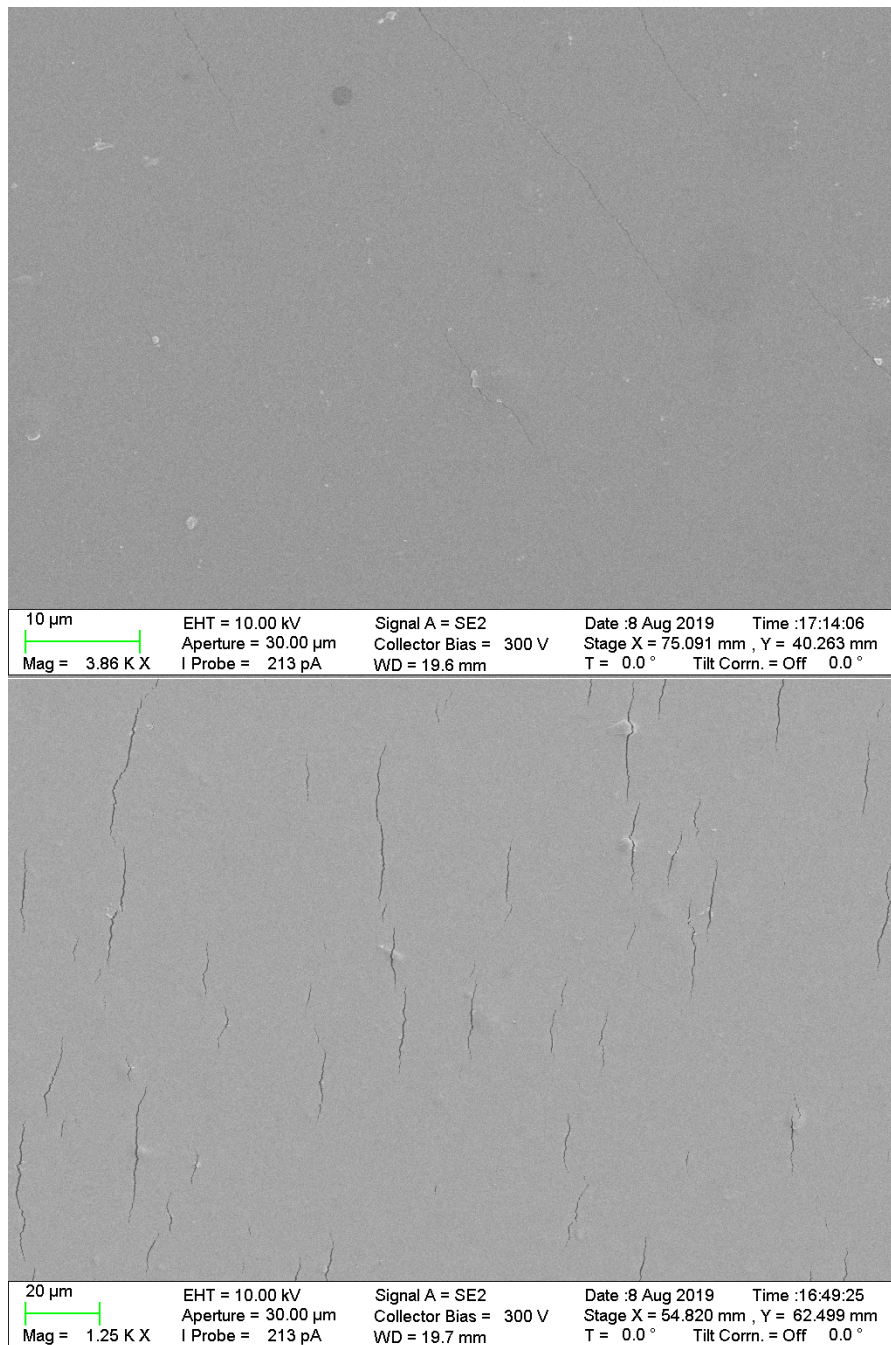
Figure 7.7: SEM images of two straw samples which were elongated by 1 mm (top image) and 1.4 mm (bottom image) in horizontal direction. On the top image first cracks can be seen. On the bottom images the cracks are clearly discernible.

### 7.3.2 *High accuracy measurement*

In the previous design of the tensioning frame the samples were elongated by directly driving an M4 nut with a pitch of 0.7 mm. This meant that to achieve small elongations of 0.15 mm the nut needed to be turned by 0.21 revolutions. In practice, this turned out to be quite difficult to achieve which likely lead to errors in the elongation. Additionally it was difficult to ensure that the installed samples had no initial sagging. Thus, the design of the original tensioning device was refined.

The design of the advanced frame is based on the design of the simpler frame and shown in figure 7.8. Compared to the simple frame
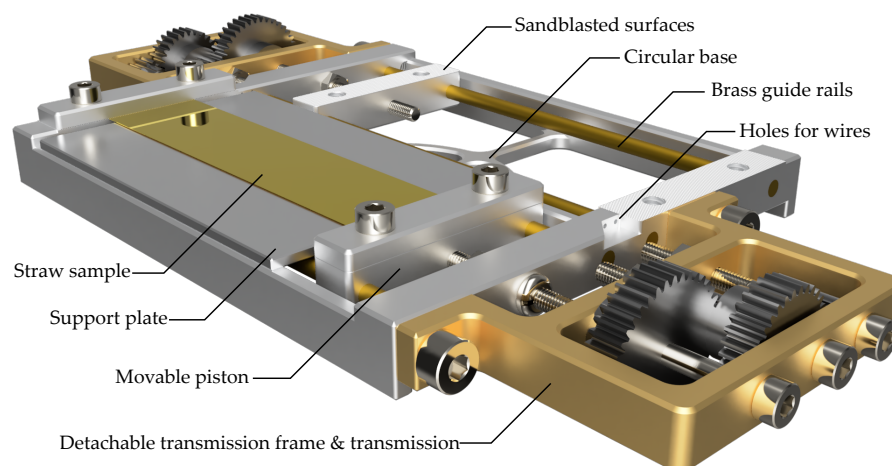


Figure 7.8: The second version of the tensioning device with improved tensioning accuracy. Compared to the first version the frame was enlarged to accommodate longer samples. Additionally, a transmission was implemented allowing to fine-control the movement of the pistons and thus the elongation of the samples. The frame also has holes to mount a pair of anode wires (not shown).

the advanced frame was enlarged with total outer dimensions of 90 mm × 106 mm aluminium with a thickness of 11 mm. This allows larger samples of a straw tube to be microscoped. An additional 2.525 mm wide brace is added between the pistons to improve rigidity. A circular frame construction located in the centre at the bottom of the frame serves as a secure base on which the frame is placed inside the scanning electron microscope. The sections of the straw tubes are on one side clamped into the frame and on the other side clamped between two jaws of a movable aluminium piston. Compared to the earlier frame the pistons were widened such that the screws pressing the upper and lower jaws of the piston together no longer have to pass through the sample. Note that the surfaces of the jaws are sandblasted to improve the grip and minimise the possibility of the sample slipping during the tensioning procedure. The pistons are still guided by a pair of brass guide rails each. Instead of using M4 screws to move the

pistons and thus tension the samples M3 screws are used in the new design. Compared to the M4 screws, which have a pitch of 0.7 mm the M3 screws have a pitch of 0.5 mm meaning that the samples can be tensioned more accurately. To further improve the accuracy of the tensioning mechanism the tensioning screws are no longer directly driven by hand. Instead, they are driven by a detachable dual stage transmission mounted in a separate brass frame. The fact that the transmission frame can be detached is necessary to maintain a compact footprint. Moreover, the gears used in the transmission are magnetic and can thus alternate the SEM measurements. A total of four gears are used in the transmission. The main tensioning screw is driven by a 40-tooth gear. This gear is driven by a 10-tooth gear resulting in a transmission ratio for the second stage of $i_2 = {}^{40}/_{10} = 4$. The 10-tooth gear is rigidly fixed on the same axle as a 30-tooth gear. Finally, the 30-tooth gear is manually driven by a 10-tooth gear, meaning the transmission ratio of the first stage is given by $i_1 = {}^{30}/_{10} = 3$ In total, this results in a total transmission ratio $i$ given by

$$i = i_1 \cdot i_2 = 3 \cdot 4 = 12. \tag{7.4}$$

This means that a full revolution of the tensioning screw requires twelve full turns of the drive screw resulting in much improved accuracy. Due to the space requirement of the transmission frame each of the two pistons is driven from another side of the frame. To ensure that the samples do not have an initial sagging 2 mm aluminium support plates are placed under the samples during installation ensuring that it sits flat. Moreover, the frame features a section in the middle of either side where anode wires can be mounted and tensioned to analyse them under the microscope.

In this more accurate frame two 19 mm wide and 70 mm long sections of a straw were elongated by 0.3 mm and 0.6 mm. This corresponds to elongations of 21.4 mm and 42.9 mm for a 5 m long straw. The results look very similar to the ones achieved using the previous iteration of the frame and are shown in figure 7.9. At both elongations no significant cracks or other damages can be seen, except for occasional small cracks on bumps – confer figure 7.5. This was cross-checked at different locations including in the direct vicinity of the weld seam, where likewise no damage could be seen.

Besides elongating sections of a straw tube two anode wires with a diameter of 45 µm were imaged. One wire was tensioned using a mass of 180 g while the other one was loosely fitted to serve as a control sample. The results can be seen in figure 7.10. On neither wire damages such as cracks caused by the tensioning can be discerned. This was checked at different positions showing the same results. It is thus confirmed that neither elongating the wires nor elongating the straws within their expected operating ranges causes significant damage affecting the detector's performance.

| 20 µm | EHT = 10.00 kV | Signal A = SE2 | Date :23 Sep 2019    Time :15:59:31 |
| Mag =    1.86 K X | Aperture = 30.00 µm<br>I Probe =    213 pA | Collector Bias =    300 V<br>WD = 15.0 mm | Stage X = 64.279 mm , Y = 73.979 mm<br>T =    0.0 °      Tilt Corrn. = Off    0.0 ° |



| 2 µm | EHT = 10.00 kV | Signal A = SE2 | Date :23 Sep 2019    Time :16:12:51 |
| Mag =    23.49 K X | Aperture = 30.00 µm<br>I Probe =    213 pA | Collector Bias =    300 V<br>WD = 14.6 mm | Stage X = 61.799 mm , Y = 39.125 mm<br>T =    0.0 °      Tilt Corrn. = Off    0.0 ° |
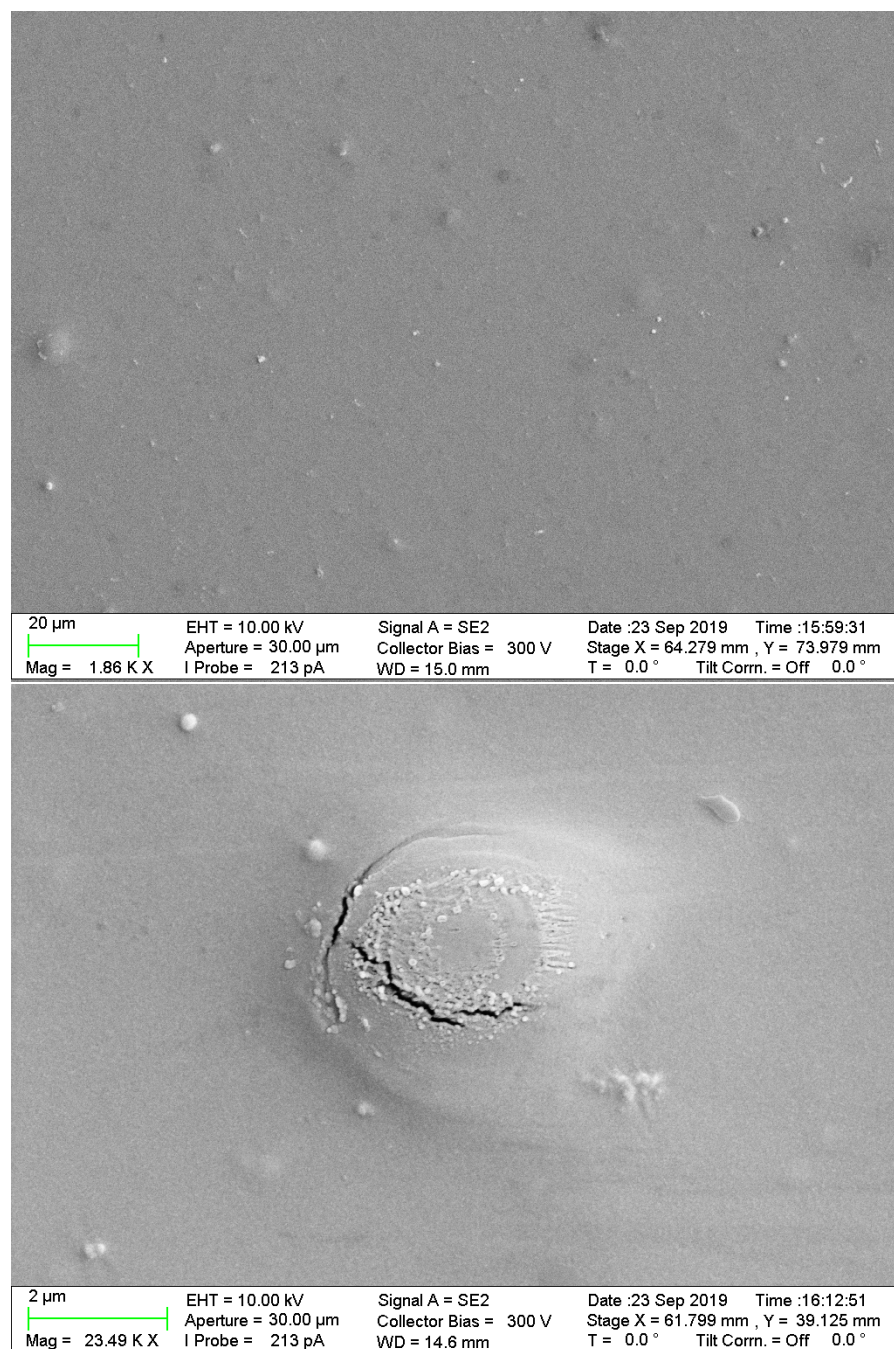
Figure 7.9: SEM images of two straw samples which were elongated by 0.3 mm (top image) and 0.6 mm(bottom image) in horizontal direction using the revised tensioning device. Both samples looked mostly like the top image, although the sample elongated by 0.6 mm showed several fine cracks on surface irregularities as shown in the bottom image.
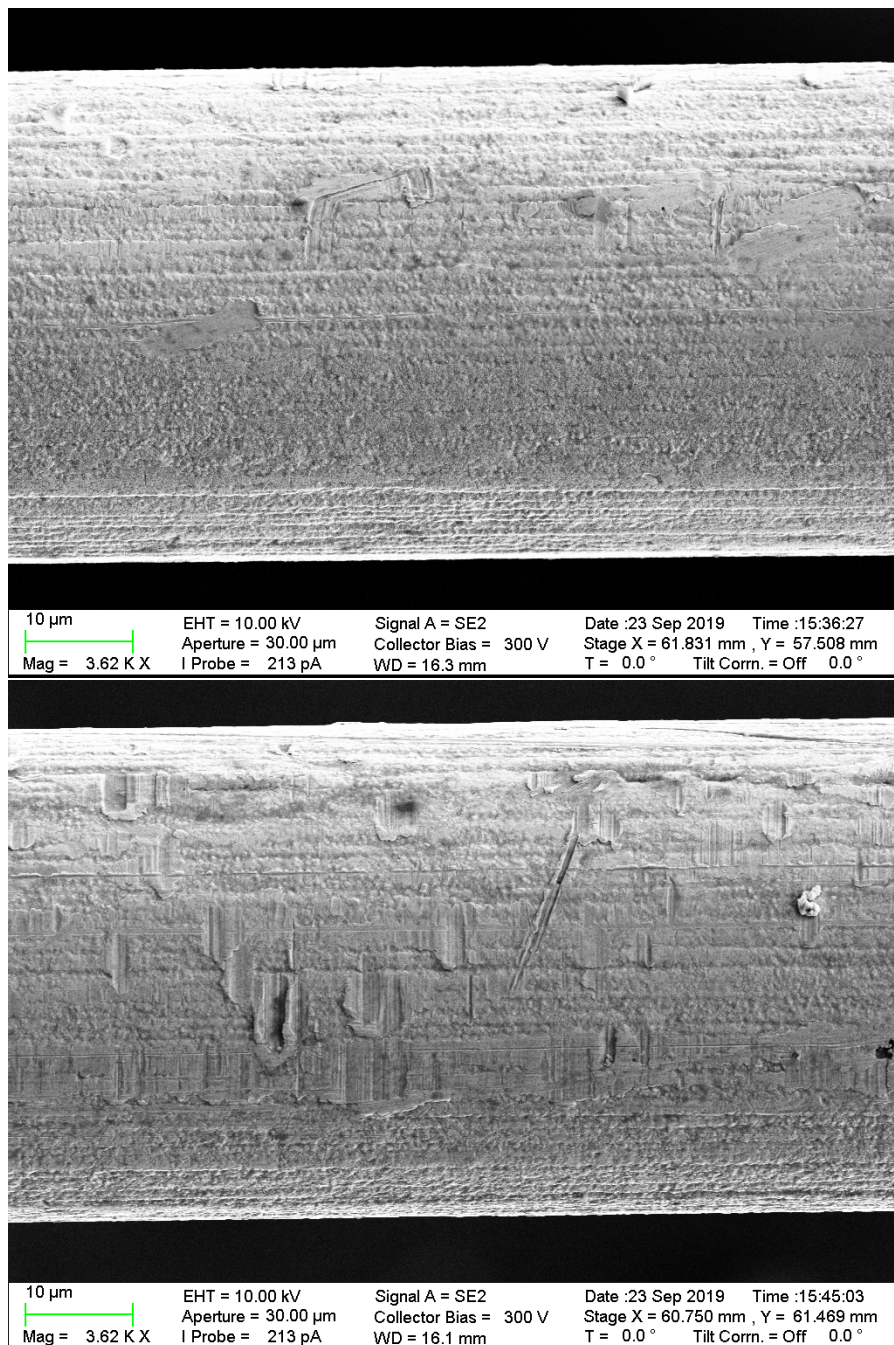
Figure 7.10: SEM images of a loose ∅45 µm anode wire (top image) and a wire tensioned using a mass of 180 g (bottom image). No damages caused by the tensioning can be seen on either image.

## 7.4    EXAMINATION OF THE WELD SEAM

The straws are manufactured by welding a narrow sheet of coated Mylar into the shape of a tube. The weld was examined under a scanning electron microscope. Figure 7.11 shows the weld seam magnified by factors of 110 and 2000.

In particular under 2000× magnification sections with no coating can be seen. These appear very light in the SEM image and have widths of up to 5 µm. An Energy-Dispersive X-Ray Analysis – EDX in short – was performed on a small section of the sample. This is shown in figure 7.12. It confirms that significant parts of the seam weld consist of carbon. Here, no coating is applied. Sections with low carbon content are covered equally with copper and gold – the materials the coating is made of. A uniform distribution of oxygen was likely caused by residual humidity on the sample's surface. The total detected element ratio is 25 % carbon, 9 % oxygen, 45 % copper and 20 % gold. It is possible that the uncoated zones affect the electric field in the straw tube.
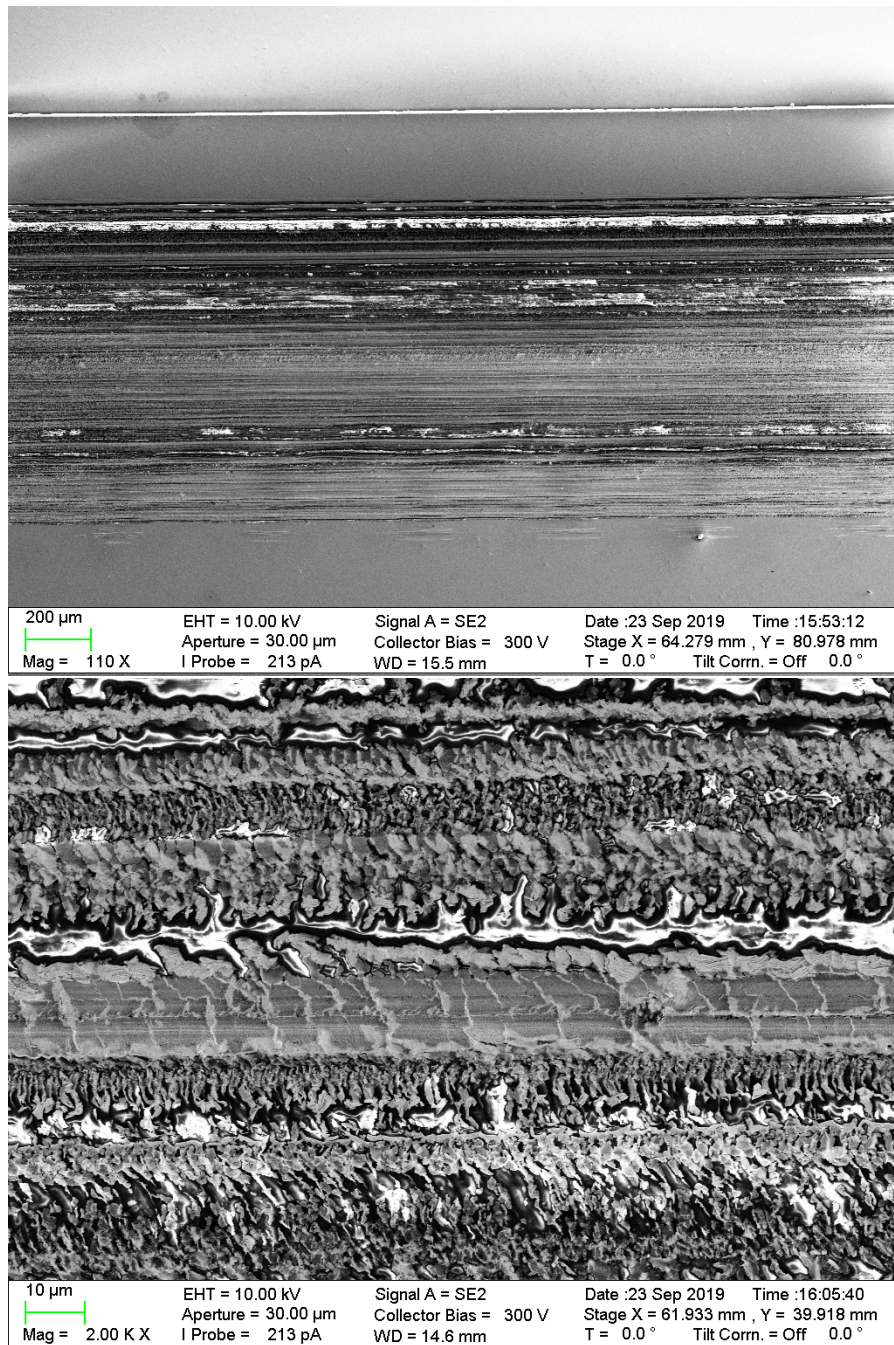
Figure 7.11: SEM images of a straw's weld seam. The top image shows a magnification by a factor of 110, the bottom one by a factor of 2000. Light areas are not covered by the conductive coating.
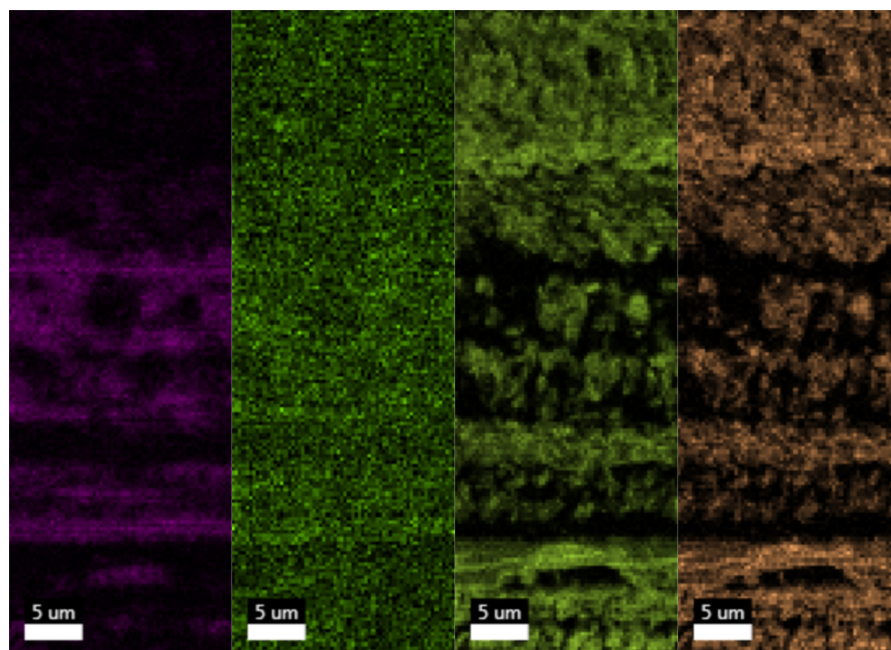
Figure 7.12: Energy-Dispersive X-Ray Analysis (EDX) of a straw's weld seam showing the main chemical elements contained in the weld seam. From left to right: Carbon, oxygen, copper, gold.

## 7.5 SUMMARY AND OUTLOOK

Due to a straw's fragile nature damages, especially to the conductive coating, can easily occur. Several types of damage, in particular scratches caused by a magnetic nut required to install the anode wire as well as kinks were analysed using a scanning electron microscope. The images revealed significant damage to the conductive coating possibly affecting the detector's performance. In future methods must be found to reduce or – if possible – completely prevent such damages to the straw tubes. Furthermore the effect on the detector performance must be analysed, either experimentally or by using simulations. In the latter case more data, especially about the depth of scratches and cracks will be required. This data could be acquired using an atomic force microscope (AFM).

Moreover, the effect of elongating the straws on the conductive coating was examined. For that purpose sections of a straw were tensioned using two different iterations of a custom-made tensioning device. While some localised damages were discernible it could be verified that, in general, elongating the straws within their expected operating range does not cause considerable damage to the conductive coating. Additionally, an anode wire was tensioned within its expected operating range. Similar to the straw, no significant difference between the tensioned wire and a control sample could be seen.

Lastly, the weld seam of a straw tube was studied. Using regular SEM imaging combined with a Energy-Dispersive X-Ray analysis it

was found that significant portions of the weld seam are not covered with the conductive coating. Similar to the kinks and scratches this may possibly affect the detector's performance and must be studied further in future. For this, too, more image data will be required.

# LARGE-SCALE INTEGRATION

The Spectrometer Straw Tracker of the SHiP experiment is part of the magnetic spectrometer and will consist of four tracking stations, two of which are located on either side of the SST magnet. This is shown in figure 8.1. Due to particle kinematics and the location within
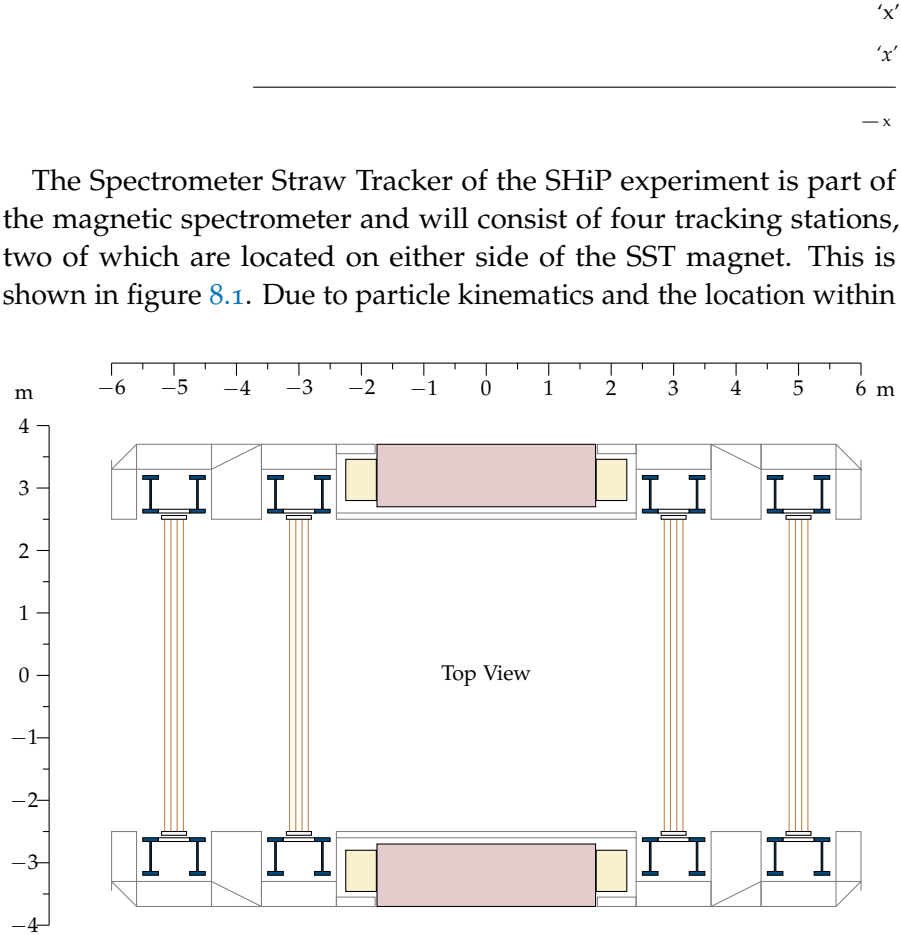


Figure 8.1: Layout of the magnetic spectrometer. Two SST stations each are located on either sides of the magnet (red: magnet yoke, yellow: magnet coils). Each stations consists of a frame made out of beams (blue) which houses modules in which the straws (brown) are installed.

the SHiP experiment the SST needs to have an active area of around $5\,\mathrm{m} \times 10\,\mathrm{m}$ (width × height). In total, this means that each station will consist of almost 4000 straw tubes. These straw tubes are mounted in larger modules, which will use the design tested in the quad-straw prototype. Two different iterations of these modules are explained in section 8.1. The modules themselves will be held in a large mounting frame that is designed to sustain the forces created by the straw tubes, the carbon fibres and the gas pressure. The design of two different iterations of the mounting frames is outlined in section 8.2.

## 8.1    MODULES

The roughly 4000 straws per station are installed in modules. The quad-straw prototype explained in section 6 was designed to be a small-scale prototype for such a module. However, considering the total amount of straws required, the installation of only four straws per module is impractical. Hence, the modules are much larger – although their basic design is identical to the quad-straw prototype's design.

The first design iteration is depicted in figure 8.2. This module holds a total of 256 straws in a *u-y-y-v* layout, which was chosen to maximise the stability of the endplate. Per view, 32 pairs of straws are stacked on top of each other, in the same layout that was used in the quad-straw prototype. This means, that the endplates have a base height of 640 cm, however, the total height of the endplates is approximately 1 m due to the overlapping 'wings' which are a result of the 5° stereo angle. Fifteen modules were planned to be stacked by inserting them into the mounting frame from the top. However, this would have meant that possible maintenance would be difficult, as all modules above the one requiring maintenance would have to be removed completely to allow to access the module in need of repair.

Thus, the module design was changed. Instead of one large endplate for all four views, each view has its own pair of endplates. These endplates are still made out of 3 cm thick aluminium plates but have a smaller size of 640 cm × 10 cm. Each endplate holds 64 straw tubes and is planned to be inserted into the mounting from the front and no longer from the top. That way maintenance is much simplified as only two modules must be removed in order to access the one requiring maintenance. Each station will consist of 16 horizontal and 15 stereo modules per view, bringing the total number of straw tubes per station up to 3968. Since endplate stability is no longer of concern the four modules are arranged in the more common *y-u-v-y* arrangement. The current design of the modules is shown in figure 8.3.
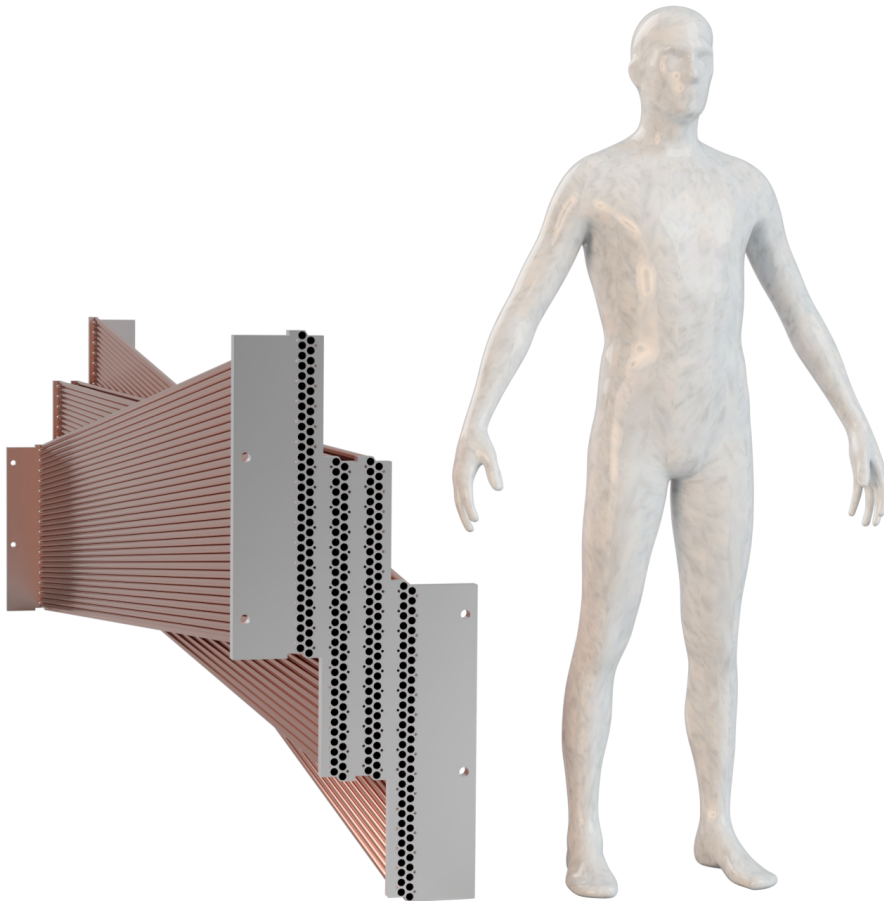
Figure 8.2: First design iteration of a single module. Each modules holds 256 straws in a *u-y-y-v* layout. Fifteen modules were planned to be stacked on top of each other, which would, however, have complicated maintenance.
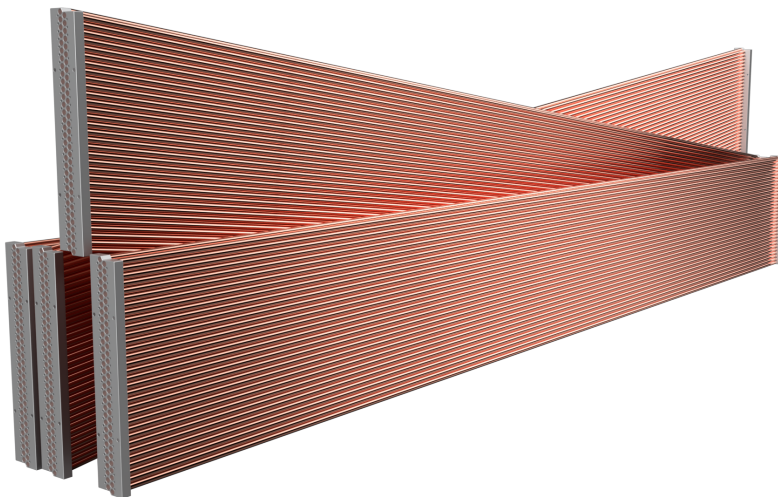


Figure 8.3: Current design iteration of the modules. Four modules arranged in a *y-u-v-y* layout are shown. Each module holds 64 straw tubes. Compared to the first design iteration these modules simplify possible maintenance significantly.

## 8.2    MOUNTING FRAME

The SHiP SST will consist of four different stations. Each station will consist of one large mounting frame housing the modules which in turn hold the straw tubes. Since two stations each are located on either side of the SST magnet the mounting frame must be made out of a non-magnetisable material. Additionally, the total mass of each station must be below 40 t as this is the maximum the crane in the experimental hall can lift – the maximum mass allowed for each frame was set to 30 t. Assuming that the straws and the carbon fibres are tensioned with a force of $\Delta F_T = 60\,\mathrm{N}$ each, the frame needs to be able to withstand a total force of $F_T \approx 36\,\mathrm{t}$. However, the magnitude of this force is not the most challenging issue. Two additional forces, namely the vacuum force and the Mylar relaxation force, create a dynamic load setup acting on the frame. This dynamic load causes the frame to unbend during operation, thus elongating the straws, carbon fibres and anode wires.

When the straw tubes are being operated in vacuo, the gas mixture with which the straws are operated creates an overpressure which exerts a force on the frame. This is the vacuum force $\Delta F_V$. It is given by

$$\Delta F_V = 31.4\,\mathrm{N}. \tag{8.1}$$

Note that this force is irrelevant for straw tubes operated under ambient air pressure, such as the quad-straw prototype from chapter 6.

The Mylar relaxation force $\Delta F_R$ is a result of the mechanical properties of the Mylar. In general, Mylar tends to flow meaning that the initial tension of the straw tubes decreases over time. Specifically, after ten years the tension of $F_T = 60\,\mathrm{N}$ is expected to be reduced to its halve;

$$\Delta F_R = 30\,\mathrm{N}. \tag{8.2}$$

In total, this results in two worst-case scenarios concerning the forces. This is shown in figure 8.4. In the first worst-case scenario the SST station is newly built and not subjected to the vacuum. Then, the only force acting on the frame is the total tensioning force $F_T = 36\,\mathrm{t}$ of the straws and the carbon fibres which results in the walls of the frame bending inwards. In the second worst-case scenario the SST station is ten years old – or even older – and located inside the evacuated vessel. Then, the Mylar relaxation force of $\Delta F_M = 30\,\mathrm{N}$ per straw acts with a total of $F_M = 12.23\,\mathrm{t}$ in the outwards direction. Additionally, the vacuum force of $\Delta F_V = 31.4\,\mathrm{N}$ per straw points outwards with a total force of $F_V = 12.8\,\mathrm{t}$. Thus, the initial inwards force of 36 t has diminished to only 10.97 t. The dynamic force of roughly 25 t causes the frame to un-bend over time resulting in an elongation of both the straw tubes and the anode wires which are mounted in the frame. This elongation changes the sagging of the carbon fibre tows and the wires,
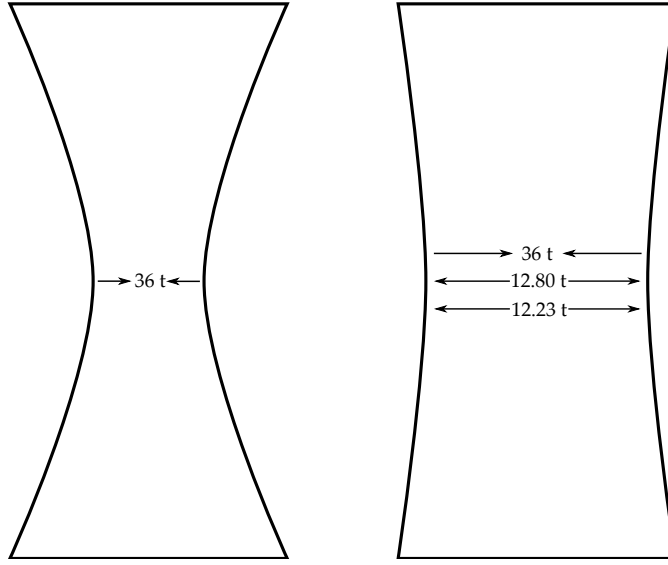
Figure 8.4: Schematic depiction of the two worst-case scenarios created by the dynamic forces on an SST frame. On the left image, the station is new and not in vacuo, meaning that the frame bends inwards to the tensioning force. On the right image the station is ten years old and in vacuum. Then, the Mylar relaxation force and the vacuum force cause the frame to un-bend.

both of which have different sagging behaviours. Since two straws are carried by a single carbon fibre tow their sagging is governed by the sagging $s_C$ of the carbon fibre tow connected to it. The technical specifications of the carbon fibre tow were introduced in table 6.1. It has a spring constant of

$$k_C = 6.67 \, \text{N} \, \text{mm}^{-1}. \tag{8.3}$$

This value was determined experimentally. The sagging $s_C$ and the wire's sagging $s_W$ are described by:

$$s_C = \frac{m_{CS} g L_0}{8 k_C \Delta L}, \tag{8.4}$$

$$s_W = \frac{\rho g L_0^2}{8 E \Delta L}. \tag{8.5}$$

Here, $m_{CS} = 2 m_S + m_C = 31.9 \, \text{g}$ is the weight of two straws and one carbon fibre tow and $g = 9.81 \, \text{m} \, \text{s}^{-2}$ is the gravitational acceleration. The initial length of both the carbon tows and the wires is given by $L_0 = 5 \, \text{m}$. They are elongated by $\Delta L$. The quantities $\rho = 19\,250 \, \text{kg} \, \text{m}^{-3}$ and $E = 409 \times 10^9 \, \text{N} \, \text{m}^{-2}$ are the wire's density and elastic modulus. Figure 8.5 shows $s_C$ and $s_W$ graphically. The plot clearly shows how the sagging behaviours differ with varying elongation. For example, assuming an elongation from 10 mm to 20 mm the sagging of the carbon fibre tow would reduce from roughly 3 mm to 1.5 mm – a decrease of roughly 1.5 mm. The sagging of the wire however would
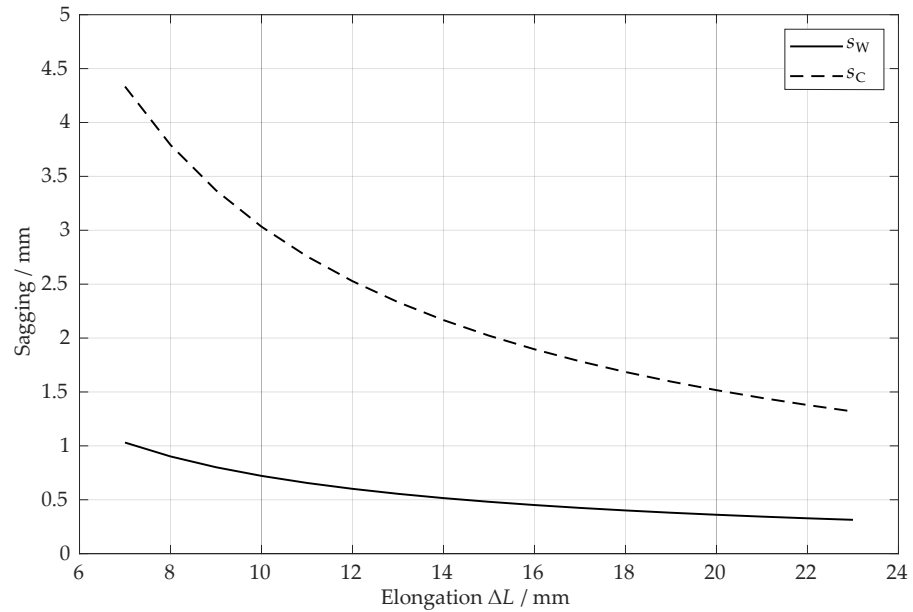
Figure 8.5: The sagging of the carbon fibre tow carrying two straws (dashed line) and the anode wire (continuous line). For large changes of $\Delta L$ the sagging of the tow and the wire change differently, causing a net wire displacement.

only decrease by around 0.35 mm, meaning that the wire would be displaced by 1.15 mm with respect to the straw's centre. In total, this leaves two options, namely to (A) either minimise the elongation $\Delta L$ such that the relative changes of $s_W$ and $s_C$ are minimal or (B) to allow a significant elongation but to equalise the sagging behaviours by modifying either $s_C$ or $s_W$ – or both.

### 8.2.1    *Option A: Minimising the elongation*

The first option under consideration was to construct a large frame that is strong enough such that the dynamic movement $\Delta L$ due to unbending is small, resulting in almost similar sagging behaviours for the anode wire and the carbon fibre tow. This frame is shown in figure 8.6. It mainly consists of four HEM1000 stainless steel wide-flanged beams. Each HEM1000 beam has a standardised I-profile with a height of 1008 mm and a width of 604 mm mm as shown in figure 8.7 Two pairs of these beams with a length of 5 m are used horizontally, two pairs of 12 m long beams are used vertically. The distance between the beams in each pair is 0.5 m. This results in a total outer dimension of 12 m × 7.096 m × 1.104 m (height × width × depth) and an active area of 9.984 m × 5 m (height × width). All of the beams are connected to each other using bolts as well as 40 mm thick steel buffer plates. Additional steel braces increase the structural rigidity further. Moreover, the horizontal beams are equipped with additional 30 mm thick steel plates in-between the beams. These plates

*Standardised DIN 1025 wide-flanged beams are available in three categories, HEA, HEB and HEM. HEM beams are the strongest ones.*
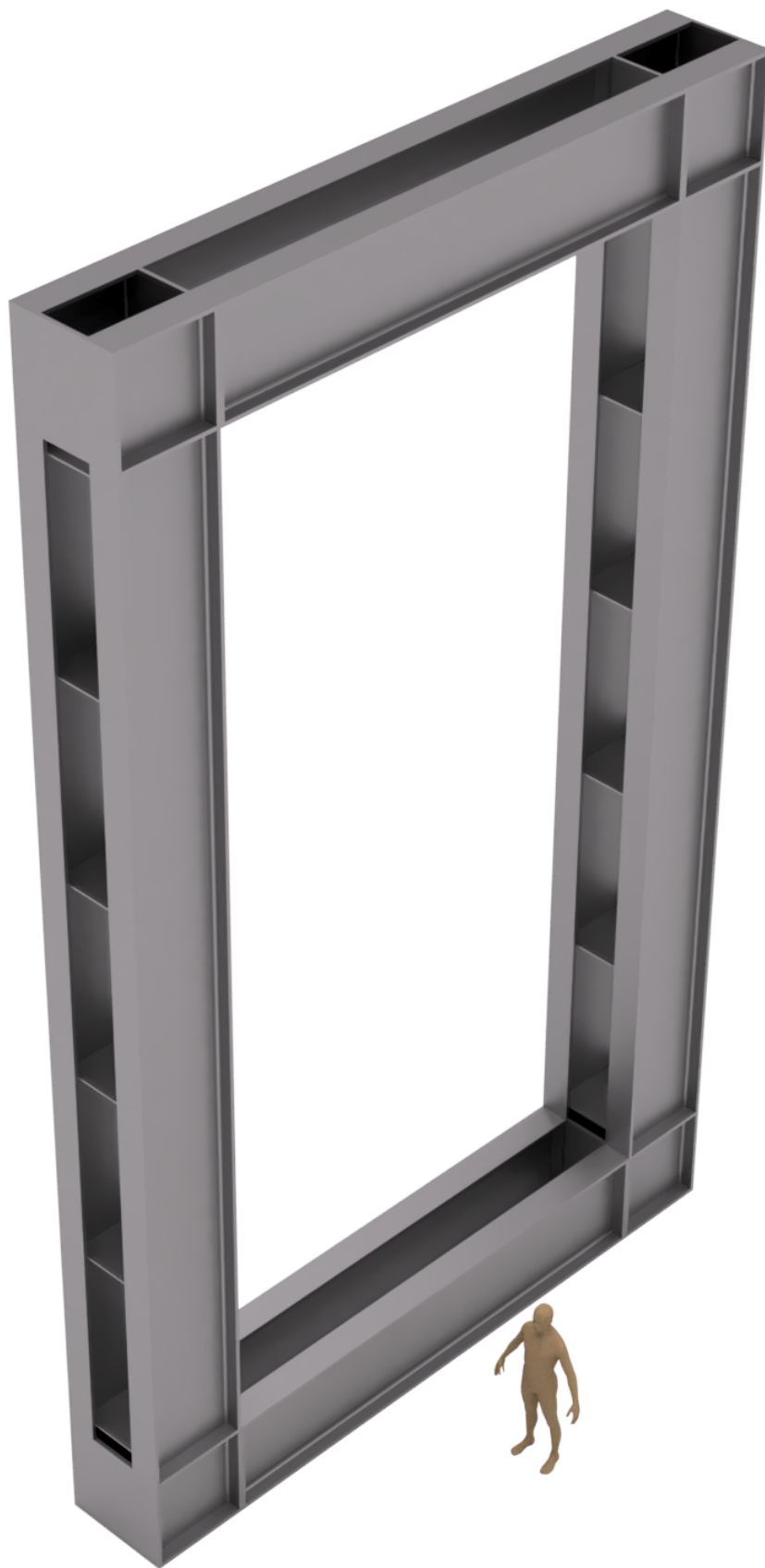
Figure 8.6: The strong frame designed to minimise the elongation $\Delta L$. It consists of four 12 m long vertical HEM1000 stainless steel beams and four 5 m long vertical HEM1000 stainless steel beams. Between each pair of vertical beams floors are installed.
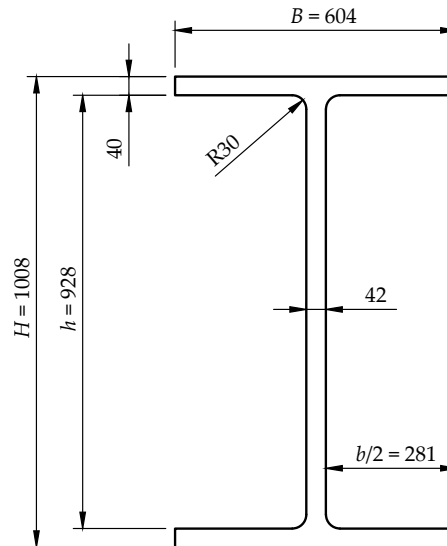
Figure 8.7: Dimensions of the profile of a HEM1000 wide-flange beam. The HEM1000 is the largest and strongest readily available beam.

act as intermediate floors. They have a distance of 1.92 m from each other and are designed to allow personnel to walk into the sides of the frame in order to perform necessary work, such as installation or maintenance, on the modules' endplates. This version of the frame has a total mass of roughly 28.41 t, which is well below the required 30 t mark.

Using the simulation toolbox of Fusion 360 the bending of the frame was simulated using the Finite Element Method (FEM). A load of 36 t and a load of 11 t were put on the frame. The results for the 36 t load setup are shown in figure 8.8. Note that only the movement in $z$ direction is depicted. The simulation shows an expected behaviour with both walls of the frame bending inwards by approximately 0.6 mm. For the 12 t load setup the bending per wall was approximately 0.19 mm. This results in a total elongation of 0.82 mm which ensures that the relative change in the sagging is in an acceptable range.

While the frame is designed sufficiently strong, its largest downside is the size. A frame of this size would mean that the vacuum vessel, which houses the frame, would require significant structural changes to accommodate the frame. Thus, the option of minimising the elongation using a strong but large frame is currently no longer being developed actively.
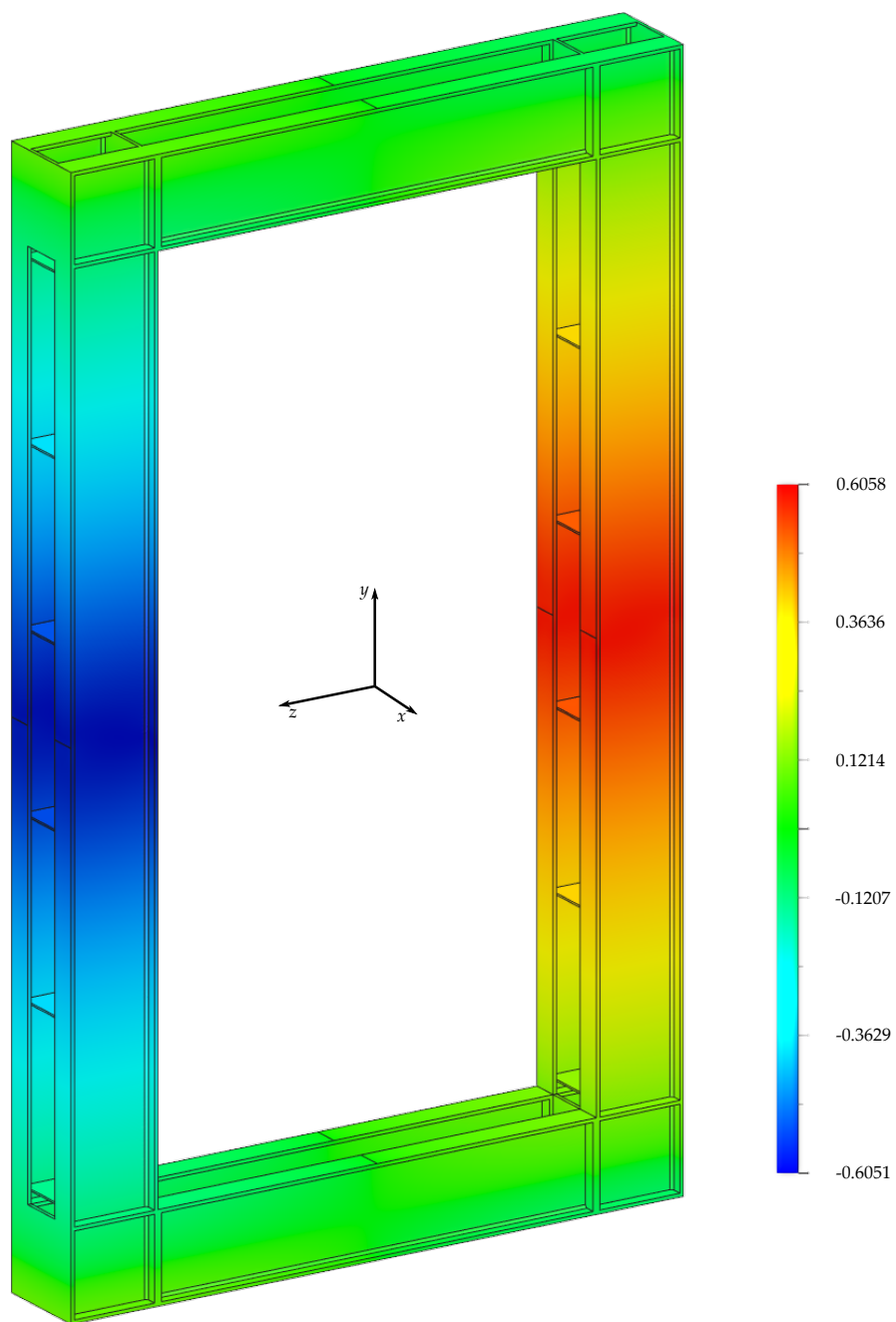
Figure 8.8: Results of an FEM analysis for the large frame. A total force of 36 t pulls both walls inwards, resulting in a maximum bending of 0.61 mm per wall. Note that for the simulation it was assumed that the frame is a single solid part. The colour scale indicates the displacement in $z$ direction in units of millimetres.

### 8.2.2  *Option B: Changing the sagging behaviour*

Minimising the elongation resulted in an inconveniently large frame. Thus, a new frame with an overall smaller size which allows to bend more under the forces was designed. However, in this case the difference in the sagging of the anode wire and the sagging of the carbon fibre tow and thus the straws is no longer negligible and causes a significant net wire displacement. This can be changed by modifying either the wire's or the tow's sagging behaviour. While changing the sagging behaviour of the wire would require a significant change in the design of the module's endplates the sagging behaviour of the carbon fibre tow can be changed relatively simply. This is done using compression springs which hold the carbon fibre tow on either side, as shown in figure 8.9. This creates a constellation where – assuming
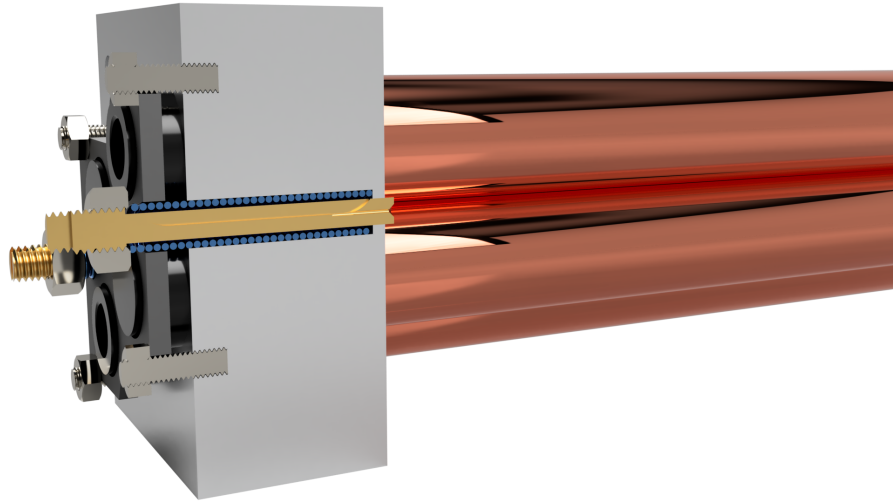


Figure 8.9: Cut through a possible redesign of the quad-straw prototype's endplate to accommodate a spring, which, for reasons of clarity, is depicted in blue. The spring pushes a nut, which is screwed on to the head of the carbon fibre holder, outwards. The carbon fibre tow is not depicted in this image.

the correct choice of springs – the sagging behaviour of the carbon fibre tow corresponds exactly to the sagging behaviour of the anode wires.

The main constraint for the bending of the frame is the elastic range of the anode wires. For the wire elongation, two values are important: The minimum elongation $\Delta L_{\min}$ and the maximum elongation $\Delta L_{\max}$. The minimum elongation ensures that the wire is not significantly affected by electrostatic forces acting within the straw tubes. The maximum elongation is governed the wire's elastic limit and the rupture probability. To determine the wire's elastic range several tungsten wires of different radii (45 µm and 30 µm) were tensioned and their behaviour analysed. This work was done as part of [**LARA**].

Table 8.1: Technical specifications of the Febrotec 0X-RDF1661 spring. The data was taken from [Gmb19b].

| Parameter | Symbol | Value |
|-----------|--------|-------|
| Outside diameter | $d_o$ | 6.7 mm |
| Inside diameter | $d_i$ | 4.7 mm |
| Wire diameter | $d_w$ | 1 mm |
| Length | $\ell_0$ | 81 mm |
| Loaded length | $\ell_1$ | 35.89 mm |
| Force at loaded length | $F_{\ell_1}$ | 72.27 N |
| Spring rate | $k_S$ | 1.602 N mm$^{-1}$ |
| Mass | $m_{spring}$ | 3.4915 g |
| Direction of helix | | right |

It was found that $\Delta L_{min} \simeq 10\,\text{mm}$ and $\Delta L_{max} \simeq 20\,\text{mm}$. This means that the wire, and thus the frame, is not allowed to bend by more than

$$\lambda \equiv \Delta L_{max} - \Delta L_{min} = 10\,\text{mm}. \tag{8.6}$$

A suitable spring is Febrotec's readily available OX-RF-1661. The technical data of this spring is given in table 8.1 Using the spring constant

$$k_S = 1.6\,\text{N mm}^{-1} \tag{8.7}$$

the spring constant of a carbon fibre held in by two springs on either end can be calculated to:

$$k_{CS} = \frac{1}{\frac{1}{k_S} + \frac{1}{k_C} + \frac{1}{k_S}} = \frac{k_C k_S}{2k_C + k_S} \simeq 0.71\,\text{N mm}^{-1}. \tag{8.8}$$

Assuming the elongation increases from $\Delta L_{min}$ by the allowed range of $\lambda$ the change of the wire's sagging $\Delta s_W$ and the carbon fibre tow's sagging $\Delta s_C$ can be made equal; $\Delta s_W = \Delta s_C$. This gives the following equation:

$$\frac{\rho g L_0^3}{8E} \left( \frac{1}{\Delta L_{min}} - \frac{1}{\Delta L_{min} + \lambda} \right) = \frac{m_{CS} g L_0}{8} \left( \frac{1}{T_C} - \frac{1}{T_C + k_{CS}\lambda} \right). \tag{8.9}$$

Here, $m = 2m_S + m_C = 31.9\,\text{g}$ is the weight of two straws and one carbon fibre tow. The equation is meaningfully solved by

$$T_C = -\frac{k_{CS}\lambda}{2} + \sqrt{\left( \frac{k_{CS}\lambda}{2} \right)^2 + \frac{E m_{CS} k_{CS} \Delta L_{min}(\Delta L_{min} + \lambda)}{\rho L_0^2}} \tag{8.10}$$

$$= 55.4\,\text{N}. \tag{8.11}$$

This is the minimum tension required for the carbon fibre tow and the springs. Using $T_C$ the sagging of the carbon fibre tow held in at both sides by springs and carrying a pair of two straws can be written as:

$$s_{CS} = \frac{m_{CS} g l}{8} \frac{1}{T_C + T_{CS}} = \frac{m_{CS} g l}{8} \frac{1}{T_C + k_{CS}(\Delta L - \Delta L_{min})}. \tag{8.12}$$

This is shown in figure 8.10 as a dotted line. Within the shaded area the sagging of the spring-held carbon fibre tow and the wire behaves almost identically.
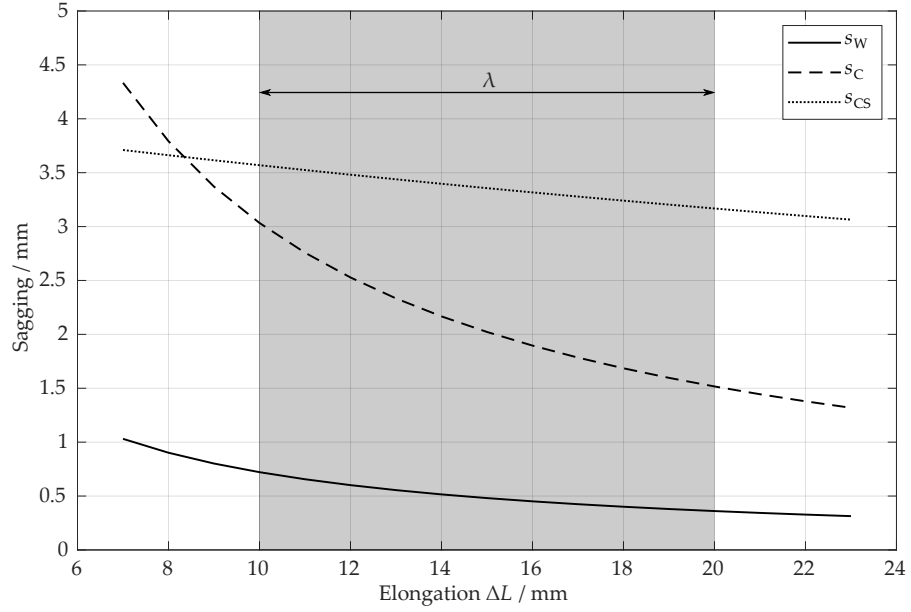


Figure 8.10: The sagging of the dual spring-held carbon fibre tow carrying two straws (dotted line) compared to the sagging without the springs (dashed line) and the sagging of the anode wire (continuous line). Within the allowed range $\lambda$ the sagging of the spring-held tow and the wire behave almost identically.

The design of the new frame is based on a model where the parts of each SST station are considered as a spring. In figure 8.11 an equivalence diagram illustrates the model including its temporal dynamic. In this model the Mylar is described by Maxwell's model of viscoelasticity and is depicted as a combination of a piston and a spring with a spring constant $k_M$. The description via the model of viscoelasticity is required to characterise the Mylar's relaxation via the force $F_R$. The wire, the carbon fibre tow with its two springs as well as the mounting frame are described as springs with spring constants $k_W, k_C, k_S$ and $k_F$ respectively. Using the vacuum force $F_V$ the vacuum-induced elongation $\Delta L_V$ can be written as

$$\Delta L_V = \frac{\Delta F_V}{\frac{1}{2}\left(k_F + k_{CS}\right) + k_R + k_W}. \tag{8.13}$$

Similarly, the elongation due to the Mylar relaxation $\Delta L_M$ can be described as

$$\Delta L_R = \frac{\Delta F_R}{\frac{1}{2}\left(k_F + k_{CS}\right) + k_W}. \tag{8.14}$$

The sum of both elongations is not allowed to be larger than the elastic range:

$$\Delta L_V + \Delta L_R = \lambda = 10\,\text{mm}. \tag{8.15}$$
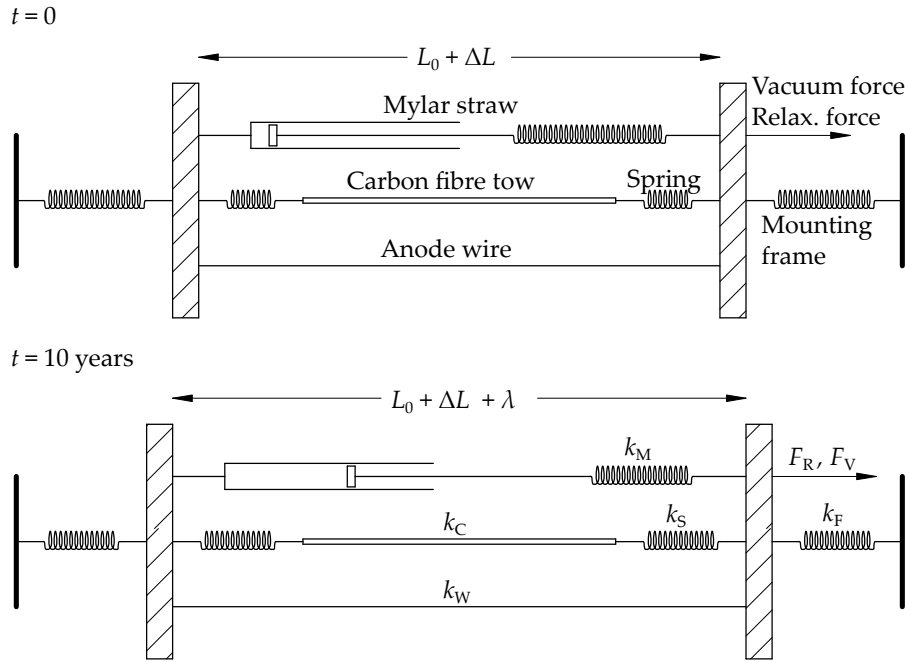
Figure 8.11: Equivalence diagram of the mechanical elements in the frame at the beginning and after ten years, where the frame will have unbent by $\lambda$. The straw is partly a spring but also partly elastic. The spring-held carbon fibre tow as well as the wire and the frame itself are assumed to be springs.

Equations (8.13), (8.14) and (8.15) form an equation system with three unknowns. Physically valid solutions are

$$\Delta L_V \simeq 5.02\,\text{mm} \tag{8.16}$$

$$\Delta L_M \simeq 4.98\,\text{mm} \tag{8.17}$$

$$k_F \simeq 10.39\,\text{N}\,\text{mm}^{-1}. \tag{8.18}$$

The spring constant of the frame can be translated into the elastic bending of the frame's walls. The value $k_F = 10.39\,\text{N}\,\text{mm}^{-1}$ means that if each straw pulls with a force of 10.39 N each wall may bend by exactly 1 mm. Roughly, the frame carries 4000 straws per 10 m resulting in $n = 0.4$ straws per millimetre. Thus, for a distributed load of

$$q = nk_F = 4.16\,\text{N}\,\text{mm}^{-1} \tag{8.19}$$

a wall may bend by 1 mm. The text-book relation [XXX] for the bending $\delta$ of a single steel beam with a length of $l$, a modulus of elasticity $E$ and an area moment of inertia $I$ is given by

$$\delta = \frac{5ql^4}{384EI}. \tag{8.20}$$

From this relation the required area moment of inertia $I$ can be calculated as

$$I = 4.29 \times 10^{-3}\,\text{m}^4. \tag{8.21}$$

Here it was assumed that $E = 1.9 \times 10^{11}\,\mathrm{N\,m^{-2}}$ as is the case for many types of austenitic steels. Using this value a suitable frame consisting out of smaller beams was designed. Figure 8.12 compares the profile of the older HEM1000 beams to the newly designed beams. For each
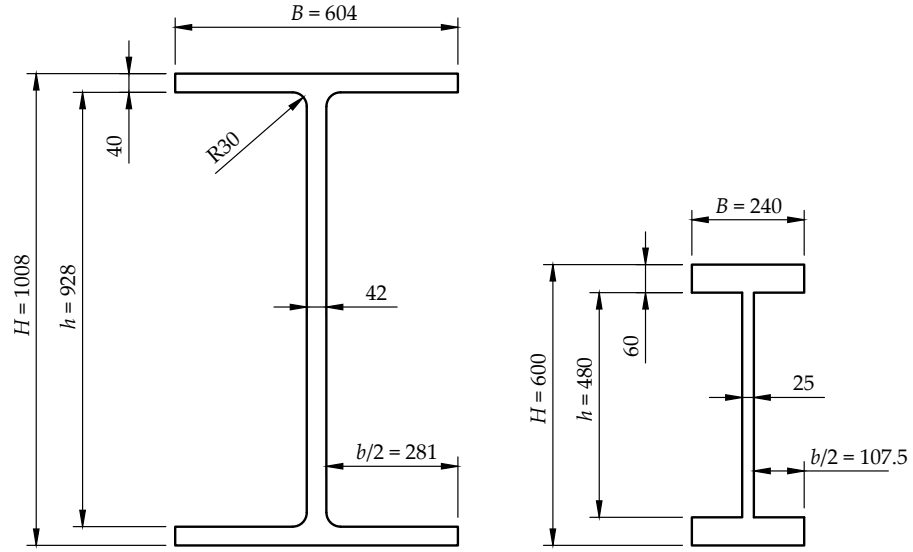


Figure 8.12: Comparison between the profile of the HEM1000 beams utilised in the large frame (left) and the beams used in the smaller frame (right). The smaller beams are not standardised. A standardised beam with an equivalent strength, the HEM600 would be slightly larger than the custom beam. All quantities are given in units of millimetres.

beam the relevant area moment of inertia is given by

$$I_{\text{beam}} = \frac{1}{12}\left(BH^3 - bh^3\right). \tag{8.22}$$

with $B, b, H, h$ as indicated in figure 8.12. Thus, each wall consisting of two beams has an area moment of inertia of

$$I = 2I_{\text{beam}} = 4.67 \times 10^{-3}\,\mathrm{m^4}. \tag{8.23}$$

Note that the newly designed beams are not standardised beam profiles that cannot be bought readily. Instead, they are welded together out of three steel plates. This step had to be taken as an equivalently strong standardised beam profile like the HEM600 would be larger with $H = 600\,\mathrm{mm}$ and $B = 305\,\mathrm{mm}$. The new frame is shown in figure 8.13. This frame follows the same design as the HEM1000 based frame. However, with a height of 11 460 mm, a width of 6400 mm and a depth of 990 mm it is considerably smaller than the old design. Note that the distance between the two walls of the frame has increased from 5000 mm in the old design to 5200 mm in the new design. This is because in the new design the modules are no longer planned to be installed from the top of the frame but rather from the front. To do so,

Figure 8.13: Comparison between the larger and the smaller frame. The smaller frame is 0.54 m less tall, 0.696 m less wide and 0.114 m less deep. Otherwise, the basic design features such as the intermediate floors are similar.

extra space is needed. With a mass of 25.8 t the smaller frame is about 2.6 t lighter than its larger precursor.

Similar to the old frame an FEM-analysis of the new frame was done using Fusion 360. The results are shown in figure 8.14. For a total load of 36 t each wall of the frame bends inwards by 1.64 mm. A similar study was done for a load of 11 t resulting in a bending of 0.50 mm. This indicates a maximum elongation of 2.28 mm over the lifetime of the SST station. This is well below the maximum allowed bending of 10 mm and leaves an ample safety factor.
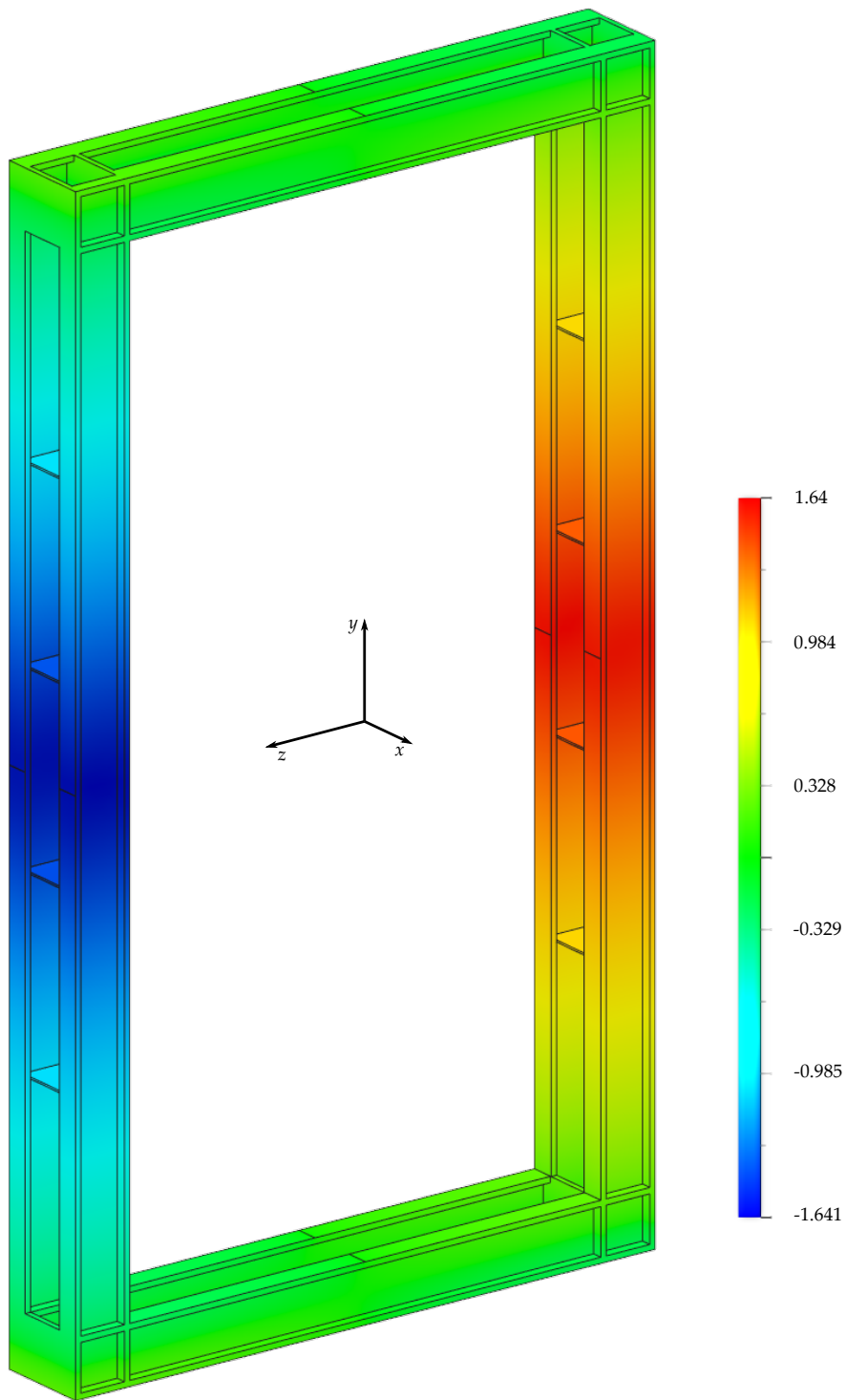
Figure 8.14: Results of an FEM analysis for the smaller frame. A total force of
36 t pulls both walls inwards, resulting in a maximum bending
of 1.6 mm per wall. Note that for the simulation it was assumed
that the frame is a single solid part. The colour scale indicates
the displacement in $z$ direction in units of millimetres.

## 8.3    SUMMARY AND OUTLOOK

The SST will consist of four stations, each consisting of a large mounting frame housing several modules which hold the straw tubes. A small-scale prototype for a module, the quad-straw prototype was described in detail in chapter 6. For the actual modules several designs were considered. In the first design a single module held 256 straws and 15 modules were planned to be stacked on top of each other. In each module the straws were arranged in a u-y-y-v layout. However, this specific design would have complicated possible maintenance work. Thus, the design was revised. Currently, smaller modules are planned which hold 64 straws each. Four of these modules can then be arranged in a $y - u - v - y$ layout with 16 horizontal and 15 stereo modules per view. In future the modules will have to be further revised, especially as required design changes which are revealed by the quad-straw prototype are incorporated in the design. Furthermore, a temporary support structure must be designed, as the two endplates of modules are just connected to each other by the straws, the wires and the carbon fibre tows meaning that a module by itself is completely unstable. Since it is planned to assemble the modules off-site a temporary frame must be designed giving each module enough rigidity such that they can be transported and installed securely. Moreover, the method of how to attach the modules to the mounting frame must be specified.

For the mounting frames which will hold the modules several designs were considered too. The main difficulty are the dynamic forces acting on the mounting frame. Initially, a tensioning force of 36 t acts on the frame, however, over the course of ten years, this force diminishes to roughly 11 t. This results in the frame unbending and thus changing the sagging of the wires and the carbon fibre tows. The different sagging behaviours cause a net wire displacement. In the first design of the frame the total elongation was minimised, resulting in a very strong, but inconveniently large frame manufactured out of stainless steel beams. Accommodating this frame into the vacuum vessel would have required significant changes to the vessel. Thus, the design was revised resulting in a smaller frame which bends more under the occurring forces – but less than 10 mm. However, this means that additional springs are required in the modules to match the carbon tows' sagging behaviour to the one of the wires. An FEM-analysis of the frame was performed, which indicated that over ten years the frame will unbend by roughly 2 mm. This is well below the limit of 10 mm although it has to be considered that the simulation is likely rather optimistic. This is because in the simulation it was assumed that the frame is a single, solid part and not a large assembly consisting of various different parts. In future, it is planned to improve the accuracy of the simulation results. To do so it has to determined

how the steel beams of the mounting frame are connected to each other. Afterwards, these features must be implemented in the 3D-model and the simulation can be redone. Furthermore, the material choice for the beams must be defined such that accurate values for the beams' moments of inertia can be used in the simulation. Moreover, the proposed way of changing the sagging behaviour of the carbon fibre tow under elongation must be verified experimentally in future. It is currently investigated whether or not the existing quad-straw prototype will be adapted such that the design with the springs can be tested, or whether a new prototype will be built.

# GENERAL CONCLUSION AND OUTLOOK

'Acta est fabula, plaudite!'

*'The play is over, applaud!'*

— Augustus. In Suetonius *Divus Augustus*, Book 99, Paragraph 1, as translated by Evelyn
S. Shuckburgh, Polybius, Histories Press

Within the scope of this thesis a single-straw functional model for SHiP's Spectrometer Straw Tracker was developed. After the parts were designed and manufactured they were assembled successfully. A simple gas-system and read-out electronics were connected and the single-straw functional model was put into operations. Some measurements of the drift-time spectra gave the expected form with lengths between 700 ns to 800 ns while other measurements indicated significant noise. The signal attenuation of the single straw was measured by acquiring signals of a Fe-55 source placed at different locations along the straw.

Two different methods were used to determine the signal attenuation. Using the pulse height gave an attenuation of roughly 1 % while using the signal integral gave an attenuation of approximately 17 %. Given the signal attenuation in OPERA's drift tubes the latter value seems to be more realistic. Both methods however did not show an exponential attenuation, which was likely caused by the sagging of the straw. During the operation of the single-straw functional model high noise levels were observed. It was found that these were caused by an improper grounding of the mounting frame. They were solved by directly connecting the functional model's mounting hardware with a ground pin of the electronics. Nevertheless some noise remained, especially during working hours where the noise rate was significantly higher than at night. This is likely caused by electromagnetic pickup and planned to be remedied in future using an electromagnetic shield around the functional model.

After the single-straw functional model was successfully commissioned a quad-straw prototype using four straw tubes was designed with the goal of testing the mechanics for the proposed SST modules. In this design the straws are glued onto straw endpieces which are screwed into endplates using special screws. The anode wires are held in using special holders. Using carbon fibre tows the sagging of the straw tubes can be controlled. After all required parts were designed as a 3*D* model they were manufactured and most of them assembled. During assembly some changes to the endpieces were required. It also became apparent that the current design of the wire holders was improvable. Furthermore, it became clear that the method of pulling the

wire through the straw tube must be revised. Pulling the wire through the straw using a magnet resulted in visible damage to the straw tube. Better methods based on air pressure or using a special sled with soft rubber wheels will be investigated in future. The sagging of the straw without the support of a carbon fibre tow was determined using an optical level. The maximum sagging in the middle is given by 2.1 mm which corresponds well with the expected value. For the wire the sagging was determined using two different ways, both of which relied on an LED system. This LED system was specifically designed and built for the purpose of shining light through the straws to make the wires visible. The first method of measuring the wire's sagging relied on an optical microscope and gave inconsistent and unrealistic results. This behaviour was likely to be caused by the microscope's unstable holder as well as the straw tube's inconsistent height and the fact that at some locations overlapping straw tubes had to be moved out of the way manually. The second method was based on the optical level and indicated a maximum sagging of 0.58 mm corresponding well with the expected sagging. In future the support mechanism of the straw tubes remains be installed. After that the sagging of the straws can be re-measured such that the effectiveness of the sagging countermeasures can be verified experimentally. Most importantly however, meaningful signals must be measured with the quad-straw prototype. Currently, the noise rate of the prototype is in the order of $\mathcal{O}(10^6)$ Hz. This effect is very likely caused by improper grounding of the frame mounting frame, as the single-straw functional model shows the same issues. Both the functional model and the prototype are planned to be isolated from the mounting frame to alleviate the grounding problems. Additionally an electromagnetic shield will be implemented.

Another aspect that was covered within this thesis are surface analyses of the straws' electrical coating which were performed using a scanning electron microscope. Damages to this coating can easily occur, especially during installation. It was found that the current method of installing the wire by pulling it through the straw using a magnet caused significant scratches with a width of 2 μm. Almost unavoidable kinks in the straw tube showed clear damages to the coating with up to 6 μm wide cracks. Moreover, it was found that significant portions of the straws' weld seam are not covered by the coating. This was verified by means of an energy-dispersive X-ray analysis. The effect of these damages and the absence of the coating at the weld seam on the detector performance is currently unknown and needs to be determined in future. To do so, either simulations may be used or a straw tube may be damaged deliberately so that the effect can be determined experimentally. Another aspect analysed within the scope of this thesis is the effect of the straws' tensioning – and thus their elongation – on the coating. For this purpose two

tensioning devices were built which allow a small section of a straw to be tensioned accurately. Here it was found that no significant damages occur within the straws' expected operating range (elongations less than 40 mm). Significant damage only occurred for elongations larger than approximately 167 mm.

Finally, the current status of the large-scale integration was presented within this thesis. The Spectrometer Straw Tracker will consist of four stations two of which are each located on either side of the dipole magnet. Each station will consist of a large mounting frame made out of stainless steel beams. The main problem with these frame are the dynamic forces acting on it. While initially the total force is given by 36 t this force diminishes down to 11 t over the course of 10 years. This causes the frame to un-bend, changing the sagging of the carbon tows and the wires. Due to the different sagging behaviours this results in a net wire displacement. The first mounting frame was designed to bend by such a small amount that no significant net wire displacement would occur. However, this frame turned out to be too large to integrate it into the vacuum vessel. Currently, a smaller frame is proposed which is allowed to bend more. To alleviate a net wire displacement the sagging behaviour of the carbon fibre tows is matched to the one of the wires by means of compression springs. Using the finite element method it was verified that the de-bending of the smaller frame is well below the maximum allowed bending. Concerning the modules two different versions were considered. In the first design each module held 256 straws in a *u-y-y-v* order. This design was later revised, as it would have made maintenance more complicated. In the current design each module holds 64 straws. Due to the design, four modules can be arranged in the more common *y-u-v-y* layout. Each frame will hold 16 horizontal and 15 stereo modules. in future, the module and frame design will have to be finalised. In particular, it must be checked how the required spring for the carbon fibre tow can be integrated into the module design. For the frame, more accurate FEM analyses may be done in future, when the design is further specified.

# NOISE ANALYSES OF THE SINGLE-STRAW FUNCTIONAL MODEL

## A.1 NOISE

Measuring the long-term base noise of the single straw functional model revealed that at workdays the noise rate is significantly increased during working hours – see section 5.3.2 and figures **??** and 5.16. A zoom into the regions with high noise reveals a striking substructure. It can be seen that the measured signal consists of a plenitude of different signal rate pulses, as illustrated in figure A.1 showing a six-hour excerpt of figure 5.15. A further zoom on a single
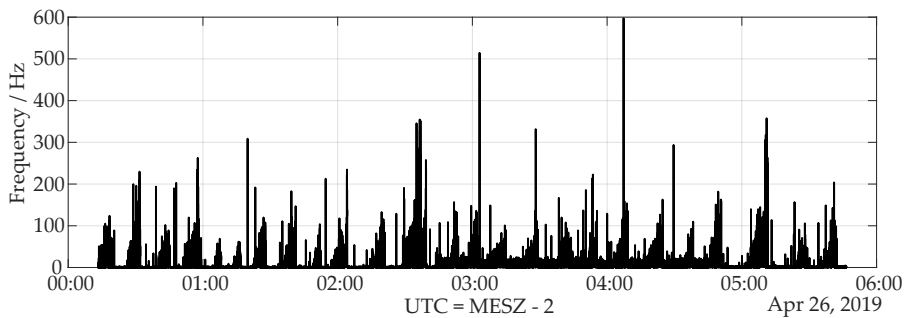
Figure A.1: A zoom into part of figure 5.15. It is clearly shown how the noise frequency consist of several signal rate pulses.

pulse, shown in figure A.2, reveals that in each pulse the signal rate fluctuates almost alternatingly from or near the base-level to an increasingly higher level before decreasing rapidly. In order to further
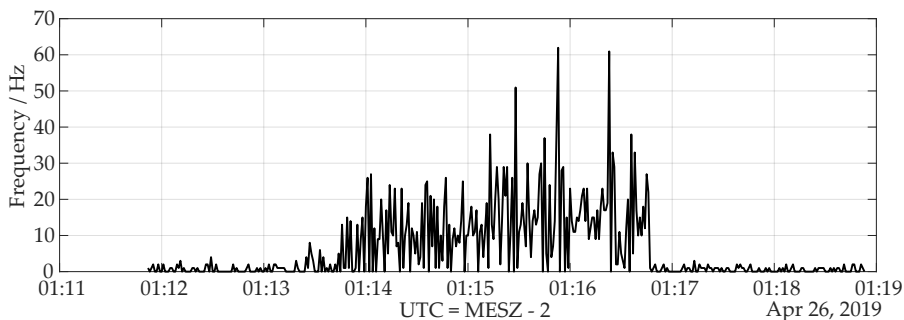
Figure A.2: A further zoom into part of figure A.1. It shows a single signal rate pulse where the frequency alternates between the base level and an increased level.

analyse these pulses the complete data-set was smoothed using a Gaussian kernel with a width of $\sigma = 10\,\mathrm{s}$. Figure A.3 shows the

*Width in this case means the full-width at half maximum (FWHM).*

smoothed pulses originally depicted in figure A.1. For these smoothed
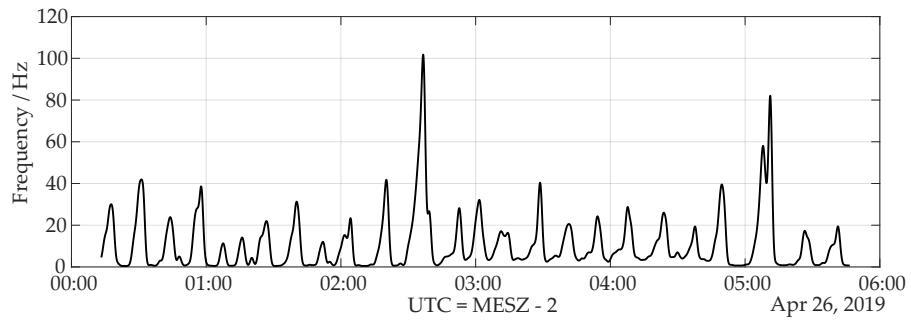


Figure A.3: A smoothed zoom into figure figure 5.15. The shown area is identical to the one depicted in figure A.1. The smoothing was achieved by various passes of a gaussian kernel.

pulses the FWHM – i.e. the pulse width – as well as the pulse heights and the time between pulses was determined. The results are shown as histograms in figures A.4, A.5 and A.6 respectively.

The pulse widths follow a symmetrical distribution around a mean of

$$\bar{w} = (194.77 \pm 74.55)\,\text{s}. \tag{A.1}$$

The pulse height distribution is slightly skewed towards smaller heights with a total mean of

$$\bar{h} = (44.88 \pm 40.91)\,\text{Hz}. \tag{A.2}$$

The symmetrical distribution of the time between frequency pulses ranges around a mean of

$$\bar{t} = (718.13 \pm 240.82)\,\text{s}. \tag{A.3}$$

Thus, during working hours approximately every twelve minutes the noise rate is increased by 45 Hz for around three minutes. There are no clear, distinct causes for this behaviour other than the possibility of electromagnetic pickup that may be caused by a device running only during daytime. Sources from within the laboratory are unlikely to cause this effect as no changes to the measurement setup were made during the measurement. Also, turning unnecessary devices off yielded no improvement in further tests. This leaves devices from neighbouring laboratories or the adjacent PETRA III experimental hall as possible noise sources, which may be investigated more closely in future.
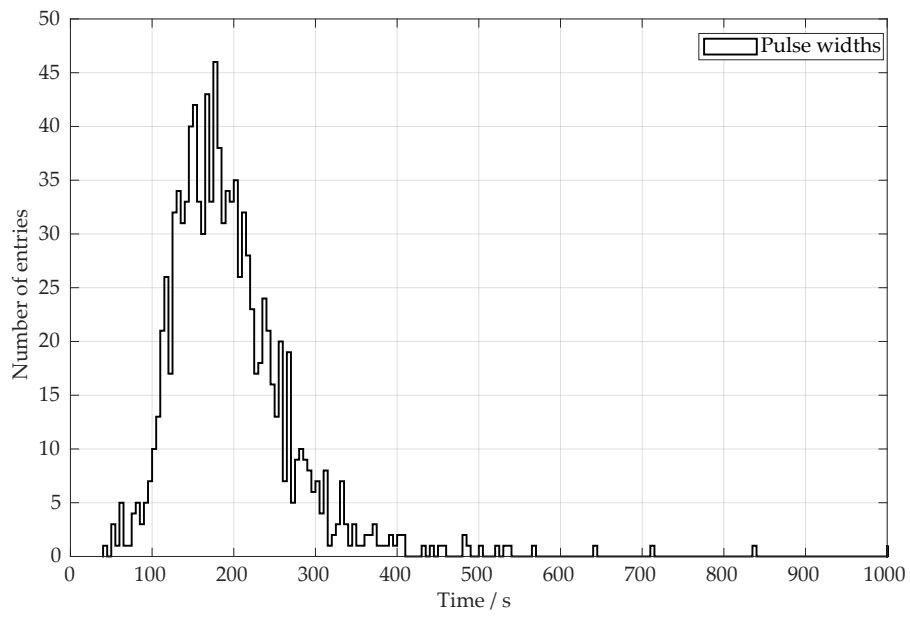
Figure A.4: Histogram of the widths of the frequency pulses. The histogram shows a symmetrical distribution around an average of $(197 \pm 75)$ s.
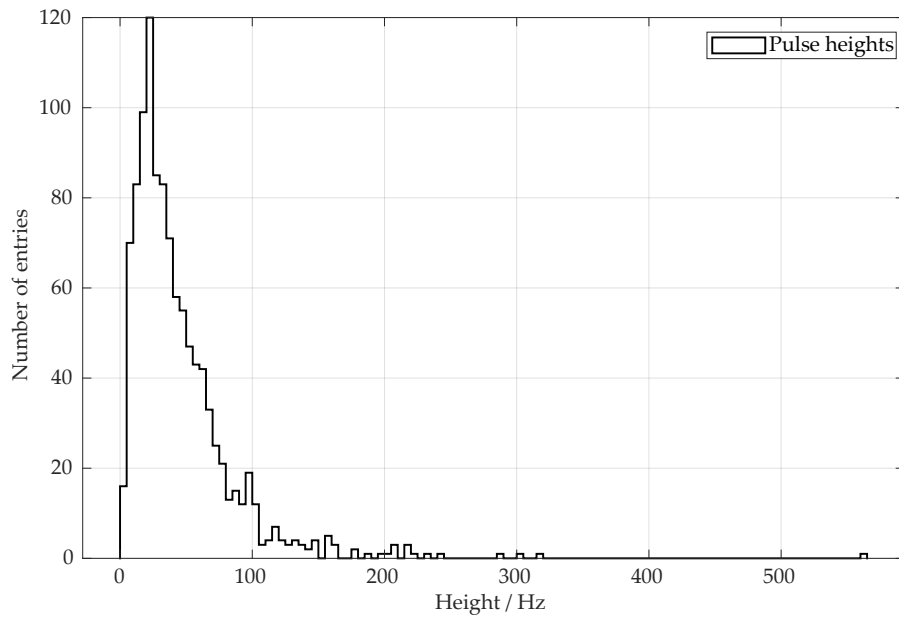


Figure A.5: Histogram of the heights of the frequency pulses. The histogram shows a distribution skewed towards lower heights with an average of $(45 \pm 41)$ Hz.
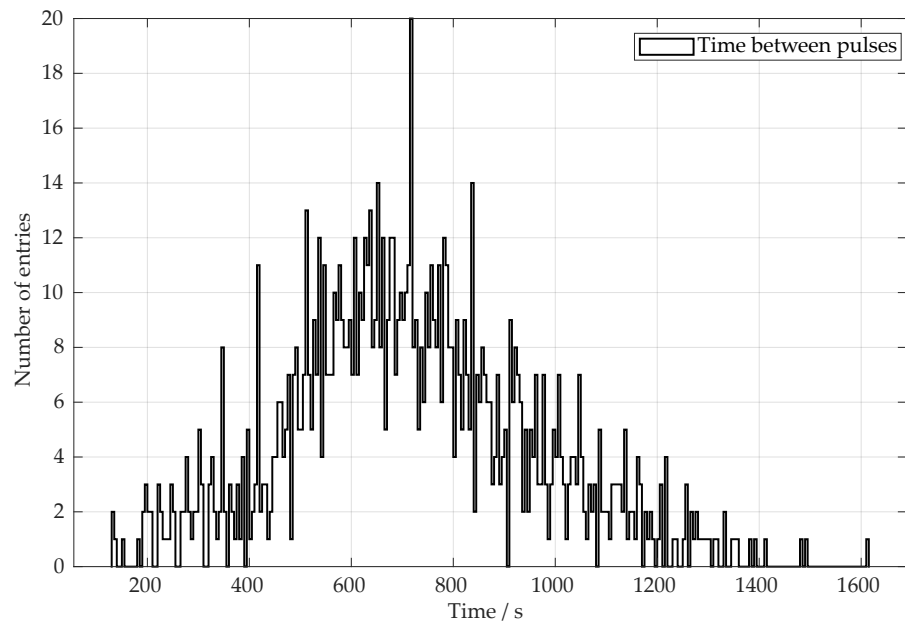
Figure A.6: Histogram of the times between two frequency pulses. The histogram shows a symmetrical distribution around an average of $(718 \pm 241)\,\text{s}$.

# B

SOFTWARE

---

B.1 FIJI

Fiji is an open-source image processing package based on the java-based image processing program ImageJ – hence the name 'Fiji is just ImageJ' (Fiji). ImageJ is an image analysis program used in various sciences, including biology and physics.

B.2 MATLAB

B.3 AUTODESK FUSION 360

B.4 AUTODESK CFD 2019

B.5 SPRINT LAYOUT

B.6 KICAD

# C

TECHNICAL DRAWINGS
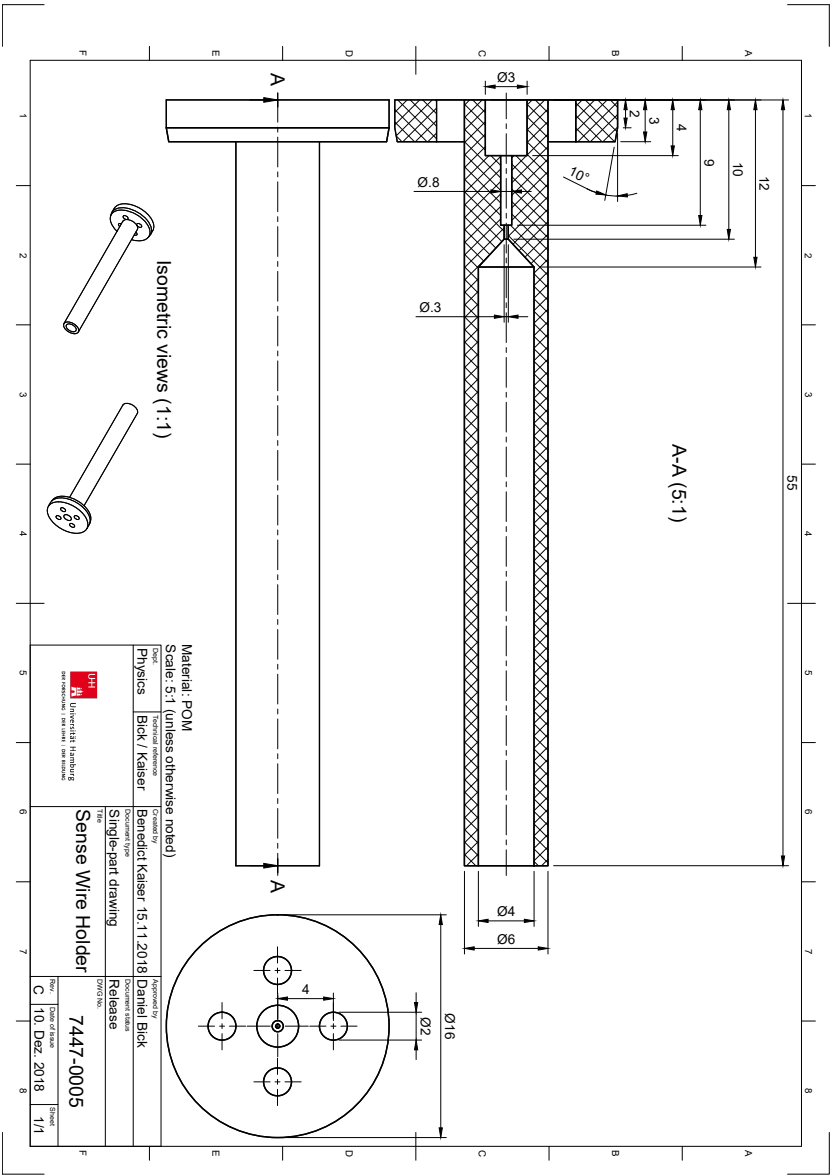
Figure C.1: Technical drawing of the wire holder. The drawing is not to scale.

## LIST OF FIGURES

# LIST OF TABLES

## BIBLIOGRAPHY

[05]        *AX-2S, AC-2S, AP-8 Auto Level User Guide*. NIKON Trimble Construction Division. 1st Aug. 2005.

[18]        *DURIS S10. Datasheet GW P7LM32.EM*. Version 1.2. OS-RAM Opto Semiconductors GmbH. 17th Jan. 2018.

[19a]       *Datenblatt Produkt SK 48 …* Fischer Elektronik GmbH & Co. KG. 2019.

[19b]       *Dino-Lite AM7515MZT - EDGE*. IDEAL-TEK SA. 2019.

[Aad+12]    G. Aad et al. 'Observation of a new particle in the search for the Standard Model Higgs boson with the ATLAS detector at the LHC'. In: *Physics Letters B* 716.1 (Sept. 2012), pp. 1–29. DOI: 10.1016/j.physletb.2012.08.020.

[Aar+13]    M. G. Aartsen et al. 'First Observation of PeV-Energy Neutrinos with IceCube'. In: *Physical Review Letters* 111.2 (July 2013). DOI: 10.1103/physrevlett.111.021103.

[Aar+89]    P. Aarnio et al. 'Measurement of the mass and width of the Zo-particle from multihadronic final states produced in $e^+e^-$ annihilations'. In: *Physics Letters B* 231.4 (Nov. 1989), pp. 539–547. DOI: 10.1016/0370-2693(89)90706-5.

[AB18a]     Nobel Media AB, ed. *The Nobel Prize in Physics 1957*. 4th Oct. 2018. URL: https://www.nobelprize.org/prizes/physics/1957/summary/.

[AB18b]     Nobel Media AB, ed. *The Nobel Prize in Physics 1979*. 19th Oct. 2018. URL: https://www.nobelprize.org/prizes/physics/1979/summary/.

[AB19]      Nobel Media AB, ed. *The Nobel Prize in Physics 2002*. 28th Aug. 2019. URL: https://www.nobelprize.org/prizes/physics/2002/press-release/.

[Abd+06]    J. N. Abdurashitov et al. 'Measurement of the response of a Ga solar neutrino experiment to neutrinos from a $^{37}$Ar source'. In: *Physical Review C* 73.4 (Apr. 2006). DOI: 10.1103/physrevc.73.045805.

[Abd+96]    J. N. Abdurashitov et al. 'The Russian-American Gallium Experiment (SAGE) Cr Neutrino Source Measurement'. In: *Physical Review Letters* 77.23 (Dec. 1996), pp. 4708–4711. DOI: 10.1103/physrevlett.77.4708.

[Abr+13]    H. Abramowicz et al. 'Measurement of charm fragmentation fractions in photoproduction at HERA'. In: *Journal of High Energy Physics* 2013.9 (Sept. 2013). DOI: 10.1007/jhep09(2013)058.

[Acc+15]    R. Acciarri et al. *A Proposal for a Three Detector Short-Baseline Neutrino Oscillation Program in the Fermilab Booster Neutrino Beam*. 5th Mar. 2015. arXiv: `http://arxiv.org/abs/1503.01520v1 [physics.ins-det]`.

[Ach+65]    C. V. Achar et al. 'Detection of muons produced by cosmic ray neutrinos deep underground'. In: *Physics Letters* 18.2 (Aug. 1965), pp. 196–199. DOI: `10.1016/0031-9163(65)90712-2`.

[Ade+89]    B. Adeva et al. 'A determination of the properties of the neutral intermediate vector boson Z0'. In: *Physics Letters B* 231.4 (Nov. 1989), pp. 509–518. DOI: `10.1016/0370-2693(89)90703-x`.

[Aga+18]    N. Agafonova et al. 'Final Results of the OPERA Experiment on $\nu\tau$ Appearance in the CNGS Neutrino Beam'. In: *Physical Review Letters* 120.21 (16th Apr. 2018). DOI: `10.1103/physrevlett.120.211801`.

[Agu+01]    A. Aguilar et al. 'Evidence for neutrino oscillations from the observation of $\bar{\nu}_e$ appearance in a $\bar{\nu}_\mu$ beam'. In: *Physical Review D* 64.11 (Nov. 2001). DOI: `10.1103/physrevd.64.112007`.

[Agu+13]    A. A. Aguilar-Arevalo et al. 'Improved Search for $\bar{\nu}_\mu \rightarrow \bar{\nu}_e$ Oscillations in the MiniBooNE Experiment'. In: *Physical Review Letters* 110.16 (Apr. 2013). DOI: `10.1103/physrevlett.110.161801`.

[Agu+18]    A. A. Aguilar-Arevalo et al. *Observation of a Significant Excess of Electron-Like Events in the MiniBooNE Short-Baseline Neutrino Experiment*. 30th May 2018. arXiv: `http://arxiv.org/abs/1805.12028v1 [hep-ex]`.

[Agu+98]    M. Aguilar-Benítez et al. 'Study of magnetic field effects in drift tubes for the barrel muon chambers of the CMS detector at the LHC'. In: *Nuclear Instruments and Methods in Physics Research Section A: Accelerators, Spectrometers, Detectors and Associated Equipment* 416.2-3 (Nov. 1998), pp. 243–252. DOI: `10.1016/s0168-9002(98)00681-0`.

[Ahm+01]    Q. R. Ahmad et al. 'Measurement of the Rate of $\nu_e + d \rightarrow p + p + e^-$ Interactions Produced by $^8B$ Solar Neutrinos at the Sudbury Neutrino Observatory'. In: *Physical Review Letters* 87.7 (July 2001). DOI: `10.1103/physrevlett.87.071301`.

[Ahm+02]    Q. R. Ahmad et al. 'Direct Evidence for Neutrino Flavor Transformation from Neutral-Current Interactions in the Sudbury Neutrino Observatory'. In: *Physical Review Letters* 89.1 (June 2002). DOI: `10.1103/physrevlett.89.011301`.

[Ake+03]    T. Akesson et al. 'Aging studies for the ATLAS Transition Radiation Tracker (TRT)'. In: *Nuclear Instruments and Methods in Physics Research Section A: Accelerators, Spectrometers, Detectors and Associated Equipment* 515.1-2 (Dec. 2003), pp. 166–179. DOI: 10.1016/j.nima.2003.08.145.

[Akh00]    E. Kh. Akhmedov. *Neutrino physics*. 25th Jan. 2000. arXiv: http://arxiv.org/abs/hep-ph/0001264v2 [hep-ph].

[Akr+89]    M.Z. Akrawy et al. 'Measurement of the Z0 mass and width with the opal detector at LEP'. In: *Physics Letters B* 231.4 (Nov. 1989), pp. 530–538. DOI: 10.1016/0370-2693(89)90705-3.

[Ale+16]    Sergey Alekhin et al. 'A facility to search for hidden particles at the CERN SPS: The SHiP physics case'. In: *Reports on Progress in Physics* 79.12 (Oct. 2016), p. 124201. DOI: 10.1088/0034-4885/79/12/124201.

[Ale+88]    E. N. Alexeyev et al. 'Detection of the neutrino signal from SN 1987A in the LMC using the INR Baksan underground scintillation telescope'. In: *Physics Letters B* 205.2-3 (Apr. 1988), pp. 209–214. DOI: 10.1016/0370-2693(88)91651-6.

[All15]    James Sircom Allen. *The Neutrino. (IP-5)*. Princeton University Press, 2015. 180 pp. ISBN: 0691626472. URL: https://www.ebook.de/de/product/25086850/james_sircom_allen_the_neutrino_ip_5.html.

[Ams+08]    C. Amsler et al. 'Review of Particle Physics'. In: *Physics Letters B* 667.1-5 (Sept. 2008), pp. 1–6. DOI: 10.1016/j.physletb.2008.07.018.

[An+16]    Fengpeng An et al. 'Neutrino physics with JUNO'. In: *Journal of Physics G: Nuclear and Particle Physics* 43.3 (Feb. 2016). DOI: 10.1088/0954-3899/43/3/030401.

[Ane+15]    M. Anelli et al. *A facility to Search for Hidden Particles (SHiP) at the CERN SPS*. Technical Proposal. European Ogranization for Nuclear Research (CERN), 2015. arXiv: http://arxiv.org/abs/1504.04956v1 [physics.ins-det].

[Ara+05]    T. Araki et al. 'Experimental investigation of geologically produced antineutrinos with KamLAND'. In: *Nature* 436.7050 (July 2005), pp. 499–503. DOI: 10.1038/nature03980.

[Arn+89]    W. David Arnett et al. 'Supernova 1987A'. In: *Annual Review of Astronomy and Astrophysics* 27.1 (Sept. 1989), pp. 629–700. DOI: 10.1146/annurev.aa.27.090189.003213.

[Art18]    American Academy of Arts & Sciences, ed. *Recipients of the Rumford Prize*. 2018. URL: https://www.amacad.org/content/about/about.aspx?d=17&t=4&s=0 (visited on 16/10/2018).

[AS09]     E. Kh. Akhmedov and A. Yu. Smirnov. 'Paradoxes of neutrino oscillations'. In: *Physics of Atomic Nuclei* 72.8 (Aug. 2009), pp. 1363–1381. DOI: 10.1134/s1063778809080122.

[BD64]     J. N. Bahcall and R. Jr. Davis. *On the Problem of Detecting Solar Neutrinos*. Tech. rep. Brookhaven National Lab., Upton, N.Y.; California Inst. of Tech., Pasadena, CA, Jan. 1964. DOI: 10.2172/4002837.

[Bee16]    Johan H. de Beer. *The history of geophysics in Southern Africa*. African Sun Media, 31st Jan. 2016. ISBN: 9781920689803.

[Ber+12]   J. Beringer et al. 'Review of Particle Physics'. In: *Physical Review D* 86.1 (July 2012). DOI: 10.1103/physrevd.86.010001.

[Ber+86]   G. Bernardi et al. 'Search for neutrino decay'. In: *Physics Letters B* 166.4 (Jan. 1986), pp. 479–483. DOI: 10.1016/0370-2693(86)91602-3.

[Ber+88]   G. Bernardi et al. 'Further limits on heavy neutrino couplings'. In: *Physics Letters B* 203.3 (Mar. 1988), pp. 332–334. DOI: 10.1016/0370-2693(88)90563-1.

[Bet30]    H. Bethe. 'Zur Theorie des Durchgangs schneller Korpuskularstrahlen durch Materie'. In: *Annalen der Physik* 397.3 (1930), pp. 325–400. DOI: 10.1002/andp.19303970303.

[Bet32]    H. Bethe. 'Bremsformel für Elektronen relativistischer Geschwindigkeit'. In: *Zeitschrift für Physik* 76.5-6 (May 1932), pp. 293–299. DOI: 10.1007/bf01342532.

[Bie16]    Stefan Bieschke. 'Examination of different drift gas mixtures for the muon magnetic spectrometer for the SHiP experiment. Untersuchung verschiedener Driftgase für das Myon-Magnetspektrometer im SHiP Experiment'. MA thesis. Universität Hamburg, 2016.

[Bio+87]   R. M. Bionta et al. 'Observation of a neutrino burst in coincidence with supernova 1987A in the Large Magellanic Cloud'. In: *Physical Review Letters* 58.14 (Apr. 1987), pp. 1494–1496. DOI: 10.1103/physrevlett.58.1494.

[BKL92]    S. A. Bludman, D. C. Kennedy and P. G. Langacker. 'Seesaw model solutions of the solar neutrino problem'. In: *Nuclear Physics B* 374.2 (Apr. 1992), pp. 373–391. DOI: 10.1016/0550-3213(92)90358-i.

[Bon+18]    Kyrylo Bondarenko et al. 'Phenomenology of GeV-scale heavy neutral leptons'. In: *Journal of High Energy Physics* 2018.11 (6th Nov. 2018). DOI: 10.1007/jhep11(2018)032.

[Buo17]    Annarita Buonaura. 'Status and Physics of the SHiP experiment at CERN'. In: *Proceedings of XXV International Workshop on Deep-Inelastic Scattering and Related Subjects - PoS (DIS2017)*. Vol. 297. Sissa Medialab, Oct. 2017. DOI: 10.22323/1.297.0079.

[CA+08a]    The ATLAS TRT Collaboration, E Abat et al. 'The ATLAS TRT Barrel Detector'. In: *Journal of Instrumentation* 3.02 (Feb. 2008), P02014–P02014. DOI: 10.1088/1748-0221/3/02/p02014.

[CA+08b]    The ATLAS Collaboration, G Aad et al. 'The ATLAS Experiment at the CERN Large Hadron Collider'. In: *Journal of Instrumentation* 3.08 (Aug. 2008), S08003–S08003. DOI: 10.1088/1748-0221/3/08/s08003.

[Cap+14]    F. Capozzi et al. 'Status of three-neutrino oscillation parameters, circa 2013'. In: *Physical Review D* 89.9 (May 2014). DOI: 10.1103/physrevd.89.093018.

[CD13]    G. D. Coughland and James Dodd. *Elementarteilchen - Eine Einführung für Naturwissenschaftler*. Berlin Heidelberg New York: Springer-Verlag, 2013. ISBN: 978-3-322-83120-0.

[CER12]    CERN. *Dark matter*. Jan. 2012. URL: http://cds.cern.ch/record/1997200.

[CH16]    Jun Cao and Miao He. 'Neutrino oscillation: discovery and perspectives'. In: *Science Bulletin* 61.1 (Jan. 2016), pp. 48–51. DOI: 10.1007/s11434-015-0969-7.

[Cha32a]    J. Chadwick. 'Possible Existence of a Neutron'. In: *Nature* 129.3252 (Feb. 1932), pp. 312–312. DOI: 10.1038/129312a0.

[Cha32b]    J. Chadwick. 'The Existence of a Neutron'. In: *Proceedings of the Royal Society A: Mathematical, Physical and Engineering Sciences* 136.830 (June 1932), pp. 692–708. DOI: 10.1098/rspa.1932.0112.

[Col18]    Icecube Collaboration. 'Neutrino emission from the direction of the blazar TXS 0506+056 prior to the IceCube-170922A alert'. In: *Science* (July 2018). DOI: 10.1126/science.aat2890.

[Cow+56]    C. L. Cowan et al. 'Detection of the Free Neutrino: a Confirmation'. In: *Science* 124.3212 (July 1956), pp. 103–104. DOI: 10.1126/science.124.3212.103.

[Cra11]    Glen Crawford. *Office of High Energy Physics. Program and Budget Status*. AAAC meeting. 23rd Feb. 2011.

[Dan+62]    G. Danby et al. 'Observation of High-Energy Neutrino Reactions and the Existence of Two Kinds of Neutrinos'. In: *Physical Review Letters* 9.1 (July 1962), pp. 36–44. DOI: 10.1103/physrevlett.9.36.

[Dec+90]    D. Decamp et al. 'A precise determination of the number of families with light neutrinos and of the Z boson partial widths'. In: *Physics Letters B* 235.3-4 (Feb. 1990), pp. 399–411. DOI: 10.1016/0370-2693(90)91984-j.

[DHH68]    Raymond Davis, Don S. Harmer and Kenneth C. Hoffman. 'Search for Neutrinos from the Sun'. In: *Physical Review Letters* 20.21 (May 1968), pp. 1205–1209. DOI: 10.1103/physrevlett.20.1205.

[Die56]    Ward Diethorn. 'A Methane Proportional Counter System for Natural Radiocarbon Measurements'. Thesis. Pittsburgh, Pennsylvania: Carnegie Institute of Technology, 16th Mar. 1956.

[Dor+86]    J. Dorenbosch et al. 'A search for decays of heavy neutrinos in the mass range $0.5 - 2.8\,\text{GeV}$'. In: *Physics Letters B* 166.4 (Jan. 1986), pp. 473–478. DOI: 10.1016/0370-2693(86)91601-1.

[Dub11]    Jörg Dubbert. 'EDIT 2011 - Drift Tubes'. 31st Jan. 2011.

[Dvo11]    Maxim Dvornikov. 'Field theory description of neutrino oscillations'. In: *Neutrinos: Properties, Sources and Detection*. Ed. by J. P. Greene. Nova Science Publishers New York, 2011, pp. 23–90. arXiv: https://arxiv.org/abs/1011.4300v2 [hep-ph].

[Egu+03]    K. Eguchi et al. 'First Results from KamLAND: Evidence for Reactor Antineutrino Disappearance'. In: *Physical Review Letters* 90.2 (Jan. 2003). DOI: 10.1103/physrevlett.90.021802.

[Ele19]    Electrolube. *Technical Data Sheet. HTC Heat Transfer Compound*. 8th Jan. 2019. URL: https://www.electrolube.com/pdf/tds/044/HTC.pdf.

[Eno+07]    S. Enomoto et al. 'Neutrino geophysics with KamLAND and future prospects'. In: *Earth and Planetary Science Letters* 258.1-2 (June 2007), pp. 147–159. DOI: 10.1016/j.epsl.2007.03.038.

[Fer06]    Torben Ferber. 'Messung der Gaseigenschaften unter Einfluss von molekularem Sauerstoff und Aufbau eines Gassystems für das Driftröhren-Myon-Spektrometer des OPERA-Detektors. Measurement of gas properties with respect to the influence of molecular oxygen and design of a gas system for the drifttube myon spectrometer of the OPERA detector'. Diplomarbeit. Universität Hamburg, 2006.

[Fer33]   Enrico Fermi. 'Tentativo di una teoria dellemissione dei raggi'. In: *La Ricerca Scientifica*. 2nd ser. 12 (1933).

[Fer34]   Enrico Fermi. 'Versuch einer Theorie der $\beta$-Strahlen. I'. In: *Zeitschrift für Physik* 88.3-4 (Mar. 1934), pp. 161–177. DOI: 10.1007/bf01351864.

[Fil03]   DuPont Teijin Films. *Mylar polyester film*. 1st June 2003.

[Fou18]   Wolf Foundation, ed. *Chien-Shiung Wu Winner of Wolf Prize in Physics - 1978*. 4th Oct. 2018. URL: http://www.wolffund.org.il/index.php?dir=site&page=winners&cs=381.

[Fuk+98]   Y. Fukuda et al. 'Evidence for Oscillation of Atmospheric Neutrinos'. In: *Physical Review Letters* 81.8 (Aug. 1998), pp. 1562–1567. DOI: 10.1103/physrevlett.81.1562.

[Gai69]   Yves Gaillard. 'Magnet specification 1969 - Note'. EDMS 1326984. 1969.

[Gar+19]   Diego Garcia-Gamez et al. 'A novel electrical method to measure wire tensions for time projection chambers'. In: *Nuclear Instruments and Methods in Physics Research Section A: Accelerators, Spectrometers, Detectors and Associated Equipment* 915 (21st Jan. 2019), pp. 75–81. DOI: 10.1016/j.nima.2018.09.031.

[GGS58]   M. Goldhaber, L. Grodzins and A. W. Sunyar. 'Helicity of Neutrinos'. In: *Physical Review* 109.3 (Feb. 1958), pp. 1015–1017. DOI: 10.1103/physrev.109.1015.

[GH02]   T. K. Gaisser and M. Honda. 'Flux of Atmospheric Neutrinos'. In: *Annual Review of Nuclear and Particle Science* 52.1 (Dec. 2002), pp. 153–199. DOI: 10.1146/annurev.nucl.52.050102.090645.

[Gia09]   Douglas C. Giancoli. *Physik: Lehr- und Übungsbuch*. Pearson Studium, 2009. ISBN: 9783868940237. URL: https://www.amazon.com/Physik-%C3%9Cbungsbuch-Douglas-C-Giancoli/dp/3868940235?SubscriptionId=AKIAIOBINVZYXZQZ2U3A&tag=chimbori05-20&linkCode=xm2&camp=2025&creative=165953&creativeASIN=3868940235.

[Giu16]   Carlo Giunti. 'Light sterile neutrinos: Status and perspectives'. In: *Nuclear Physics B* 908 (July 2016), pp. 336–353. DOI: 10.1016/j.nuclphysb.2016.01.013.

[GL11]   Carlo Giunti and Marco Laveder. 'Statistical significance of the gallium anomaly'. In: *Physical Review C* 83.6 (June 2011). DOI: 10.1103/physrevc.83.065504.

[GLP16]   Giorgio Gratta, John Leaned and Sandip Pakvasa. *A Neutrino Timeline*. 2016. URL: http://kamland.stanford.edu/Timeline/.

[Gmb19a]    Evonik Resource Efficiency GmbH. *Product Information ROHACELL IG-F*. Evonik Resource Efficiency GmbH, 1st Jan. 2019.

[Gmb19b]    Febrotec GmbH. *Schraubendruckfedern - Artikelnummer Febrotec: 0X-RDF1661*. 2019. URL: https://www.febrotec.de/content.php?seite=shop/produkte.php&hauptrubrik=2&details=7149.

[Gol+16]    Christine G. Golding et al. 'The scanning electron microscope in microbiology and diagnosis of infectious disease'. In: *Scientific Reports* 6.1 (May 2016). DOI: 10.1038/srep26516.

[GP55]      M. Gell-Mann and A. Pais. 'Behavior of Neutral Particles under Charge Conjugation'. In: *Physical Review* 97.5 (Mar. 1955), pp. 1387–1389. DOI: 10.1103/physrev.97.1387.

[Gra19]     E. Graverini. 'The detectors of the SHiP experiment at CERN'. In: *Nuclear Instruments and Methods in Physics Research Section A: Accelerators, Spectrometers, Detectors and Associated Equipment* 936 (21st Aug. 2019), pp. 724–725. DOI: 10.1016/j.nima.2018.08.108.

[Gre61]     *Proceedings*. International Conference on Instrumentation for High Energy Physics, Berkeley, California, 1960. Lawrence Berkeley Lab, 1961. 321 pp.

[GS96]      W. Grimus and P. Stockinger. 'Real oscillations of virtual neutrinos'. In: *Physical Review D* 54.5 (Sept. 1996), pp. 3414–3419. DOI: 10.1103/physrevd.54.3414.

[Hab15]     Anja Habersetzer. '$\tau$ Vector Spectral Function from a Chirally Invariant Hadronic Model with Weak Interaction'. In: *Acta Physica Polonica B Proceedings Supplement* 8.1 (2015), p. 175. DOI: 10.5506/aphyspolbsupp.8.175. arXiv: https://arxiv.org/abs/1411.7881 [hep-ph].

[Hai+86]    T. J. Haines et al. 'Calculation of Atmospheric Neutrino-Induced Backgrounds in a Nucleon-Decay Search'. In: *Physical Review Letters* 57.16 (Oct. 1986), pp. 1986–1989. DOI: 10.1103/physrevlett.57.1986.

[Ham+98]    W. Hampel et al. 'Final results of the $^{51}$Cr neutrino source experiments in GALLEX'. In: *Physics Letters B* 420.1-2 (Feb. 1998), pp. 114–126. DOI: 10.1016/s0370-2693(97)01562-1.

[Hen13]     Philipp Henkenjohann. 'Theoretische Beschreibung und mögliche experimentelle Unterscheidung von Dirac- und Majorana-Neutrinos'. Bachelor's thesis. Universität Bielefeld, Fakultät für Physik, 19th Sept. 2013.

[Hir+87]    K. Hirata et al. 'Observation of a neutrino burst from the supernova SN1987A'. In: *Physical Review Letters* 58.14 (Apr. 1987), pp. 1490–1493. DOI: 10.1103/physrevlett.58.1490.

[Hol10]    Annika Hollnagel. 'Separation of Muons and Pions in the Electronic Detector of OPERA. Separation von Myonen und Pionen im Elektronischen Detektor von OPERA'. Corrected Version. Diplomarbeit. Universität Hamburg, 2010.

[ILS16]    *Duris S10 Family PowerStar*. Intelligent LED Solutions. 1st Mar. 2016.

[Inc18]    Cree Incorporated. *Cree XLamp CXA3070 LED. Product Family Data Sheet*. 3rd Dec. 2018.

[Kae+10]    F. Kaether et al. 'Reanalysis of the Gallex solar neutrino flux and source experiments'. In: *Physics Letters B* 685.1 (Feb. 2010), pp. 47–54. DOI: 10.1016/j.physletb.2010.01.030.

[Kai16]    Benedict Oliver Albert Kaiser. 'Inbetriebnahme eines Teststandes zur Charakterisierung von JUNO Photomultipliern. Commissioning of a test facility to characterise JUNO photomultipliers'. Bachelor's thesis. Universität Hamburg, 14th Nov. 2016. 139 pp.

[Kay08]    Boris Kayser. *Neutrino Oscillation Phenomenology*. 7th Apr. 2008. arXiv: http://arxiv.org/abs/0804.1121v3 [hep-ph].

[Kay81]    Boris Kayser. 'On the quantum mechanics of neutrino oscillation'. In: *Physical Review D* 24.1 (July 1981), pp. 110–116. DOI: 10.1103/physrevd.24.110.

[KG10]    Carbon Werke Weißgerber GmbH & Co. KG. *100g Carbon fiber roving NF-3*. 26th Mar. 2010.

[Kod+01]    K. Kodama et al. 'Observation of tau neutrino interactions'. In: *Physics Letters B* 504.3 (Apr. 2001), pp. 218–224. DOI: 10.1016/s0370-2693(01)00307-0.

[Kuc+17]    N. A. Kuchinskiy et al. '2-D straw detectors with high rate capability'. In: *Physics of Particles and Nuclei Letters* 14.3 (May 2017), pp. 493–503. DOI: 10.1134/s1547477117030116. URL: https://link.springer.com/article/10.1134/S1547477117030116.

[Kuc14]    Horst Kuchling. *Taschenbuch der Physik*. Hanser Fachbuchverlag, 8th Oct. 2014. 711 pp. ISBN: 3446442189.

[KW16]    Hermann Kolanoski and Norbert Wermes. *Teilchendetektoren*. Springer Berlin Heidelberg, 2016. DOI: 10.1007/978-3-662-45350-6.

[Leo94]    William R. Leo. 'The NIM Standard'. In: *Techniques for Nuclear and Particle Physics Experiments*. Springer Berlin Heidelberg, 1994, pp. 257–261. DOI: 10.1007/978-3-642-57920-2_12.

[Lor16]    Sebastian Lorenz. 'Topological Track Reconstruction in Liquid Scintillator and LENA as a Far-Detector in an LBNO Experiment'. PhD thesis. Universität Hamburg, 2016.

[LS05]     Thierry Lasserre and Henry W. Sobel. 'Reactor neutrinos'. In: *Comptes Rendus Physique* 6.7 (Sept. 2005), pp. 749–757. DOI: 10.1016/j.crhy.2005.08.002.

[LW06]     C. Lourenço and H.K. Wöhri. 'Heavy-flavour hadro-production from fixed-target to collider energies'. In: *Physics Reports* 433.3 (Oct. 2006), pp. 127–180. DOI: 10.1016/j.physrep.2006.05.005.

[Mal36]    Louis Malter. 'Thin Film Field Emission'. In: *Physical Review* 50.1 (July 1936), pp. 48–58. DOI: 10.1103/physrev.50.48.

[Mar60]    M. A. Markov. 'On high energy neutrino physics'. In: *Proceedings of the 1960 Annual International Conference on High Energy Physics at Rochester*. Ed. by E. C. G. Sudarshan, J. H. Tinlot and A. C. Melissinos. Interscience Publishers Inc., 1960, pp. 578–580.

[Men+11]   G. Mention et al. 'Reactor antineutrino anomaly'. In: *Physical Review D* 83.7 (Apr. 2011). DOI: 10.1103/physrevd.83.073006.

[MNS62]    Ziro Maki, Masami Nakagawa and Shoichi Sakata. 'Remarks on the Unified Model of Elementary Particles'. In: *Progress of Theoretical Physics* 28.5 (Nov. 1962), pp. 870–880. DOI: 10.1143/ptp.28.870.

[MS86]     S. P. Mikheyev and A. Yu. Smirnov. 'Resonant amplification of $\nu$ oscillations in matter and solar-neutrino spectroscopy'. In: *Il Nuovo Cimento C* 9.1 (Jan. 1986), pp. 17–26. DOI: 10.1007/bf02508049.

[Nak+86]   Masayuki Nakahata et al. 'Atmospheric Neutrino Background and Pion Nuclear Effect for KAMIOKA Nucleon Decay Experiment'. In: *Journal of the Physical Society of Japan* 55.11 (Nov. 1986), pp. 3786–3805. DOI: 10.1143/jpsj.55.3786.

[Oli16]    K. A. Olive. 'Review of Particle Physics'. In: *Chinese Physics C* 40.10 (Oct. 2016), p. 100001. DOI: 10.1088/1674-1137/40/10/100001.

[Pau30]    Wolfgang Pauli. *Liebe Radioaktive Damen und Herren. Of-fener Brief an die Gruppe der Radioaktiven bei der Gauvereins-Tagung zu Tübingen*. 1930. URL: http://microboone-docdb.fnal.gov/cgi-bin/RetrieveFile?docid=953&filename=pauli%20letter1930.pdf&version=1.

[Per+75]   M. L. Perl et al. 'Evidence for Anomalous Lepton Pro-duction in $e^+ - e^-$ Annihilation'. In: *Physical Review Letters* 35.22 (Dec. 1975), pp. 1489–1492. DOI: 10.1103/physrevlett.35.1489.

[Pet97]    Bradley M. Peterson. *An Introduction to Active Galactic Nuc-lei*. Cambridge University Press, 1997. ISBN: 978-0521473484. DOI: 10.1017/cbo9781139170901.

[Pic12]    Antonio Pich. *The Standard Model of Electroweak Interac-tions*. 2nd Jan. 2012. arXiv: http://arxiv.org/abs/1201.0537v1 [hep-ph].

[Pie18]    Cyril Patrick Pietsch. 'Standard Model Extensions with an Extra Higgs Singlet. One-Loop Renomalization and Col-lider Phenomenology'. PhD thesis. Technische Universität München, 2018. URL: http://mediatum.ub.tum.de?id=1432235.

[Pon57]    Bruno Pontecorvo. 'Mesonium and Antimesonium'. In: *Soviet Journal of Experimental and Theoretical Physics* 6 (1957). Zh. Eksp. Teor. Fiz.33,549(1957), p. 429.

[Pon58]    B. Pontecorvo. 'Inverse beta processes and nonconserva-tion of lepton charge'. In: *Soviet Journal of Experimental and Theoretical Physics* 7 (1958). [Zh. Eksp. Teor. Fiz.34,247(1957)], pp. 172–173.

[RA52]     George W. Rodeback and James S. Allen. 'Neutrino Re-coils Following the Capture of Orbital Electrons A$^{37}$'. In: *Physical Review* 86.4 (May 1952), pp. 446–450. DOI: 10.1103/physrev.86.446.

[RC59]     Frederick Reines and Clyde L. Cowan. 'Free Antineutrino Absorption Cross Section. I. Measurement of the Free Antineutrino Absorption Cross Section by Protons'. In: *Physical Review* 113.1 (Jan. 1959), pp. 273–279. DOI: 10.1103/physrev.113.273.

[Rei+65]   F. Reines et al. 'Evidence for High-Energy Cosmic-Ray Neutrino Interactions'. In: *Physical Review Letters* 15.9 (Aug. 1965), pp. 429–433. DOI: 10.1103/physrevlett.15.429.

[Ric14]    Ciro Riccio. 'Study of neutrino and anitneutrino inter-action in the near detector of the T2K experiment'. MA thesis. Università degli Studi di Napoli "Ferderico II", 2014.

[RRB08]    Luigi Rolandi, Werner Riegler and Walter Blum. *Particle Detection with Drift Chambers*. Springer Berlin Heidelberg, 2008. ISBN: 978-3-540-76683-4. DOI: 10.1007/978-3-540-76684-1.

[Sau18]    Fabio Sauli. *Gaseous Radiation Detectors*. Cambridge University Press, 18th Dec. 2018. 512 pp. ISBN: 1107043018. URL: https://www.ebook.de/de/product/22170332/fabio_sauli_gaseous_radiation_detectors.html.

[Sau77]    Fabio Sauli. *Principles of Operation of Multiwire Proportional and Drift Chambers*. 1977.

[Sch11]    Friederike Schöck. 'Studies on atmospheric neutrino oscillations with the ANTARES neutrino telescope. Studien zur Oszillation atmosphärischer Neutrinos mit dem ANTARES Neutrinoteleskop'. PhD thesis. Friedrich-Alexander-Universität Erlangen-Nürnberg (FAU), 14th Feb. 2011. URL: https://nbn-resolving.org/urn:nbn:de:bvb:29-opus-23875 (visited on 18/10/2018).

[Sch13]    Norbert Schmitz. *Neutrinophysik*. 8th Mar. 2013.

[SDJ87]    Ian Shelton, Oscar Duhalde and Albert Jones. 'SUPERNOVA 1987A IN THE LARGE MAGELLANIC CLOUD'. Central Bureau for Astronomical Telegrams, IAUC 4316. 24th Feb. 1987.

[Sew06]    Jan Sewing. 'Entwicklung und Bestimmung der Nachweiseigenschaften des Myon-Detektors für das OPERA-Experiment. Development and determination of the efficiency of the myon detector for the OPERA experiment'. PhD thesis. Universität Hamburg, 2006.

[SI46]    Shoichi Sakata and Takesi Inoue. 'On the Correlations between Mesons and Yukawa Particles'. In: *Progress of Theoretical Physics* 1.4 (Nov. 1946), pp. 143–150. DOI: 10.1143/ptp.1.143.

[Suz06]    Atsuto Suzuki. 'Physics in Next Geoneutrino Detectors'. In: *Earth, Moon, and Planets* 99.1-4 (Dec. 2006), pp. 359–368. DOI: 10.1007/s11038-006-9131-5.

[Tan+18]    M. Tanabashi et al. 'Review of Particle Physics'. In: *Physical Review D* 98.3 (Aug. 2018). DOI: 10.1103/physrevd.98.030001.

[Tim17]    Ashley Michael Timmons. *Search for Sterile Neutrinos with the MINOS Long-Baseline Experiment*. Springer International Publishing, 10th Aug. 2017.

[Tok90]    Walter H. Toki. *Review of Straw Chambers*. Review. SLAC-PUB-5232. Stanford Linear Accelerator Center, 1990. URL: http://slac.stanford.edu/pubs/slacpubs/5000/slac-pub-5232.pdf.

[Vai+99]   A. Vaitaitis et al. 'Search for Neutral Heavy Leptons in a High-Energy Neutrino Beam'. In: *Physical Review Letters* 83.24 (Dec. 1999), pp. 4943–4946. DOI: 10.1103/physrevlett.83.4943.

[Van08]    F. Vannucci. 'Sterile neutrinos: From cosmology to the LHC'. In: *Journal of Physics: Conference Series* 136.2 (Nov. 2008), p. 022030. DOI: 10.1088/1742-6596/136/2/022030.

[Vir01]    T. Virgili. 'Study of the production of strange and multi-strange particles in lead–lead interactions at the CERN SPS: the NA57 experiment'. In: *Nuclear Physics A* 681.1-4 (Jan. 2001), pp. 165–173. DOI: 10.1016/s0375-9474(00)00499-1.

[Wol78]    L. Wolfenstein. 'Neutrino oscillations in matter'. In: *Physical Review D* 17.9 (May 1978), pp. 2369–2374. DOI: 10.1103/physrevd.17.2369.

[Wu+57]    C. S. Wu et al. 'Experimental Test of Parity Conservation in Beta Decay'. In: *Physical Review* 105.4 (Feb. 1957), pp. 1413–1415. DOI: 10.1103/physrev.105.1413.

[Zim+05]   R. Zimmermann et al. 'The precision tracker of the OPERA detector'. In: *Nuclear Instruments and Methods in Physics Research Section A: Accelerators, Spectrometers, Detectors and Associated Equipment* 555.1-2 (Dec. 2005), pp. 435–450. DOI: 10.1016/j.nima.2005.09.003.

[Zub11]    Kai Zuber. *Neutrino Physics, Second Edition (Series in High Energy Physics, Cosmology and Gravitation)*. CRC Press, 2011. ISBN: 1420064711. URL: https://www.amazon.com/Neutrino-Physics-Second-Cosmology-Gravitation/dp/1420064711?SubscriptionId=0JYN1NVW651KCA56C102&tag=techkie-20&linkCode=xm2&camp=2025&creative=165953&creativeASIN=1420064711.

## EIDESSTATTLICHE ERKLÄRUNG

Hiermit erkläre ich an Eides Statt, dass die vorliegende Arbeit von mir selbständig verfasst wurde und ich keine anderen als die angegebenen Hilfsmittel, insbesondere keine im Quellenverzeichnis nicht benannten Internet-Quellen, benutzt habe. Sämtliche Stellen der Arbeit, die im Wortlaut oder dem Sinn nach anderen gedruckten oder im Internet verfügbaren Werken entnommen sind, habe ich durch genaue Quellenangaben kenntlich gemacht. Die Arbeit wurde von mir vorher nicht in einem anderen Prüfungsverfahren eingereicht. Die eingereichte schriftliche Fassung entspricht der auf dem elektronischen Speichermedium. Ich bin damit einverstanden, dass das Werk veröffentlicht wird.

_Freie und Hansestadt Hamburg, Datum_                    _Unterschrift_

## STATUTORY DECLARATION

I hereby declare that I have authored this thesis independently and that I have not used other than the declared resources, in particular no Internet resources that are not labelled in the bibliography. I have explicitly marked all material which has been quoted either literally or by content from the used sources. This thesis has not been submitted in another examination procedure before. The submitted, written version conforms with the one on the electronic storage medium. I agree that the thesis will be published.

_Free and Hanseatic City of Hamburg, date_                    _Signature_